UCSF
UC San Francisco Electronic Theses and Dissertations

Title
Multi-modality imaging for improved staging of prostate cancer

Permalink
https://escholarship.org/uc/item/3jk0t1ns

Author
Wong, Kenneth Howard

Publication Date
2002

Peer reviewed|Thesis/dissertation

eScholarship.org Powered by the California Digital Library
University of California

Multi-Modality Imaging for Improved Staging of Prostate Cancer

by

Kenneth Howard Wong

DISSERTATION

Submitted in partial satisfaction of the requirements for the degree of

DOCTOR OF PHILOSOPHY

in

Bioengineering

in the

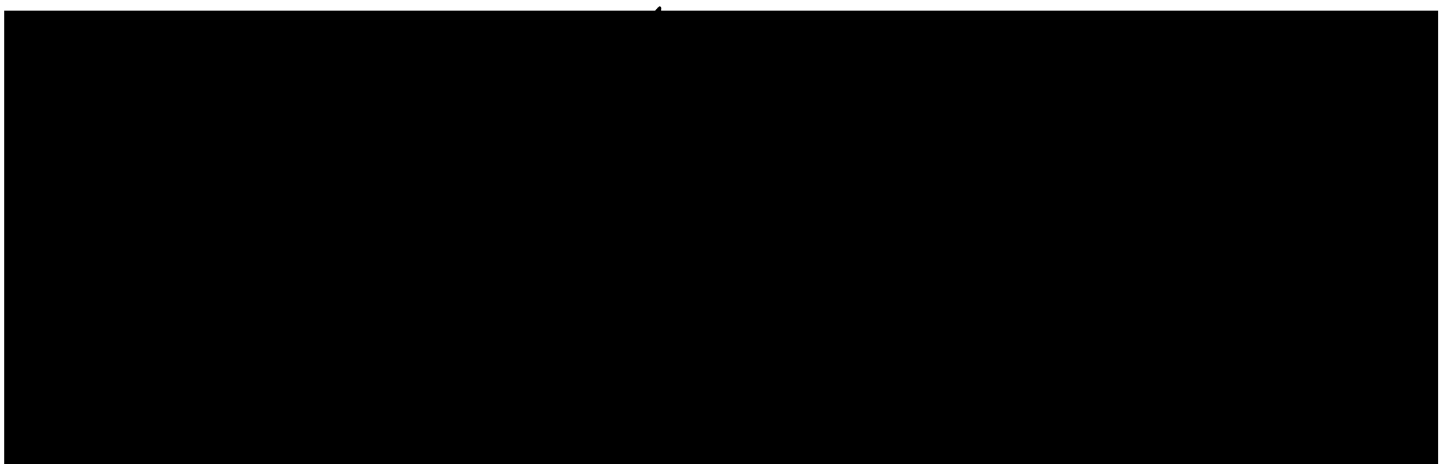
GRADUATE DIVISIONS

of the

UNIVERSITY OF CALIFORNIA SAN FRANCISCO

and

UNIVERSITY OF CALIFORNIA BERKELEY



Date University Librarian

Degree Conferred: .....

copyright 2002

by

Kenneth Howard Wong

Dedication

From my earliest years, when I dreamt of becoming a scientist and learning more about the world and how it worked, my family has been a wellspring of optimism and a rock of stability in my life. Knowing that I could always count on their unconditional love (and indomitable sense of humor) has made every step of my life easier, and I would not have made it this far without them. I thank my brother, Peter, for his dedication and spirit of stewardship, which continually inspire me. I hope that we will have many more late night discussions about the state of the world and the chance to travel to interesting places. I thank my sister, Donna, for cheering me on and for being able to share my experiences with research and science. Online chats (and countless Starcraft battles against the Zerg) with her and her husband Chris have kept us all close across the miles, and made for many great memories. For my Mom, I am eternally thankful, both for the gift of my life and the wisdom and strength of character to find my way in the world. I think that I am only beginning to understand the magnitude of the sacrifices that she made to help us all grow and flourish, but with each bit of understanding I appreciate her more and more. We've shared a lot of good times and bad times, and these experiences have helped us to forge an incredible bond, and I know that the future will make it even stronger.

To my 'other brother' Peter C. Wong, who was one of my first friends during my undergraduate years at Brandeis and my best man when I got married: you are the friend who is like a brother to me and my family. Thanks for being there during both the pivotal and the mundane times with a quick, funny wit and a boundless desire to help.

When I arrived in California for graduate school, I had the amazing good fortune to share a house with Aron Clymer, a new graduate student in geology. Through him, I also came to know another geology student, Tim Culler. These essentially random events have grown into some of my most cherished friendships, and along the way both of them have married truly excellent partners, Laury Clymer and Beth Culler. Our friendships have been nourished by plenty of late night gaming, backyard grilling, pasta dinners, TV nights, camping trips, and shared holidays, and it would be a huge understatement to say that they are one of the highlights of living in the Bay Area. I know that they are all very happy to see my thesis done and my life returning to normal, especially Tim, who has been searching high and low for a Lem rune.

Debra Harris, the 'den mother' and former administrative coordinator for Bioengineering, deserves special mention for her support of me after a pretty rocky start to graduate school. There were a lot of times during the first year when I felt completely out of place, but she was always enthusiastic about what I could contribute to Bioengineering.

I've also been lucky to work with a terrific group of scientists during my time here, who have shown me the ropes and helped guide my career in the right directions. Roger Tang taught me a lot about clever programming, physical insight, image analysis, and where to poke the CT/SPECT scanner when it broke down. Max Wu always provided a good sounding board for ideas and an inspiring ability for tackling tough research problems; he

was also kind enough to let me learn by fumbling around with his mouse experiments. Sharing an office with them was great, even when they turned out to be much better at Quake 3 than me. Angela DaSilva and Koji Iwata provided excellent mentoring as postdocs in our lab, and helped me learn the finer points of experimental imaging, grant writing, and just being a good scientist. During the last year or so the lab has acquired a new generation of scientists: Bill Barber, Andrew Hwang, and Anne Sakdinawat. They've brought in fresh new perspectives and vigor, and I know that they will continue to make the lab a fun place to work.

My research advisors have been true mentors to me and have given me fantastic examples of the sort of professor that I one day hope to be. Stan Prussin's incredible enthusiasm and love of science and engineering are truly infectious, and I see my time working with him in the Nuclear Engineering department as being a real turning point in my graduate career. Even though I didn't ultimately end up doing my dissertation work there, I learned a lot about nuclear physics and angiogenesis, and it was great fun. Hopefully we'll have the chance to work on other projects in the future. My dissertation advisor, Bruce Hasegawa, has provided me with much insight in the fields of medical imaging and scientific writing. He's also shown me by example how to run a great lab, where younger scientists can explore the field and mature in their own directions, yet they always know that the research group is ready and willing to help them out. His concern and respect for students has always impressed me and many other students in Bioengineering, and with luck I will be able to emulate those qualities as I go out into the research world. David Price in the Nuclear Medicine Section at UCSF helped me to more fully understand the clinical problems of prostate imaging, and how advanced technology translates into better patient care.

Finally, I want to thank my beautiful, loving, and wonderful wife, Andrea C. Kramer, who has been there with me through all of the tribulations and successes of graduate school. From the early times when I was filled with self-doubt, through the ups and downs of a complex research project, and finally on all those nights when it seemed my thesis was an insurmountable task, she was always there with enthusiasm and faith. She is the seal that I have set upon my heart, and marrying her was one of the best things that ever happened to me. As my time in graduate school was coming to a close, she was beginning her own graduate studies in Theology, so I am looking forward to sharing this new experience and many others with her as we walk the road of life together.

Since I am, as usual, writing this late at night, I'm sure that I've forgotten someone important, so I'll just close with a blanket statement thanking all those who have helped me accomplish this mighty work.

Woohoo! It's all done!

Preface

Components of the CT/SPECT system used in this research were provided by an equipment grant from GE Medical Systems. Funding support for this research project was provided through the UCSF Radiology Research and Education Fund, a National Institutes of Health grant (NIH 5R21-CA86893 "Improved Prostate Staging with Dual-Mode Imaging"), and an unrestricted gift from Cytogen Corporation.

We also wish to acknowledge the assistance and guidance of the physicians, technologists, and staff in the Nuclear Medicine Section: Randall Hawkins, David Price, Mohan Ramaswamy, Gary Caputo, Juanita Yun, Sylvia Corpuz, Carole Schreck, and Julia Clark. The collaboration of referring physicians Mack Roach, III and I-Chow Joe Hsu from the Department of Radiation Oncology was essential for the success of this project, as was the technical advice from Paula Zeiter and Barbara Rogers at Cytogen.

Patients for this dissertation work were recruited from the UCSF patient population according to institutional guidelines established by the Committee on Human Research (CHR). The research protocol was initially approved and annually reviewed by the CHR as approval number H5294-16260-01B.

Abstract

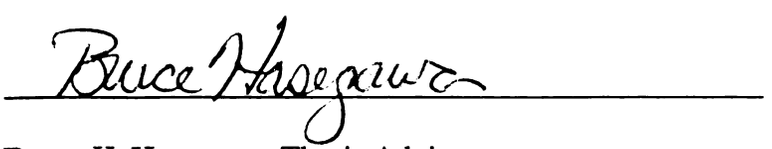
Multi-Modality Imaging for Improved Staging of Prostate Cancer
by Kenneth Howard Wong

The treatment of patients with prostate cancer depends heavily on determining disease extent, but such information is difficult to obtain with conventional empirical staging methods or structural imaging. ^{111}In-ProstaScint® is a nuclear medicine agent that binds to the prostate-specific membrane antigen (PSMA), enabling it to identify prostate cancer cells anywhere in the body. Despite this useful biological property, ^{111}In-ProstaScint® suffers limitations inherent to nuclear medicine studies: poor photon statistics, attenuation, collimator blurring, and non-specific uptake.

To overcome these limitations, we developed a method of ^{111}In-ProstaScint® imaging based on a combined CT/SPECT system. This system acquires CT and SPECT images of the patient sequentially and registers the images together using fiducial markers. The CT provides anatomic localization, which can discriminate potential tumor sites from non-specific uptake, and is also used to generate a patient-specific attenuation map, which models the dual-energy emissions from ^{111}In. This attenuation map and a model of the distance-dependent collimator resolution are incorporated into an iterative SPECT reconstruction that increases the quality and quantitative accuracy of the SPECT image. Components of the reconstruction are also used to apply template-projection reconstruction techniques for measuring the activity concentration in CT-defined regions of interest.

We tested the quantitative accuracy of the CT/SPECT system by imaging phantoms that simulated ^{111}In-ProstaScint® patients. In these phantoms, we were able to measure the activity concentration of simulated tumors to within 10% accuracy for large (3.2 cm) objects and 30% to 40% accuracy for smaller (1.8 cm and 1.2 cm) objects. We

also performed a pilot clinical study of combined CT/SPECT ^{111}In-ProstaScint® imaging on patients undergoing conventional ^{111}In-ProstaScint® SPECT studies. The iterative reconstruction (with corrections for photon attenuation and collimator blurring) significantly improved the quality of the nuclear medicine images. Furthermore, in three of thirteen patients, the ability to register CT and SPECT images together clarified SPECT images that might otherwise have produced equivocal results. Quantitative measurements of ^{111}In-ProstaScint® uptake did not correlate well with empirical staging algorithms predicting lymph node metastases; however, future studies with a larger patient population could help illuminate the relationship between these two different measures of disease.



Bruce H. Hasegawa, Thesis Advisor

Chapter 1: Prostate Cancer
A Background Inf
B Epidemiology
C The Importance of P
D Methods for Staging P
1 TNM Classification
2 Partin Tables
3 Pelvic Lymph N
4 MRI: Magnetic
5 CT: Computed
6 FDG-PET: P
7 Choline-based-PET
8 Bone Scintigraphy
9 In-Pr
E Project Goals

Chapter 2: Fundamentals of
A Interaction of Ionizing
1 Incoherent Scatter
2 Photoelectric Effect
3 Attenuation Coefficients
B X-Ray Computed
1 Hardware
2 Tomographic Reco
3 Image Properties
C Single Photon Emission
1 Hardware Fundamentals
2 Tomographic recon
3 Image Properties
D Summary

Chapter 3: Combined CT SPE
A Introduction
1 Clinical rationale for
2 Limitations of current
3 Advantages of a com
B Multimodality imaging
1 The ETCT System
2 The Combined CT SP
C Summary

Chapter 4: CT SPECT Image Re
A Introduction
1 The need for image re

Table of Contents

Chapter 1: Prostate Cancer 1
A. Background Information 1
B. Epidemiology 2
C. The Importance of Prostate Cancer Staging 3
D. Methods for Staging Prostate Cancer 8
1. TNM Classification 9
2. Partin Tables 10
3. Pelvic Lymph Node Dissection 11
4. MRI /S (Magnetic Resonance Imaging/Spectroscopy) 12
5. CT (Computed Tomography) 13
6. ^{18}FDG-PET (Positron Emission Tomography) 15
7. Choline-based-PET 17
8. Bone Scintigraphy 17
9. ^{111}In-ProstaScint® SPECT 19
E. Project Goals 21

Chapter 2: Fundamentals of Imaging Physics 24
A. Interaction of Ionizing Radiation and Matter 25
1. Incoherent scattering 26
2. Photoelectric Effect 28
3. Attenuation Coefficients 29
B. X-Ray Computed Tomography (CT) 31
1. Hardware 31
2. Tomographic Reconstruction for CT 35
3. Image Properties 41
C. Single Photon Emission Computed Tomography (SPECT) 43
1. Hardware Fundamentals 44
2. Tomographic reconstruction for SPECT 48
3. Image Properties 54
D. Summary 57

Chapter 3: Combined CT/SPECT Imaging 59
A. Introduction 59
1. Clinical rationale for multi-modality imaging 59
2. Limitations of current methods 60
3. Advantages of a combined CT/SPECT system 61
B. Multi-modality imaging devices 64
1. The ETCT System 64
2. The Combined CT/SPECT system 66
C. Summary 67

Chapter 4: CT/SPECT Image Registration 70
A. Introduction 70
1. The need for image registration 71

2 Approaches to
3 The UCSF CT SPE
B Mathematics of Proje
C Implementation of the
1 Introduction and O
2 Ellipsoid Marker Det
3 Determination of M
4 Transforms Between
5 Optimization of In
D Validation of the Re
1 Introduction and O
2 Experimental Meth
3 Results
4 Discussion
E Summary

Chapter 5: Improved Recon
A Introduction
1 Clinical Motivation
2 Overview
B Modeling the Imaging Pr
1 Overview
2 Photon Attenuation
3 Dual-Energy Atten
4 Collimator Blurring
5 Computational Imple
6 Advantages of this re
7 Limitations of this re
C Basic Experimental Tests
1 Overview
2 Dual-energy attenuation
3 Spatial Uniformity mea
D Experimental Results
1 Dual-energy attenuation
2 Spatial Uniformity mea
E Discussion
1 Benefits of the dual-ene
2 Benefits of attenuation
F Summary

Chapter 6: In SPECT Phantom
A Introduction
1 Motivation
2 Limitations of existing
B CT SPECT Quantitation Te
1 Direct measurements f

2. Approaches to image registration 72
3. The UCSF CT/SPECT approach 76
B. Mathematics of Fiducial Marker Registration 77
C. Implementation of the Registration System 80
1. Introduction and Overview 80
2. Fiducial Marker Design 81
3. Determination of Marker Centers 84
4. Transforms Between Coordinate Spaces 85
5. Optimization of Imaging Parameters 86
D. Validation of the Registration System in Patient Studies 92
1. Introduction and Overview 92
2. Experimental Methods 93
3. Results 96
4. Discussion 99
E. Summary 104

Chapter 5: Improved Reconstruction for SPECT 106
A. Introduction 106
1. Clinical Motivation 106
2. Overview 107
B. Modeling the Imaging Process 109
1. Overview 109
2. Photon Attenuation 110
3. Dual-Energy Attenuation Correction 120
4. Collimator Blurring 127
5. Computational Implementation of Iterative Reconstruction 133
6. Advantages of this reconstruction technique. 136
7. Limitations of this reconstruction technique 136
C. Basic Experimental Tests of the Reconstruction Algorithm 138
1. Overview 138
2. Dual-energy attenuation test 139
3. Spatial Uniformity measurements 140
D. Experimental Results 143
1. Dual-energy attenuation results 143
2. Spatial Uniformity measurements 146
E. Discussion 152
1. Benefits of the dual-energy attenuation theory 152
2. Benefits of attenuation and collimator corrections. 152
F. Summary 154

Chapter 6: ^{111}In SPECT Phantom Studies 156
A. Introduction 156
1. Motivation 156
2. Limitations of existing quantitation techniques. 157
B. CT/SPECT Quantitation Techniques 161
1. Direct measurements from the reconstructed image 161

2 Template-proj
3 Previous
C Experimental Meth
1 Overview
2 Uniform Ca
3 Phantom Sim
D Experimental Res
1 Uniform Ca
2 In-Pro
E Discussion
F Summary

In-Pro
A Introduction and M
1 Prostate cancer
2 Review of Res
B Experimental Methods
1 Overview
2 Patient Recruitment
3 Imaging Protocol
4 Image Reconstruc
5 Quantitative Measure
C Results
1 Comparison of Image
2 Advantages of CT-SPE
3 Quantitative Res
D Discussion
1 Limitations of this
2 Quantitation results
3 Improved image
E Summary

Future Possibilities
A Future developments for
1 A brief historical
2 A new system for
B The future for In-Pro
1 Image-guided radiation
2 PSMA-based therapies
C Conclusions

2. Template-projection-reconstruction methods 162
3. Previous quantitative studies using these methods 170
C. Experimental Methods 171
1. Overview 171
2. Uniform Calibration Tanks 172
3. Phantom Simulation of ^{111}In-ProstaScint® Study 175
D. Experimental Results 183
1. Uniform Calibration Tank 183
2. ^{111}In-ProstaScint® Phantom 184
E. Discussion 190
F. Summary 193

Chapter 7: ^{111}In-ProstaScint® Patient Studies with the CT/SPECT System 196
A. Introduction and Motivations 196
1. Prostate cancer staging and ^{111}In-ProstaScint® 196
2. Review of Research Goals 198
B. Experimental Methods 199
1. Overview 199
2. Patient Recruitment and Selection 200
3. Imaging Protocol 202
4. Image Reconstruction and Analysis 206
5. Quantitative Measurements 208
C. Results 216
1. Comparison of Image Reconstruction Methods 216
2. Advantages of CT/SPECT ^{111}In-ProstaScint® Imaging. 219
3. Quantitative Results 224
D. Discussion 232
1. Limitations of this study 232
2. Quantitation results 234
3. Improved image reconstruction and combined CT/SPECT 236
E. Summary 238

Chapter 8: Future Possibilities for ^{111}In-ProstaScint® and CT/SPECT Imaging 240
A. Future developments for combined CT/SPECT Imaging. 241
1. A brief historical perspective 241
2. A new system for combined CT/SPECT imaging. 242
B. The future for ^{111}In-ProstaScint® 246
1. Image-guided radiation therapy. 247
2. PSMA-based therapies 248
C. Conclusions 250

List of Tables

Table 1-I: Explanation of the TNM classification for prostate cancer. 10

Table 5-I: Chemical composition of the solutions in the calibration phantoms. 114

Table 5-II: Hounsfield Unit values from the CT calibration phantom. 115

Table 5-III: Mean and standard deviation of the pixel values in the central region of the uniform tank phantom, for the different reconstruction methods. 150

Table 5-IV: Mean and standard deviation of the pixel values in a smaller central region of the uniform tank phantom, for the different reconstruction methods. 151

Table 6-I: List of the spheres that were used to simulate tumors inside the cylindrical phantom.....178

Table 6-II: Template-projection-reconstruction measurements for the ^{111}In-ProstaScint®-simulating phantom. 189

Table 7-I: Indicators for ^{111}In-ProstaScint® scanning for newly diagnosed prostate cancer patients.....200

Table 7-II: Research patient demographics. 202

Table 7-III: Pearson product-moment correlations between the different measures of quantitative uptake. 231

Table 8-I: Comparison of CT parameters between the Hawkeye System and Conventional CT. 244

Li

Figure 1-1: Anatomy of the p

Figure 1-2: Epidemiological data
as a function

Figure 1-3: Prostate cancer pa

Figure 1-4: Schematic of a typ

Figure 1-5: Schematic diagram

Figure 1-6: Schematic diagram

Figure 2-1: Schematic of Comp

Figure 2-2: Illustration of pr

Figure 2-3: Bremsstrahlung X-r
with a peak

Figure 2-4: Geometry for fan-b

Figure 2-5: CT Image reconstr

Figure 2-6: Spatial and frequ

Figure 2-7: Example CT image
backprojection

Figure 2-8: Illustration of gamm

Figure 2-9: Example In-Proje
reconstructed w

Figure 2-10: Example SPECT im
ML-EM algorithm

Figure 2-11: Collimator effects o

Figure 3-1: Schematic diagram
(ETCT) system

List of Figures/Illustrations

Figure 1-1: Anatomy of the prostate, surrounding tissues, and pelvic lymph nodes. 1

Figure 1-2: Epidemiologic data on the incidence of newly diagnosed prostate cancer as a function of age. 3

Figure 1-3: Prostate cancer patient management flowchart 5

Figure 1-4: Schematic of a typical x-ray CT system. 14

Figure 1-5: Schematic diagram of a PET system 16

Figure 1-6: Schematic diagram of gamma camera imaging. 18

Figure 2-1: Schematic of Compton scattering event 26

Figure 2-2: Illustration of photon attenuation in a uniform material. 30

Figure 2-3: Bremsstrahlung x-ray spectral output from a typical x-ray tube operated with a peak voltage of 150kV. 33

Figure 2-4: Geometry for fan-beam reconstruction of CT images. 36

Figure 2-5: CT Image reconstructed using simple backprojection 38

Figure 2-6: Spatial and frequency domain representations of the filter function H(w). 39

Figure 2-7: Example CT image of a patient's pelvis, reconstructed with filtered backprojection. 40

Figure 2-8: Illustration of gamma camera position determination. 47

Figure 2-9: Example ^{111}In-ProstaScint® SPECT image of a patient's pelvis, reconstructed with filtered backprojection 51

Figure 2-10: Example SPECT image of a patient's pelvis, reconstructed using an ML-EM algorithm 53

Figure 2-11: Collimator effects on resolution 56

Figure 3-1: Schematic diagram of the Emission-Transmission Computed Tomography (ETCT) system. 64

Figure 3.2: Schematic diagram

Figure 4.1: Schematic diagram
registration

Figure 4.2: Photograph of the

Figure 4.3: CT and NPI (CT im

Figure 4.4: Photograph
and the phan

Figure 4.5: Effect of

Figure 4.6: Average regist
images of patient

Figure 4.7: Example of a CT NPI

Figure 4.8: Example of a CT NPI

Figure 5.1: "In-Prostascint" NPI
filtered backpro

Figure 5.2: Schematic diagram
the CT system

Figure 5.3: CT scan of the bone
Hounsfield Units

Figure 5.4: Linear Attenuation
materials in the C

Figure 5.5: Calibration curve rela
300 keV photons

Figure 5.6: Decay scheme for

Figure 5.7: Schematic for attenu

Figure 5.8: Plot and logarithmic
vs photon energy

Figure 5.9: Variation in the effec
function of mater

Figure 3-2: Schematic diagram of the Combined CT/SPECT system.....66

Figure 4-1: Schematic diagram of the fiducial marker used for CT/SPECT image registration. 81

Figure 4-2: Photograph of the fiducial marker used for CT/SPECT image registration. ..82

Figure 4-3: CT and SPECT images illustrating the appearance of fiducial markers.....83

Figure 4-4: Photograph illustrating placement of fiducial markers on the imaging table and the phantom. 88

Figure 4-5: Effect of various CT slice thicknesses on marker center localization. 90

Figure 4-6: Average registration error over each patient's markers for CT/SPECT images of patient studies. 97

Figure 4-7: Example of a CT/SPECT image with problematic registration. 100

Figure 4-8: Example of a CT/SPECT image with excellent registration.....101

Figure 5-1: ^{111}In-ProstaScint® SPECT image of the pelvis, reconstructed using filtered backprojection. 107

Figure 5-2: Schematic diagram of the phantom used for attenuation calibration of the CT system. 113

Figure 5-3: CT scan of the bone densitometry phantom used to calibrate Hounsfield Units to attenuation coefficients.....115

Figure 5-4: Linear Attenuation Coefficients as a function of photon energy for the materials in the CT calibration phantoms. 117

Figure 5-5: Calibration curve relating CT numbers to attenuation coefficients for 300 keV photons. 118

Figure 5-6: Decay scheme for ^{111}In. 121

Figure 5-7: Schematic for attenuation of a dual-energy isotope. 122

Figure 5-8: Plot and logarithmic fitting of water linear attenuation coefficients vs. photon energy. 125

Figure 5-9: Variation in the effective attenuation coefficient μ_{eff} for water as a function of material thickness x. 126

Figure 5-11: Illustration of
Figure 5-12: Example image
Figure 5-13: Radial profiles
Figure 5-14: Plot of
distance betwe
Figure 5-15: Basic geometry
iterative rec
Figure 5-16: Direct measure
photons in p
Figure 5-17: Direct measure
photons in p
Figure 5-18: Tomographic im
with filtered
Figure 5-19: Tomographic ima
an iterative
Figure 5-20: Tomographic ima
using an iterative
collimator correc
Figure 5-21: Tomographic ima
using an iterative
collimator correc
Figure 5-22: Illustration of the
an iterative
Figure 6-1: Illustration of the
In-ProstaScint
Figure 6-2: Illustration of the
Figure 6-3: Diagram of the
Figure 6-4: Illustration of
reconstruction

Figure 5-10: Illustration of collimator blurring effect. 127

Figure 5-11: Example images of collimator blurring effect. 130

Figure 5-12: Radial profiles of the images shown in Figure 5-11. 130

Figure 5-13: Plot of collimator blurring width parameter as a function of distance between the source and collimator 131

Figure 5-14: Basic geometry for the object-rotating-resampling iterative reconstruction 135

Figure 5-15: Direct measurement of the effective attenuation coefficient for ^{99m}Tc photons in polyethylene. 144

Figure 5-16: Direct measurement of the effective attenuation coefficient for ^{111}In photons in polyethylene.. 145

Figure 5-17: Tomographic image and line profile of the uniform tank, reconstructed with filtered backprojection. 146

Figure 5-18: Tomographic image and line profile of the uniform tank, reconstructed using an iterative algorithm without attenuation or collimator correction. 147

Figure 5-19: Tomographic image and line profile of the uniform tank, reconstructed using an iterative algorithm with attenuation correction, but without collimator correction. 147

Figure 5-20: Tomographic image and line profile of the uniform tank, reconstructed using an iterative algorithm without attenuation correction, but with collimator corrections. 148

Figure 5-21: Tomographic image and line profile of the uniform tank, reconstructed using an iterative algorithm with attenuation and collimator correction. 148

Figure 5-22: Illustration of the central ROI used for calculating image uniformity 150

Figure 6-1: Illustration of semi-quantitative imaging approach used for ^{111}In-ProstaScint® by Sodee, et al 158

Figure 6-2: Illustration of the template-projection-reconstruction process. 164

Figure 6-3: Diagram of the cylindrical ^{111}In-ProstaScint® phantom. 178

Figure 6-4: Illustration of background regions used for template-projection reconstruction 182

Figure 5: Reconstructed
indium tank

Figure 6: CT-measured
of the CT

Figure 7: CT-measured
function

Figure 8: Direct measure
on iterative
corrections

Figure 9: Direct measure
on iterative
collimator

Figure 1: Example of
In-Prostas

Figure 2: Illustration of

Figure 3: Illustration of

Figure 4: Illustration of the

Figure 5: Illustration of the

Figure 6: SPECT images
iterative

Figure 7: SPECT images
correction only
collimator

Figure 8: SPECT image
correction only
filter (right)

Figure 9: CT SPECT
the lower abdo

Figure 10: CT SPECT
uptake at prostate

Figure 6-5: Reconstructed voxel values versus activity concentration for the uniform indium tank. 183

Figure 6-6: CT-measured target sphere volume (for the 32 mm sphere) as a function of the CT value threshold. 185

Figure 6-7: CT-measured target sphere volume (for the 18 and 12 mm spheres) as a function of the CT value threshold. 185

Figure 6-8: Direct measurement of the activity concentration in the tumor spheres, based on iterative reconstruction with attenuation correction and collimator corrections. 187

Figure 6-9: Direct measurement of the activity concentration in the tumor spheres, based on iterative reconstruction with attenuation correction, but without collimator corrections. 187

Figure 7-1: Example of templates used to measure the concentration of ^{111}In-ProstaScint® within the prostate. 210

Figure 7-2: Illustration of region of interest in the descending aorta. 212

Figure 7-3: Illustration of region of interest in the iliac spine. 212

Figure 7-4: Illustration of the region of interest in the obturator muscle 213

Figure 7-5: Illustration of the region of interest in the intestines. 214

Figure 7-6: SPECT images reconstructed with filtered backprojection (left) and iterative reconstruction with attenuation correction only (right). 216

Figure 7-7: SPECT images reconstructed with iterative reconstruction with collimator correction only (left) and iterative reconstruction with attenuation and collimator correction (right). 217

Figure 7-8: SPECT image reconstructed using iterative reconstruction with attenuation correction only (left) and the same image after application of a low-pass filter (right) 218

Figure 7-9: CT/SPECT ^{111}In-ProstaScint® images from patient with abnormal uptake in the lower abdomen. 219

Figure 7-10: CT/SPECT ^{111}In-ProstaScint® images of patient with elevated radiotracer uptake at prostate base. 220

Figure 7-11 CT SPECT [illegible]
liver uptake

Figure 7-12 Total counts [illegible]

Figure 7-13 Histogram [illegible]
the In-Pr[illegible]

Figure 7-14 In-Pr[illegible]

Figure 7-15 In-Pr[illegible]

Figure 7-16 In-Pr[illegible]

Figure 7-17 In-Pr[illegible]

Figure 7-18 In-Pr[illegible]

Figure 7-19 Summary chart [illegible]
In-Pr[illegible]

Figure 7-20 Plot of the pr[illegible]
Positivity [illegible]

Figure 8-1 Schematic of the [illegible]

Figure 7-11: CT/SPECT ^{111}In-ProstaScint® image of patient with abnormal but benign liver uptake.....222

Figure 7-12: Total counts in SPECT projection data from the CT/SPECT system.....224

Figure 7-13: Histogram of anatomical locations of the maximum voxel value in the ^{111}In-ProstaScint® SPECT image.....225

Figure 7-14: ^{111}In-ProstaScint® concentration within the prostate or prostate bed. 226

Figure 7-15: ^{111}In-ProstaScint® concentration within the descending aorta.....227

Figure 7-16: ^{111}In-ProstaScint® concentration within the iliac spine. 228

Figure 7-17: ^{111}In-ProstaScint® concentration within the obturator muscle.....228

Figure 7-18: ^{111}In-ProstaScint® concentration within the intestinal region.....229

Figure 7-19: Summary chart of quantitative measurements of ^{111}In-ProstaScint® uptake.....230

Figure 7-20: Plot of the prostate/obturator ratio versus percentage risk of lymph node positivity. 232

Figure 8-1: Schematic of the GE Medical Systems Hawkeye CT/SPECT system.....242

Chapter 1: Prostate Cancer

A. Background Information

The prostate is a walnut-sized glandular organ found only in men. It is located in the pelvis, posterior to the pubic symphysis, anterior to the rectum, and inferior to the bladder as shown in Figure 1-1. The physiological function of the prostate is to produce seminal fluids that assist in the travel and metabolic support of sperm cells produced in the testes. These fluids are introduced into the urethra, which passes through the prostate interior. Internally, the prostate can be divided into three zones. The transition zone encircles the urethra. The peripheral zone forms the outer surface of the prostate gland. This area of the prostate is typically the largest and contains the most glandular tissue, so most prostate cancers originate in this zone. The central zone is located between the transition zone and the peripheral zone. The most anterior portion of the gland is referred to as the apex, and the most posterior portion is referred to as the base. The prostate is also divided into left and right lobes.

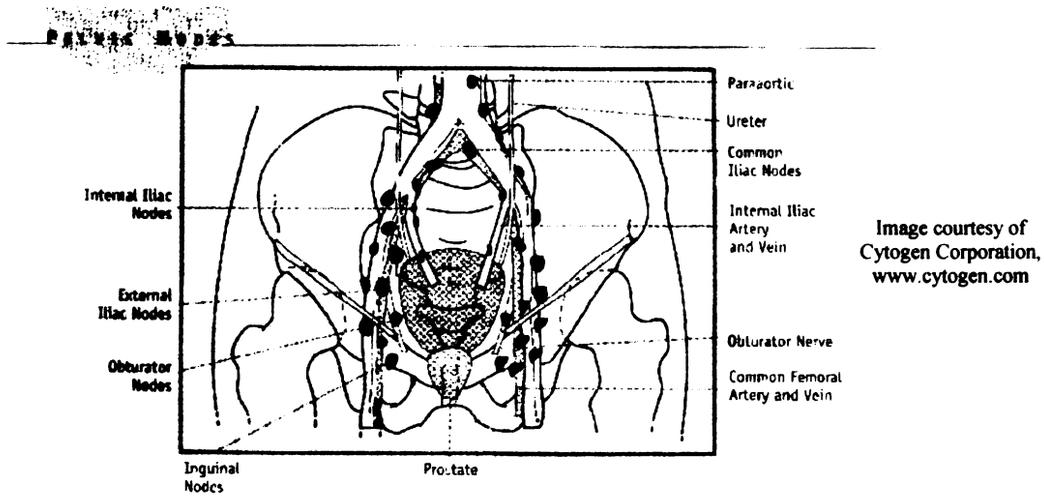


Figure 1-1: Anatomy of the prostate, surrounding tissues, and pelvic lymph nodes.

The prostate gland is encased in a membranous capsule, which serves to isolate the gland from surrounding structures. The capsule also limits the expansion of the prostate in hyperplastic states, and prevents the physical egress of cancer cells. Prostate cancer that is limited to the gland is said to be organ-confined, and typically has a much better prognosis than prostate cancers where the capsule has been breached. If the capsule is no longer intact, the cancer can spread locally, and typically will involve the seminal vesicles, the rectum, or the bladder.

The pelvic lymphatic system is also of importance for prostate cancer, since natural drainage channels from the prostate can provide a means for prostate cancer cells to metastasize into the lymph nodes and ultimately to other organs. Some of these lymph nodes are shown in Figure 1-1. Typically, prostate cancer will be found in a progression of lymph nodes from those closest to the prostate to distant nodes, but so called 'skip metastases' can also occur where the cancer is first detected in a distant node without the presence of regional disease[1].

B. Epidemiology

Prostate cancer is a significant disease among older men. The incidence of prostate cancer in U.S. men is second only to nonmelanoma skin cancer, and only lung cancer causes more deaths. Projections from the American Cancer Society estimated that during 2001, roughly 198,000 new cases of prostate cancer would have been diagnosed and 31,500 men would have died of this disease. This figure represents approximately 11% of the overall male death rate.[2]. The incidence of prostate cancer also rises significantly with age, as demonstrated by epidemiological data collected by the National Cancer Institute between 1992 and 1997 (Figure 1-2)[3]:

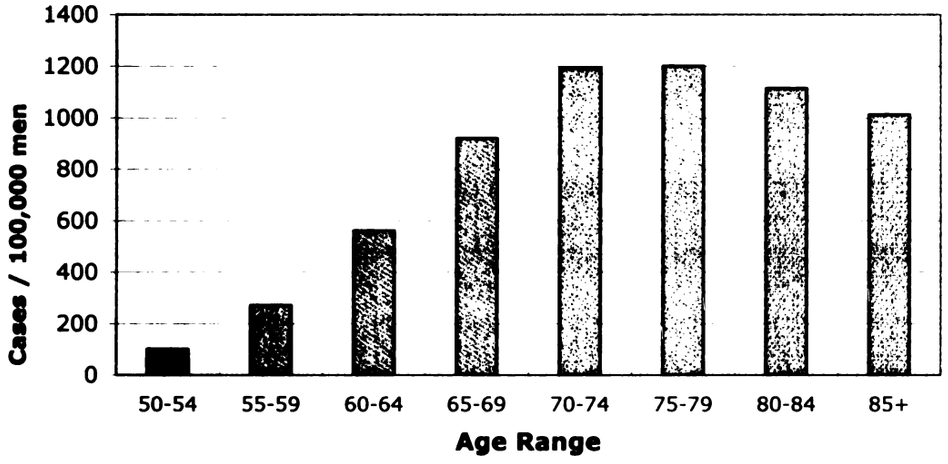


Figure 1-2: Epidemiologic data on the incidence of newly diagnosed prostate cancer as a function of age.

In general, African-American men have the highest incidence of prostate cancer, whereas Asian and Native American men have the lowest rates. Although the causes of prostate cancer are not yet completely understood, both genetic and environmental factors (such as diet) can contribute to one's overall risk[4].

C. The Importance of Prostate Cancer Staging

At the time of a patient's initial diagnosis of prostate cancer, the disease can present in a wide variety of forms. In the early phases of the disease, the cancer is confined to the prostate gland itself and its surrounding fibrous capsule. Its rate of growth is usually slow, and the prostate cells are only slightly changed from their normal glandular phenotype. As the disease progresses, the cancer cells change more dramatically, and the tumor begins to invade the surrounding tissue. In the final stages, the cancer spreads through the circulatory system and metastasizes to the lymph nodes and distant organs, especially the skeletal system, lungs, and liver. As the disease progresses, it becomes

more and more difficult to treat successfully, which is why early detection of prostate cancer is so important.

It is generally accepted that prostate cancer starts as a slow-growing, confined disease and irrevocably progresses through these evolutionary steps to metastatic disease. However, the biochemical triggers for these changes and the time scales over which these changes take place are unknown. In some men, the cancer is indolent and grows very slowly over the course of many years, causing few complications and having little effect on the patient's life. Autopsy series performed on men have demonstrated that a large percentage of elderly men who die for other reasons have early stage prostate cancer[5]. However, it is also possible for prostate cancer to be highly aggressive and to metastasize rapidly through the body, thereby becoming life-threatening in a short span of time. Furthermore, there are significant differences in individual patient physiology and the frequency with which patients are screened for prostate cancer. Thus, when a patient is diagnosed with prostate cancer, it is vitally important to know the severity or stage of the disease in that patient.

The typical process of managing a patient with prostate cancer is shown schematically in Figure 1-3, along with some of the medical procedures used in this process. Most patients first begin to suspect prostate cancer because of physical symptoms, such as difficulty in urinating or incontinence, irregularities on digital rectal exam, or results from PSA screening. PSA (prostate-specific antigen) is expressed by all prostate tissue, but is normally present only in very low (< 1ng/ml) levels in the blood. Elevation of PSA hints that something is amiss in the body, but PSA testing has a low specificity because the levels of PSA can be elevated by many non-malignant

conditions[6]. Furthermore, there are many steps between the expression of PSA by prostate cancer cells and its appearance in the blood, so PSA levels are not well correlated to disease state. Thus, these initial tests provide a warning, but are not conclusive.

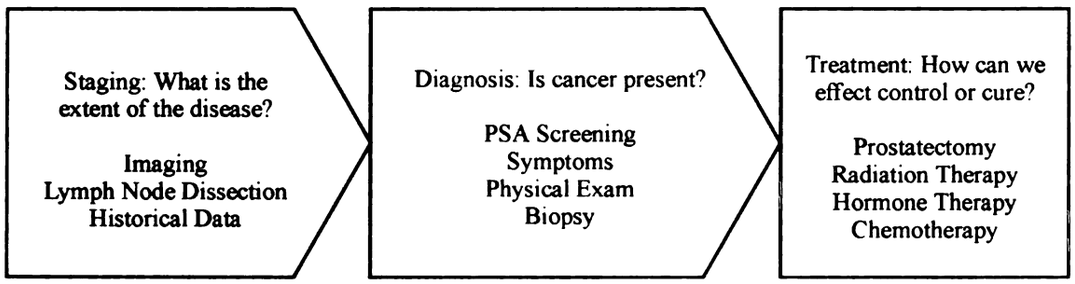


Figure 1-3: Prostate cancer patient management flowchart

Once the screening has revealed something of concern, patients typically undergo biopsy. Small samples of tissue are taken from the prostate using an ultrasound-guided needle. The surgeon uses the ultrasound to locate different regions of the prostate, and removes tissue from two to six locations in the prostate. These samples are then fixed on a slide and sent for pathological analysis. The pathologist evaluates the morphology of the cells and, if they are malignant, grades them using a rating system known as the Gleason score. The Gleason score ranges from 1 to 5, with 1 being very close to normalcy, and 5 being highly characteristic of cancer. Typically, the Gleason scores of the most common cells in the sample are combined with the score from the second most common cells in the sample, which gives the Gleason sum. The Gleason sum can be expressed as a single number i.e. (Gleason 9) or as its component scores (Gleason 4+5). The results of the biopsy thus firmly establish whether or not the patient has cancer, and are considered to be a gold standard.

Although the biopsy can definitively assess the presence or absence of cancer in the prostate, it cannot by itself answer a key question: has the prostate cancer spread beyond the prostate? This question is important because the extent of the prostate cancer determines which therapies are most appropriate for the patient.

Patients with disease confined strictly to the prostate stand to benefit tremendously from an aggressive local approach. A common and effective form of local treatment is prostatectomy, which is the surgical removal of the prostate and a small margin of surrounding tissue. Another local approach is to apply radiation to the prostate by implanting small radioactive pellets directly into the prostate (brachytherapy) or by directing high-energy radiation at the prostate from outside the body (external beam therapy). The radiation is distributed so that it destroys the prostate cancer cells and most of the prostate, but has less of an effect on surrounding tissues such as the rectal wall. Still other local therapies are being developed that use extreme heat or cold to destroy the prostate cancer cells. The common thread in these therapies is that they have the potential to cure the patient by completely eliminating the diseased tissue along with a small amount of normal tissue. The potential side effects of these approaches stem from the fact that numerous important anatomical structures pass through or near the prostate, and these structures can be damaged or destroyed by the therapy. However, improvements in these techniques have significantly reduced their complication rate, and many patients are willing to accept these risks in the hope of a durable cure.

However, patients who have disease outside of the prostate require a much different approach, because a much wider area of effect is needed. One possible therapy is to use external beam radiation, but apply it over a much larger area, such as the entire

pelvis. This has the advantage of treating a large number of potential disease sites, even ones whose location is not precisely known. The concomitant disadvantage is that a much larger amount of normal tissues will also be affected by the radiation, increasing the potential for adverse side effects, such as radiation damage to the gastrointestinal tract. Another approach is hormone therapy, wherein the male hormones are removed from the body's biochemical environment. This can be done surgically, by removal of the testes, or medically, with chemicals designed to either suppress hormone production or remove hormones from the bloodstream. Since male hormones are a growth stimulator for many types of prostate cancer cells, this approach will often halt or slow the growth of the prostate cancer cells. However, the side effects of this approach are significant, as there are many other organ systems that depend on these hormones for their normal function. Furthermore, the removal of growth-stimulating hormones creates selective evolutionary pressure on the cancer cells, which could enhance the survival rate of those cells which do not depend on hormones for their growth. A third treatment option would be chemotherapy. In this therapy, drugs are administered to the patient that selectively attack rapidly dividing cells. Because cancer cells grow at an accelerated rate, these drugs preferentially eradicate the cancer sites. The difficulty with this option is that other cells in the body, such as the bone marrow and the mucus membranes, also contain rapidly dividing cells; these systems are thus also exposed to cytotoxic effects.

Clearly, these non-local treatment options carry with them a much larger potential for adverse side effects, so it is imperative that they not be administered haphazardly to patients who do not need them. Conversely, patients who have disease over a large area are not good candidates for a local therapy. Such therapies would expose the patients to

all of the potential morbidity, yet produce very little therapeutic effect. The staging process must therefore give patients a complete and accurate evaluation of their health and provide the information that will guide them towards the most appropriate treatment for their particular condition.

Up until this point, we have discussed prostate cancer as a newly diagnosed condition. However, staging information is also vital for many of the same reasons in patients with recurrent disease. In these situations, the patient has already received some kind of therapy (and likely experienced a temporary remission), but now manifests new problems related to the cancer. The role of staging here is usually to determine which therapeutic approach should be used as the 'next line of defense'. As an example, consider a patient who has had his prostate removed after the initial diagnosis of localized prostate cancer. If this patient develops new symptoms, it is important to know their source. If the prostate cancer persists locally (i.e., in the prostate fossa), the patient could potentially benefit from radiation therapy to the region. However, if the symptoms appear to stem from metastatic disease that either was missed during the initial staging or has developed since that time, radiation therapy is unlikely to produce any lasting benefit and other therapies would be more appropriate.

D. Methods for Staging Prostate Cancer

Current staging of prostate cancer makes use of many different tests, each with its own strengths and weaknesses. Typically, a patient will receive several of these tests, since each approach is testing a fundamentally different aspect of the patient's health. The radiological tests all have the advantage that they are noninvasive and can search for disease over a fairly wide area at once. Surgical staging methods are considered to be the

most sensitive (since the tissue is examined directly), but they are much more limited in scope and can be prone to sampling errors. There are also empirical formulas based on the past experiences of a large patient population. In this section, we will review these staging methods and discuss their advantages and disadvantages.

1. TNM Classification

The TNM classification of prostate cancer is not by itself a staging technique, but provides a simple nomenclature for categorizing prostate cancer patients. It was developed to provide an objective and uniform staging system, so that patients in many different medical centers could be consistently staged. A summary of the classification is listed in Table 1-I. In this classification system, the T refers to the status of the primary tumor, the N refers to the status of the pelvic lymph nodes, and the M refers to the status of metastatic disease. Thus, a patient who is T3baN1M0 has no distant metastases, but has cancer in the pelvic lymph nodes and penetration of the prostate capsule. Note that the grade of the tumor (see the T1 classification) refers to a pathological evaluation of the type of cells removed from the prostate at the time of biopsy. Low grade cells are those which do not appear significantly different from those of normal prostate tissue, whereas high grade cells are dramatically different from normal prostate tissue.

One useful feature of the TNM system is that the evaluation of the prostate's T stage can be done using simple clinical tests, because this staging criterion is based on the physical extent of the tumor. Thus, the patient's general condition and the digital rectal exam are usually sufficient to determine the T stage, except for perhaps distinguishing between T3ba and T4 tumors. The T stage thus can provide important adjunct information about the state of a patient's cancer. When combined with Gleason scoring

and PSA levels, the T stage forms the basis for the Partin empirical staging system discussed in the following section. The N and M stages for a patient are usually determined by lymph node dissection or the radiologic tests described later in this chapter.

TNM Staging Classifications

TNM Stage	Description
Tx	Primary tumor cannot be assessed
T0	No evidence of primary tumor
T1	Clinically inapparent tumor not palpable nor visible by imaging
T1a	Nonpalpable, with 5% or less of resected tissue with cancer, low grade
T1b	Nonpalpable, with greater than 5% of resected tissue with cancer, and/or high grade
T1c	Nonpalpable, but serum PSA elevated
T2	Tumor confined within prostate
T2a	Palpable, half of 1 lobe or less
T2b	Palpable, greater than half of 1 lobe, but not both lobes
T2c	Palpable, involves both lobes
T3ba	Palpable, unilateral, capsular penetration
T4	Tumor is fixed and invades adjacent structures: bladder neck, rectum, pelvic wall, etc.
Nx	Regional lymph nodes cannot be assessed
N0	No regional lymph node metastasis
N1	Metastasis in regional lymph node or nodes
Mx	Distant metastasis cannot be assessed
M0	No distant metastasis
M1	Distant metastasis

Table 1-I: Explanation of the TNM classification for prostate cancer.

2. Partin Tables

Partin *et al* collected data on PSA levels, Gleason score, and clinical T stage from a large cohort of prostate cancer patients, and correlated these data with evidence of local invasion and lymph node metastases[7]. Multivariate analysis techniques were applied to these data to develop nomograms that describe the likelihood of a particular patient having certain physiological conditions. For example, a patient with a PSA of 12 ng/ml,

a clinical stage of T2b, and Gleason sum of 7 has an 87% chance of having extracapsular disease and a 17% chance of lymph node involvement.[8]

A key advantage of this technique is that it draws from a large patient pool and makes use of readily available data about the patient's condition. It provides a method for counseling patients as to which therapies might be appropriate for them, and can be especially useful when trying to determine what subsequent testing might be appropriate for a newly diagnosed prostate cancer patient. However, it is limited in that it only expresses outcomes in terms of likelihood, rather than being patient specific. For patients who have a very high or very low likelihood of lymph node involvement, this information can be very useful, whereas those patients with a median score will not gain much additional information.

3. Pelvic Lymph Node Dissection

Because pathological results are often used as a gold standard for the presence or absence of disease, removal and study of the approximately 20 pelvic lymph nodes is sometimes used to stage prostate cancer. However, this procedure has a high morbidity because of the location of the lymph nodes, the number of overlying structures that must be removed to gain access to the lymph nodes, and the subsequent loss of lymphatic function in the pelvis. Furthermore, this technique is, by its nature, limited to assessing disease in the pelvis alone, and could therefore miss disease in other locations. Techniques to locate and sample the 'sentinel node' (defined as the first downstream lymph node from the prostate) for cancer, rather than the entire lymphatic chain, are currently being evaluated[9, 10].

4. MRI /S (Magnetic Resonance Imaging/Spectroscopy)

Magnetic resonance imaging (MRI) exploits the natural magnetic properties of the single proton that is the nucleus of hydrogen, an abundant element in the body. The protons in the body are induced to oscillate by the application of strong magnetic fields and radiofrequency pulses. The signals emitted from the protons stem from the density of protons in the material and their chemical environment, thus allowing MRI to detect differences between many types of tissue such as bones, organs, muscles, connective tissue, gray and white matter in the brain, and blood vessels. These differences alone are sometimes sufficient to reveal cancer cells, especially when their presence is associated with an anatomical change such as the invasion of the seminal vesicles in prostate cancer. MRI can also use a contrast agent -- typically a paramagnetic atom (i.e. gadolinium) complexed to a chelator – to provide information about blood flow. This can be especially useful for some tumors that have poorly organized and leaky blood vessels, as the contrast agent will be lost from the blood and remain in the interstitial space of the tumor. MRI has excellent resolution (typically on the order of 1 mm) and contrast, but is fundamentally a structural imaging technique. As such, it depends on changes in the patient's anatomy and may not be able to detect very early stage disease, especially in distant locations such as lymph nodes.

Magnetic resonance spectroscopy (MRS) interrogates areas of the body for the presence or absence of certain chemicals and uses this information to classify regions as to whether or not they contain cancer cells. MRS can distinguish between normal prostate tissue, prostate cancer, and necrotic tissue (which can often be hard to distinguish from cancer on normal MRI). Prostate cancer typically demonstrates elevated

levels of choline and lowered levels of citrate as compared to normal prostate tissue, and necrotic tissue is lacking in both of these metabolites. Combined MRI and MRS have produced excellent results in examining tissues in the prostate and surrounding regions, demonstrating an accuracy similar to or exceeding biopsy for intraprostatic localization of cancer[11] and establishing that MRS can discriminate between prostate adenocarcinoma and normal or benign hyperplastic tissue[12]. Its primary limitation is that it requires a receiving antenna to be placed as close to the tissue as possible. Transrectal coils generally are needed for MRS of the prostate, but the signal-to-noise limitations of this technique prevent it from studying tissue more than about 5 cm from the prostate. Thus, it is not yet suitable for examining distant sites for metastasis.

5. CT (Computed Tomography)

Computed tomography (CT) uses an x-ray tube and an arc of detectors, which rotate about a common axis to acquire x-ray projection data at fine angular increments from around the body (Figure 1-4). These x-ray data are mathematically reconstructed into a three-dimensional map of the electron density of the patient. Thus, the CT scanner can distinguish between bony structures, muscles, connective tissues, and different organs in the body. Additional information can be obtained by introducing a contrast agent into the body, either via injection or by ingestion. The contrast agent is a solution containing a compound with a high-Z (atomic number) element such as iodine, which highlights the blood vessels or the digestive tract. The contrast agent can also provide a limited amount of physiological information since its distribution changes over time as the body processes it, excretes it, or removes it from the bloodstream in tumor sites. Further details about the technology behind CT can be found in Chapter 2.

CT provides excellent anatomic detail (resolution on the order of 1 mm) and is extremely fast (a typical image set covering the abdomen can be acquired in only a few minutes). Its primary limitation in prostate cancer staging is that, like MRI, it too depends on gross anatomical changes to show evidence of disease. This can be useful in assessing morphological changes in the prostate region, but discovering distant disease is significantly more difficult. Staging of prostate cancer patients with CT usually involves searching for metastatic deposits in other organs or identifying lymph nodes that are abnormally large. Unfortunately, such findings are usually only evident once the disease has reached a fairly advanced stage. Lymph nodes may also be enlarged due to non-cancerous conditions[13]. These caveats make CT a fairly insensitive technique for staging prostate cancer[14].

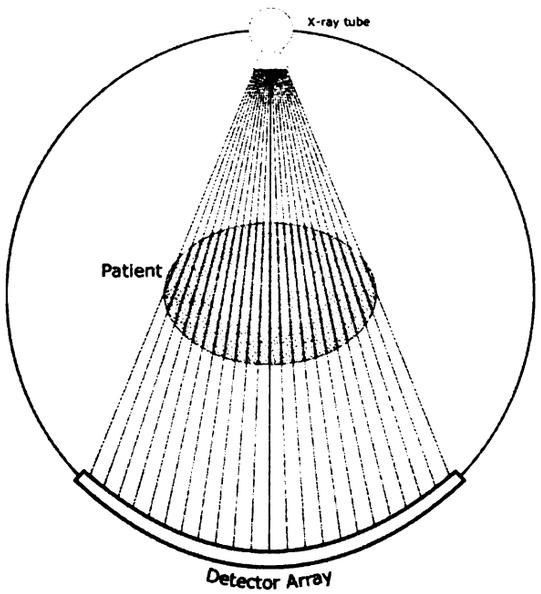


Figure 1-4: Schematic of a typical x-ray CT system.

6. ^{18}FDG-PET (Positron Emission Tomography)

Cancer cells have a higher metabolic rate (and concordant need for glucose fuel) than other cells because of their rapid growth. Thus, in comparison to normal cells, the cancer cells are more avid for ^{18}F-fluoro-deoxyglucose (^{18}FDG), a glucose molecule that has had one of its oxygen atoms replaced with the positron emitter ^{18}F. ^{18}FDG also is sufficiently different from normal glucose that the normal intracellular metabolic processes do not recognize it, which means that once the cell takes it up, the ^{18}FDG will remain trapped inside. Thus, the cancer cells contain a higher concentration of ^{18}FDG than normal tissue. By virtue of its ^{18}F radiolabel, ^{18}FDG emits positrons (i.e., antimatter electrons) which combine and annihilate with free electrons in the body, causing the coincident emission of two antiparallel annihilation photons, each having an energy of 511 keV. The annihilation photons can be detected using positron emission tomography (PET). PET scan data is acquired using a specialized scanner that contains a ring of detectors surrounding the patient (Figure 1-5). Opposing detectors in the ring observe the near-simultaneous arrival of these annihilation photons and can therefore isolate their origin to a line between the two detectors. These data are collected for many events, and then used to tomographically reconstruct the distribution of ^{18}F in the patient, thereby revealing areas of increased ^{18}FDG uptake.

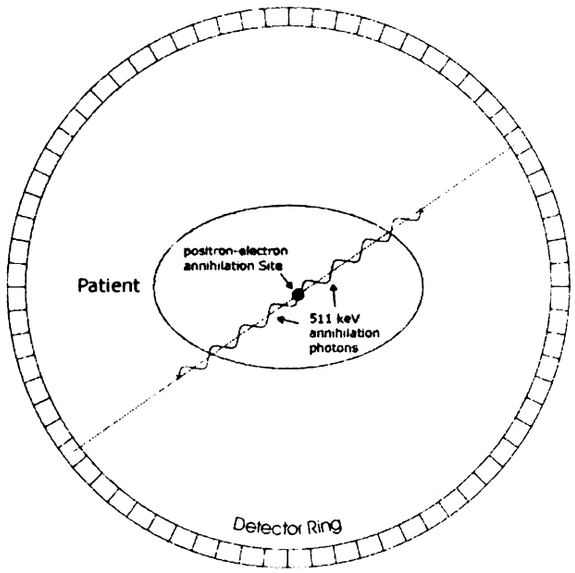


Figure 1-5: Schematic diagram of a PET system.

^{18}FDG-PET has high resolution and contrast because of its detection system, and ^{18}FDG is a very sensitive tracer because it depends only on increased metabolism, which almost all cancer cells have. Evidence also exists that glucose metabolism is higher in advanced stages of prostate cancer[15]. However, ^{18}FDG has some important limitations in prostate cancer examinations. Normal prostate cells have high glucose uptake, and ^{18}FDG is primarily excreted via the bladder (which is located immediately superior to the prostate). These two effects make it very difficult to assess uptake in the region of the prostate and definitively identify cancer cells. ^{18}FDG-PET is thus not helpful in the evaluation of organ-confined prostate cancer[16, 17]. However, ^{18}FDG-PET may be very useful in locating distant metastatic disease[18], especially when PSA is high[19].

7. Choline-based-PET

Choline is a molecule used for synthesis of phosphatidyl choline, an important component of the lipid bilayer that forms cell membranes. In areas of cancer, the need for choline is higher because of the rapid growth of new cells. Exogenous choline is preferentially taken into cancer cells, so a radiolabeled choline could be used to search for metastatic tumors and local spread of disease. Initial tests of this concept were carried out using choline synthesized with ^{11}C, a radionuclide that emits positrons; these demonstrated that choline had a higher target-to-background ratio than ^{18}FDG. Furthermore, the choline was not taken up significantly by normal prostate cells and did not concentrate in the bladder, all of which made image evaluation easier with ^{11}C-choline than with ^{18}FDG[20]. Recently, researchers have begun to develop ^{18}F-based choline analogs, because of the more favorable half-life characteristics of ^{18}F (110 minutes) over ^{11}C (20 minutes). These compounds exhibit behavior very similar to choline in cellular and animal models, are capable of localizing metastatic sites in human subjects[21], and therefore have the potential to be useful as prostate-specific imaging agents for positron emission tomography.

8. Bone Scintigraphy

A nuclear medicine bone scintigraphy exam, or "bone scan", uses methylene diphosphonate labeled with the gamma-emitter ^{99m}Tc (^{99m}Tc-MDP) to locate skeletal metastases. MDP is taken up by all bony structures, but its uptake is increased in areas of bone metastases because of the higher level of bone destruction and reformation in these

areas, with consequent increase in bone blood flow. Images of ^{99m}Tc-MDP are obtained using a scintillation camera, shown schematically in Figure 1-6.

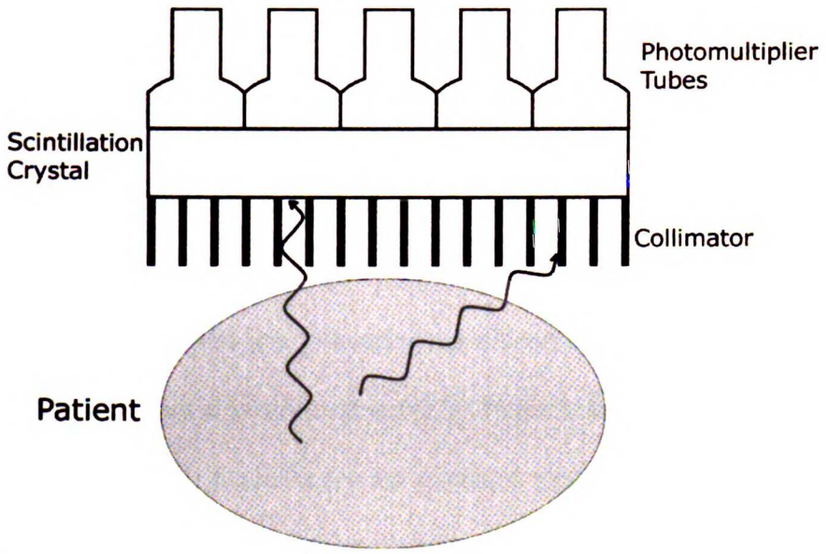


Figure 1-6: Schematic diagram of gamma camera imaging.

Gamma photons emitted from the patient along rays that pass through the openings in the collimator interact with a crystal that converts the photon's energy into a burst of light. The crystal is viewed by an array of photomultiplier tubes that analyze the emitted light and determine the location and energy of the gamma ray photon absorbed within the crystal. This information is fed to a computer that stores the location of each gamma ray and uses that information to accumulate an image (a more complete description of the scintillation camera can be found in Chapter 2). In bone scintigraphy, a pair of scintillation cameras traverses over the patient's anterior and posterior surfaces, creating a pair of planar images. Bone metastases show up on these scans as foci of increased activity, although previous fractures or degenerative skeletal diseases can also give rise to such 'hot spots'. A bone scan is considered to be a definitive test for the presence or

absence of skeletal metastases, but it is unable to detect metastases in soft tissues, and as such cannot be used as a sole staging test for cancers of the prostate or other organs.

9. ^{111}In-ProstaScint® SPECT

^{111}In-ProstaScint® (capromab pendetide) is a radiotracer based on an antibody (CYT-356) that was raised against the prostate specific membrane antigen (PSMA). PSMA is similar to PSA, but generally is bound in the cell membrane instead of being shed into the bloodstream. Although PSMA is expressed at some level in all prostate tissues, it is present in greater numbers in prostate cancer[22]. There is also considerable evidence that upregulation of PSMA is a hallmark for advanced stage cancer[23], poorly differentiated cells[24], androgen resistance, and metastatic activity[25]. These qualities make PSMA an ideal target for a prostate cancer diagnostic radiotracer. ^{111}In-ProstaScint® is synthesized by binding a linking molecule to the antibody, and then chelating the ^{111}In atom onto the linking molecule. This allows for the creation of a stable compound that retains much of the antibody's biological properties. ^{111}In produces gamma rays at 171 keV and 245 keV, which are ideal energies for scintillation camera imaging, and has a half-life of 2.83 days. The relatively long half-life is useful, because ^{111}In-ProstaScint® is administered intravenously to the patient and requires a minimum of 4 days to bind to its target cells and clear sufficiently from the bloodstream and sites of non-specific binding.

Once the ^{111}In-ProstaScint® has labeled its target cancer cells, its gamma ray emissions can be imaged using a scintillation camera. ^{111}In-ProstaScint® imaging is normally performed simultaneously with ^{99m}Tc-labeled red blood cell imaging, which

helps to delineate the vasculature, so that residual ^{111}In-ProstaScint® in the bloodstream is not mistaken for metastatic tumor sites. The imaging study records both planar image data (as for a bone scan) and single-photon emission computed tomography (SPECT) data, where images are acquired from many angles around the pelvis and abdomen and then reconstructed into three-dimensional images of radiotracer uptake.

Although imaging with ^{111}In-ProstaScint® provides a unique biochemical window on the patient's prostate cancer, it also has significant limitations. The low activity of the radiotracer by the time of imaging (despite the relatively long half-life of ^{111}In) creates images that are photon-starved and noisy. Anatomic landmarks in the images are very simple – bone marrow, major blood vessels, and the liver are visible, but there are few precise markers of structures. Even locating the prostate can sometimes be challenging. There is also significant non-specific uptake of ^{111}In-ProstaScint® by the bowel and liver, which can severely complicate interpretation of the SPECT images. Despite these difficulties, however, encouraging results have been reported as more physicians gain experience with these scans:

^{111}In-ProstaScint® scanning has been shown to be 15 times more sensitive than CT and 4 times more sensitive than MRI in detecting metastatic lymph nodes. The scan also has tremendous value in ruling out metastases in patients with moderately high risk (Gleason <7, PSA < 40 ng/ml); the negative predictive value (NPV) was 92%[26].

In a direct comparison with empirical staging methods (Partin tables), ^{111}In-ProstaScint® had a positive predictive value (PPV) of 67% for lymph node involvement, compared to a

PPV of 41-47% for the tables themselves. When combined, the two techniques had a PPV of 72%[27].

For patients undergoing both PET scans and ^{111}In-ProstaScint® scans, the PPV, NPV, and sensitivity of the ^{111}In-ProstaScint scan was 60%, 75%, and 86% respectively. By contrast, the PET scan produced values of 33%, 29%, and 17%[28].

E. Project Goals

^{111}In-ProstaScint® SPECT is already a useful tool in the staging of prostate cancer patients who are at risk for lymph node metastases. The primary end goal of this dissertation work was to determine whether or not we could enhance the utility of ^{111}In-ProstaScint®, and increase its ability to accurately stage prostate cancer.

References:

[1] A. A. Elgamal, M. J. Troychak, and G. P. Murphy, "ProstaScint scan may enhance identification of prostate cancer recurrences after prostatectomy, radiation, or hormone therapy: analysis of 136 scans of 100 patients," *Prostate*, vol. 37, pp. 261-9, 1998.

[2] American Cancer Society, "What are the key statistics about prostate cancer?," American Cancer Society website, www.cancer.org, 2000.

[3] National Cancer Institute, "SEER Surveillance, Epidemiology, and End Results) Crude Incidence Rates, 11 Registries, 1992-1997," vol. 2001: National Cancer Institute, 2001.

[4] B. Miller, L. Kolonel, L. Bernstein , J. Young Jr., G. Swanson, D. West, C. Key, J. Liff, C. Glover, and G. A. Alexander, "Racial/Ethnic Patterns of Cancer in the United States 1988-1992," NIH Pub. No. 96-4104, Bethesda, MD: National Cancer Institute, 1996.

[5] G. W. Chodak, "Early detection and screening for prostatic cancer," *Urology*, vol. 34, pp. 10-2; discussion 46-56., 1989.

[6] M. Perrotti, "Understanding PSA and prostate cancer risk assessment," *New Jersey Medicine*, vol. 98, pp. 35-8, 2001.

[7] A. W. Partin, L. A. Mangold, D. Lamm, P. Walsh, J. Epstein, and J. Pearson, "Contemporary update of prostate cancer staging nomograms (Partin Tables) for the new millennium," *Urology*, vol. 58, pp. 843-8, 2001.

[8] T. J. Polascik, J. D. Pearson, and A. W. Partin, "Multivariate models as predictors of pathological stage using Gleason score, clinical stage, and serum prostate-specific antigen," *Seminars in Urologic Oncology*, vol. 16, pp. 160-71, 1998.

[9] F. Wawroschek, H. Vogt, D. Weckermann, T. Wagner, and R. Harzmann, "The sentinel lymph node concept in prostate cancer - first results of gamma probe-guided sentinel lymph node identification," *European Urology*, vol. 36, pp. 595-600, 1999.

[10] F. Wawroschek, H. Vogt, D. Weckermann, T. Wagner, M. Hamm, and R. Harzmann, "Radioisotope guided pelvic lymph node dissection for prostate cancer," *Journal of Urology*, vol. 166, pp. 1715-9, 2001.

[11] A. E. Wefer, H. Hricak, D. B. Vigneron, F. V. Coakley, Y. Lu, J. Wefer, U. Mueller-Lisse, P. R. Carroll, and J. Kurhanewicz, "Sextant localization of prostate cancer: comparison of sextant biopsy, magnetic resonance imaging and magnetic resonance spectroscopic imaging with step section histology [see comments]," *Journal of Urology*, vol. 164, pp. 400-4, 2000.

[12] J. Kurhanewicz, D. B. Vigneron, S. J. Nelson, H. Hricak, J. M. MacDonald, B. Konety, and P. Narayan, "Citrate as an in vivo marker to discriminate prostate cancer from benign prostatic hyperplasia and normal prostate peripheral zone: detection via localized proton spectroscopy," *Urology*, vol. 45, pp. 459-66, 1995.

[13] K. Weingartner, A. Ramaswamy, A. Bittinger, E. W. Gerharz, D. Voge, and H. Riedmiller, "Anatomical basis for pelvic lymphadenectomy in prostate cancer: results of an autopsy study and implications for the clinic," *Journal of Urology*, vol. 156, pp. 1969-71, 1996.

[14] M. J. Manyak and M. C. Javitt, "The role of computerized tomography, magnetic resonance imaging, bone scan, and monoclonal antibody nuclear scan for prognosis prediction in prostate cancer," *Seminars in Urologic Oncology*, vol. 16, pp. 145-52, 1998.

[15] N. Oyama, H. Akino, Y. Suzuki, H. Kanamaru, N. Sadato, Y. Yonekura, and K. Okada, "The increased accumulation of [18F]fluorodeoxyglucose in untreated prostate cancer," *Japanese Journal of Clinical Oncology*, vol. 29, pp. 623-9, 1999.

[16] I. J. Liu, M. B. Zafar, Y. H. Lai, G. M. Segall, and M. K. Terris, "Fluorodeoxyglucose positron emission tomography studies in diagnosis and staging of clinically organ-confined prostate cancer," *Urology*, vol. 57, pp. 108-11, 2001.

[17] G. Sanz, J. E. Robles, M. Gimenez, J. Arocena, D. Sanchez, F. Rodriguez-Rubio, D. Rosell, J. A. Richter, and J. M. Berian, "Positron emission tomography with 18fluorine-labelled deoxyglucose: utility in localized and advanced prostate cancer," *BJU International*, vol. 84, pp. 1028-31, 1999.

[18] R. Heicappell, V. Muller-Mattheis, M. Reinhardt, H. Vosberg, C. D. Gerharz, H. Muller-Gartner, and R. Ackermann, "Staging of pelvic lymph nodes in neoplasms of the bladder and prostate by positron emission tomography with 2-[(18)F]-2-deoxy-D-glucose," *European Urology*, vol. 36, pp. 582-7, 1999.

[19] M. A. Seltzer, Z. Barbaric, A. Belldegrun, J. Naitoh, F. Dorey, M. E. Phelps, S. S. Gambhir, and C. K. Hoh, "Comparison of helical computerized tomography, positron emission tomography and monoclonal antibody scans for evaluation of lymph node metastases in patients with prostate specific antigen relapse after treatment for localized prostate cancer," *Journal of Urology*, vol. 162, pp. 1322-8, 1999.

[20] T. Hara, N. Kosaka, and H. Kishi, "PET imaging of prostate cancer using carbon-11-choline," *Journal of Nuclear Medicine*, vol. 39, pp. 990-5, 1998.

[21] T. R. DeGrado, R. E. Coleman, S. Wang, S. W. Baldwin, M. D. Orr, C. N. Robertson, T. J. Polascik, and D. T. Price, "Synthesis and evaluation of 18F-labeled choline as an oncologic tracer for positron emission tomography: initial findings in prostate cancer," *Cancer Research*, vol. 61, pp. 110-7, 2001.

[22] M. C. Gong, S. S. Chang, M. Sadelain, N. H. Bander, and W. D. W. Heston, "Prostate-specific membrane antigen (PSMA)-specific monoclonal antibodies in the treatment of prostate and other cancers," *Cancer Metastasis Reviews*, vol. 18, pp. 483-90, 1999.

[23] G. P. Murphy, A. A. Elgamal, S. L. Su, D. G. Bostwick, and E. H. Holmes, "Current evaluation of the tissue localization and diagnostic utility of prostate specific membrane antigen," *Cancer*, vol. 83, pp. 2259-69, 1998.

[24] A. K. Gregorakis, E. H. Holmes, and G. P. Murphy, "Prostate-specific membrane antigen: current and future utility," *Seminars in Urologic Oncology*, vol. 16, pp. 2-12, 1998.

[25] A. A. Elgamal, E. H. Holmes, S. L. Su, W. T. Tino, S. J. Simmons, M. Peterson, T. G. Greene, A. L. Boynton, and G. P. Murphy, "Prostate-specific membrane antigen (PSMA): current benefits and future value," *Seminars in Surgical Oncology*, vol. 18, pp. 10-6, 2000.

[26] M. J. Manyak, "Clinical Application of Radioimmunoscintigraphy With Prostate-Specific Antibodies for Prostate Cancer," *Cancer Control Journal of the Moffitt Cancer Center*, vol. 5, pp. 493-99, 1998.

[27] T. J. Polascik, M. J. Manyak, M. K. Haseman, R. T. Gurganus, B. Rogers, R. T. Maguire, and A. W. Partin, "Comparison of clinical staging algorithms and ^{111}Indium-capromab pendetide immunoscintigraphy in the prediction of lymph node involvement in high risk prostate carcinoma patients," *Cancer*, vol. 85, pp. 1586-92, 1999.

[28] M. K. Haseman, N. L. Reed, and S. A. Rosenthal, "Monoclonal antibody imaging of occult prostate cancer in patients with elevated prostate-specific antigen. Positron emission tomography and biopsy correlation," *Clinical Nuclear Medicine*, vol. 21, pp. 704-13, 1996.

Chapter 2: Fundamentals of Imaging Physics

In the previous chapter, we discussed several different medical imaging techniques that could play a role in staging prostate cancer patients. In this chapter, we will focus on two of these modalities: x-ray computed tomography (CT) and single photon emission computed tomography (SPECT). For prostate cancer patients, SPECT is used with ^{111}In-ProstaScint® to examine the functional state of tissues in the body, because ^{111}In-ProstaScint® targets the prostate specific membrane antigen (PSMA) and can thereby locate prostate cancer cells that have spread beyond the prostate and/or areas of elevated PSMA density. SPECT can be used with nanomolar amounts of radiotracers, and thus it is extremely sensitive to minute changes in the PSMA density. By contrast, CT is used to image the structures in the body, including bony anatomy and different soft tissues such as muscle, fat, and glandular tissue. CT by itself is not particularly useful for locating prostate cancer cells, since metastatic prostate cancer only creates morphological changes when the disease is very advanced. However, CT generates exquisitely detailed anatomical maps of the body's structures with high spatial resolution, and can therefore visualize anatomical features that would be invisible to SPECT imaging. Thus, these two modalities are acquired with distinct machines, and provide different, yet complementary information about the patient's health.

Despite their differences, SPECT and CT also share some common features. Both modalities make use of ionizing radiation, so the same physical principles govern both CT and SPECT imaging. Both modalities also make use of tomography, which is the reconstruction of three-dimensional objects from a series of two-dimensional planar projections. Tomography is an extremely valuable feature for medical imaging, because

it allows the visualization of internal structures that would simply be superimposed on top of each other (without depth information) in a planar image. This ability is especially useful for imaging ^{111}In-ProstaScint®, because the tracer can be taken up in many locations deep inside the body, and it is critical to precisely identify these locations and their anatomical surroundings.

In this chapter, we will cover some of the fundamental physics that governs the formation of images in CT and SPECT systems, and discuss how these effects influence the design of the imaging machines and the radiological images that they produce. This information will allow us to compare and contrast these modalities, and examine the particular strengths and weaknesses of each technique. This discussion will also provide the groundwork for future chapters, wherein we will cover the particular imaging devices used for our research and how the combination of CT and SPECT can bring unique advantages to prostate cancer staging.

A. Interaction of Ionizing Radiation and Matter

The subject of how radiation interacts with matter is one that could fill several volumes; we will review here a small portion that is most relevant to this dissertation project. Ionizing radiation in medical imaging typically uses photons in the energy range from about 15 keV (for mammography) to 511 keV (for positron emission tomography). When these photons encounter matter, they interact with the material primarily through two mechanisms: incoherent scattering and the photoelectric effect. (Photons used in medical imaging can also interact with matter through coherent scattering, but the cross-section for coherent scattering is usually much lower than the cross-sections for

incoherent scattering and the photoelectric effect, so we will not specifically discuss coherent scattering here.)

1. Incoherent scattering

Incoherent scattering occurs when an incident photon interacts with an outer shell atomic electron and is deflected from its initial trajectory; in other words, the photon leaving the interaction has a different direction and a lower energy than the incident photon. The electron also recoils from the collision, carrying away some of the incident photon's energy. In the limit where the electron is initially unbound and at rest, this interaction is referred to as Compton scattering. Although this limit is not entirely met by the conditions in CT and SPECT imaging, it is approximately true: the ionization energies of atomic electrons in light elements such as oxygen and carbon are on the order of tens of eV, whereas the photon energies in medical imaging are tens to hundreds of keV. Thus, it is an excellent approximation to treat the electron as being free and at rest, and to treat the incoherent scattering interactions as Compton scattering. A schematic diagram of the Compton scattering interaction is therefore shown in Figure 2-1.

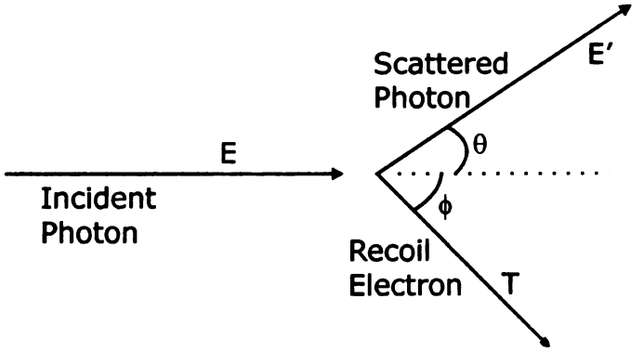


Figure 2-1: Schematic of Compton scattering event.

The incident photon has energy E, and the scattered photon has energy E' and leaves the interaction at a plane angle θ relative to its original direction. (This diagram is only shown in 2 dimensions for simplicity, so the scattering angle θ represents a conical surface of possible scatter trajectories.) The recoiling electron with kinetic energy T appears at an angle ϕ relative to the direction of the incident photon. By invoking conservation of energy and momentum, we can determine the energy of the Compton scattered photon and the recoil electron as a function of the scattering angle θ:

$$E'(\theta) = \frac{E}{1 + \alpha(1 - \cos\theta)} \quad \text{and} \quad T = E - E', \tag{2.1}$$

where $\alpha = E/(m_0c^2)$ is the photon energy in units of the electron rest mass m_0 (recall that the electron rest mass is $m_0c^2 = 511$ keV). At the energies typically used in diagnostic imaging, the recoil electron has a very short range (tens of microns), and thus essentially does not leave the interaction site, whereas the photon can travel millimeters or centimeters before interacting again.

For the materials typically present in the body, Compton scattering is the dominant interaction process for those photons with energies above 100 keV. For example, a 100 keV photon interacting in water is 95% likely to be Compton scattered, whereas the same photon interacting in sodium iodide is only 7% likely to be Compton scattered. In general, the likelihood of a Compton scattering event occurring is roughly proportional to the density of electrons in the material, and decreases with increasing atomic number (Z), although this latter effect becomes smaller as the photon energy increases above 200 keV.

There are several important implications of Compton scattering for medical imaging. First, Compton scattering causes the photon to be deflected from its original trajectory. The deflection angle of each individual photon is random, so once a photon is scattered we have no means of precisely determining its initial trajectory. Thus, the scattered photon has essentially lost any positional information about its origin. Second, the energy of the scattered photon is less than that of the original photon, so if the original photon energy is known and we have a means of measuring the energy of the photons, we can use this information to determine which photons have scattered and which ones have not. Finally, a Compton scattering event in the detector may only deposit part of the photon's energy into the detector (because we detect the signal from the recoil electron), unless the scattered photon interacts again within the detector by the photoelectric effect. Thus, radiation detectors are typically made from high Z materials, so that if a Compton scattering event does occur in the detector, the scattered photon is more likely to have a photoelectric interaction close by. Later in this chapter, we shall see how these properties affect the design of both CT and SPECT imaging systems.

2. Photoelectric Effect

The photoelectric effect is characterized by the complete absorption of the energy of an incident photon. When the photon interacts with an atom, the photon gives its energy to a bound atomic electron (typically an inner shell electron), which then enables the electron to break free from the atom, leaving behind a positively charged ion. The kinetic energy T of the escaping electron is given simply by

$$T = E - B_e \tag{2.2}$$

where B_e is the binding energy of the electron and E is the energy of the incident photon. As discussed in the previous section, the photoelectric effect is the dominant interaction mechanism for low energy photons (below 100 keV) in high Z materials. The likelihood of a photoelectric interaction is heavily dependent on atomic number and the photon energy, scaling roughly as Z^4/E^3.

The major impact of the photoelectric effect on CT and SPECT imaging is that the incident photon vanishes and gives its energy to an electron, which then travels only a very short distance (a few microns) from the interaction site. Thus, a photoelectric event in a patient results in the loss of the photon and a concordant loss of information to the radiation detector. However, a photoelectric event in the detector means that all of the photon's energy will be deposited in the detector. Therefore, detectors typically are made from high-Z materials, in order to enhance the likelihood of a photoelectric event, which allows the detector to absorb all of the photon's energy.

3. Attenuation Coefficients

Incoherent scattering, the photoelectric effect, and coherent scattering all remove photons from their original trajectory through a material. Thus, if we were to direct a beam of photons into some object and place a detector on the other side of the object, we would record fewer photons at the exit surface. This is shown schematically in Figure 2-2. Some of the incident photons are scattered out of the beam, whereas others undergo photoelectric interactions and are absorbed in the material (as discussed previously, only a very small percentage of the photons are deflected by coherent scattering). We will assume that the source and detector are both collimated, so that the detector only accepts photons from a narrow angular range relative to the normal of the detector.

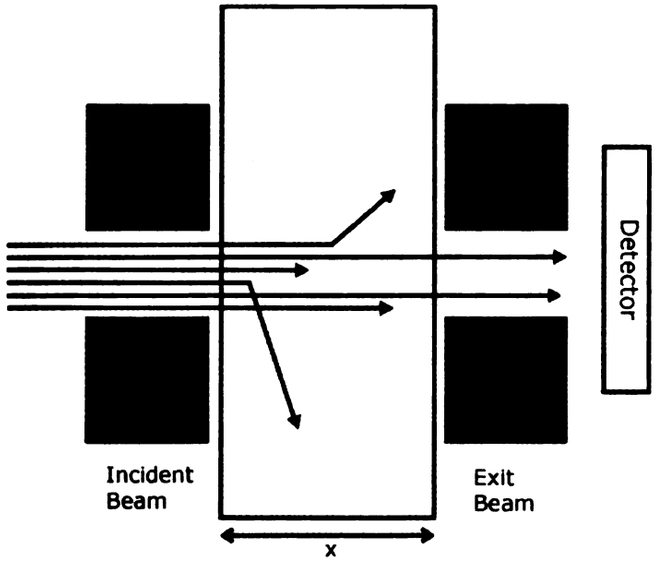


Figure 2-2: Illustration of photon attenuation in a uniform material.

As the photon beam passes through a uniform material, there is a fixed probability per unit distance that an individual photon will be scattered or absorbed. This means that the fluence rate (in units of photons/m^2/sec) of the incident beam will be reduced in an exponential fashion as the beam passes through the material. We can express this behavior in the following equation:

$$\phi = \phi_0 \exp(-\mu x) \tag{2.3}$$

where ϕ is the fluence rate of the exit beam, ϕ_0 is the fluence rate of the incident beam, and x is the thickness of the material. The parameter μ is called the linear attenuation coefficient, and is dependent on the energy of the photon and the physical characteristics of the attenuating material. Generally speaking, higher energy photons are less likely to

be attenuated in a material, and denser materials are more efficient at blocking the passage of photons.

Strictly speaking, Equation 2.3 refers to a 'narrow beam' geometry. This constraint means that the detector at the exit surface only records photons that have not interacted in the material. In other words, photons that have scattered in the material are not counted by the detector. We can achieve this in a physical experiment by placing tiny apertures over the incident and exit surfaces of the object, so that once an incident photon is scattered out of the beam, it has a vanishingly small chance of ever reaching the detector. Figure 2-2 approximates the 'narrow-beam' geometry, and becomes exactly the 'narrow-beam' case in the limit where the opening in the gray-colored collimators shrinks to zero. The converse situation is referred to as a 'broad beam' geometry, where the incident and exit surfaces are left uncollimated. In this situation, a detector placed at the exit surface of the object would see a somewhat higher fluence rate than $\phi_0 \exp(-\mu x)$, because it is possible that a photon could scatter in the material and still be recorded by the detector. Because the detectors used in medical imaging typically are collimated or have some other way of rejecting scattered radiation, the narrow-beam situation is reasonably accurate, and so we will model photon attenuation using Equation 2.3.

B. X-Ray Computed Tomography (CT)

1. Hardware

Computed tomography is a medical imaging technique in which a radiation source and a detector array are configured to record the radiation transmission (ϕ/ϕ_0) at multiple angles

around a patient or other object. Thus, we are essentially mapping out the attenuation of the x-ray beam in the patient. The fundamental elements of a modern CT scanner are a high-powered x-ray tube and associated detector array, which are mounted on a gantry that rotates the x-ray source and detector around the patient (see Fig. 1-6). X-rays are produced in the tube by directing a beam of electrons into a rotating tungsten target. The electrons come to a rapid halt once they strike the target, and this deceleration produces x-rays (this phenomenon is called *bremsstrahlung* radiation, after the German phrase for 'braking radiation'). The current and accelerating potential of the electron beam can be varied to change the output of the x-ray tube; CT tubes generally operate in the range of 70-300 mA of current and 80-150 kV potential. The tube potential determines the maximum energy of the x-rays produced by the system, and both the tube potential and tube current determine the photon fluence produced by the tube. The bremsstrahlung process produces a continuous spectrum of photons with energies between zero and *e*× the tube potential (i.e. 150 keV for a 150 kVp tube potential), but self-filtration in the tungsten target absorbs many of the low-energy photons. Additional thin metal plates are used to further attenuate the low-energy bremsstrahlung radiation, so the most likely photon energy is about one-third of the maximum energy. The spectral output from a typical x-ray tube is shown schematically in Figure 2-3. The lines superimposed on the spectrum are due to characteristic x-rays emitted when electron vacancies in the tungsten target are filled.

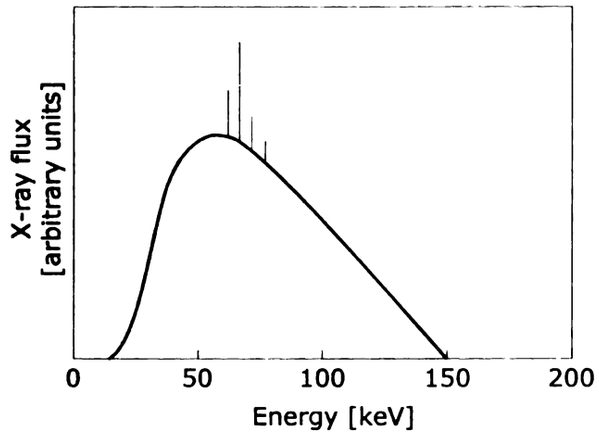


Figure 2-3: Bremsstrahlung x-ray spectral output from a typical x-ray tube operated with a peak voltage of 150kV[1].

For a CT scanner, the output of the x-ray tube is collimated so that the x-rays are emitted from the tube in a fan shape, the width of which determines the size of the object that can be scanned. The width of the fan is usually enough to cover a transaxial slice diameter of 48 cm or greater, and the slice thickness can be varied from 1.5mm to 10mm.

The x-rays are transmitted through the patient and attenuated by the materials that they encounter along the line from the x-ray source to the detector. Bones and similar hard structures allow proportionally fewer x-rays to pass through, whereas lighter materials like muscle, fat, and air allow proportionally more x-rays through. Scattered x-rays are deflected from the line between the source and the detector, so their trajectories are different from the primary, unscattered x-rays. Thus, the scattered radiation is largely eliminated by collimation – an array of lead strips placed in front of the detector so that only primary x-rays in a narrow angular range (relative to the normal of the detector) reach the detector.

The detector is usually made from a solid scintillator or high-pressure xenon gas, and is pixellated (typically on the order of 700 elements) so the x-ray fan beam can be

spatially sampled by individual elements each having a width of 1 to 2 mm. When x-rays are absorbed in a detector element, the detector generates an electrical current, which is then read by an amplifier to form the detector signal. Each detector signal is sampled at a rate of approximately 1 to 2 kHz, with the detector and detector electronics designed to handle a large dynamic range of photons of 10^6 to 1 between the maximum and minimum signals produced at different points in the imaging field. Data acquisition systems in computed tomography always are operated in current mode, and therefore do not determine the energy or event rate of individual photons. This limitation turns out to be unimportant in CT, for two reasons. First, the CT system measures the amount of attenuation that the total x-ray beam experiences in passing through the patient, and so energy discrimination is not needed. Second, the image is formed by a directed x-ray beam from a finite source, and the detector collimation blocks out most scattered radiation, so there is no need to measure the photon energy to reject scattered radiation. Current mode operation of the radiation detector also allows the attenuation measurement to be made at significantly higher photon fluence rates than can be measured with photon counting detectors. This allows the CT scans to be performed using x-ray tubes rather than radioisotope sources, and with significantly shorter scan times than could be performed using photon counting detectors.

The CT gantry rotates around the patient to record x-ray data transmission from all angles. Older CT scanners rotate the gantry around the patient to acquire a single slice of CT data, stop the gantry, and then move the table to take the next slice. Newer CT scanners are capable of continuously rotating while the patient is in motion, and thus acquire the data in a tightly spiraling helix around the patient. Finally, the most recent

CT designs incorporate "multislice" detectors, in which the detector array is pixellated both along the fan angle and in the axial direction. The combination of spiral scanning with multislice detectors allows the CT scans of extended regions of the body to be completed within a few seconds. Regardless of the specific detector geometry, the CT data are always acquired by recording x-ray views of the body from multiple angles, which can then be mathematically reconstructed into tomographic slices through the body.

2. Tomographic Reconstruction for CT

The goal of the CT reconstruction process is to recover the spatial distribution of attenuation coefficients from the x-ray projection data (ϕ/ϕ_0 for a set of angular views of the body). Techniques for accomplishing this type of reconstruction were first described in the late 1970s by Lakshminarayanan[2], Herman and Naparstek[3], and Scudder[4]; we will simply review the algorithm here.

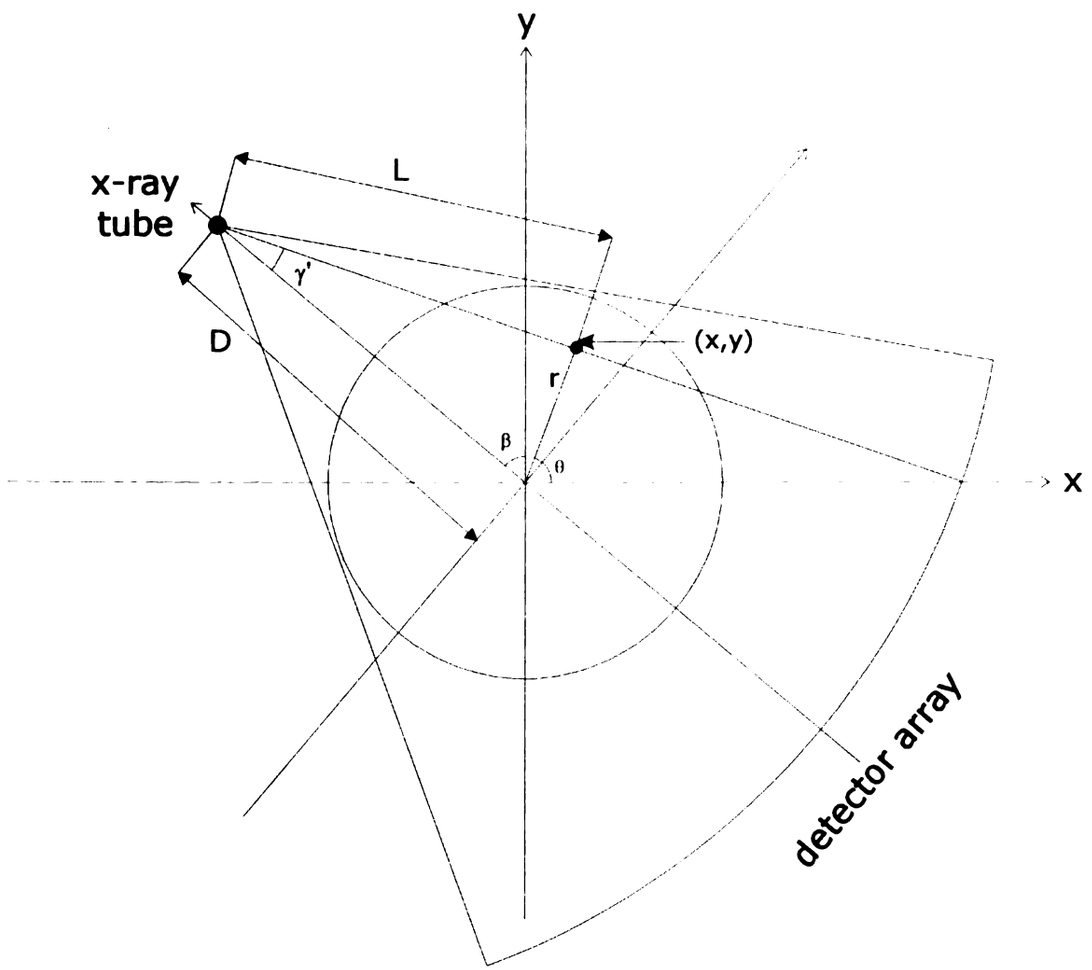


Figure 2-4: Geometry for fan-beam reconstruction of CT images.

The geometry for the reconstruction is illustrated in Figure 2-4. A fan-shaped x-ray beam is directed from the x-ray tube to the detector array through the reconstruction volume (represented by the circle). The attenuation coefficients of the object can be represented as a function $f(x,y)$, or $f(r,\theta)$ in polar coordinates. The projection $R_\beta(\gamma)$ represents the logarithmically-transformed detector response for a particular projection angle β, where γ is the angle between the central ray of the fan and a single projection ray through the

object. The detector thus records a value that is proportional to the line integral of attenuation coefficients along the ray:

$$R_\beta(\gamma) = \ln\left[\frac{\phi_\beta(\gamma)}{\phi_o}\right] = \int_{ProjectionRay} f(r,\theta)dl \tag{2.4}$$

Given a collection of projection data gathered from all around the object, we can recover the attenuation coefficients of the object using:

$$f(r,\theta) = \int_0^{2\pi} \frac{1}{L^2} \int_{-\gamma_m}^{\gamma_m} R_\beta(\gamma)\delta(\gamma'-\gamma)D\cos(\gamma)d\gamma d\beta\,. \tag{2.5}$$

The integration limits run from 0 to 2π for the projection angles β, and from $-\gamma_m$ to γ_m for an x-ray fan-beam having an angular extent of $-\gamma_m \le \gamma \le \gamma_m$. A typical CT fan-beam has a total angular extent of about 40°, so γ_m is roughly 20°. The angle γ' represents the specific projection ray that passes through the point labeled (r, θ). The factors L and D define the geometry of the imaging system where L is the distance from the source to the point (r,θ) within the object, and D is the distance between the x-ray source and the coordinate system origin. The delta function δ selects out only those projection rays that pass through the point labeled (r, θ).

Conceptually, Equation 2.5 determines the value of $f(r, \theta)$ by summing the contribution of all of the rays within the projection data that pass through that point. All points that lie along a projection ray γ' receive an equal contribution, so this process is known as backprojection, since the value of $R_\beta(\gamma)$ is 'smeared out' or backprojected along the ray. However, it can be shown via Fourier analysis of the imaging/reconstruction

process that this backprojection operation introduces a 1/r blurring into the image[5]. The backprojection process essentially damps out high frequency components of the image, resulting in a loss of image detail as illustrated in Figure 2-5.

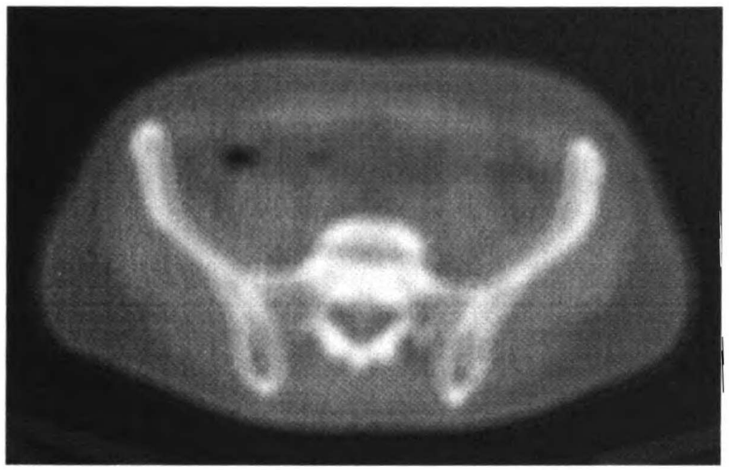


Figure 2-5: CT Image reconstructed using simple backprojection

To address this problem, we replace the delta function with a function g(γ'-γ), which selectively compensates for this loss by applying a high-pass spatial filter to the projection data before they are backprojected:

$$f(r,\theta) = \int_0^{2\pi} \frac{1}{L^2} \int_{-\gamma_m}^{\gamma_m} R_\beta(\gamma) g(\gamma'-\gamma) D\cos(\gamma) d\gamma d\beta . \tag{2.6}$$

In the spatial domain, the filter function is defined as:

$$g(\gamma) = \frac{1}{2}\left(\frac{\gamma}{\sin\gamma}\right)^2 h(\gamma) . \tag{2.7}$$

The function $g(\gamma)$ is a fan-beam adaptation of the conventional filter function $h(\gamma)$ used for parallel beam tomographic reconstruction, where h(γ) is the inverse Fourier transform of a simple frequency ramp H(w) given by:

$$H(w) = \begin{cases} |w| & |w| < W \\ 0 & |w| \geq W \end{cases}. \tag{2.8}$$

Figure 2-6 presents the shape of this filter $H(w)$ in both the frequency and spatial domains.

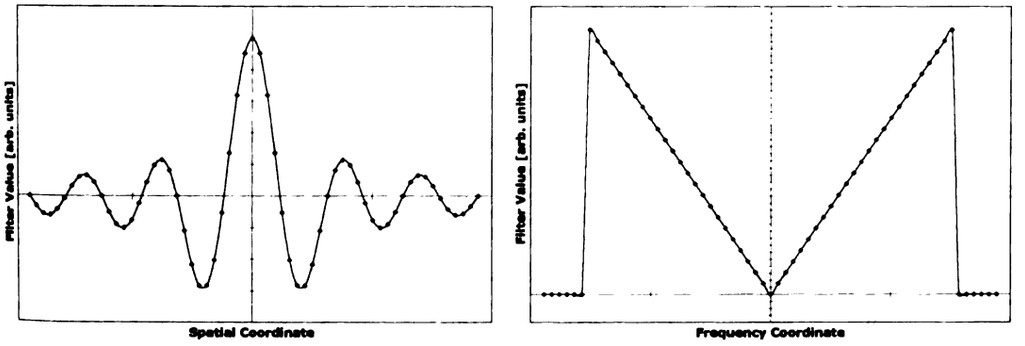


Figure 2-6: Spatial and frequency domain representations of the filter function $H(w)$.

When the filter (Equation 2.7) is applied to the projection data, the low frequency information is suppressed, which balances out the high frequency losses caused by the backprojection operation. The result is an accurate tomographic slice. An example of a properly reconstructed CT image is shown in Figure 2-7, which is a sharper and more accurate version of the CT image than is obtained with simple backprojection (Figure 2-5).



Figure 2-7: Example CT image of a patient's pelvis, reconstructed with filtered backprojection.

It should be noted that although most CT systems use a fan-beam algorithm similar to the one presented here, the particular implementation of the algorithm (including adaptations for discretely sampled projection data) and the filter parameters used in the reconstruction have been highly refined to minimize artifacts. Furthermore, the tomographic images produced by a modern CT scanner have been corrected for perturbations due to scatter radiation, beam-hardening, and other physical effects. Because the tomographic reconstruction software is such an important aspect of the CT system, commercial algorithms and specific implementations of the reconstruction code are highly proprietary, with relevant details never released to users. As such, the end product of the CT imaging process is a series of tomographic slices, and the raw projection data are usually inaccessible to the user. For this reason, we treated the image reconstruction process in the CT scanner as a 'black box', and used the tomographic images that were generated by the scanner's own reconstruction software. Fortunately, the tomographic images produced by a modern CT scanner are accurate and relatively free of artifacts, so

treating the scanner as a 'black box' has not been a major problem for research in our group.

3. Image Properties

The technology for CT scanning and tomographic reconstruction is designed to produce highly detailed anatomical images, and these images have several characteristic properties. In this section, we will discuss some of those properties and describe how they affect the diagnostic information that can be obtained from a CT scan. This information will help us to understand the benefits and limitations of CT imaging, and also facilitate a comparison between CT and SPECT images.

a) Spatial Resolution

A modern CT scanner incorporates a detector array with a large number of elements configured with a pixel pitch of approximately 1 mm. The detector array is irradiated with a high-power x-ray source having a focal spot size approximately 1 mm. These characteristics of the CT scanner enable spatial resolution on the order of 1 mm, although the thickness of the slice is usually 3-5 mm. This level of detail, combined with the three-dimensional nature of CT imaging, allows for the visualization of small anatomical structures in the patient.

b) Contrast

Image contrast in CT is provided by the inherent variations in density and elemental composition among the tissues in the body. For some tissues, these contrasts are dramatic, as in the difference between bone and the lungs. For others, the contrast is very

limited, such as that between blood vessels and the blood inside them, or the intestines and surrounding supporting tissues. In particular, the biochemical changes in cells associated with their transition from normal to cancerous, or even from living to dead, do not generate any contrast in a CT image. This implies that if one wants to use CT to detect physiological changes in tissue, one must either find some anatomical proxy for that change (such as enlargement or deformation of an organ) or somehow modify the tissue composition in a way that allows the physiological difference to be detected with x-rays. In CT, this usually means the introduction of a contrast material that modifies the attenuation of body tissues.

A common implementation of this technique is to inject a patient with a solution containing iodine, which has a fairly high atomic number and density when compared to the components of the body. Virtually all diagnostic CT images are obtained with iodinated contrast media that is injected intravenously; this material is distributed through the bloodstream and fills the lumen of the blood vessels, causing these spaces to appear as bright regions on the image and differentiating them from other soft tissues. Furthermore, because the contrast redistributes itself over time, one is able to crudely determine regional blood flow. In particular, one can determine whether blood vessels in a region are more permeable, which often is a sign of cancerous activity. CT images also are commonly obtained with oral contrast media, which is ingested and used to delineate the gastrointestinal system for studies of the abdomen or pelvis.

c) Noise

The x-ray tubes in a CT scanner are capable of producing a photon flux rate that is several orders of magnitude larger than that available from the injected radiotracers used

in nuclear medicine. In addition, the CT scanner uses a beam of radiation that is directed through the patient from a small source (with an apparent area of roughly 1 mm^2) and into a collimated detector array. Thus, the photons are generated in such a way that they are mostly emitted in the direction of the patient and the detector, which helps the overall efficiency of the system. A typical tube current of 100 mA contains roughly 10^{18} electrons/sec, so even after one factors in the poor efficiency of the bremsstrahlung process (about 1%) and the solid angle subtended by the detector (about $5x10^{-4}$ steradians, or 0.004% of a sphere) there are still hundreds of billions of photons per second available to form the image. Even though many of these photons will be absorbed or scattered by the patient, the CT image is still generated with roughly 10^9 photons/slice; this high photon density allows the CT image to be relatively free of photon statistical noise.

C. Single Photon Emission Computed Tomography (SPECT)

The task of SPECT imaging is quite unlike that of CT imaging. In SPECT, the radiation source is introduced into the patient, having been injected or ingested in the form of a radioactive element bound to a molecule with useful physiological properties. As such, the image formation process is fundamentally different from that of CT, because the location of the radioactive source is unknown. Furthermore, once the pharmaceutical is given to the patient, there is little that one can do to adjust its strength or energy output. Accordingly, the SPECT imaging process can be characterized as passive. The patient contains an unknown distribution of radioactive tracer material, and the goal of the imaging system is to measure that distribution. Because of this goal, the detector hardware and reconstruction algorithms used for SPECT imaging are very different from

those of CT imaging, and the images produced by the SPECT system do not have the same properties as CT images. In this section, we will describe the technology for SPECT imaging in greater detail, and describe how this technology gives rise to the characteristics of a typical SPECT image.

1. Hardware Fundamentals

The scintillation camera (also known as a gamma camera or Anger camera, after its developer), forms the heart of a SPECT imaging system. It consists of 3 basic elements, as shown in Figure 1-6. A collimator covers the front face of the camera. Typically, this collimator is a grid or honeycomb shape constructed of lead, and is oriented so that the long axis of the collimator holes is perpendicular to the face of the camera. The collimator holes are usually tall (~40mm) and narrow (~3mm), and the septa are sufficiently thick (~1mm) so that only radiation entering from a narrow angular range can reach the scintillation crystal. The collimator limits the acceptance angle of the detector, thus allowing the camera to form images; it also plays a dominant role in determining the camera resolution and detection efficiency, as will be discussed below.

Gamma rays that successfully pass through the collimator openings are able to interact with the scintillation crystal. When the gamma rays interact in the crystal, they generate electron vacancies in the crystal atoms (either by Compton scattering or the photoelectric effect), and these atoms then emit a characteristic frequency of visible light as the vacancies are filled. The crystal needs to have high efficiency in order to be able to detect the majority of the photons that enter it; therefore, the crystal is made from a dense, high-Z material, which increases the likelihood of photoelectric interactions or multiple Compton scattering events in a small region. The crystal also needs to be

transparent to the light generated by the gamma rays. Thallium-activated sodium iodide (NaI(Tl)) is a material that meets these criteria, and is the most common scintillator material used in current gamma cameras. The crystal is typically ¼" to ½" thick, which gives it an efficiency of over 90% for the typical photons used in nuclear medicine. Because the gamma rays have many orders of magnitude more energy than a visible light photon, a single gamma ray entering the crystal creates a shower of light photons. This process tends to amplify the signal, but also results in a loss of spatial information, as the light photons are created in several places along the photon's path and are emitted essentially isotropically.

The final component of the camera is an array of roughly 90 photomultiplier tubes (usually arranged in a hexagonal or rectangular close-pack) which observe the light generated in the crystal. The photomultiplier tube operates by converting light photons into electrons, which are then accelerated by a succession of dynodes to amplify the signal. When the electrons strike the first dynode, their increased kinetic energy causes the emission of more electrons, resulting in an amplification of the electronic signal (typically by a factor of 5 for each dynode stage). These electrons then in turn are accelerated into a secondary dynode, and then a tertiary dynode, and so on, until the electrons reaching the anode of the photomultiplier tube are collected to form an amplified signal pulse that is delivered to the detector electronics.

The absorption of a single incident gamma ray by the crystal will generate a signal in several of the photomultiplier tubes. Each tube reports a signal proportional to the number of light photons that it receives, creating a two-dimensional distribution of photomultiplier tube signals for each gamma ray interaction. This process is illustrated in

Figure 2-8, in which the solid horizontal and vertical lines represent the row and column sums from the array. The sum of the energy received by all of the photomultiplier tubes is proportional to the energy of the incident gamma ray. Similarly, a location for the gamma ray interaction can be calculated from a weighted positional average of the signal generated by the different photomultiplier tubes, corresponding to the location of the dashed lines in Fig 2-8.

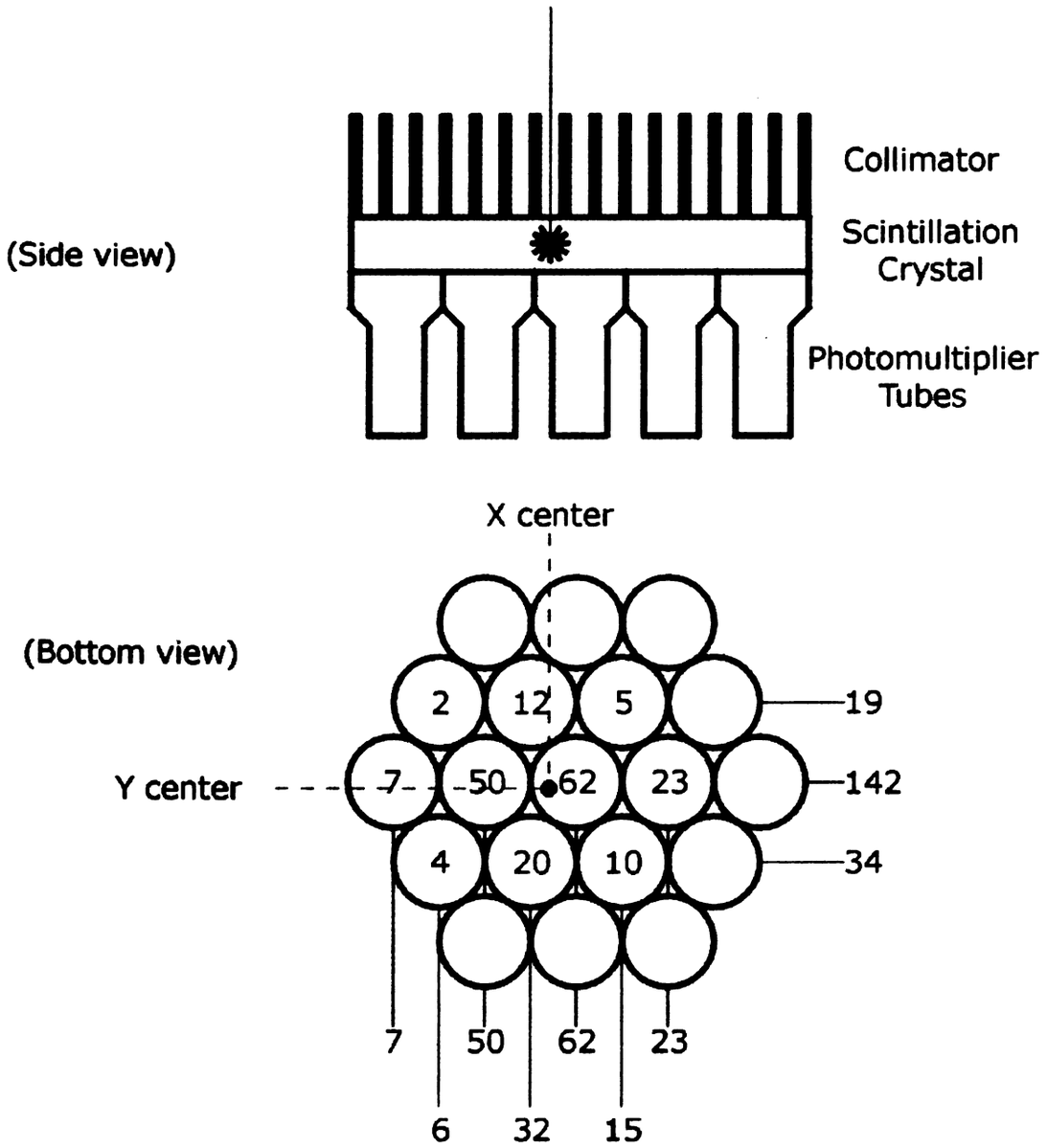


Figure 2-8: Illustration of gamma camera position determination.

An important aspect of this type of imaging is that the gamma camera records gamma-ray photons on an individual basis (hence, this process is typically referred to as 'photon counting'), rather than *en masse*, as is done with a CT detector. This allows the detector to determine the energy and position of each individual event, but severely limits the

event rate of the detector. However, this detection method is very appropriate for nuclear medicine, for two reasons. First, since the location of the radiotracer is unknown and the radiotracer emits photons isotropically, the camera cannot reject scatter on the basis of directionality. Thus, it is necessary to measure the energy of each photon individually, so that scattered photons can be rejected based on their lower energy. Second, as we shall see below, the event rate of a SPECT study is quite low when compared to CT. Indeed, the count-rate in nuclear medicine is inherently limited by the level of radioactivity that can be injected into the body, making this type of detection scheme well suited to the task of radionuclide imaging.

In order to acquire tomographic data, the SPECT camera is mounted on an arm or gantry that allows it to rotate around the patient. Early SPECT cameras used a single camera mounted on a gantry; more modern designs use two or three cameras mounted at opposing angles, in order to maximize the number of photons that can be collected per unit time. Because the camera is an area detector and is typically 40-60 cm across, patients can remain stationary while the camera rotates around them, and the table supporting the patient does not have to be moved as in a CT examination, where only a few tomographic slices are acquired for each detector rotation.

2. Tomographic reconstruction for SPECT

Once the projection data have been acquired by the gamma camera, they must be reconstructed tomographically into a three-dimensional map of the radiotracer distribution in the body. Although many of the principles from CT reconstruction can be used for SPECT reconstruction, there are important and fundamental differences between the two types of projection data, so the filtered backprojection method used for CT may

not be appropriate for SPECT. In this section, we will examine those differences and explain how they relate to the limitations of the filtered backprojection algorithm. We will then describe an iterative reconstruction algorithm that is more suited to the task of SPECT imaging.

a) Limitations in SPECT projection data.

One key property of SPECT projection data is that the number of photons available to generate a SPECT image is orders of magnitude lower than the number of photons available to a CT image. Several factors contribute to the low count density in SPECT projection data. First, the radiopharmaceutical given to the patient is constantly depositing dose into the patient's body over a period of hours to days. Therefore, one limits the amount of radiopharmaceutical given to the patient to keep the radiation dose at a tolerable level. In a typical study, the total activity injected is between 5 and 20 mCi (18.5 to 74.0 MBq), so the photon production rate is roughly 10 orders of magnitude below that of the x-ray tube in a CT scanner. Second, the photons are emitted isotropically from the source; most of the photons thus have no chance of ever reaching the detector. Assuming typical SPECT examination parameters with a detector area of roughly 1800 cm^2 at a distance of 27 cm from the center of rotation, we can estimate the simple geometric efficiency by comparing the area of the detector against the full sphere of potential emission angles:

$$\frac{1800}{4\pi(27)^2} = \frac{1800}{9160} = 0.1965 \qquad (2.9)$$

Third, not all of the photons emitted by the radioactive tracer will escape the body. Attenuation and scattering will prevent many of these photons from ever reaching the detector, and scattered photons will be rejected by the camera's energy discriminator. In comparison with CT, a smaller fraction of photons will be stopped in the patient's body because the photon energies of the gamma rays are typically higher than that of x-rays, but the effect is still significant. Most importantly, the collimator's lead walls and narrow tubes only allow approximately 1 in 10^4 (or fewer) gamma rays to pass through it and to reach the detector. When all of these factors are taken into account, a typical SPECT image contains only $6x10^4$ to $3x10^5$ counts per slice. If we wish to reconstruct this information into a typical image matrix that is 128 × 128 pixels, this leaves us with a mere 3 to 18 photons per pixel. If we assume that the noise in the image follows Poisson statistics, then the standard deviation is between 1.7 and 4.2, making the noise in the image a significant problem.

Furthermore, the SPECT projection data are corrupted by the effects of photon attenuation, photon scattering, and the divergent geometry of the radionuclide collimator (we will discuss this effect in greater detail below). Obviously, photon attenuation and scattering occur in CT imaging as well, but in the case of CT imaging the radiation source is essentially a known constant, so it is easier to devise tables of pre-calculated corrections for these effects. By contrast, the location and strength of the radiation sources are completely unknown in SPECT, so the corrections should be calculated for each individual imaging session.

However, filtered backprojection has no means of compensating for any of these potential limitations. It inherently assumes that the projection data are noiseless, and

there is no way for it to include the effects of attenuation, scattering, and collimator blurring. Thus, when applied to SPECT projection data, the resulting images are usually quite poor, as illustrated in Figure 2-9.

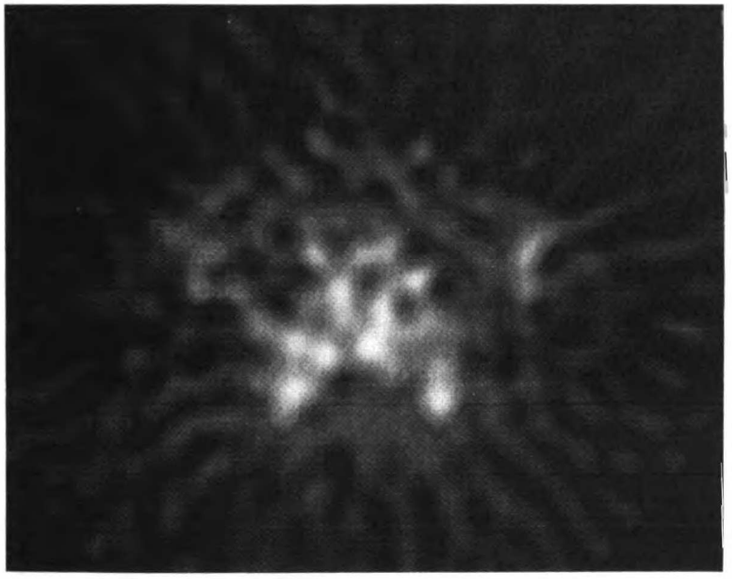


Figure 2-9: Example ^{111}In-ProstaScint® SPECT image of a patient's pelvis, reconstructed with filtered backprojection.

b) Iterative reconstruction techniques for SPECT

Fortunately, there are other means of reconstructing SPECT images that do not suffer from the same limitations as filtered backprojection. Specifically, iterative techniques increasingly are used to reconstruct radionuclide images since they provide a means to incorporate the statistical nature of the image data as well as compensating the image for physical effects such as photon attenuation, scattered radiation, and the spatial resolution characteristics of the collimator. The heart of the iterative reconstruction algorithm is a set of equations that model the projection of the radionuclide photons from their distribution in the object onto the detector array. The estimated projection data calculated

from this process are compared against the projection data measured during the image acquisition process to determine the difference between the estimated and measured projection data. A correction term is then calculated from the difference image, which is used to correct the original estimate of the radionuclide distribution in the object. The resulting estimates of the image are repeatedly refined until a final image estimate is calculated that (1) meets some pre-specified convergence criteria (i.e. the new image only differs from the old image by ±5%), or (2) has gone through a fixed number of iterations.

A common and useful algorithm for iterative SPECT reconstruction is the maximum-likelihood expectation-maximization (ML-EM) algorithm [6]:

$$\lambda_{k+1}(b) = \frac{1}{\sum_{d=1}^{N_d} p(b,d)} \sum_{d=1}^{N_d} \left[\frac{n'(d)\lambda_k(b)p(b,d)}{\sum_{b'=1}^{N_b} \lambda_k(b')p(b',d)} \right] \tag{2.10}$$

In this algorithm, λ refers to a voxel in the reconstructed SPECT image and k is the iteration number. The index b (and b') runs from 1 to N_b and enumerates all of the voxels in the reconstructed image. The index d runs from 1 to N_d and enumerates all of the pixels in the projection data; accordingly, the value of $n'(d)$ is the number of counts in the dth detector pixel. The function $p(b,d)$ represents the likelihood that a photon emitted from object voxel b arrives at detector pixel d. Thus, we begin with an estimate of the image expressed as $\lambda_k(b)$; then, using the measured detector counts and a model of the imaging process, we can determine a new and improved estimate of the image $\lambda_{k+1}(b)$.

Although we will not attempt to prove them here, the ML-EM algorithm also has several useful properties. First, the pixel values are updated in each iteration by

calculating ratios between the estimated and measured projection values, which ensures that the activity in the object voxels is never a negative number. Second, the ML-EM algorithm is based on a Poisson model of detector counts which models the photon statistics of the radionuclide imaging more exactly than does filtered backprojection. Third, the algorithm converges monotonically, so the process is always getting closer and closer to the optimal solution. Finally, the inclusion of the probability function *p(b,d)* also gives us a framework to describe any radiation-matter interactions that occur in the imaging process.

Figure 2-10 shows an iterative ML-EM reconstruction of the same patient slice as Figure 2-9. If we compare these two images, we observe that the iterative reconstruction generates a clearer and smoother image, and eliminates the streak artifacts that can be seen on the filtered backprojection image. The structures of the body that contain radiotracer (bones in the pelvis and spine) are more clearly visualized and more closely resemble their anatomical counterparts in the corresponding CT scan (Figure 2-7).

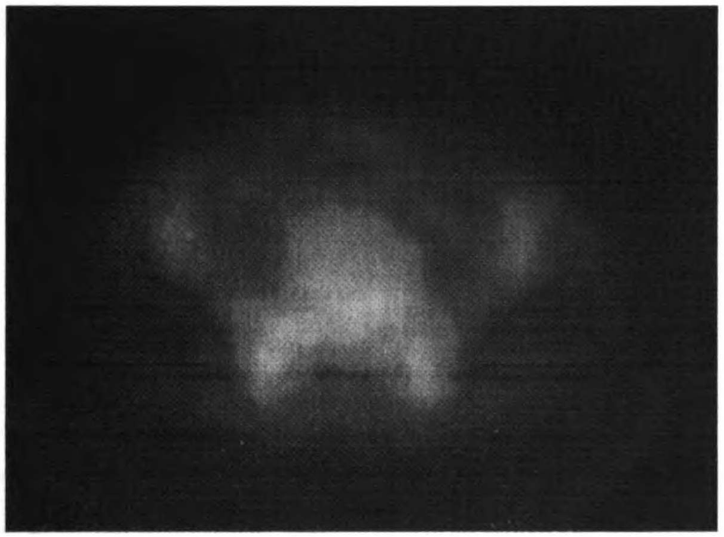


Figure 2-10: Example SPECT image of a patient's pelvis, reconstructed using an ML-EM algorithm.

The main penalty of the iterative reconstruction process is that the computations involved in an iterative reconstruction are more complex than filtered backprojection, and thus require a combination of more processor time or faster processors. For comparison, Figure 2-9 required about 0.1 seconds (per slice) of computer time, whereas Figure 2-10 required about 2.5 seconds (per slice) of computer time. Over the last 5 years, computer speeds have increased to the point where iterative reconstruction is now practical for a nuclear medicine department, and iterative techniques are gradually replacing filtered backprojection for clinical applications.

3. Image Properties

We have seen that the detector and reconstruction algorithms used for SPECT are quite different from those used for CT, so it is not surprising that the images should be very different as well. In this next section, we will discuss some of the characteristic properties of SPECT images, and how they differ from those of CT images.

a) Spatial Resolution

The spatial resolution of a radionuclide imaging system is characterized both by its intrinsic spatial resolution and by the system spatial resolution. The intrinsic spatial resolution is defined as the spatial resolution obtained when an infinitesimal point source is placed on the surface of the detector. In this case, the scintillation crystal, photomultiplier tubes, and decoding electronics determine the location of a photon interaction based on a statistical average of the signals from the individual photomultiplier tubes. This process means that the position of the gamma ray's entrance into the crystal cannot be measured with infinite precision, but the large number of light

photons created in the crystal does allow this combination to achieve intrinsic resolutions of a few mm.

The intrinsic spatial resolution of the detector is the fundamental limit to the performance of the imaging system. However, when the detector is used for imaging, it has a system spatial resolution that includes the spatial resolution characteristics of both the detector and the collimator. As discussed earlier, the collimator used in SPECT is an array of small lead tubes that allow radionuclide photons to be recorded only if they enter the imaging system approximately perpendicular to the detector surface. The collimator aperture is not infinitesimal and is characterized by an acceptance angle that diverges slightly from this perpendicular direction. Therefore, each point on the detector surface sees photons emitted from a region of the object that diverges with distance from the collimator surface. The divergent geometry of the collimator introduces a fundamental limit on spatial resolution in a SPECT system, and generates an inherent 'blurriness' in the image. As illustrated in Fig. 2-11, a single point in the detector views the outside universe through a conical region defined by the collimator geometry. All radioactive objects (e.g., those labeled "1", "2", and "3" in Figure 2-11) viewed within the conical region of a single detector element cannot be separated spatially unless the detector is moved or data from additional detector elements are used to form the image. Furthermore, even if the labeled objects were presented to the detector individually, the detector would not be able to distinguish the objects based on their relative sizes.

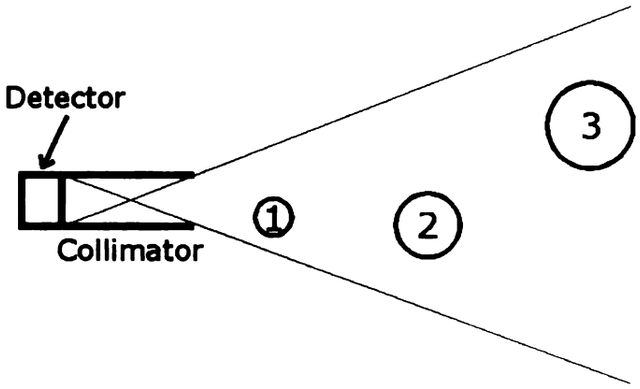


Figure 2-11: Collimator effects on resolution.

This effect also implies that the camera resolution is dependent on the distance between the camera and the object, as the diverging cone intersects a wider and wider area as one changes that distance. In a typical clinical gamma camera, the smallest objects that can be resolved are those about 7-8 mm in size, which is far less than the 1 mm resolution of a CT scan. The example SPECT slice shown in Fig. 2-10 illustrates this point – although some structures are visible within the object, the edges are not very sharp and the overall image is blurry.

b) Contrast

SPECT usually is used to assess physiology or function in the body, as opposed to CT which measures variations in anatomical structure. For example, it can be used to answer whether or not a particular tissue is receiving blood flow or expresses some biological receptor. Consequently, the contrast in a SPECT image is produced by differential uptake of a radiopharmaceutical in a way that depicts physiological differences between tissues. This contrast could (in principle) be infinite if a perfect chemical were designed that was only taken up by diseased tissue and was never bound to normal tissue.

However, real radiopharmaceuticals are far from perfect – a more realistic value for the difference in uptake is 5:1 or 10:1. Still, this ratio is quite high, and when combined with the fact that the detector is capable of recording the arrival of individual photons, it enables the gamma camera system to detect the presence of picomolar or nanomolar concentrations of radioactive material. For comparison, intravenous CT contrast agents contain millimolar concentrations of a heavy element such as iodine or barium. The high sensitivity of the gamma camera allows the SPECT image to reveal biochemical changes in the body long before associated structural changes become apparent with anatomical imaging techniques such as ultrasound, computed tomography, x-ray imaging, or magnetic resonance imaging.

c) Noise

As discussed in the previous section, the number of photons available to generate the SPECT image is much lower than that for CT. Thus, SPECT images are much noisier than CT images. An iterative reconstruction can help to address this problem, but cannot eliminate it completely.

D. Summary

In this chapter we have covered the basic physics of the interaction of radiation and matter and the engineering fundamentals for CT and SPECT imaging systems. We have also discussed the imaging properties of CT and SPECT, and how the two systems produce different types of information about a patient. This background will provide the foundation for Chapter 3, wherein we will discuss a novel approach to combined CT and SPECT imaging, and the potential advantages of such an approach.

References:

[1] E. Geldner, "Generation of x-ray and gamma radiation," in *Imaging Systems for Medical Diagnostics*, E. Krestel, Ed. Berlin: Siemens Aktiengesellschaft, 1988, pp. 61-70.

[2] A. V. Lakshminarayanan, "Reconstruction from divergent ray data," State University of New York, Buffalo, NY Department of Computer Science Tech. Rep. 92, 1975.

[3] G. T. Herman and A. Naparstek, "Fast image reconstruction based on a Radon inversion formula appropriate for rapidly collected data," *SIAM Journal of Applied Mathematics*, vol. 33, pp. 511-533, 1977.

[4] H. J. Scudder, "Introduction to computer aided tomography," *Proceedings of the IEEE*, vol. 66, pp. 628-637, 1978.

[5] R. H. T. Bates and T. M. Peters, "Toward improvements in tomography," *New Zealand Journal of Science*, vol. 14, pp. 883-896, 1971.

[6] L. A. Shepp and Y. Vardi, "Maximum likelihood reconstruction for emission tomography," *IEEE Transactions on Medical Imaging*, vol. 1, pp. 113-122, 1982.

Chapter 3: Combined CT/SPECT Imaging

A. Introduction

1. Clinical rationale for multi-modality imaging

Patients and physicians need the most complete medical information possible to make informed decisions about the patient's health care. CT and SPECT provide very different types of information, and thus have a complementary role in the assessment of a patient's condition. CT provides anatomical information with very high spatial resolution, enabling the radiologist to discern and measure small morphological changes from the body's normal structure. Unfortunately, it provides limited functional information about the biological state of organs and tissues. SPECT, on the other hand, measures minute quantities of radioactive tracers, which are specifically designed to reflect the biochemical state of tissue or the function of an organ system. However, the photon-starved nature of SPECT imaging creates noisy images with poor spatial-resolution, where the lack of structural information further complicates their clinical interpretation. For the task of staging prostate cancer, CT can be used to determine whether the prostate capsule has been breached or to measure the size of the prostate and enlarged lymph nodes. Conversely, SPECT can be used with a tracer like ^{111}In-ProstaScint® to determine the level of expression of prostate specific membrane antigen (PSMA) within the prostate or a distant lymph node. Both imaging modalities thus provide important, yet distinctively different, information about the patient's health.

2. Limitations of current methods

Clearly, there is a potential benefit to performing both CT and SPECT imaging to stage a patient with prostate cancer. However, in current clinical practice, these scans are acquired on separate machines, where the CT scan might be acquired several days before or after the SPECT scan. Since the internal structures of the patient are not static, there may be significant daily variations in the shape, size, and photon attenuation of organs such as the bowel and the bladder, especially if CT contrast materials are used. Furthermore, the radiologic interpretation of these scans usually is not a unified process. In most cases, different physicians read the CT and SPECT scans at different times, with integration of the relevant clinical information occuring only when the primary care physician receives the resulting reports. In other cases, the scans may be read at the same time, but the complementary information in the two images is interpreted by simply placing the images side-by-side on a lightbox or computer screen. The radiologist then must attempt to mentally merge two studies that vary in signal type, clinical information, spatial resolution, slice thickness, pixel size, noise, and contrast. Even for experienced readers, this task can be quite challenging. Recently, image registration software has been developed to take separate CT and SPECT scans and generate matching or 'fused' images on computer workstations, but this approach often demands significant time, training, and sophistication from the operator. Researchers also are developing automated image registration software, and have had some success in fusing images of the head, but a robust image fusion routine for less rigid regions (such as the thorax and abdomen) remains elusive.

3. Advantages of a combined CT/SPECT system

a) Image registration and comparison

There is a need for techniques that will allow the radiologist to view and compare images acquired with two different modalities in a direct and efficient manner. Although post-acquisition fusion of data from two different imaging systems can provide a degree of image registration, a more direct method would be to incorporate both CT and SPECT imaging on a single, integrated platform. This system could acquire images with a single detector, possibly with simultaneous acquisition of the CT and SPECT data. In this case, the system would generate images that are inherently registered. Unfortunately, it is difficult and perhaps impossible to design radiation detectors which are capable of current-mode imaging of a high x-ray flux for CT while simultaneously performing photon-counting imaging of gamma-rays for radionuclide imaging. Therefore, it is more feasible and practical to implement a combined CT/SPECT imaging system using separate detectors mounted on a single platform. Even though the CT and SPECT images may not be acquired simultaneously with a single detector, the image data can be acquired and registered in a consistent way using either spatially-correlated features of the two data sets or *a priori* knowledge of the system geometry. The fact that the CT and SPECT data will be taken during the same imaging session is also quite useful, because it assures that the patient can remain stationary on the patient table. This allows both imaging scans to be performed with the patient in roughly the same physical position and in the same physiological state. Combined CT/SPECT imaging makes it possible to correlate features in the CT and SPECT images with a higher degree of confidence than

images acquired with separate imaging systems. For example, suppose that one were to examine a CT image of the liver and found that one portion of it was slightly deformed. This could be caused by many different conditions, but having a SPECT image that exactly corresponded to the CT image would give valuable insight into the physiological state of that tissue, which could assist in forming the proper diagnosis.

b) Image quantitation

As noted above, a combined CT/SPECT system can improve our ability to correlate structure with function by providing coregistered image data from the CT and SPECT systems. In addition, combined CT/SPECT imaging can improve the quantitative accuracy of radionuclide measurements in comparison to those obtained with SPECT imaging alone. Since radiotracers have great sensitivity to the biochemical conditions that characterize a physiological process, it is important that the reconstructed image accurately reflect the true distribution of the radiotracer within the body. However, there are key barriers to obtaining such information from a conventional SPECT scan[1, 2]. The first is that a significant fraction of the photons emitted by the radiotracer will be attenuated or scattered in the patient and will not reach the detector. This does more than simply depress the amount of available signal; for example, if a strong source was located deep in the body, it might be missed or assumed to be weak, as few of its photons would make it to the body surface. Conversely, the intensity of a faint source close to the skin could be overestimated if its relative lack of attenuation were not considered. The second key barrier is that SPECT's poor and distant-dependent resolution creates severe blurring in the projection data, so the reconstructed image does not accurately reflect the true size or radionuclide concentration of the object. The combination of CT and SPECT can help

to overcome both of these barriers. The information in the CT scan provides a map of the patient's x-ray attenuation, which is an excellent proxy for gamma ray attenuation and scattering properties of the body. Thus, the CT information can be used to model the effects of photon attenuation and scatter during the SPECT reconstruction process. CT also provides us with high spatial resolution *a priori* information about the size and shape of structures in the body. With these corrections, it is then possible to directly relate reconstructed counts in the SPECT image to the true concentration of radionuclide, measured in MBq/cm^3 or MBq/g for the tissue or organ of interest.

Obviously, we would like to provide the interpreting physician with the most accurate image possible, but the power of quantitative SPECT extends beyond this goal. Quantitative imaging can facilitate the comparison of patient data gathered at many different sites or over a long time period, because the measurement is based on a real quantity that should be invariant with respect to any particular imaging device or protocol. By contrast, subjective assessment of SPECT images is highly dependent on the particular imaging device, and can have significant inter-observer and intra-observer biases. Furthermore, quantitative imaging makes it easier to correlate SPECT image data with other numerical metrics of the patient's health. In the case of ^{111}In-ProstaScint®, the tracer binds to an intracellular portion of the prostate specific membrane antigen (PSMA). Researchers have correlated the expression of PSMA with measures of biological aggressiveness[3], different tumor subtypes[4], and androgen resistance[5], but all of these measures have been made using excised tissue or cell lines. Quantitative ^{111}In-ProstaScint® SPECT holds the potential for making these measurements noninvasively and over a large region of the body. This result could add important

information about the patient's condition, beyond the standard binary determination of whether or not uptake occurs in a particular location.

B. Multi-modality imaging devices

1. The ETCT System

Our laboratory is pursuing two different approaches to combined CT/SPECT imaging, with the goal of achieving the potential advantages of multimodality imaging outlined above. The first of these is a system designed to obtain CT and SPECT information using a single detector (Figure 3-1), which is capable both of handling the high fluence rate for CT data and of providing good energy discrimination for SPECT. This system is referred to as the ETCT system, since it can acquire both *E*mission and *T*ransmission data for a patient, and was first developed in our laboratory in 1990[6, 7].

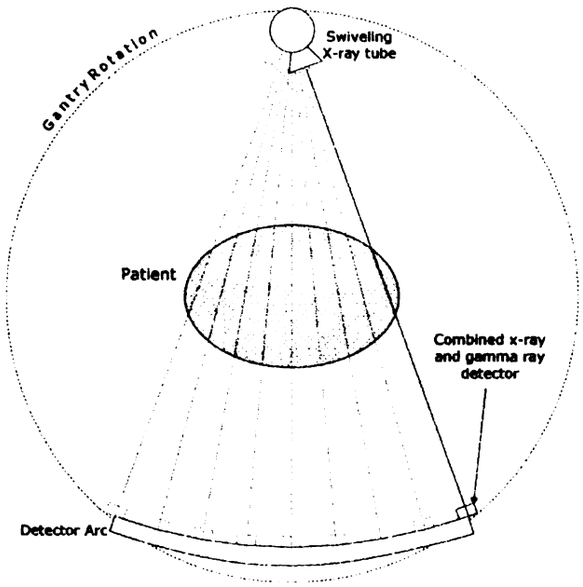


Figure 3-1: Schematic diagram of the Emission-Transmission Computed Tomography (ETCT) system.

This system uses a single solid-state detector with an area of about 4 cm^2, divided into 4 to 32 pixels. During data acquisition, the x-ray tube swivels and the detector moves along an arc-shaped track to simulate a third generation CT geometry with an single x-ray fan beam projection. The gantry also rotates to collect projection data from all angles around the patient. The x-ray tube can be operated at a lower energy than the 140 keV photon energy emitted by a radiopharmaceutical labeled with ^{99m}Tc. In concept, this allows the radionuclide and x-ray data to be acquired simultaneously using energy discrimination to differentiate the two data sets. In practice, the x-ray data are acquired at high flux rates, and pulse pile-up poses a significant problem that can contaminate the higher-energy radionuclide data[8]. Therefore, sequential acquisition of the CT and SPECT data is simpler and more accurate since this prevents contamination of the SPECT image by pulse pile-up from the high-flux x-ray data. In a typical sequential acquisition, a single CT slice is acquired over 30 minutes, and a SPECT slice is then acquired over the following 8 hours.

The obvious advantages of using a single detector are that the registration of CT and SPECT images is completely automatic and the detection system is physically compact. Although the system was originally conceived and tested using a segmented high-purity germanium detector[9], recent revisions use a cadmium zinc telluride detector instead[10], because of cost efficiency and its ability to operate at room temperature. The ETCT system faces several challenges which have prevented clinical implementation. First, it is difficult to design a detector that has adequate performance characteristics for both CT and SPECT. Second, the candidate detectors for the ETCT system (including high-purity germanium and cadmium zinc telluride), are expensive, making it prohibitive

to configure a detector with the detection area of a modern scintillation camera. However, the system is an important research tool and test platform for new solid-state detectors, so development of this system is continuing at our laboratory.

2. The Combined CT/SPECT system

The ETCT system described above uses a single detector for simultaneous or sequential CT/SPECT imaging. A second approach, more suitable for clinical studies, was designed to make use of existing commercial imaging machines by placing a SPECT camera and a CT gantry in tandem, with a table spanning the two systems, as shown in Figure 3-2.

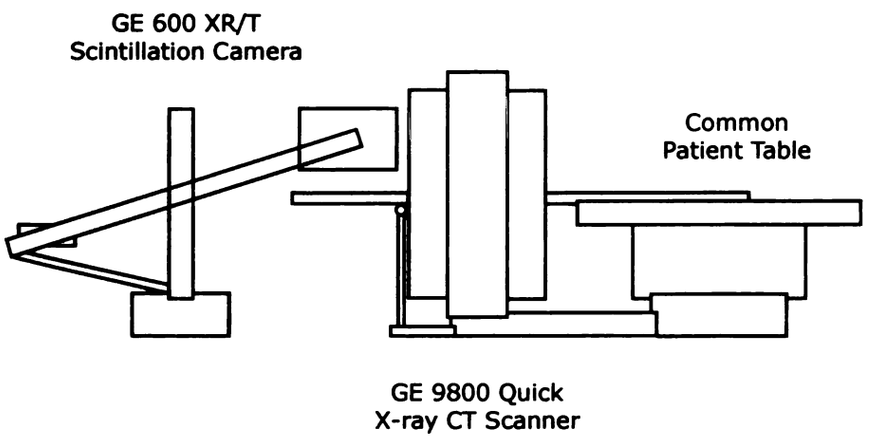


Figure 3-2: Schematic diagram of the Combined CT/SPECT system.

Our laboratory has implemented this system using a clinical single-slice CT scanner (GE 9800 Quick) and a clinical scintillation camera (GE 600 XR/T). To facilitiate patient handling and allow CT and SPECT imaging without moving the patient during the imaging study, we constructed an extra long patient table by bonding two standard CT patient tables together. This table is supported on one side of the CT gantry by the

standard CT table base, which contains drive motors and position sensors; on the other side, an adjustable-height metal roller provides stability for the cantilevered section of the table. This allows a patient to be translated from one imaging machine into the other without having to reposition the patient on the table. Although the images are not automatically registered as occurs with the ETCT system, we have developed a system of fiducial markers that are imaged during both the CT and the SPECT acquisition. These markers allow us to define the coordinate systems of the two imaging systems with sufficient accuracy so that the two image volumes can be correlated to each other.

The primary advantage of this system is that it allows for the acquisition of clinically realistic images in a relatively short time, so that the principles of combined CT/SPECT imaging can be tested on large phantoms, animal models or human research patients. A complete study on this machine can be completed in approximately 2-3 hours, depending on the complexity of the study (by contrast, the ETCT system would require roughly 2.5 weeks of imaging time to achieve the same volume coverage and count density). Accordingly, the combined CT/SPECT system has been used to demonstrate improved SPECT reconstruction[11], absolute quantitation in phantoms[12, 13], and absolute quantitation in a porcine myocardial perfusion model[14]. We are currently investigating the utility of this imaging system for other applications, including quantitation of ^{111}In-ProstaScint® uptake in prostate cancer patients.

C. Summary

A combined CT/SPECT imaging approach can provide improved images for radiologic interpretation and also enables absolute quantitation of radiotracer uptake. Acquiring these images on a single, unified machine maximizes the benefits of this approach,

because the patient is imaged in essentially the same state for both exams and the image registration task is much simpler. In succeeding chapters, we will cover our specific methodologies for image registration and quantitative reconstruction, and discuss how we have adapted the CT/SPECT system for the particular task of ^{111}In-ProstaScint® imaging.

References:

[1] B. M. Tsui, E. C. Frey, K. J. LaCroix, D. S. Lalush, W. H. McCartney, M. A. King, and G. T. Gullberg, "Quantitative myocardial perfusion SPECT," *Journal of Nuclear Cardiology*, vol. 5, pp. 507-22, 1998.

[2] M. S. Rosenthal, J. Cullom, W. Hawkins, S. C. Moore, B. M. Tsui, and M. Yester, "Quantitative SPECT imaging: a review and recommendations by the Focus Committee of the Society of Nuclear Medicine Computer and Instrumentation Council [see comments]," *Journal of Nuclear Medicine*, vol. 36, pp. 1489-513, 1995.

[3] S. D. Sweat, A. Pacelli, G. P. Murphy, and D. G. Bostwick, "Prostate-specific membrane antigen expression is greatest in prostate adenocarcinoma and lymph node metastases," *Urology*, vol. 52, pp. 637-40, 1998.

[4] M. C. Gong, S. S. Chang, F. Watt, D. S. O'Keefe, D. J. Bacich, A. Uchida, N. H. Bander, V. E. Reuter, P. B. Gaudin, P. L. Molloy, M. Sadelian, and W. D. Heston, "Overview of evolving strategies incorporating prostate-specific membrane antigen as target for therapy," *Mol Urol*, vol. 4, pp. 217-22;discussion 223, 2000.

[5] A. A. Elgamal, E. H. Holmes, S. L. Su, W. T. Tino, S. J. Simmons, M. Peterson, T. G. Greene, A. L. Boynton, and G. P. Murphy, "Prostate-specific membrane antigen (PSMA): current benefits and future value," *Seminars in Surgical Oncology*, vol. 18, pp. 10-6, 2000.

[6] B. H. Hasegawa, E. L. Gingold, S. M. Reilly, S. C. Liew, and C. E. Cann, "Description of a simultaneous emission-transmission CT system," presented at International Society for Optical Engineering Annual Meeting, 1990.

[7] T. F. Lang, B. H. Hasegawa, S. C. Liew, J. K. Brown, S. C. Blankespoor, S. M. Reilly, E. L. Gingold, and C. E. Cann, "Description of a prototype emission-transmission CT imaging system," *Journal of Nuclear Medicine*, vol. 33, pp. 1881-1887, 1992.

[8] X. Wu, J. K. Brown, K. Kalki, and B. H. Hasegawa, "Characterization and correction of pulse pile-up in simultaneous emission-transmission computed tomography," *Medical Physics*, vol. 23, pp. 569-75, 1996.

[9] B. H. Hasegawa, B. Stebler, B. K. Rutt, A. Martinez, E. L. Gingold, C. Barker, K. G. Faulkner, C. E. Cann, and D. P. Boyd, "A prototype high-purity germanium detector system with fast photon counting circuitry for medical imaging," *Medical Physics*, vol. 18, pp. 900-909, 1991.

[10] K. Iwata, B. H. Hasegawa, J. A. Heanue, P. R. Bennett, K. S. Shah, C. D. Boles, and B. E. Boser, "CdZnTe detector for combined X-ray CT and SPECT," presented at Ninth Symposium on Radiation Measurements and Applications, Ann Arbor, MI, USA, 1998.

[11] S. C. Blankespoor, X. Wu, K. Kalki, J. K. Brown, C. E. Cann, and B. H. Hasegawa, "Attenuation correction of SPECT using X-ray CT on an emission-transmission CT system: Myocardial perfusion assessment," presented at IEEE Nuclear Science Symposium and Medical Imaging Conference, San Francisco, CA, USA, 1995.

[12] H. R. Tang, J. K. Brown, and B. H. Hasegawa, "Use of X-ray CT-defined regions of interest for the determination of SPECT recovery coefficients," presented at IEEE Nuclear Science Symposium and Medical Imaging Conference, Anaheim, CA, USA, 1996.

[13] A. J. Da Silva, H. R. Tang, M. C. Wu, and B. H. Hasegawa, "Absolute quantitation of myocardial activity in phantoms," presented at IEEE Nuclear Science Symposium and Medical Imaging Conference, Toronto, Ont., Canada, 1998.

[14] A. J. Da Silva, H. R. Tang, K. H. Wong, M. C. Wu, M. W. Dae, and B. H. Hasegawa, "Absolute quantification of regional myocardial uptake of 99mTc-sestamibi with SPECT: experimental validation in a porcine model. [Comment In: J Nucl Med. 2001 May;42(5):780-1 UI: 21235439]," *Journal of Nuclear Medicine*, vol. 42, pp. 772-9, 2001.

Chapter 4: CT/SPECT Image Registration

A. Introduction

As discussed in the previous chapter, the ability to correlate anatomical and physiological data is a powerful property of dual-modality imaging, making accurate image registration essential to any combined imaging system. For the combined CT/SPECT system, the ability to precisely correlate images on a voxel-by-voxel basis is the foundation for all of the advantages discussed in the previous chapter: easier image interpretation, increased diagnostic information, and quantitative radionuclide measurements with SPECT. However, even if the x-ray and radionuclide images are acquired using an integrated dual-modality imaging system such as the system used for this research project, the possibility of inconsistency between the two data sets still exists. There are differences between the image formats, slice thicknesses, and slice positions. In addition, the CT and SPECT data are acquired sequentially over different time periods (5 min vs. 60 min), so the images will reflect small differences in patient position, respiratory state, and internal structure. Finally, the patient is imaged on a cantilevered patient table that can deflect different amounts when the patient is moved between the separated CT and SPECT detectors. Therefore, several specific steps are needed to register the CT and SPECT data accurately, even with this dual-modality imaging system. In this chapter, we will first review the challenges involved in dual-modality imaging and describe some possible image registration techniques. Then, we will cover the specific image registration methodology used for the UCSF CT/SPECT system. Finally, we will describe

experimental results that validate the use of these image registration techniques for the task of dual-modality imaging of ^{111}In-ProstaScint®.

1. The need for image registration

The process of image registration involves matching structural or anatomical data from one point or region in the x-ray or CT image with functional or physiological data from the corresponding point or region in the radionuclide image. The most basic (and still the most common) means of registering images is performed simply by placing a series of medical images (either as films or as softcopy displays) next to or overlapping one another. The interpreting physician then can see both sets of images and integrate the information mentally. Although this method is simple to implement, it is far from ideal. The first problem is that images acquired on different systems are usually different sizes. The pixels in a typical CT image are roughly 1 mm on a side, whereas those on a typical SPECT system are 4-5 mm on a side. Correspondingly, the CT image is typically 512 pixels x 512 pixels, whereas the SPECT image is usually 128 pixels x 128 pixels. The amount of patient covered by the images can also vary: CT images are often sized to closely match the patients body contours, whereas SPECT images often contain a large margin of blank pixels along the borders. Furthermore, the CT and SPECT images may not present data from the same regions of the patient. Finally, the slice thickness used to acquire CT images generally differs from that used for SPECT. CT slices can range from 3 mm to 10 mm in thickness, and may even change during a single study if there is a particular body region under close scrutiny. As an example, CT scans through the pelvis may sample most of the pelvis with 7 mm slices, but use 3 mm slices through the prostate to gain higher detail. SPECT slices typically match the size of the image pixels (4-5 mm)

and are fixed over the entire volume. This last difference can be especially frustrating, because it means that a feature that spans 4 slices in the SPECT study might span 3-8 slices on the CT study; keeping a mental record of this disparity can be cumbersome. Although an experienced physician can compensate for many of these potential problems, the differences between the CT and SPECT images create an unnecessary distraction. Clearly, we would prefer to have a system where the two images can be mapped into a common coordinate space, so that the coordinate origins, pixel sizes, slice thicknesses, and volumes exactly match one another. With such a system, correlating objects would be as simple as pointing to that object with a cursor on one image, and observing where that point fell on the corresponding image.

2. Approaches to image registration

a) Manual image manipulation

Software tools generally are available on medical image display workstations that enable the operator to register images manually. In this technique, an operator, usually a physician with knowledge of the relevant anatomy, can scale, rotate, and shift the images until they are aligned with each other. Although this method incorporates the experience of the physician in the image registration process, the procedure usually is time-consuming and tedious. Moreover, even under the best conditions, the visual registration of the images is limited by the spatial resolution of the SPECT image, which is approximately 1 cm. Under more common and realistic conditions, the patient probably has been imaged in two different imaging systems, in different anatomical positions, and on differently shaped tables, so that rigid body transformations (magnification,

translation, and rotation) are not sufficient to register common locations in the CT and SPECT images. If the image manipulations available to the operator do not reflect the differences in the image, or if they are too awkward to use effectively, the entire image registration process becomes unreliable and impractical. For these reasons, manual image registration techniques have only had limited success in a clinical setting.

b) Image registration using external fiducial markers

In many instances, the need for image registration is recognized only after the images have been acquired and the patient is no longer easily available for additional studies. In these cases, the technologist or physicist must use internal landmarks to try to correlate the CT and SPECT data when image registration is desired. If the need for image registration is recognized before the patient is scanned, then the images can be acquired with fiducial markers that are placed on the patient to facilitate the image registration process. The markers must be designed so that they can be visualized in both the CT and SPECT images. In addition, they should be relatively small, so that they provide specific points that can be correlated between the two data sets. Finally, at least three and generally more noncolinear points need to be placed on the patient so that the spatial registration process is not ambiguous for the three dimension imaging geometry visualized with CT and SPECT. Assuming that these markers do not move relative to the patient's anatomy and that their locations are invariant with respect to the imaging modality, these markers can define a coordinate system for the CT and SPECT images. The transformation between these two coordinate systems can then be computed and applied to register the image data. This method has the advantage that the system depends on recognizing and identifying distinct artificial points rather than anatomical

features, so it is easier to automate and is more reliable than relying on internal anatomical landmarks alone.

This use of external fiducial markers has been successfully applied in the field of stereotactic radiosurgery, where millimeter precision is necessary to irradiate small structures in the brain precisely. Patients receiving this type of procedure are imaged on different machines (usually CT and MRI), and the markers also serve to define a coordinate system for the radiosurgery machine. However, the fiducial markers for radiosurgery are part of a rigid frame that is attached to the patient's skull using small screws – a method that is too invasive for use in standard diagnostic imaging. One can imagine a non-invasive immobilization frame made from thermoplastic or foam materials, but patients still would likely find such confinement uncomfortable for the 90-180 minutes required for a diagnostic SPECT scan. For this reason, it generally is desirable to perform image registration using fiducial markers without an immobilization frame, although immobilization frames could be used to insure a consistent patient geometry, especially when the CT and SPECT scans are acquired using separate systems rather than with dual-modality imaging.

c) Mutual-information methods for image registration

Recently, there has been much effort to develop automated or semi-automated image registration using the information contained in the CT and SPECT image. In addition, automated image correlation techniques may be necessary if there are internal shifts in anatomical structure that are not reflected by changes in the positions of the external fiducial markers. If one images roughly the same region of the body with CT and SPECT, some common features such as skeletal landmarks, blood vessels, or external

body contours can be seen on both images. These common features form an internal coordinate system that can be used to align the two images. These methods have been used to register PET and MRI images of the brain[1], serial PET brain studies[2], serial MRI brain studies[3], PET and CT studies in the thorax[4], and SPECT and CT brain studies[5]. For prostate imaging, methods exploiting the similarity between Tc^{99m} labeled red blood cell images and the contrast-enhanced vasculature on CT have proven fairly successful in the pelvis[6], but this method is only semi-automated since the outlines of the blood vessels must be determined by the operator. Success rates for these different methods vary, but one of their primary difficulties is that they implicitly assume that the images from different modalities share some common features. In the brain, the skull is a rigid surface and the internal components are relatively immobile, but in the abdomen and pelvis there is considerable organ motion. This means that simply aligning the bony anatomy may not be sufficient to ensure accurate registration of the soft tissue. The other caveat with this approach is that the assumption of common features may actually be wrong if, for example, a 'hot spot' on the SPECT image does not correspond to any remarkable feature on the CT image.

d) Mechanical approaches to image registration

The most robust way to solve the image registration problem is to acquire the CT and SPECT images in a consistent geometry using a dual-modality system. This provides a consistent means of controlling several inconsistencies typical of acquiring images from separate machines, including patient table shape, gross patient position, image matrix format, and different coordinate systems for the image acquisition and image reconstruction processes. Accurate image registration is most easily accomplished by

using a single, common detector for the CT and SPECT imaging as implemented with the ETCT system described in Chapter 2. However, this design is not currently practical for clinical systems due to the high cost and small area of the detector. Therefore, all current dual-modality imaging systems intended for clinical use place the CT and SPECT detectors in tandem and acquire images sequentially rather than simultaneously. This approach acquires the CT and SPECT data with the patient in a similar position, so that differences in the acquisition and reconstruction parameters (e.g. pixel size) can be resolved by calibration measurements performed before the patient data are acquired. The dual-modality imaging systems also incorporate a common patient table that is either rigid or mechanically well characterized. This allows one to derive a set of transformations that map the CT coordinate space into the SPECT space, and vice versa. The main advantage to this approach is that the patient will be imaged in a single session, so that the internal structures and functional state of the body will be as similar as possible between the two image datasets. The disadvantage is that this approach requires that the patient be imaged on a particular device with dual-modality imaging capability, so there is little flexibility to bring in data from another scanner or another modality.

3. The UCSF CT/SPECT approach

For imaging studies performed with the UCSF CT/SPECT system, we use an image registration approach that combines many of the features described above. Patients are imaged on a system where the CT and SPECT gantries share a common axis and patient table, as described in Chapter 3. The patients are first scanned with the CT scanner, and then immediately (within approximately a minute) moved under the SPECT camera for radionuclide imaging. This ensures that the patient's physical state and body habitus will

be as similar as possible in the two image sets. We also use fiducial markers on the table and (non-invasively) on the patient surface, to provide a common set of coordinates between the two images. This has the advantage of providing a means to register the images that does not depend on complex manipulations by the operator or the appearance of internal anatomical structures. Although it might be possible in our situation to mechanically characterize the table for patient registration, using fiducial markers is a more reliable method because it allows us to calculate and confirm the image registration in every patient. It is also fairly easy to implement, and has a history of providing accurate registration for past imaging studies in our research group. In the next section, we will provide a theoretical review of the methodology for registering images using fiducial markers. This theoretical background will provide a foundation for discussing our specific implementation of this system and the experimental tests of the registration system.

B. Mathematics of Fiducial Marker Registration

The geometry and mathematics of coordinate transformations is well known, so in this section we will review its adaptation to this particular research problem. Suppose that we have a hypothetical object that consists of N points held together by some rigid structure. These points cannot move relative to one another, are not coplanar, and are visible in both CT and SPECT imaging. They also are true mathematical points in that they have both infinitesimal size and infinite contrast. We image this object using CT and SPECT, and then determine the location of each of these points on both images. Thus, each point has three-dimensional CT coordinates and corresponding three-dimensional SPECT coordinates, that can be represented as:

$$(x_{CT}^{(i)}, y_{CT}^{(i)}, z_{CT}^{(i)}), (x_{SPECT}^{(i)}, y_{SPECT}^{(i)}, z_{SPECT}^{(i)}) \tag{4.1}$$

where the index (i) enumerates each individual point, with integer values from 1 to N. We may then define a transformation matrix that relates the CT coordinates to the SPECT coordinates:

$$\begin{bmatrix} x_{CT}^{(i)} \\ y_{CT}^{(i)} \\ z_{CT}^{(i)} \\ 1 \end{bmatrix} = A \begin{bmatrix} x_{SPECT}^{(i)} \\ y_{SPECT}^{(i)} \\ z_{SPECT}^{(i)} \\ 1 \end{bmatrix} = \begin{bmatrix} a_{11} & a_{12} & a_{13} & a_{14} \\ a_{21} & a_{22} & a_{23} & a_{24} \\ a_{31} & a_{32} & a_{33} & a_{34} \\ 0 & 0 & 0 & 1 \end{bmatrix} \begin{bmatrix} x_{SPECT}^{(i)} \\ y_{SPECT}^{(i)} \\ z_{SPECT}^{(i)} \\ 1 \end{bmatrix}. \tag{4.2}$$

This equation defines a transformation that converts a location in SPECT space to a location in CT space. By determining the inverse matrix A^{-1}, one can perform the inverse operation and transform CT coordinates into SPECT coordinates. The transformation can include translation, rotation, and scaling. It cannot model 'warping' transformations, e.g. a circular object becoming a rectangle, but since we are dealing with fiducial markers that do not move relative to each other, this limitation is not important.

Equation 4.2 has 12 unknown elements, so the data recorded from a single fiducial marker is not sufficient to solve for all 12 of these elements. However, we can use symmetry arguments to recast Equation 4.2 into a set of equations that uses data from all of the fiducial markers:

$$\begin{bmatrix} x_{SPECT}^{(1)} & y_{SPECT}^{(1)} & z_{SPECT}^{(1)} & 1 \\ x_{SPECT}^{(2)} & y_{SPECT}^{(2)} & z_{SPECT}^{(2)} & 1 \\ \vdots & \vdots & \vdots & \vdots \\ x_{SPECT}^{(N)} & y_{SPECT}^{(N)} & z_{SPECT}^{(N)} & 1 \end{bmatrix} \begin{bmatrix} a_{11} \\ a_{12} \\ a_{13} \\ a_{14} \end{bmatrix} = \begin{bmatrix} x_{CT}^{(1)} \\ x_{CT}^{(2)} \\ \vdots \\ x_{CT}^{(N)} \end{bmatrix} \tag{4.3}$$

$$\begin{bmatrix} x_{SPECT}^{(1)} & y_{SPECT}^{(1)} & z_{SPECT}^{(1)} & 1 \\ x_{SPECT}^{(2)} & y_{SPECT}^{(2)} & z_{SPECT}^{(2)} & 1 \\ \vdots & \vdots & \vdots & \vdots \\ x_{SPECT}^{(N)} & y_{SPECT}^{(N)} & z_{SPECT}^{(N)} & 1 \end{bmatrix} \begin{bmatrix} a_{21} \\ a_{22} \\ a_{23} \\ a_{24} \end{bmatrix} = \begin{bmatrix} y_{CT}^{(1)} \\ y_{CT}^{(2)} \\ \vdots \\ y_{CT}^{(N)} \end{bmatrix} \tag{4.4}$$

$$\begin{bmatrix} x_{SPECT}^{(1)} & y_{SPECT}^{(1)} & z_{SPECT}^{(1)} & 1 \\ x_{SPECT}^{(2)} & y_{SPECT}^{(2)} & z_{SPECT}^{(2)} & 1 \\ \vdots & \vdots & \vdots & \vdots \\ x_{SPECT}^{(N)} & y_{SPECT}^{(N)} & z_{SPECT}^{(N)} & 1 \end{bmatrix} \begin{bmatrix} a_{31} \\ a_{32} \\ a_{33} \\ a_{34} \end{bmatrix} = \begin{bmatrix} z_{CT}^{(1)} \\ z_{CT}^{(2)} \\ \vdots \\ z_{CT}^{(N)} \end{bmatrix}. \tag{4.5}$$

So long as N has a value of 4 or greater, we have sufficient information to solve these equations. The goal of the registration operation, then, is to determine the values for the elements labeled a_{ij} so that we can transform a point on the SPECT image into a point on the CT image, and vice versa. This can be accomplished by combining Equations 4.3, 4.4, and 4.5 into a single matrix equation composed of three parts:

$$C = \begin{bmatrix} x_{SPECT}^{(1)} & y_{SPECT}^{(1)} & z_{SPECT}^{(1)} & 1 & 0 & 0 & 0 & 0 & 0 & 0 & 0 & 0 \\ 0 & 0 & 0 & 0 & x_{SPECT}^{(1)} & y_{SPECT}^{(1)} & z_{SPECT}^{(1)} & 1 & 0 & 0 & 0 & 0 \\ 0 & 0 & 0 & 0 & 0 & 0 & 0 & 0 & x_{SPECT}^{(1)} & y_{SPECT}^{(1)} & z_{SPECT}^{(1)} & 1 \\ x_{SPECT}^{(2)} & y_{SPECT}^{(2)} & z_{SPECT}^{(2)} & 1 & 0 & 0 & 0 & 0 & 0 & 0 & 0 & 0 \\ 0 & 0 & 0 & 0 & x_{SPECT}^{(2)} & y_{SPECT}^{(2)} & z_{SPECT}^{(2)} & 1 & 0 & 0 & 0 & 0 \\ 0 & 0 & 0 & 0 & 0 & 0 & 0 & 0 & x_{SPECT}^{(2)} & y_{SPECT}^{(2)} & z_{SPECT}^{(2)} & 1 \\ \vdots & \vdots & \vdots & \vdots & \vdots & \vdots & \vdots & \vdots & \vdots & \vdots & \vdots & \vdots \\ x_{SPECT}^{(N)} & y_{SPECT}^{(N)} & z_{SPECT}^{(N)} & 1 & 0 & 0 & 0 & 0 & 0 & 0 & 0 & 0 \\ 0 & 0 & 0 & 0 & x_{SPECT}^{(N)} & y_{SPECT}^{(N)} & z_{SPECT}^{(N)} & 1 & 0 & 0 & 0 & 0 \\ 0 & 0 & 0 & 0 & 0 & 0 & 0 & 0 & x_{SPECT}^{(N)} & y_{SPECT}^{(N)} & z_{SPECT}^{(N)} & 1 \end{bmatrix} \tag{4.6}$$

$$\boldsymbol{b}^T = \begin{bmatrix} x_{CT}^{(1)} & y_{CT}^{(1)} & z_{CT}^{(1)} & x_{CT}^{(2)} & y_{CT}^{(2)} & z_{CT}^{(2)} & \cdots & x_{CT}^{(N)} & y_{CT}^{(N)} & z_{CT}^{(N)} \end{bmatrix} \tag{4.7}$$

$$\boldsymbol{d}^T = \begin{bmatrix} a_{11} & a_{12} & a_{13} & a_{14} & a_{21} & a_{22} & a_{23} & a_{24} & a_{31} & a_{32} & a_{33} & a_{34} \end{bmatrix}. \tag{4.8}$$

Using this notation, we can restate the transformation equation, including information from all of the N points, as simply:

$$\boldsymbol{b} = \boldsymbol{C}\boldsymbol{d} \,. \tag{4.9}$$

This is a conventional (albeit somewhat large) matrix equation that can be solved numerically for the unknown vector $\boldsymbol{d}$ using a technique such as singular value decomposition (SVD)[7]. SVD is an iterative technique for matrix inversion that has several advantages for this application. The first is that SVD is robust and will almost always converge to a solution that is the best fit to the available data, even if no exact solution exists. The second is that SVD can easily adapt to an overspecified problem. In this example, an overspecified problem is one in which coordinates from more than 4 fiducial markers are available to compute a solution. This adaptability helps SVD find solutions in the presence of noise or measurement error, because we can measure an arbitrary number of points and SVD will compute the best fit using all available data. Finally, SVD is fairly simple to implement on a computer, and requires only a few seconds of computation time to solve a matrix equation of this size.

C. Implementation of the Registration System.

1. Introduction and Overview

In a realistic imaging situation, the fiducial markers are not points with infinite contrast and infinitesimal size, and the measurement systems used to locate them have noise and finite spatial resolution. Thus, the accuracy of a realistic imaging system could be significantly poorer than the accuracy of the theoretical system. In this section, we will discuss the methodology for implementing the registration mathematics for real imaging situations. We will begin by describing the fiducial markers used for registration of

images from the combined CT/SPECT system. Then, we will discuss the methods used to locate the marker centers on the image and to transform from CT coordinates into SPECT coordinates. Finally, we will examine how the image acquisition parameters can affect our ability to locate the marker centers. This latter analysis will be used to help choose an optimum slice thickness for the CT scans of patients undergoing ^{111}In-ProstaScint® CT/SPECT imaging.

2. Fiducial Marker Design

The fiducial markers used in these tests are based on a design that has been used to successfully register CT/SPECT images in previous phantom and animal studies[8, 9]. These markers are constructed by sealing the tubular opening of a standard injection port (Baxter, Deerfield, IL) with plastic and epoxy (Figures 4-1 and 4-2).

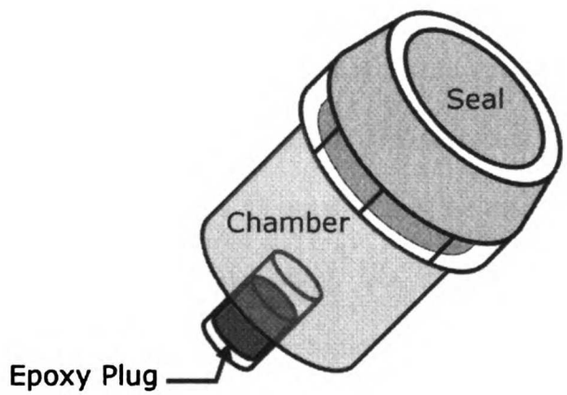


Figure 4-1: Schematic diagram of the fiducial marker used for CT/SPECT image registration.

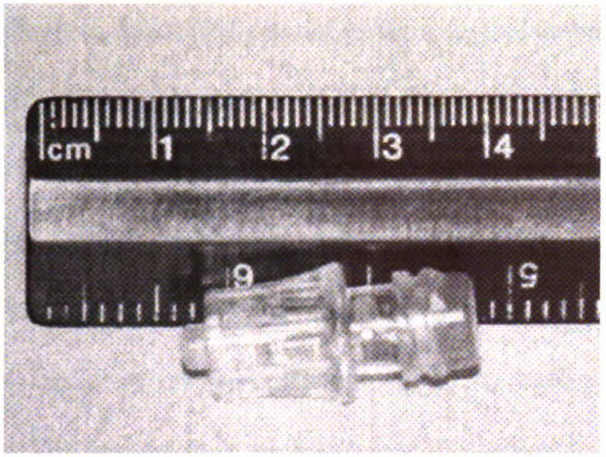


Figure 4-2: Photograph of the fiducial marker used for CT/SPECT image registration.

The interior of the marker is a thus a small cylindrical volume (approximately 0.2 ml) that can be accessed through the polymer seal of the injection port. This volume is filled with a solution containing CT contrast material and radioisotope, so that it can be visualized on both the CT and the SPECT images. The design allows the markers to be easily filled and emptied using syringes, yet prevents the leakage of the solution during an imaging study. The small size of the markers (approximately 2 cm long and 1 cm in diameter) means that the markers are much smaller than the patient being imaged, and thus do not interfere with the radiological image. The markers are also inexpensive, easy to handle, and can be refilled and used for multiple studies.

For the ^{111}In-ProstaScint® patient studies, the markers were filled with a solution containing 300 mg/ml of K_2HPO_4 and 33 μCi/ml of Tc^{99m}. K_2HPO_4 is a material with attenuation properties similar to those of bone, so the markers appear as bright points on the CT image. This brightness, combined with the fact that the markers are located outside the patient, makes the markers easy to visualize on CT. The radioactivity

concentration in the markers was initially based on the expected count density of the nuclear medicine image. Patients typically receive 3.5 to 5 mCi of Tc^{99m} intravenously before ^{111}In-ProstaScint® imaging, so that the blood pool can be visualized. This equates to a concentration of approximately 1 μCi/ml of blood. We initially used a radioactivity concentration in the markers of 100 μCi/ml, but the interpreting physicians felt that this made the markers too intense on the final patient images. Decreasing the radioactivity concentration to 33 μCi/ml produced an acceptable level of radiological brightness for the markers, yet still allowed visualization of the markers for the image registration program.

Figure 4-3 shows example CT and SPECT slices that include the fiducial markers. The markers are visible as bright dots in the upper left and lower right of the images, and are highlighted by circles.

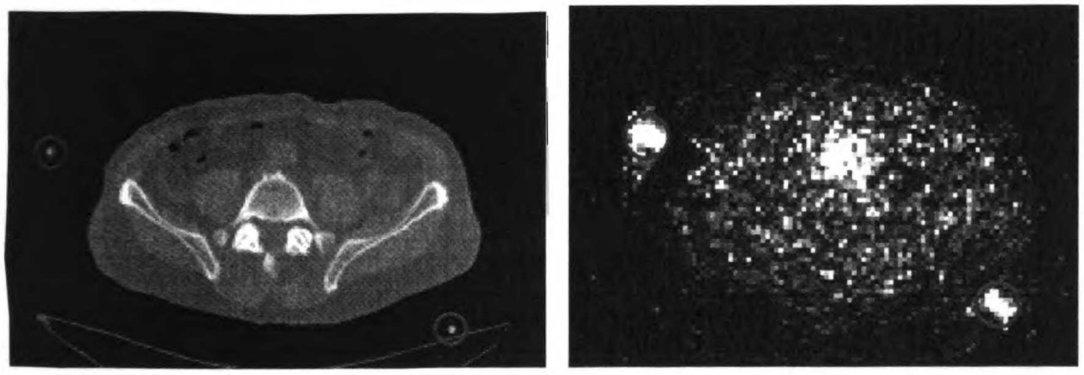


Figure 4-3: CT and SPECT images illustrating the appearance of fiducial markers.

3. Determination of Marker Centers

Figure 4-3 reveals that the fiducial markers do not appear as sharp, noiseless points in the CT and SPECT images, so it is necessary to adapt the theoretical framework described above for the practical reality of the actual images. This task is accomplished by computing the location of the centroid of the fiducial markers, which occurs in three steps. First, an observer reviews the images and estimates the approximate center of each marker on both the CT and SPECT images. This measurement is based solely on visual information, and is akin to determining an 'eyeball best-fit line' to a series of x-y points.

Once the locations of these approximate centers have been entered into the computer program, the program searches a cylindrical volume around the approximate centers for image pixels that exceed a specified threshold. This search volume is based on the size of the markers plus a 1 cm margin, so it is roughly 4 cm tall and 3 cm in diameter. The circles in Figure 4-3 are approximately the size of the search volume. The threshold values for the CT image are chosen based on the expected value of the markers, which is approximately 200 Hounsfield Units (HU). The HU is the standard measure of CT attenuation, and is defined so that water is 0 HU and air is –1000 HU. For the SPECT image, the relationship between radioactivity concentration and pixel value in the tomographic image is complex, so it is difficult to determine a threshold in advance. Thus, we typically use a threshold value of half of the maximum pixel value within the search volume.

The final step of this process is to compute a centroid location based on the (x,y,z) coordinates of all the pixels inside the search volume that exceed the threshold. This is simply a weighted average of the pixel coordinates, where the weights are the image

values of each pixel. The location of the centroid for each fiducial marker is then used as the coordinates (x_{CT},y_{CT},z_{CT}) and (x_{SPECT},y_{SPECT},z_{SPECT}) for the registration calculations defined previously, which allows us to calculate the transformation matrix *A* for the CT and SPECT images.

4. Transforms Between Coordinate Spaces

Once we have obtained the transformation matrix *A*, it is possible to convert the SPECT image into the CT image coordinates, and vice versa. Both the CT image and the SPECT image are represented as discrete spaces with rectangular voxels, so we can remodel them as as three-dimensional grids of regularly spaced points, where each voxel is replaced by a point at the center of the voxel. Using this approach, it is straightforward to transform an (x,y,z) coordinate from the SPECT space to the CT space (or *vice versa*), and it is also simple to interpolate the value of new, intermediate grid points. For example, to convert the SPECT image to the CT image coordinates, we multiply the positions of each SPECT voxels by the transformation matrix A. This gives a new grid of points that have the SPECT values, but are in the CT coordinate system. This new grid can then be interpolated so that the coordinates of the SPECT points very closely match the coordinates of the CT points. This operation ensures that the transformed SPECT image will have exactly the same image matrix size, slice thickness, and pixel dimensions as the original CT image.

5. Optimization of Imaging Parameters

a) Introduction

There are many user-defined parameters in the image acquisition process. These parameters affect the properties of the final tomographic images, and thus will also affect our ability to locate markers and ultimately register the two images together using our fiducial marker system. However, many of these parameters are constrained because of the clinical task of imaging the pelvic anatomy with CT and imaging ^{111}In-ProstaScint® with SPECT. For example, the manufacturer recommendations for optimal SPECT imaging of ^{111}In-ProstaScint® specify a 128x128 image matrix size, with a minimum of 60 views, and 50 seconds per view. Our SPECT system can acquire either 32, 64, or 128 views; we chose 64 views since 128 views would require a 107 minute acquisition, which is too long for most patients. The 128x128 image matrix size provides a reconstructed voxel having a width of 0.432 cm, so a single voxel is about 20% of the size of the marker. It is possible to acquire the SPECT projection data using a 256x256 image matrix size, but the resultant tomographic image is then dominated by noise and is unacceptable for radiological interpretation.

In the case of CT imaging, the manufacturer recommendations for pelvic examinations specify at least a 256x256 matrix with a slice thickness of at most 10 mm. This provides adequate image resolution for radiologic interpretation, but a 10 mm slice thickness only barely satisfies the sampling criteria for resolving a 2 cm long object such as the fiducial marker. For image registration, we prefer making the slice thickness as small as possible so that we can accurately locate the centroid of the marker. However,

decreasing the slice thickness increases both the time required for the acquisition and the radiation dose to the patient. Thus, we need to determine the effects of CT slice thickness on our ability to resolve the markers axially, so that we can intelligently balance this effect against the constraints of radiation dose and acquisition time.

b) Experimental Methods

We studied the selection of slice width for image coregistration by imaging a bone densitometry phantom (Mindways, San Francisco, CA) in the CT/SPECT system. Five fiducial markers were prepared and placed on both the patient table and the phantom. Markers on the patient table were taped directly to the table, and markers on the phantom were attached using small cardboard standoffs. A photograph of the phantom and markers is shown in Figure 4-4.

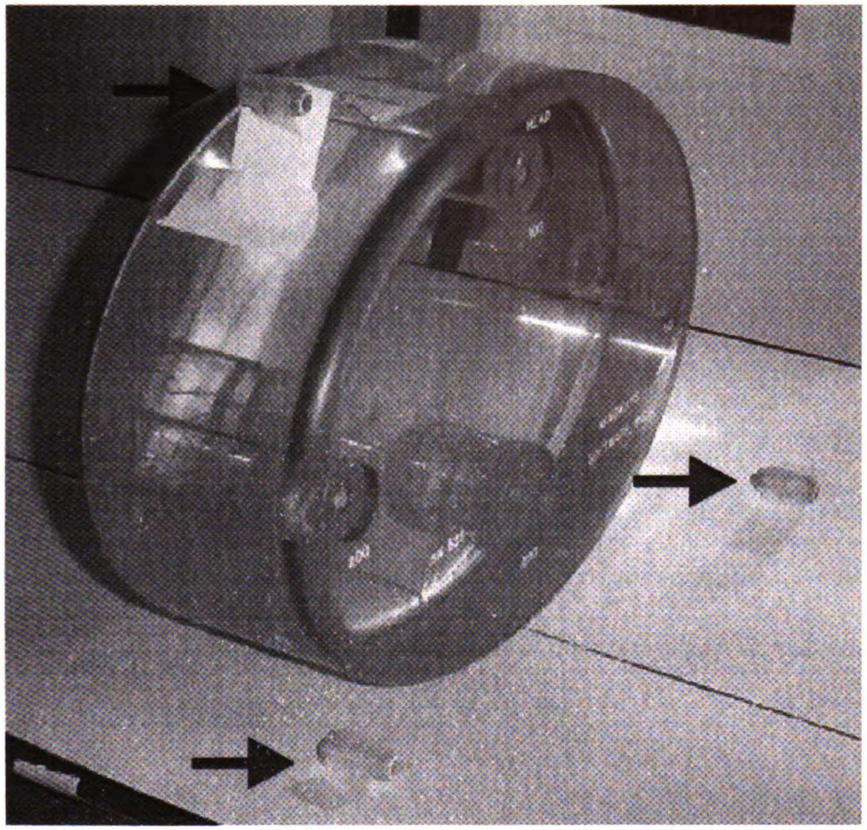


Figure 4-4: Photograph illustrating placement of fiducial markers on the imaging table and the phantom. Three markers are visible in this figure, and the others are not visible because they are on the underside of the table.

The markers were placed randomly around the phantom, with the following constraints: (1) the markers could not all lie in the same plane, (2) at least one marker was placed on the anterior surface of the phantom, and one was on the posterior surface of the patient table. These constraints satisfied the criteria for the image registration algorithm and ensured that the positions of both the table and the phantom were recorded. The phantom and fiducial markers were then imaged with the CT system. For all examination, a 256x256 image matrix size was used, but each acquisition used a different

slice thickness. All possible values of slice thickness (based on this CT system's hardware constraints) were tested, so the slice thickness was set to 1.5, 3, 5, or 10 mm. The resulting tomographic images were used as inputs to a registration program, which calculated the centroid of each marker but did not perform any other registration operations.

Because the 1.5 mm slice thickness represents the finest possible axial sampling, the z-axis locations of marker centroids calculated from the 1.5 mm thick images were considered to be the true positions of the markers. The z-coordinate of each marker was converted to an absolute z position (mm from the first CT slice of the image) by multiplying by the slice thickness. An error term was then computed for each marker, where the error was defined by:

$$Error(i, st) = z_{st}^{(i)} - z_{1.5}^{(i)}. \tag{4.10}$$

The index i enumerates the individual markers, z is the position of the marker center in mm, st is the slice thickness (3, 5, or 10), and $z_{1.5}$ represents the measurement of the z-position from the 1.5 mm thick CT slices.

c) Results and Discussion

The error measurements from Equation 4.10 are presented graphically in Figure 4-5.

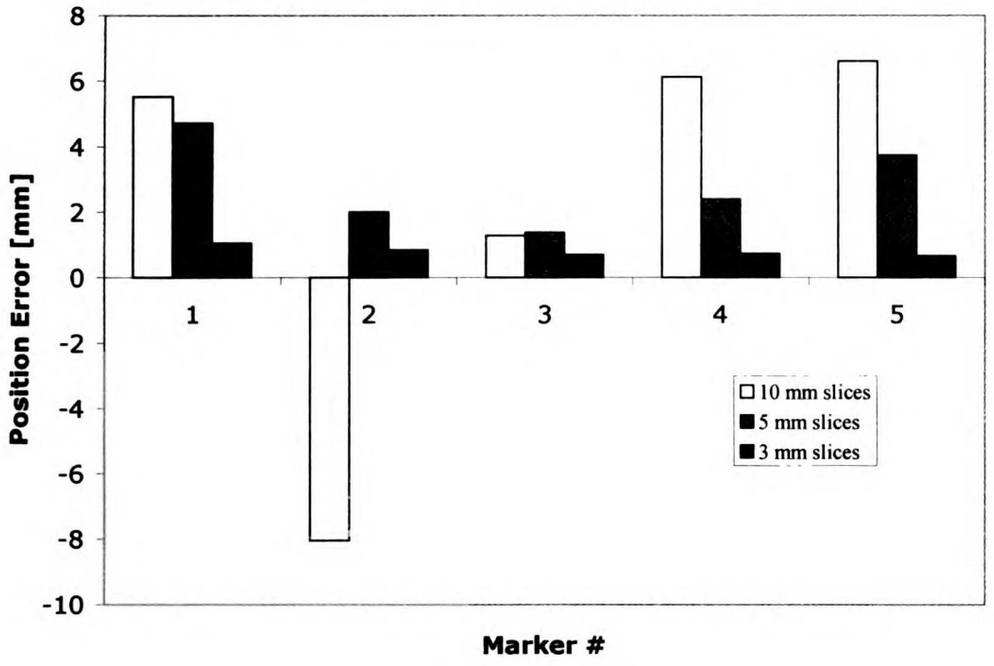


Figure 4-5: Effect of various CT slice thicknesses on marker center localization.

We also calculated the root-mean-squared error for each value of slice thickness, by using

$$RMSerror(st) = \sqrt{\frac{\sum_i Error(i,st)^2}{5}}. \tag{4.11}$$

The *RMSerror* is 6.0, 3.1, and 0.64 for the 10, 5, and 3 mm slices, respectively.

These data indicate that, in terms of our ability to find the true center of the markers, there is a clear benefit to thinner slices, which is exactly what one would expect from sampling criteria. However, we must balance this benefit against other constraints. First, the radiation dose scales approximately inversely with the slice thickness, so going from 10 mm slices to 1.5 mm slices will significantly increase the patient dose. The dose from a 10 mm slice thickness CT examination is generally low (on the order of 2-3 rads),

but we should attempt to keep the dose as low as possible unless a compelling reason exists to increase the dose. A more serious limitation is the imaging time required for thin slice CT scans. The GE 9800 used in the CT/SPECT system can only acquire data in single-slice mode, and x-ray tube heat loading requirements restrict the system to a duty cycle of approximately 1 slice every 15 seconds during an examination. The CT scan must cover at least the same area as the gamma camera, which translates to roughly 38 cm in the axial direction. This area could be covered in 10 minutes using 10 mm thick slices, but to cover the same area with 1.5 mm slices would require 67 minutes, which is quite lengthy for a diagnostic procedure. A final limitation is that the CT system is only capable of storing and processing a maximum of 100 slices at any one time, so the 1.5 mm slices would require the operator to stop acquisition, offload data onto a tape backup device, and then resume acquisition. The tape backup requires approximately 45 minutes, so this requirement would impose an intolerably long scan time.

The 5 mm slice thickness or the 3 mm slice thickness options represent a compromise between axial resolution and time/dose constraints. However, choosing the 3 mm slice thickness would again require more than 100 slices to cover the gamma camera area, so it is not a truly viable option with the CT scanner available for this study. Choosing 5 mm thick slices means that the CT imaging can be completed in a single session (approximately 80 slices) lasting 20 to 30 minutes, and from Figure 4-4 we can observe a clear advantage to using 5 mm thick slices rather than 10 mm slices.

For the patient studies, the first four patients were scanned using 10 mm thick slices in an attempt to minimize the total imaging time and dose. However, the registration system did not work well for these patients; we devised this axial sampling

experiment to test whether or not an improvement in axial sampling might potentially improve the accuracy of the registration. Based on the results of this test, we used 5 mm slice thicknesses for all subsequent patient CT scans. This change helped to improve the accuracy of the registration, as we shall see in the following section.

D. Validation of the Registration System in Patient Studies

1. Introduction and Overview

A true test of the image registration methodology must evaluate its performance in actual patient studies. In this section, we first will briefly describe the imaging of ^{111}In-ProstaScint® patients in the CT/SPECT system (a complete description of the patient imaging protocol can be found in Chapter 7). Then, we will discuss two objective tests of the image registration methodology. The first test evaluates the registration algorithm from a theoretical standpoint, assessing its accuracy at reproducing a known transformation matrix given a set of CT and SPECT coordinates. The second test assesses the quality of the registration by comparing the positions of fiducial markers in the original CT image and the transformed SPECT image(the SPECT image mapped into CT coordinates). Finally, we will discuss the radiological assessment of the registered CT and SPECT images, and show examples where the registration succeeded and failed. These subjective results will also be compared with the objective assessment of registration. Finally, we will analyze these results and suggest improvements for future studies.

2. Experimental Methods

a) Patient Preparation and Image Acquisition

The nuclear medicine studies used for this project enrolled patients injected with ^{111}In-ProstaScint® and ^{99m}Tc-labeled autologous red blood cells at the UCSF Nuclear Medicine clinic, according to standard protocols for ^{111}In-ProstaScint® SPECT imaging. Prior to patient imaging, the fiducial markers were prepared using the methods outlined previously. Seven fiducial markers were used for the patient studies, so that even if one or two markers fell outside the imaging region, we would still have sufficient information to compute the registration matrix *A*. Fiducial markers then were placed on the table using the following restrictions, which were similar to those applied to the phantom study: (1) the markers could not all lie in the same plane, and (2) at least two markers were placed on the anterior surface of the patient, and two more were placed on the posterior surface of the patient table. Markers on the anterior surface of the patient were attached to small cardboard standoffs so that they would not rest against the patient's skin. These standoffs were taped to the patient's clothing over the iliac crest, since this area of the body has minimal voluntary motion. A lightweight restraining strap also was used to further limit body motion in this area. The remaining three markers were placed on the anterior surface of the table, so that they would appear between the table and the patient. An inflatable closed-cell foam mattress and sheets were used to cover the table, so that the table would be more comfortable for the patients. Patients were positioned on the table of the CT/SPECT system so that their centerlines matched the centerline of the table, and so the pelvis would be placed within the scannable region of the table (the

portion of the table that can be viewed by both imaging systems). The table height was also adjusted so that the patient would be centered inside the CT gantry opening. These precautions helped to ensure that the tomographic images covered as much of the patient as possible. CT scans of the patient were acquired using a 256x256 image matrix and a 48 cm field of view. As discussed in the previous section, the first 4 patients were scanned with 10 mm thick CT slices, and subsequent patients were scanned with 5 mm thick CT slices. SPECT projection data were acquired using a 128x128 image matrix and 64 angular views, with 60 seconds per view. Tomographic CT slices and raw SPECT projection data were downloaded from the CT/SPECT system and transferred to a computer for further analysis. SPECT projection data were reconstructed into tomographic slices using an iterative reconstruction algorithm as described in Chapter 2. We then registered the CT and SPECT images together using the methodology outlined in the previous section.

b) Theoretical Repeatability of the Registration Algorithm

For each patient, the registration program computes the location of the centroid of each marker on both the CT and the SPECT images. The coordinates of these centroids are used as input data to a program that calculates the transformation matrix A. In this test, we first applied that transformation to the SPECT marker centroid locations (using Equation 4.2), thereby transforming these coordinates into the CT coordinate system. The original SPECT marker centroid locations and the transformed marker locations were then used as input data to a second registration program. This second program does not perform a centroid calculation, so the input coordinates are passed directly to the function that calculates the transformation matrix. The result is a new transformation

matrix A', which should be an almost exact match for the original transformation matrix A. In essence, we are determining if the registration algorithm can accurately recover a known transformation matrix. To assess this capability numerically, we calculated a difference matrix (A'-A) and then computed the quadrature sum of the elements in the difference matrix. This calculation was repeated for all of the patients.

c) Experimental Test of Registration System

After image registration, the locations of the centroids of the fiducial markers in the original CT image and the transformed SPECT image should be the same. Similarly, the locations of the centroids of the fiducial markers in the original SPECT image and the transformed CT image should be the same. Differences between these locations can be used as a metric to assess the registration objectively. Using the original and registered images, we measured the distance between the original CT markers and the transformed SPECT markers, and also the distance between the original SPECT markers and the transformed CT markers. We can express this calculation in terms of the mathematics used earlier in this chapter by defining the coordinates of the transformed SPECT marker as:

$$\begin{bmatrix} x'_{CT}{}^{(i)} \\ y'_{CT}{}^{(i)} \\ z'_{CT}{}^{(i)} \\ 1 \end{bmatrix} = A \begin{bmatrix} x_{SPECT}{}^{(i)} \\ y_{SPECT}{}^{(i)} \\ z_{SPECT}{}^{(i)} \\ 1 \end{bmatrix} \tag{4.12}$$

so that the distance between the original CT marker and the transformed SPECT marker is given by:

$$r_{CT}^{(i)} = \sqrt{(x_{CT}^{(i)} - x'_{CT}^{(i)})^2 + (y_{CT}^{(i)} - y'_{CT}^{(i)})^2 + (z_{CT}^{(i)} - z'_{CT}^{(i)})^2} \ . \quad (4.13)$$

We can convert this number to a physical distance in millimeters by using the size of a CT voxel (1.875 mm x 1.875 mm x slice thickness) as the conversion factor. The coordinates of the transformed CT marker can likewise be defined as

$$\begin{bmatrix} x'_{SPECT}^{(i)} \\ y'_{SPECT}^{(i)} \\ z'_{SPECT}^{(i)} \\ 1 \end{bmatrix} = A^{-1} \begin{bmatrix} x_{CT}^{(i)} \\ y_{CT}^{(i)} \\ z_{CT}^{(i)} \\ 1 \end{bmatrix} \quad (4.14)$$

with the distance between the original SPECT marker and the transformed CT marker given by:

$$r_{SPECT}^{(i)} = \sqrt{(x_{SPECT}^{(i)} - x'_{SPECT}^{(i)})^2 + (y_{SPECT}^{(i)} - y'_{SPECT}^{(i)})^2 + (z_{SPECT}^{(i)} - z'_{SPECT}^{(i)})^2} \quad (4.15)$$

We measured the distances r_{CT} and r_{SPECT} for all of the markers in all of the patient studies, and computed a mean value of r_{CT} and r_{SPECT} for each patient by averaging over all of the markers for that patient.

3. Results

a) Theoretical Repeatability Test

The average value (over all the patients) of the quadrature sum of the elements of the difference matrix (A'-A) was 2.2686e-10 ± 2.8908e-10. The elements of the matrices A and A' typically have a value between 0.005 and 10.0, so this test result indicates that a given transformation matrix can be recovered from transform pairs of CT and SPECT

coordinates with an accuracy of roughly 0.000005%. Thus, the singular value decomposition process is quite suitable for the task of determining the transformation matrix, and should not be a limiting factor in our ability to register patient images to one another.

b) Results from patient studies

The mean values of r_{CT} and r_{SPECT} are shown graphically in Figure 4-6.

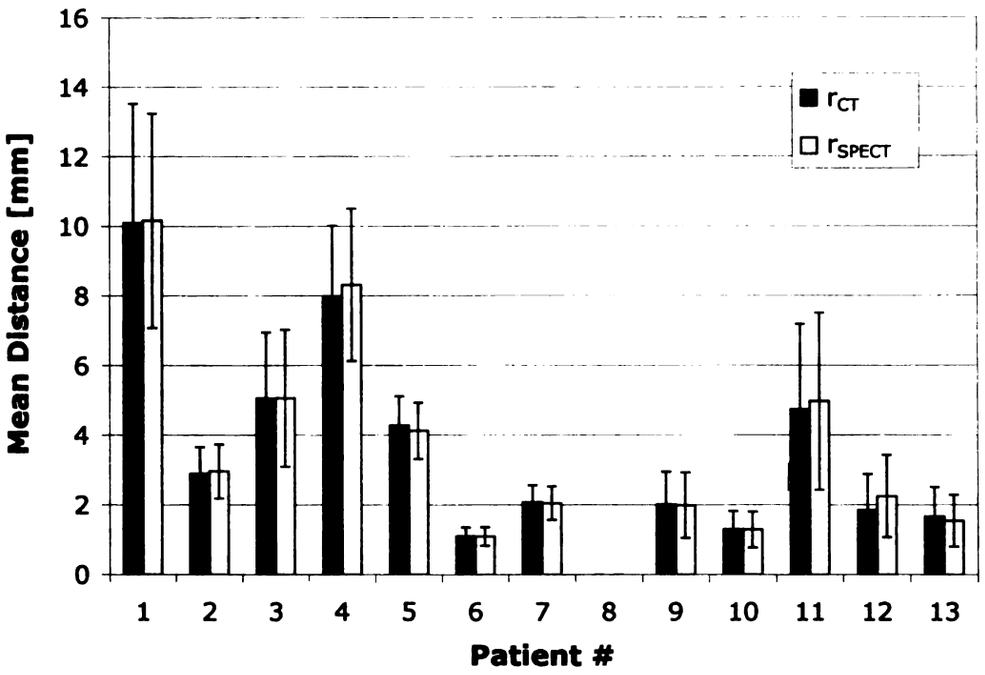


Figure 4-6: Average registration error over each patient's markers for CT/SPECT images of patient studies.

Error bars represent the standard deviation of the r_{CT} and r_{SPECT} measurements about the mean value. No data was available for patient #8, because the CT/SPECT imaging did not include enough markers to properly compute the registration due to a mistake in the

patient positioning. Patients 1 through 4 were imaged using 10 mm thick CT slices, and the remaining patients were imaged using 5 mm thick CT slices. Patient #11 was unable to complete the entire CT/SPECT exam in one session, so the exam was done in two separate sessions (one for CT and one for SPECT); the patient was repositioned on the table as closely as possible before the SPECT imaging session.

Figure 4-6 demonstrates several important properties of the registration system. First, the results from the calculation of r_{CT} and r_{SPECT} are similar, which is plausible given that they are measures of the same quantity in two different coordinate spaces. In a perfect measurement system, we would expect them to be exactly the same, but a realistic measurement system is affected by image noise, limited spatial resolution, and sampling errors. Second, the patient studies acquired with 10 mm slices tend to have much larger values of r_{CT} and r_{SPECT} than the patient studies acquired with 5 mm slices, which corresponds well with our earlier results regarding axial sampling accuracy. If the markers are not sufficiently sampled in the axial direction, the position determination for the marker will be poorer, which will negatively affect the results of the registration system. Third, the relatively high value for patient #11 is associated with the patient having gotten off the imaging table in between the CT and SPECT acquisitions, which could naturally produce some misregistration between the image sets. Finally, the average value of r_{CT} and r_{SPECT} for the patients scanned with 5 mm thick CT slices is approximately 3 mm, which is just slightly smaller than the size of a SPECT voxel. Taken together, these results indicate that the registration system is functioning properly, and that it can properly produce registered images from the CT/SPECT system.

4. Discussion

a) Subjective assessment of image registration

Although it is possible to quantify whether the positions of fiducial markers match each other on two registered tomographic images, an objective assessment of the entire image is difficult. The CT and SPECT scans have completely different contrast mechanisms, so the value of a pixel on a CT image is often unrelated to its value on the SPECT image. For evaluating the entire image and the registration process as a whole, we asked the physicians interpreting these images to decide whether or not the images were properly registered. The observers generally assessed softcopy images where the CT scan was used as a background and the SPECT scan was overlaid on the CT scan as a color map, but softcopy and hardcopy images of the separate studies also were available. Because this is a purely subjective assessment, we did not attempt to measure this impression on a linear scale, but some examples will help to illustrate how the criteria for proper image registration were defined.

Figure 4-7 shows a CT/SPECT image from patient #4, demonstrating a problem with the image registration process.

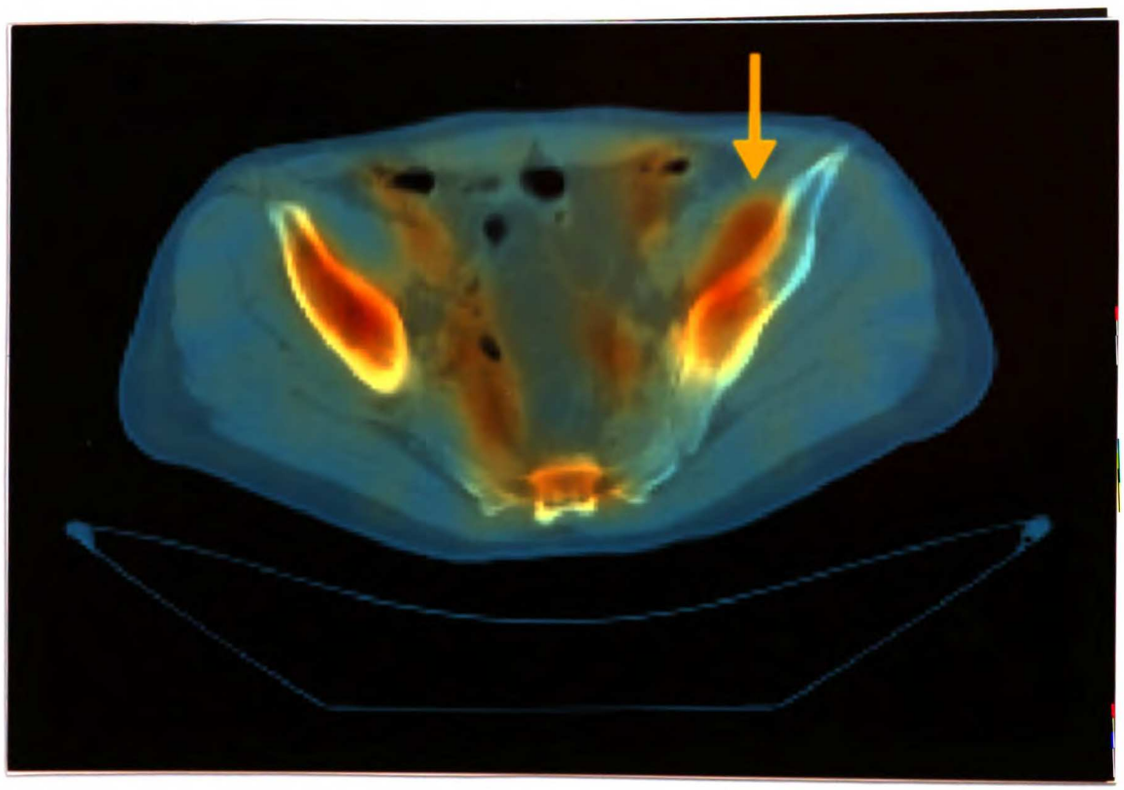


Figure 4-7: Example of a CT/SPECT image with problematic registration.

In this example, the red color corresponds to increased uptake of ^{111}In-ProstaScint®, and the blue color signifies little or no uptake. ^{111}In-ProstaScint® is taken up by the bone marrow, so one would expect the pelvic bones to match the red portions of the overlay image. On the right half of the image (which is the patient's left side), the yellow arrow highlights an area where the registration has not worked well. This image also reveals that the registration can produce mixed results, in the sense that the contralateral side of the image appears to be properly registered. Because the registration transformation is complex and can include scaling, rotation, and translation, we generally found that misregistration was not a global problem for the CT/SPECT images, but was instead limited to particular areas of the image. This tends to bias the subjective evaluation,

since an image which is mostly correct yet shows some small errors still counts as being misregistered. However, we prefer from a clinical standpoint to have exact registration over the entire image, so this conservative approach to image evaluation is justified.

We can compare the previous image with Figure 4-8, where the registration has produced excellent results. This image is taken from patient #12.



Figure 4-8: Example of a CT/SPECT image with excellent registration.

In this image, the bright areas indicating ^{111}In-ProstaScint® uptake follow the contours of the bones very closely, and the bright central region is almost exactly over the vertebral body. These particular examples do not highlight any differences in the soft tissue uptake of ^{111}In-ProstaScint®; this is because the soft tissue structures do not have as much contrast as bones on the CT image, so it is harder to evaluate any potential registration errors.

Using the criteria discussed in this section, some visual misregistration errors were noted in 6 of the 12 patients (patient numbers 1, 3, 4, 5, 7and 11), although the overall impression from the physician readers was that the registration was quite accurate. Once again, most of the images acquired with 10 mm thick CT slices were found to be visually misregistered in some area, whereas the images acquired with 5 mm slices were more likely to be free of problems. These results further convinced us that 5 mm slice thickness CT scans were a better choice than 10 mm slice thickness CT scans.

b) Comparison with previous experiments

Previous testing of this registration algorithm and this fiducial marker system with phantom studies calculated distances for r_{CT} and r_{SPECT} in the range of 0.1 to 0.4 mm[8, 10]. Although the results from the patient studies are an order of magnitude larger, they are still comparable to the spatial resolution of the SPECT system, and the registration was generally found to be acceptable by the physician observers. Furthermore, imaging actual patients presents two major new challenges to the registration system. First, human patients are not immobile and static objects. During a lengthy imaging study, patients may find it necessary to move around, in order to mitigate the effects of musculoskeletal pain or fatigue. Patients in this study only were restrained loosely with a cloth strap, and thus nothing prevented them from shifting their legs or hips during the examination. Even if the patient fully controls their voluntary motion, there are also involuntary motions, such as the settling of internal structures when the patient is placed in a supine position or the rearrangement of bowel contents due to peristalsis. In the pelvic region, natural renal activity causes the urinary bladder to fill during the examination, which alters the bladder shape and the arrangement of surrounding tissues.

Respiratory motion also happens involuntarily, though this is not a significant problem when imaging the pelvis and lower abdomen. Second, the patient table on the CT/SPECT system is only supported on either side of the CT gantry, so when the patient is under the SPECT camera, roughly 80% of their body weight is cantilevered beyond these supports. Although the fiducial markers are used to track the table deflection, there may be some subtle warping of the table and the patient that is not adequately modeled by the fiducial markers. Although it might be possible to place more markers around the patient so that the registration program has more data points, we are ultimately limited by our inability to sample the interior of the patient with the markers. For these reasons, we feel that the registration system is sufficient for the current CT/SPECT imaging system, and is not likely to be improved without either a major redesign of the table or a more restrictive immobilization device for the patient.

c) Potential future improvements

Succeeding generations of CT/SPECT systems may be able to address some of these limitations in the image registration process described above. Non-invasive immobilization devices for the pelvis have been developed for radiation therapy treatments, which allow repeatable patient positioning with millimeter accuracy over several weeks of treatment. Using such a device for imaging could be very beneficial if the CT/SPECT information were being used to plan radiation therapy. In this case, the patient would then be imaged in their treatment position, eliminating discrepancies between the CT scan acquired for treatment planning and the CT/SPECT study acquired for diagnosis. However, these devices are uncomfortable, so the patient normally is immobilized in this device for only a 10-minute treatment session. Thus, the time for

imaging would need to be shortened significantly (a full examination using the current CT/SPECT system requires that the patient remain on the table for approximately 2 hours) to make this option viable and feasible in a clinical setting. Decreasing the distance between the CT field of view and the SPECT field of view, or designing a more inflexible table could also improve the image registration. The GE Medical Systems 'Hawkeye' scanner places a low-power CT scanner on an existing SPECT gantry, which allows the systems to be in very close proximity. Further into the future, it may be possible to develop a practical clinical system based on the ETCT design of a single detector for both CT and SPECT data, which could eliminate the need for registration systems altogether.

E. Summary

In this chapter, we have explained the fiducial marker registration system used to align CT and SPECT images from the UCSF CT/SPECT system. Phantom tests were performed to study the effect of CT slice thickness on our ability to localize the fiducial markers, with these results helping to shape the patient imaging protocol. Image registration for the patient studies was evaluated retrospectively by analysis of the fiducial marker positions in the registered images and through radiological evaluation. Although some sporadic misregistration errors occurred, the registration system generally was satisfactory for the task of combined imaging of ^{111}In-ProstaScint®, and allowed the interpreting physicians to observe both the CT and SPECT images on a single combined display. This enabled simple and direct correlation between features on the CT and SPECT images. It also provided information necessary for improving the reconstruction of the SPECT images, as we shall see in the following chapter.

References:

[1] R. P. Woods, S. T. Grafton, C. J. Holmes, S. R. Cherry, and J. C. Mazziotta, "Automated image registration: I. General methods and intrasubject, intramodality validation," *J Comput Assist Tomogr*, vol. 22, pp. 139-52., 1998.

[2] R. P. Woods, S. T. Grafton, J. D. Watson, N. L. Sicotte, and J. C. Mazziotta, "Automated image registration: II. Intersubject validation of linear and nonlinear models," *J Comput Assist Tomogr*, vol. 22, pp. 153-65., 1998.

[3] E. E. Graves, A. Pirzkall, S. J. Nelson, D. Larson, and L. Verhey, "Registration of magnetic resonance spectroscopic imaging to computed tomography for radiotherapy treatment planning," *Med Phys*, vol. 28, pp. 2489-96., 2001.

[4] C. L. Aitken, F. Mahmoud, G. McGuinness, E. L. Kramer, G. Q. Maguire Gq Jr, and M. E. Noz, "Tumor Localization and Image Registration of F-18 FDG Coincidence Detection Scans with Computed Tomographic Scans," *Clin Nucl Med*, vol. 27, pp. 275-282., 2002.

[5] G. C. Kagadis, K. K. Delibasis, G. K. Matsopoulos, N. A. Mouravliansky, P. A. Asvestas, and G. C. Nikiforidis, "A comparative study of surface- and volume-based techniques for the automatic registration between CT and SPECT brain images," *Med Phys*, vol. 29, pp. 201-13., 2002.

[6] R. J. Hamilton, M. J. Blend, C. A. Pelizzari, B. D. Milliken, and S. Vijayakumar, "Using vascular structure for CT-SPECT registration in the pelvis," *Journal of Nuclear Medicine*, vol. 40, pp. 347-51, 1999.

[7] W. H. Press, B. P. Flannery, S. A. Teukolsky, and W. T. Vetterling, *Numerical Recipes in C*. Cambridge: Cambridge University Press, 1988.

[8] H. R. Tang, "A Combined X-ray CT-Scintillation Camera System for Measuring Radionuclide Uptake in Tumors," Bioengineering Ph.D. Dissertation, University of California Berkeley and University of California San Francisco, 1998, pp. 171.

[9] A. J. Da Silva, H. R. Tang, K. H. Wong, M. C. Wu, M. W. Dae, and B. H. Hasegawa, "Absolute quantification of regional myocardial uptake of 99mTc-sestamibi with SPECT: experimental validation in a porcine model. [Comment In: J Nucl Med. 2001 May;42(5):780-1 UI: 21235439]," *Journal of Nuclear Medicine*, vol. 42, pp. 772-9, 2001.

[10] S. C. Blankespoor, X. Wu, K. Kalki, J. K. Brown, C. E. Cann, and B. H. Hasegawa, "Attenuation correction of SPECT using X-ray CT on an emission-transmission CT system: Myocardial perfusion assessment," presented at IEEE Nuclear Science Symposium and Medical Imaging Conference, San Francisco, CA, USA, 1995.

Chapter 5: Improved Reconstruction for SPECT

A. Introduction

1. Clinical Motivation

Although ^{111}In-ProstaScint® has the capability to provide unique and otherwise unavailable staging information for prostate cancer patients, ^{111}In-ProstaScint® SPECT imaging is plagued by the traditional limitations of nuclear medicine images. The SPECT images have relatively few counts, and so are corrupted by statistical noise. Furthermore, the images lack anatomical information and have poor spatial resolution. These factors, combined with the extensive non-specific uptake of ^{111}In-ProstaScint® in many body tissues, have given ^{111}In-ProstaScint® a reputation as one of the most difficult nuclear medicine exams to interpret. Physicians must look for very subtle changes in uptake when interpreting these exams, often in tissues that lie deep within the body behind other structures. Unfortunately, this requirement mandates the use of tomography, but the tomographic images produced by common image reconstruction methods such as filtered backprojection are very poor. Figure 2-9 (reproduced from Chapter 2) illustrates the complex nature of a typical ^{111}In-ProstaScint® SPECT image, in which it is difficult to differentiate disease from normal uptake of the radionuclide using a conventional filtered backprojection reconstruction of the radionuclide image.

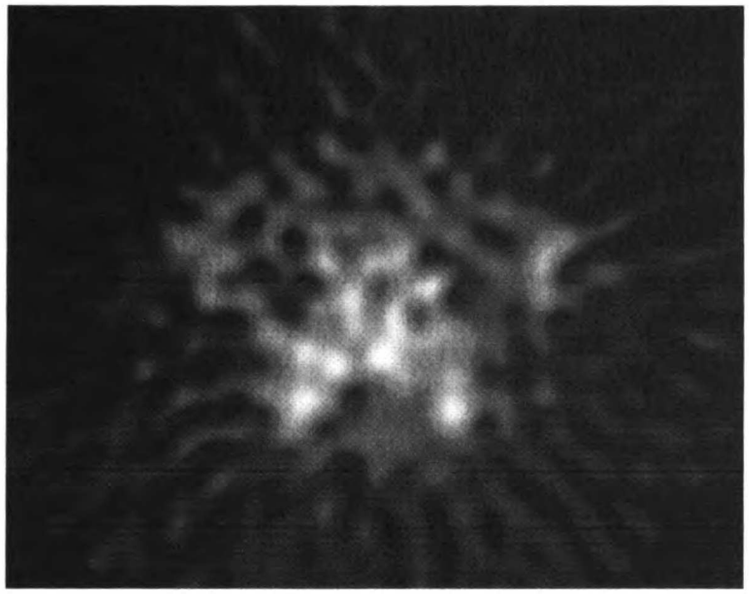


Figure 5-1: ^{111}In-ProstaScint® SPECT image of the pelvis, reconstructed using filtered backprojection.

In order to realize the full potential of ^{111}In-ProstaScint® imaging, we must improve the quality and the accuracy of the reconstructed SPECT image. Previous chapters have provided the fundamental concepts necessary for this goal. In this chapter we will consolidate those concepts to demonstrate how combined CT/SPECT imaging can achieve this goal, including the background, theory, implementation, and basic phantom tests of a significantly enhanced SPECT reconstruction. This discussion will be followed later by Chapter 7, in which will we describe the patient studies in detail.

2. Overview

In Chapter 2, we introduced several fundamental concepts that play a key role in SPECT reconstruction. The first concept was the interaction of radiation with matter, specifically the photoelectric effect and Compton scattering. These effects attenuate the number of photons escaping the patient, which lowers the number of photons available to form the

image and which exacerbates the effects of photon statistical noise in the radionuclide image. Attenuation effects also make sources located deep within the body (such as the prostate) appear less intense, because a deep object loses proportionally more photons to attenuation than a superficial object; this effect introduces a patient-dependent error in the measurement of radionuclide uptake using an external detector. The second concept was the distance-dependent spatial resolution of the gamma camera. The lead tubes of the collimator view the radionuclide distribution in the patient through a diverging conical field of view, which causes objects far from the camera to be blurred more than those close to the camera. The third concept was that iterative reconstruction can improve the quality and accuracy of reconstructed SPECT data, due to its foundation in Poisson statistics, tolerance of statistical noise, and its ability to model the physical relationship between object voxels and detector pixels. Recall that the maximum-likelihood expectation-maximization (ML-EM) algorithm for iterative reconstruction is:

$$\lambda_{k+1}(b) = \frac{1}{\sum_{d=1}^{N_d} p(b,d)} \sum_{d=1}^{N_d} \left[\frac{n'(d)\lambda_k(b)p(b,d)}{\sum_{b'=1}^{N_b} \lambda_k(b')p(b',d)} \right]. \qquad (5.1)$$

The function *p(b,d)* expresses the likelihood that a photon emitted from object voxel *b* will be recorded by detector pixel *d*, and is defined for every *(b,d)* pair. This function *p(b,d)* thus provides a means to characterize and compensate for the effects of photon attenuation and collimator blurring. Therefore, we wish to formulate a function *p(b,d)* so that it provides a complete mathematical model of the imaging process and can be included in the iterative reconstruction process (Equation 5.1). A registered CT image in the same coordinate system as the SPECT image provides a map of the x-ray attenuation

in a patient, which can then be used to determine the attenuation of the higher-energy photons used in SPECT. Measurement of collimator blurring effects does not require the information from the CT scan, but can also be performed experimentally and applied to the image reconstruction. Therefore, the combined CT/SPECT imaging system described in Chapter 3 and the image registration algorithm from Chapter 4 provide the information necessary to create this mathematical model.

In this chapter, we will combine many of these concepts from the previous chapters and derive an enhanced tomographic reconstruction algorithm for ^{111}In-ProstaScint® SPECT data, which will include corrections for photon attenuation and collimator blurring. We will validate the corrections for photon attenuation and collimator blurring experimentally, and also examine the algorithm as a whole for the reconstruction of simple phantom images. In succeeding chapters, we will apply the reconstruction algorithm to complex phantom studies to demonstrate its quantitative accuracy. We also will use these methods for the reconstruction and quantitative analysis of ^{111}In-ProstaScint® SPECT studies, thereby demonstrating that we can improve the value of ^{111}In-ProstaScint® SPECT imaging as a staging tool for prostate cancer, in comparison to currently existing techniques.

B. Modeling the Imaging Process

1. Overview

In order to build an accurate probability *(p(b,d))* model that can be used to enhance iterative SPECT reconstruction, we need to measure and characterize the physical effects that govern the SPECT imaging process. Thus, we need to calculate the attenuation of

the radionuclide photons and determine the blurring effects of the collimator. In this section, we will first cover the methods for deriving single-energy gamma ray photon attenuation maps from registered x-ray CT scans. Then, we will discuss the special case of attenuation for ^{111}In, which emits two photons that both have energies and abundances useful for SPECT imaging. Measuring and correcting for collimator blur will then be explained. Finally, we will review the computational implementation of these corrections and highlight the advantages and limitations of this reconstruction algorithm. This section will thus provide the background information required for understanding the experimental tests of the reconstruction algorithm.

2. Photon Attenuation

a) Introduction

An important component of the function $p(b,d)$ is the attenuation of radionuclide photons emitted from within the body, because attenuation plays a major role in determining whether a photon emitted from object voxel b can be detected in detector element d. We can model the attenuation of the gamma ray photons by obtaining an *a priori* map of the attenuation coefficients in the body, so that the attenuation between object voxel b and detector element d is simply the line integral of attenuation coefficients between these two points.

The coregistered CT scan is a map of x-ray attenuation in the body, so it could potentially provide the information necessary to generate the gamma ray attenuation map. However, the x-ray attenuation in the object is expressed in terms of CT numbers or Hounsfield Units (HU), which are defined by:

$$\text{CT number} = \frac{\mu_T - \mu_{water}}{\mu_{water}} \times 1000 \text{ HU}, \tag{5.2}$$

where μ_T is the attenuation coefficient of the tissue and μ_{water} is the attenuation coefficient for water at a given energy; thus, Equation 5.2 defines CT numbers so that water has a value of 0 HU and air has a value of –1000 HU. Furthermore, the CT numbers are derived from the attenuation of a polychromatic beam of x-rays; the majority of photons in this beam have an energy between 40 and 60 keV, and the maximum energy is 140 keV (see Figure 2-3 for an example CT x-ray spectrum). By contrast, the gamma ray photons are monochromatic, because they are created by a specific nuclear transition, and typically have energies between 70 keV (e.g., ^{201}Tl) and 370 keV (e.g., ^{131}I). Thus, when we generate a patient-specific attenuation map from CT, we need a method to convert the Hounsfield Units in the CT image to a map of gamma-ray attenuation coefficients for the SPECT reconstruction.

Tang has devised a method for converting CT images into gamma-ray attenuation maps that is based on calibration measurements and a piecewise linear relationship between Hounsfield Units and attenuation coefficients[1]. For CT numbers < 0, we treat the tissue as a mix of air and water, and so the attenuation coefficient as a function of photon energy E can be obtained by rearranging Equation 5.2:

$$\mu_T(E) = \mu_{water}(E)\frac{\text{CT number}}{1000} + \mu_{water}(E). \tag{5.3}$$

For CT numbers > 0, we treat the tissue as being composed of a mixture of bone and water, and since the Hounsfield Unit scale is not defined for materials other than air and water, we need a different equation for these attenuation coefficients:

$$\mu_T(E) = m_{bone}(E)\frac{\text{CT number}}{1000} + \mu_{water}(E)\,. \qquad (5.4)$$

Conceptually, Equation 5.4 treats materials with CT numbers > 0 as a combination of water and bone, and uses a coefficient $m_{bone}(E)$ to relate CT numbers to attenuation coefficients. The $m_{bone}(E)$ factor is obtained by acquiring CT images of a series of solutions that contain specific concentrations of water and K_2HPO_4, a material that has similar attenuation properties to bone. Since the composition of these solutions is known, we can calculate $\mu_T(E)$ for each solution, measure the CT number of this solution with the CT scanner, and then derive values for $m_{bone}(E)$. In essence, we are calibrating the CT scanner, so that we can obtain a quantitative relationship between CT numbers and attenuation coefficients for different photon energies.

b) Calibration measurements

We implemented this calibration technique by acquiring CT images of bone mineral densitometry phantoms (Mindways, San Francisco, CA). These phantoms have been designed to enable a CT system to precisely and consistently measure the changing bone density of patients with osteoporosis, so the chemical composition of these phantoms is very well known. Furthermore, these phantoms contain materials that have attenuation and density properties similar to physiological tissues. Thus, these phantoms provide a range of material compositions and densities that are similar to the patients that will be studied in this research project.

Two bone mineral densitometry phantoms were used for this calibration measurement. The first phantom is an abdomen-sized elliptical water tank with cylindrical chambers. The second phantom is a flat and slightly curved rectangular

plastic box containing cylindrical chambers. The chambers in both phantoms contain either aqueous solutions of K_2HPO_4 or ethanol, which is less dense than water (the ethanol-filled chamber is not used for the calibration measurements, because it produces a Hounsfield Unit value < 0). Different chambers inside the phantom contain different concentrations of K_2HPO_4, so the phantom can simulate a wide range of material densities. A schematic of the phantoms is shown in Figure 5-2.

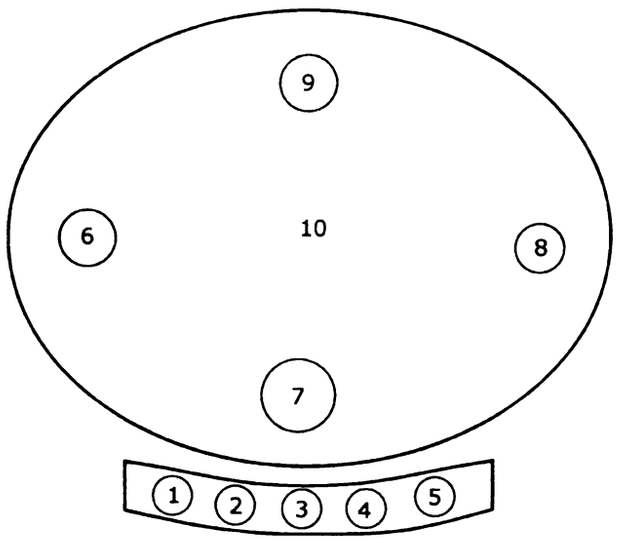


Figure 5-2: Schematic diagram of the phantom used for attenuation calibration of the CT system.

The chambers in the phantoms are regions of interest numbered 1-9, and the number 10 identifies a region of interest in the center of the water-filled elliptical tank. The compositions of the regions are listed below in Table 5-I.

CT Calibration Phantom Contents

Region Number	Composition
1,7,8	200 mg/ml K_2HPO_4
2,9	100 mg/ml K_2HPO_4
3,6	50 mg/ml K_2HPO_4
4,10	Water
5	Ethanol

Table 5-I: Chemical composition of the solutions in the calibration phantoms.

Although the two phantoms contain the same types of material, both phantoms were used in this calibration measurement to determine whether or not the form of the phantom influenced the calibration results – the elliptical phantom is larger than the flat phantom, and thus may be more affected by beam hardening.

The phantoms were scanned together on the CT/SPECT system using the same parameters for ^{111}In-ProstaScint® patient imaging: 140 kVp tube voltage, 120 mA beam current, 3 second scan time, and 5 mm slice thickness. CT projection data were reconstructed on a 256 x 256 matrix with the built-in CT reconstruction software. The final tomographic images were then transferred to a computer workstation for further analysis. An example CT image of the phantoms is shown in Figure 5-3.

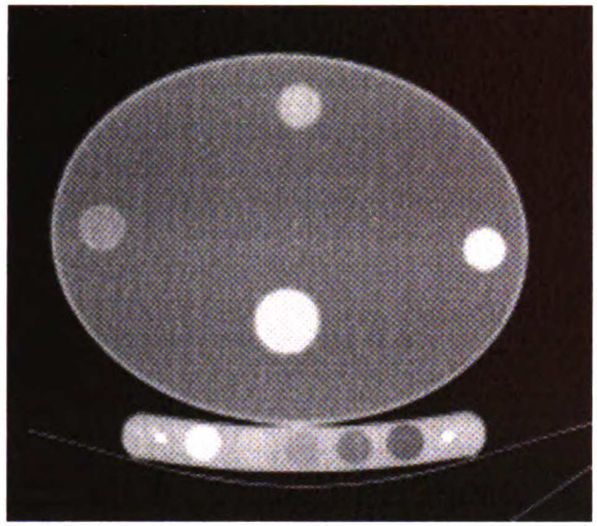


Figure 5-3: CT scan of the bone densitometry phantom used to calibrate Hounsfield Units to attenuation coefficients.

An operator drew circular regions-of-interest (approximately the size of the smallest chambers) at each of the locations enumerated in Figure 5-2, and calculated the average Hounsfield Unit (HU) value in each region. The results of this measurement are shown in Table 5-II, grouped by material composition. The standard deviation for these measurements was typically between 5 and 8 HU.

CT Calibration Phantom Measurements

	200 mg/ml K_2HPO_4			100 mg/ml K_2HPO_4		50 mg/ml K_2HPO_4		Water		Ethanol
Region Number	1	7	8	2	9	3	6	4	10	5
Mean CT Number [HU]	258	250	263	126	133	57	65	-11	-3	-74

Table 5-II: Hounsfield Unit values from the CT calibration phantom.

c) Data Analysis and Generation of Calibration Curves

The results from Table 5-II indicate that the two different phantoms produce very similar results, although the CT numbers in the larger elliptical phantom tend to be slightly higher than the CT numbers in the small flat phantom. Since the CT numbers from the two phantoms are usually within one standard deviation of each other, we averaged the results from the two phantoms together and used the overall mean CT number as the basis for our calibration.

The linear attenuation coefficients of each of the materials in the phantom were calculated based on their composition and physical reference data[2]. We calculated the linear attenuation coefficients for each material ($\mu_T(E)$) at 60, 80,100, 150, 200, 300, 400, 500 and 600 keV. The results of these calculations are plotted in Figure 5-4.

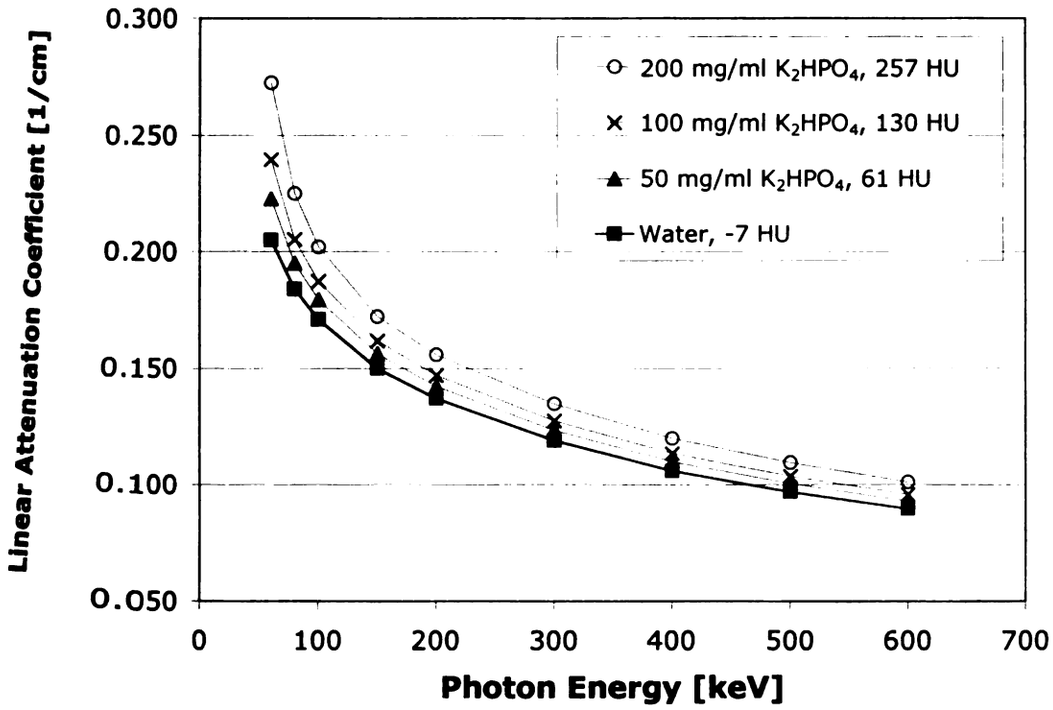


Figure 5-4: Linear Attenuation Coefficients as a function of photon energy for the materials in the CT calibration phantoms.

Using the information in Figure 5-4, we can convert Hounsfield Units to attenuation coefficients for any gamma-ray photon energy within the range plotted on the x-axis of this graph. Once a photon energy has been selected, we draw a vertical line through the graph at that energy. The points where this vertical line intersects the curves on the graph give the relationship between Hounsfield Units and photon attenuation coefficients for that particular photon energy (in essence, this process creates multiple instances of Equation 5.4). For example, if the gamma-ray photon energy were 300 keV, the relationship between HU and attenuation coefficients would look like Figure 5-5.

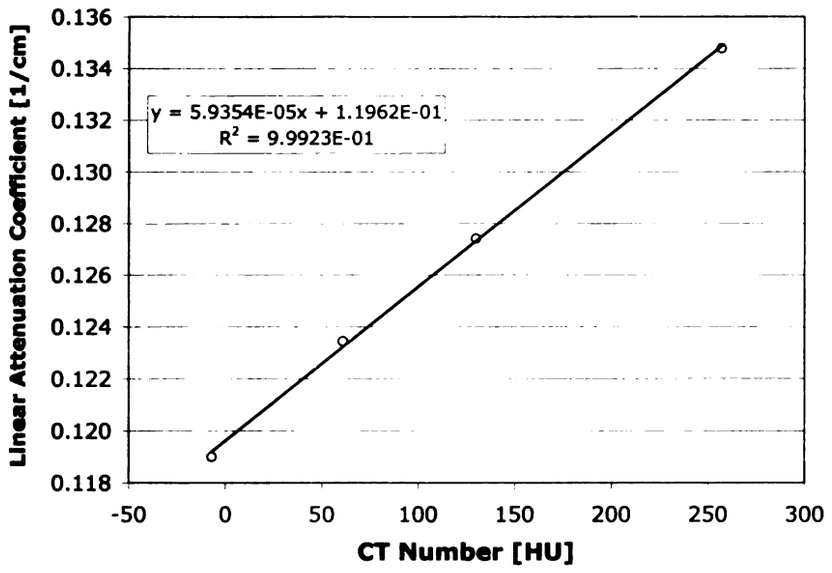


Figure 5-5: Calibration curve relating CT numbers to attenuation coefficients for 300 keV photons.

The equation for the best-fit line through these points is shown on the graph, and is the same as Equation 5.4, except for the factor of 1000. Thus, Equation 5.4 for 300 keV photons would be:

$$\mu_T(300\text{keV}) = 0.059354\frac{\text{CT number}}{1000} + 0.11962\,. \tag{5.5}$$

Since the CT number of water is defined as 0, the intercept of the best fit line should be the same as $\mu_{water}(E)$. According to the tabulated attenuation coefficients[2], the attenuation coefficient for water at 300 keV is 0.119, so the agreement is very close.

d) Discussion

This system of calibrating the CT scanner uses measurements of specific types of materials in order to derive a general relationship between CT numbers and attenuation

coefficients as a function of gamma-ray photon energy. By calculating the attenuation coefficients over a wide range of possible photon energies (60-600 keV), we can interpolate values for $m_{bone}(E)$ for arbitrary photon energies within this range. Then, using Equations 5.3 and 5.4, we can transform a coregistered CT scan into a gamma-ray attenuation map that can be used for SPECT reconstruction.

There are a few potential limitations to this method of calculating attenuation coefficients. The patient is modeled as being composed of either air and water (for CT numbers < 0) or K_2HPO_4 and water (for CT numbers > 0), which is not strictly true. However, for most physiological materials, this is a reasonable approximation, since soft tissue is composed of mostly water, empty space, and light elements such as carbon, nitrogen, phosphorus, potassium, and calcium. Furthermore, since K_2HPO_4 was chosen specifically because it mimics the attenuation properties of bone, this approach is clearly valid for the dense bony regions of the body.

Potential problems could also occur with this approach to attenuation correction if heavier elements were introduced into the body, such as iodine contrast media. However, contrast media was not used for any of the patient studies in this project. Two of the patients had tiny metallic seeds implanted in the prostate from a previous external beam radiotherapy regimen (the seeds are used to mark the boundaries of the prostate). However, these seeds typically are only a few mm in size, and thus did not produce any significant artifacts in the CT images or the SPECT attenuation maps. It is possible that future CT/SPECT ^{111}In-ProstaScint® studies may use contrast material for improved bowel visualization; in that case, Tang's method of image segmentation based on the different properties of bone and iodine contrast media[1] could improve the accuracy of

this system. For the purposes of the current research project, though, the approach detailed here should be sufficient. We will test that proposition more formally in the experimental methods section of this chapter, once we have addressed some of the other requirements for improved SPECT reconstruction.

3. Dual-Energy Attenuation Correction

a) Introduction

The decay behavior of ^{111}In (the radionuclide used in ^{111}In-ProstaScint®) is different from most other nuclear medicine radioisotopes, because it emits photons at two distinctly separate energies, both of which can be used for imaging. The disintegration of ^{111}In creates an excited state of ^{111}Cd, which then decays to the ground state by two cascading gamma emissions. This cascade produces a roughly equal number of photons at both 171 keV and 245 keV, as illustrated in Figure 5-6. This multiple energy emission poses a new challenge for the reconstruction process, because it makes correction for photon attenuation somewhat more difficult. The reconstruction algorithm must now consider two disparate photon energies when computing the amount of attenuation between a voxel and the detector.

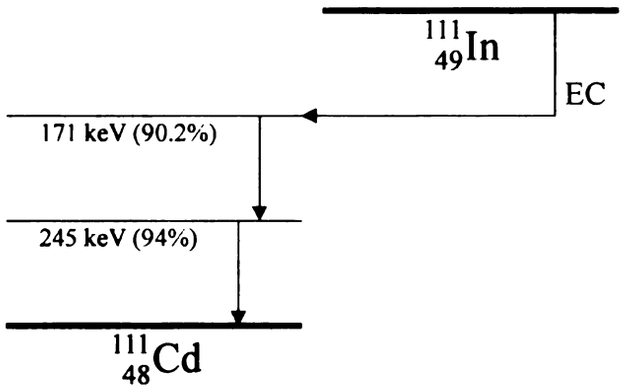


Figure 5-6: Decay scheme for ^{111}In.

One might address this difficulty by restricting the camera to a single energy window (thus allowing standard single-energy attenuation correction), but this makes inefficient use of the available photons and essentially halves the signal level in the projection data. Another tactic would be to collect the energy windows separately, reconstruct two different images using standard attenuation correction, and then sum the two images into one. However, this tactic would suffer from similar noise problems and would also require twice the computation time. The most efficient approach would be to collect emissions from both energy peaks, merge them into a single radionuclide image, and then calculate the attenuation correction for the merged image. This makes use of all of the available projection data and only requires one reconstruction. For the case of ^{111}In-ProstaScint® imaging, it is also beneficial because the standard protocol for ^{111}In-ProstaScint® SPECT imaging mandates the acquisition of a simultaneous ^{99m}Tc-labeled red blood cell image. On some gamma cameras, including the 600 XR/T used for the CT/SPECT system, it is impossible to acquire and record three separate energy windows, but it is possible to acquire two energy windows into a single combined image and have a third window form the second image. For these reasons, we will compensate for the dual

photon emissions from ^{111}In by devising an effective attenuation coefficient μ_{eff}, which will allow us to treat the dual-energy emissions of ^{111}In as a conventional single-energy isotope.

b) Theory

Our goal is to model the emission of photons from a dual-energy radionuclide like ^{111}In, and determine if we can express the attenuation characteristics of the emission data using a single attenuation coefficient rather than using separate attenuation coefficients for each photon energy. For this model, consider a dual-energy radionuclide source located behind a homogeneous block of attenuating material (with thickness x) as shown in Figure 5-7. The parent nuclide decays at a rate of A disintegrations/second, emitting photons of energies E_1 and E_2 with branching ratios r_1 and r_2. The intensity incident on the block is thus $I_{01}=Ar_1$ and $I_{02}=Ar_2$. The linear attenuation coefficients of the material are μ_1 and μ_2 for the energies E_1 and E_2. The photons transmitted through the material and entering a detector placed at the exit face have intensities of I_1 and I_2.

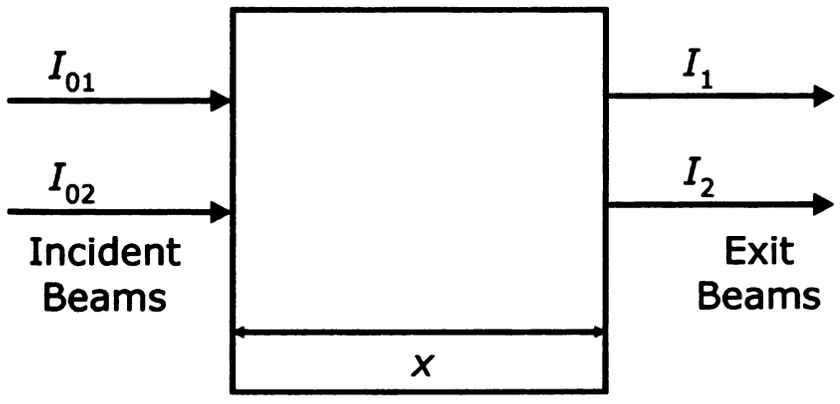


Figure 5-7: Schematic for attenuation of a dual-energy isotope.

Assuming narrow beam geometry (which is valid for nuclear medicine because of the camera's energy discrimination and collimation) where photons scattered from the beam are not detected, the exit beam intensities are labeled I_1 and I_2, and can be expressed as:

$$I_1 = I_{01}\exp(-\mu_1 x) \quad \text{and} \quad I_2 = I_{02}\exp(-\mu_2 x)\,. \tag{5.6}$$

If the detector does not discriminate between the different energies of the photons (or has been programmed to accept both photons) and has equal efficiency at both energies, then the signal received by the detector is:

$$I_1 + I_2 = I_{01}\exp(-\mu_1 x) + I_{02}\exp(-\mu_2 x)\,. \tag{5.7}$$

We can define the intensity of the dual-energy photon source as $I_{01} + I_{02}$, and then define the effective attenuation coefficient as:

$$I_1 + I_2 = [I_{01} + I_{02}]\exp(-\mu_{eff} x)\,. \tag{5.8}$$

Combining Equations 5.7 and 5.8, and solving for μ_{eff}, we obtain:

$$\exp(-\mu_{eff} x) = \frac{I_{01}\exp(-\mu_1 x) + I_{02}\exp(-\mu_2 x)}{I_{01} + I_{02}}\,. \tag{5.9}$$

To simplify this expression, we substitute αI_{01} for I_{02} and collect terms, leaving us with:

$$\mu_{eff} = \frac{\ln[\exp(-\mu_1 x) + \alpha\exp(-\mu_2 x)] - \ln[1+\alpha]}{-x}\,. \tag{5.10}$$

The term α is the ratio of the gamma intensities. For ^{111}In, if we assign the lower energy peak as I_1, then α has a value of 94/90.2, or 1.042.

We can quickly verify this equation by examining special cases for the values of μ_1 and μ_2. If the two photons have the same energy, then we can eliminate the α terms, and we are left with $\mu_{eff} = \mu_1 = \mu_2$. Similarly, if α is close to zero, corresponding to a situation where the second emission from the radioisotope is very weak, then the $\alpha\exp(-\mu_2 x)$ term essentially vanishes, and $\mu_{eff} \sim \mu_1$,. On the other hand, if α is large, corresponding to the first emission being weak, then the $\alpha\exp(-\mu_2 x)$ term dominates the numerator of Equation 5.10, and $\mu_{eff} \sim \mu_2$.

c) Implementation

The CT-based attenuation correction system discussed previously uses the photon energy as an input, and then defines a functional relationship between Hounsfield Units and attenuation coefficients for photons of that energy. Therefore, we would like to recast the effective attenuation coefficient μ_{eff} as an effective photon energy E_{eff}, so that we can easily incorporate dual-energy capabilities in our attenuation correction methodology. Using 20 cm of water as a sample material (since our typical patient is about 40 cm across) and the known linear attenuation coefficients for water at 171 keV and 245 keV[2], we can calculate μ_{eff} for ^{111}In using Equation 5.10:

$$\mu_{eff} = \frac{\ln[\exp((-0.144)(20)) + 1.042\exp((-0.128)(20))] - \ln[1 + 1.042]}{-20} = 0.135 \qquad (5.11)$$

If we then plot the attenuation coefficients for water as a function of energy, we can fit these points to a logarithmic scale and interpolate an energy that corresponds to a value of $\mu_{eff} = 0.135$, as shown in Figure 5-8.

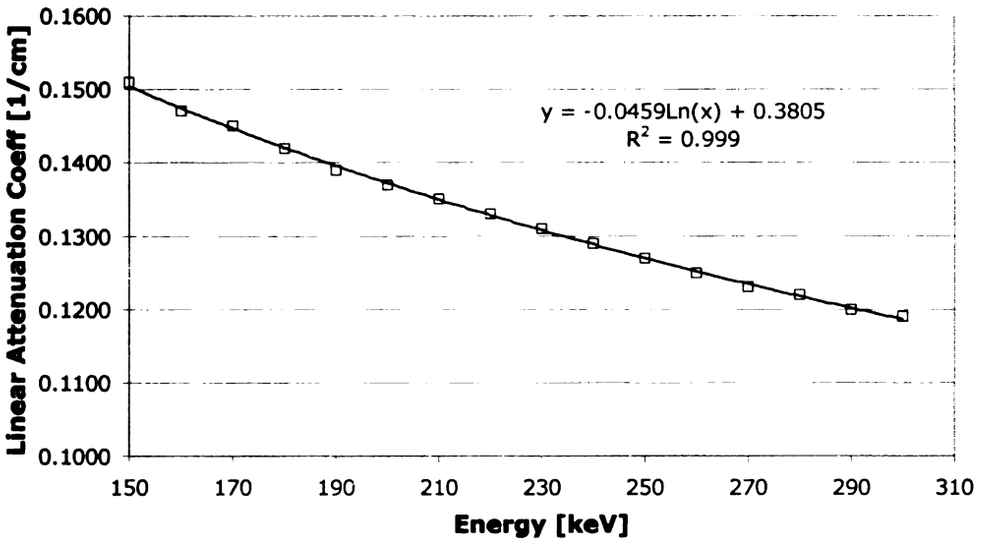


Figure 5-8: Plot and logarithmic fitting of water linear attenuation coefficients vs. photon energy.

The effective photon energy can then be calculated to be 210 keV using the equation displayed in Figure 5-8. Thus, for the purposes of the CT calibrated attenuation map, we can treat ^{111}In as a single-energy photon source with a photopeak at 210 keV. It is worth noting that the arithmetic mean of 171 keV and 245 keV is 208 keV, which is quite close to our calculated effective photon energy. This coincidence is not surprising, though, because the high and low energy photons from ^{111}In are emitted with nearly equal probability. Thus, it is not unreasonable to think that they could be treated as one photon, possessing their average energy.

The choice of 20 cm of water for computing an effective photon energy is somewhat arbitrary, and Equation 5.10 clearly shows that μ_{eff} is a function of the material thickness x. Conceptually, the lower-energy photons in the dual-energy source are preferentially attenuated by a material, so as the beam passes through more and more material, the higher-energy photons constitute a larger and larger fraction of the total

fluence. To gauge the magnitude of this effect, we repeated the calculation of μ_{eff} for water using different values of the material thickness x. Figure 5-9 shows the results of these calculations graphically.

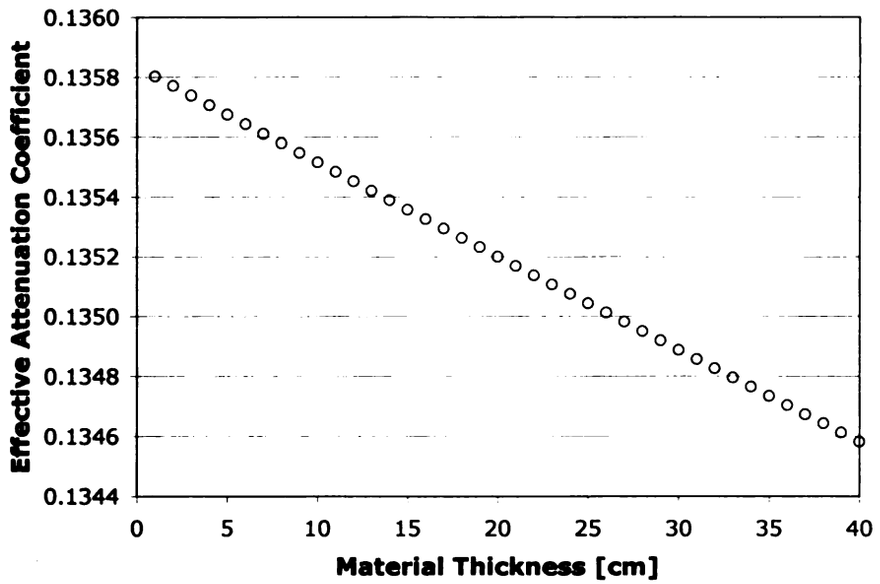


Figure 5-9: Variation in the effective attenuation coefficient μ_{eff} for water as a function of material thickness x.

At 1 cm, the value for μ_{eff} is 0.1358, whereas at 40 cm, the value for μ_{eff} is 0.1346, so the change in μ_{eff} over these values is only 0.9%. In terms of the effective photon energy E_{eff}, the range of values is 207 keV to 212 keV. Thus, we can conclude that the determination of E_{eff} is only weakly dependent on distance, so using the value of 210 keV for E_{eff} is a very reasonable approximation for the energy of photon emissions from ^{111}In radiotracers. Combined with the CT calibration methods discussed in the previous section, this information forms the basis for SPECT attenuation correction for ^{111}In-ProstaScint®.

4. Collimator Blurring

a) Introduction

In Chapter 2, we introduced the concept of the diverging field of view of the gamma camera, which derived from the array of small lead pipes that form the collimator. Although Figure 2-11 is helpful for visualizing this geometry, that picture is not completely accurate since the scintillation crystal is not divided into discrete units corresponding to the size of a collimator opening. A more appropriate illustration of the collimator blurring effect as it impacts image reconstruction is shown in Figure 5-9.

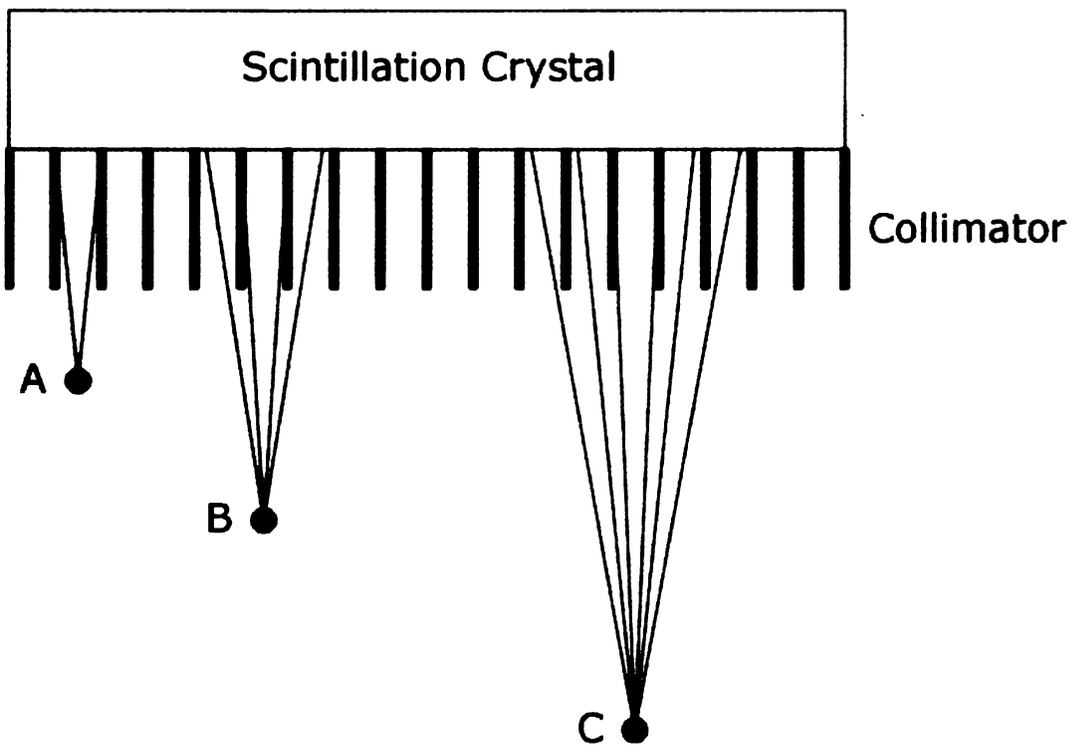


Figure 5-10: Illustration of collimator blurring effect.

In this illustration, point sources are located at three distances from the camera and are labeled A, B, and C. The lines emanating from each source indicate the region of the camera that can be 'illuminated' by the point source, as these lines connect the source and the detector without passing through any collimator septa. Thus, as we move the source further and further away from the gamma camera, a wider area can be 'illuminated', and so the point source is blurred over a wider region of the gamma camera. The image brightness will be highest at locations directly over the point source, and will decrease as we move horizontally across the camera face, because fewer rays from the source can reach the detector without crossing a septal wall. For an object such as a patient, this illustration implies that body structures located far from the camera will be blurred more than those structures that are close to the camera, so the reconstruction algorithm must have a means of simulating this effect when it determines the relationship between object voxels and detector pixels $p(b,d)$.

This blurring effect is dependent on distance, the geometry of the collimator, and the intrinsic spatial resolution of the gamma camera. In principle, we can calculate this effect based on the form of the collimator (i.e. septal thickness, spacing, and aspect ratio) and the manufacturer specifications for the gamma camera. However, it generally is more efficient to simply measure the effect directly so that we can characterize the blurring for a particular collimator and detector combination. A measurement-based approach also allows us to include all of the potential blurring effects in a few parameters, which will enable a simple and direct computational implementation.

b) Measurement of the collimator blurring effect

We measured the blurring function for the collimator by placing a radioactive point source at specific distances from the face of the gamma camera and recording the resulting images. The setup for this experiment was thus very similar to the schematic drawing in Figure 5-10 (except that all of the point sources are placed along the central axis of the camera). The point source is a small (4 mm diameter by 6 mm deep) cylinder drilled into a plastic block; the cylinder is filled with a radioactive solution and then covered with clear tape so that the solution does not leak out. For these measurements, the source was filled with approximately 40 μCi of ^{111}In. Planar gamma camera images were acquired with a medium-energy collimator and a 256 × 256 image matrix size, so each image pixel was 0.22 cm × 0.22 cm. The energy window was set to combine counts from the high and low energy emissions from ^{111}In; we used a 15% window around 171 keV and a 20% window around 245 keV, which is the manufacturer-suggested window setting for imaging ^{111}In-ProstaScint® patients. Images were acquired until 200,000 counts had been recorded, which took approximately 10 minutes per image. The distance between the camera and the source was varied by moving the gamma camera head or the patient table, and was measured for each distance setting. The gantry design on the CT/SPECT system does not allow the camera head to be moved vertically without some horizontal displacement, so the point source was repositioned to the center of the gamma camera field of view for each distance setting. Example images of the point source are shown in Figure 5-11. From left to right, these images were taken at distances of 12.1 cm, 20.0 cm, and 42.5 cm. One can clearly see the distance-dependent blurring effect in these images.

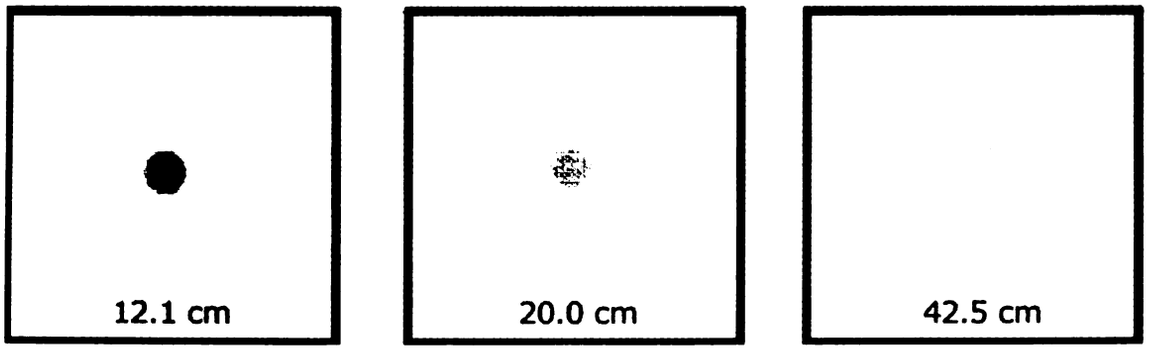


Figure 5-11: Example images of collimator blurring effect.

In order to characterize this effect mathematically, we calculated a centroid for the distribution shown in these images, using the pixel values as the weights in a standard center-of-mass calculation. We then computed a radial profile for the distribution, by determining the average pixel value as a function of distance from the location of the centroid. Radial profiles from the images shown in Figure 5-11 are plotted in Figure 5-12.

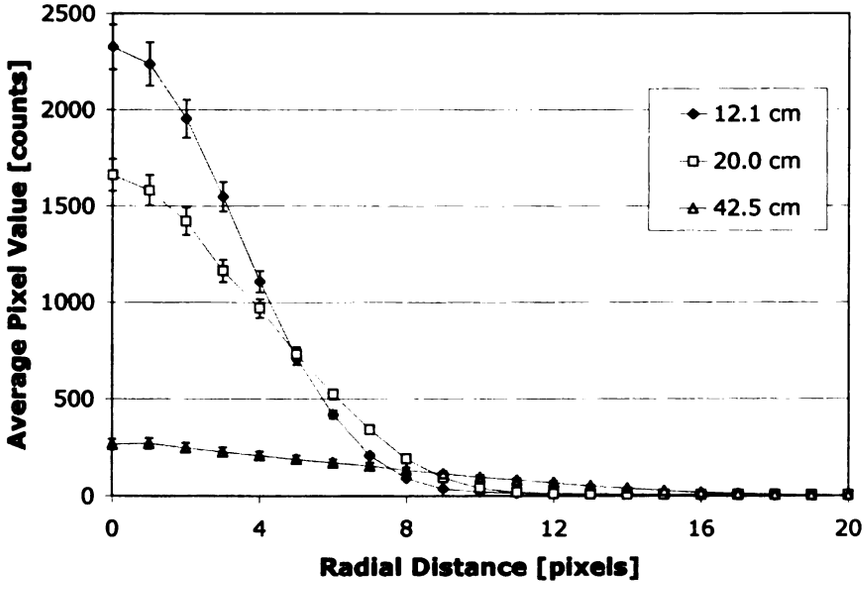


Figure 5-12: Radial profiles of the images shown in Figure 5-11.

We calculated a radial profile for each gamma camera image, and then used a least-squares fitting routine (Kaleidagraph, Synergy Software, Reading PA) to fit each profile to a one-sided Gaussian distribution given by

$$z = Z_0 \exp\left(\frac{-\pi r^2}{s^2}\right) \tag{5.12}$$

where z is the height of the profile as a function of the radial distance r, Z_0 is a constant for adjusting the peak height of the Gaussian, and s is a parameter describing the width of the distribution. Thus, the image of each point source is characterized by a single width parameter s. These width parameters are then plotted versus the distance from the source to the collimator, as shown in Figure 5-13.

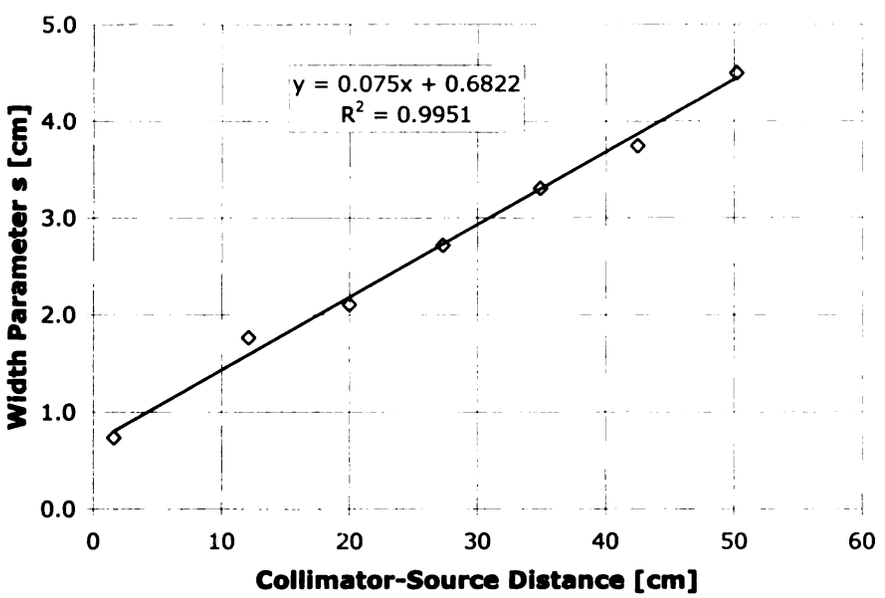


Figure 5-13: Plot of collimator blurring width parameter as a function of distance between the source and collimator.

By fitting these points to an equation for a straight line, we obtain an equation that describes the collimator blurring (in terms of the width parameter s) as a function of the collimator-source distance d, which is

$$s = 0.075d + 0.6822 \tag{5.13}$$

for the medium-energy collimator and gamma camera component of the UCSF CT/SPECT system. The equation describing the collimator blurring (Equation 5.13) then was incorporated into the reconstruction algorithm to compensate the radionuclide image for these spatial resolution effects, as will be described in the following section.

c) Discussion

The method described above uses simple measurements to characterize the blurring associated with a particular collimator and gamma camera combination. We observe the blurring of a point-like object at specific distances from the camera, and then generalize this information to a formula for the collimator blurring as a function of distance. Although the 'point-source' used for this measurement is not a true point, it is small compared to the resolution of the gamma camera (which is typically 8-10 mm). It is also roughly the size of a single reconstructed SPECT voxel in an ^{111}In-ProstaScint® image, which makes it a good model for the discrete imaging process where a voxel is the smallest possible unit in the object. Furthermore, other investigators have used this method to determine collimator blurring effects, and have demonstrated improved image reconstruction using this method[1, 3]. Thus, we feel that this method will be a suitable means of compensating for the collimator blurring associated with ^{111}In-ProstaScint® SPECT imaging.

5. Computational Implementation of Iterative Reconstruction

In the previous sections, we have covered the theory and empirical measurements necessary to more accurately model the imaging process for an iterative SPECT reconstruction. The iterative SPECT reconstruction compares simulated SPECT projection data with actual SPECT projection data to improve its estimate of the activity distribution within the object. Therefore, it is important to incorporate an accurate model of the imaging process in the reconstruction algorithm to produce more accurate simulated projections, which will in turn improve our estimate of the object's true activity concentration. In this section, we will discuss how these corrections (attenuation and collimator blurring) are implemented computationally within the framework of the ML-EM algorithm, and how they contribute to more accurate simulated SPECT projection data.

The probability function $p(b,d)$ in the ML-EM algorithm is defined for every object voxel b and every detector pixel d. However, it is not feasible to calculate the function $p(b,d)$ in advance and refer to these precalculated values, because b and d are both large numbers. A typical reconstructed SPECT image will have 128^3 (2,097,152) voxels, and the projection data for that SPECT image will typically have a 128x128 matrix size and 64 views, for a total of 1,048,576 detector pixels in the acquired data set. Thus, to store a value of $p(b,d)$ for every possible combination of b and d would require roughly 2.2×10^{12} memory locations. Assuming that we allocate 4 bytes per value in order to store these numbers in floating-point representation, this translates to a storage requirement of 8192 gigabytes. Clearly, then, we must split the problem into manageable subtasks and calculate these probability values $(p(b,d))$ as they are needed. We must

therefore have an efficient method for calculating *p(b,d)* that is also amenable to implementing the corrections described in this chapter. In order to calculate the probability values *(p(b,d))* efficiently in a way that incorporates both the attenuation characteristics of the object and the spatial resolution characteristics of the collimator, we used an 'object-rotating-resampling algorithm' for iterative SPECT reconstruction. The algorithm has been described in detail by Tang[1], so we shall review the relevant details here and describe how our corrections are incorporated into the algorithm. During the SPECT acquisition, the distance from the SPECT camera head to the center of rotation of the SPECT gantry is recorded. After the acquisition, but before reconstruction begins, a CT study is registered into the SPECT coordinates by the methods described in Chapter 4, and an attenuation map is obtained from the registered CT image using the calibration and dual-energy methods described earlier in this chapter. During reconstruction, the algorithm treats the gamma camera detector as a fixed object, and the acquisition process is simulated by rotating the patient relative to the fixed detector, as illustrated in Figure 5-14. At each rotation angle, the object is resampled into new voxels, so that all of the voxels line up along columns equivalent to the detector pixels and all of the planes in the object are parallel to the detector face.

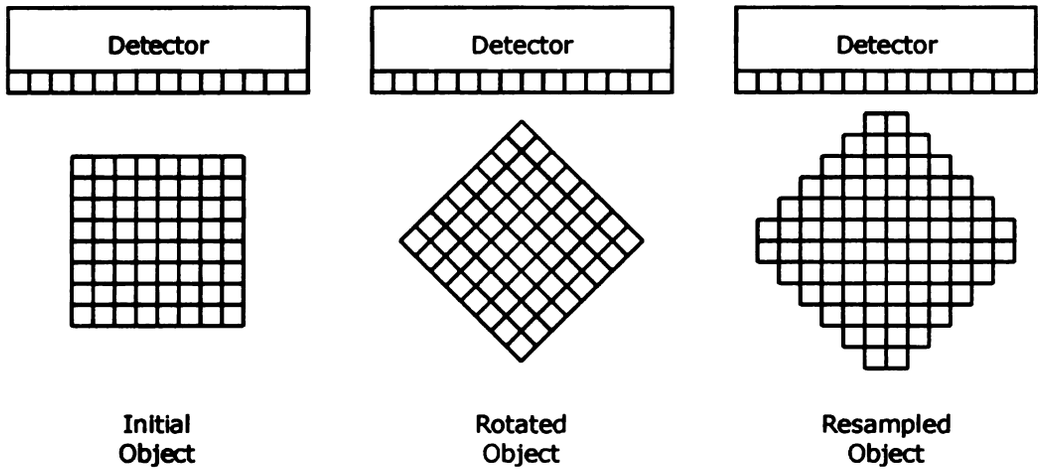


Figure 5-14: Basic geometry for the object-rotating-resampling iterative reconstruction.

Once this resampling is accomplished, each plane within the object is blurred in two dimensions according to its distance from the detector and the equation for the width parameter s (Equation 5.13). The width parameter s is used to generate a Gaussian point spread function for each plane, which is then convolved with the pixels in the plane by frequency domain multiplication.

The blurred planes then are projected into the detector along vertical lines, taking into account the attenuation in each voxel. This forms a simulated view, which can then be compared against the actual projection data for that view. The attenuation along a line between the voxel and the detector is used to calculate a value of $p(b,d)$ for the object and the single view, which allows the algorithm to calculate a correction factor based on the ratio between simulated and recorded detector counts. This correction is then applied to the object voxels (in essence, this is a backprojection operation) to update the reconstructed image. Once this update is complete, the algorithm moves to the next view and the process repeats. Once all of the views have been examined, a single iteration is complete. Further iterations are performed until either (1) the simulated projection data

match the actual projection data to within some predetermined error, or (2) a preset number of iterations has been completed.

6. Advantages of this reconstruction technique.

From a purely scientific standpoint, it is important to have a model of the imaging process that includes as many of the real physical processes that occur in imaging as possible. The object-rotating-resampling reconstruction described here meets this criterion and has several implicit advantages over filtered backprojection. First, it models photon attenuation, thereby preventing the true strength of sources from being masked by depth within the body or dense structures such as bone. Second, it models the true collimator properties by applying a distance-dependent blurring to the object data before creating projections. By contrast, filtered backprojection inherently assumes that all object voxels along the line of a detector pixel contribute equally to the counts in the detector pixel, and it assumes that 'off-axis' pixels do not contribute at all to the counts in the detector pixel. Both of these assumptions are patently wrong for SPECT imaging, and so it is impossible for filtered backprojection to approach the quality and accuracy of an iterative reconstruction. In subsequent sections of this thesis, we will provide further evidence supporting this assertion.

7. Limitations of this reconstruction technique

From a practical standpoint, the primary limitation of a physically accurate iterative reconstruction is that it requires a significant amount of computer time, because the computations for the reconstruction are much more complex. A filtered backprojection image can be generated from a typical SPECT study in a few seconds, and

an iterative image without any corrections can be generated in a few minutes. However, the typical time for an iterative reconstruction such as the one described here (including corrections for photon attenuation and collimator response) is on the order of several hours. For the patient studies that will be discussed in Chapter 7, image reconstruction of the SPECT projection data for a single study required approximately 20 hours on a 750 MHz computer. This is unfortunately too long to be clinically practical, but as processor speeds increase this processing time will continue to shrink.

Another potential limitation is that this algorithm does not model photon scattering. Compton scattering is indeed a major component of photon attenuation at nuclear medicine photon energies, but there are several reasons for not specifically modeling scattering in this current iterative reconstruction technique. The first is that the camera uses energy discrimination to reject much of the scatter radiation. This discrimination is not perfect (due to the finite energy resolution), but ensures that scattered photons constitute only a small portion of the total signal received by the camera. The second is that many scatter correction techniques rely on the measurement of data within a lower-energy window [4-6] to estimate the number of scattered photons reaching the detector. During ^{111}In-ProstaScint® imaging with the GE 6000 XR/T camera used in these studies, all of the available energy windows are used for imaging the patient, so this type of data is unavailable in our measurements. The final and most compelling reason is that previous research by our group has demonstrated that scatter modeling is not necessary for accurate quantitation. Early research on the ETCT system demonstrated that the effects of scatter were small when compared to the effects of attenuation and collimator blurring[7], and simulation studies of the CT/SPECT system

determined that collimator blurring effects were more important than scatter effects for assessing myocardial perfusion[8]. Using the combined CT/SPECT system, DaSilva demonstrated absolute quantitation in porcine myocardium to within 10% accuracy using an imaging model that included attenuation and collimator blurring effects, but not scatter[9]. Recent radiological studies of nuclear cardiac imaging have shown that scatter correction algorithms do not significantly improve the detection of defects[10] or reduce the appearance of artifacts [11], providing further support for this conclusion.

Future iterative reconstruction algorithms may potentially include scatter correction, but CT-based scattering corrections will impose a severe computational burden on an already lengthy reconstruction. Accurate modeling of the Compton scattering distribution requires much more complex operations than computing the attenuation in a voxel, and are thus better suited to an iterative reconstruction that uses Monte Carlo methods to calculate the $p(b,d)$ functions. Research on this topic is still in its early stages [12, 13].

C. Basic Experimental Tests of the Reconstruction Algorithm

1. Overview

In previous sections, we have described an iterative SPECT reconstruction that includes corrections for dual-energy photon attenuation and collimator blurring. Although this approach should be able to increase the quality and quantitative accuracy of the reconstructed SPECT image, the definitive tests of the reconstruction must be done experimentally. In this section, we will discuss some of the initial validation tests of the reconstruction algorithm. These tests will primarily evaluate the dual-energy attenuation

correction, since this is a new innovation for the object-rotating-resampling projector. These results will demonstrate the basic characteristics of the reconstruction process; in Chapter 6, we will evaluate the reconstruction algorithm in more demanding quantitative tasks.

2. Dual-energy attenuation test

In this section, we test whether we are able to model the dual-photon emissions from ^{111}In as a single photon with an effective energy E_{eff} and attenuation coefficient μ_{eff}. We tested the accuracy of this method by making direct measurements of the emissions from ^{111}In after passage through varying thicknesses of an attenuating material. A point source was used (as described in section A4b on collimator blurring), which contained roughly 0.5 mCi of ^{111}In. This point source was placed on the patient imaging table and the CT/SPECT system was configured so that the point source was 25 cm away from the face of the gamma camera and centered in the gamma camera field of view. The positions of the gamma camera head and the point source remained fixed during the experiment, so that any distance-dependent blurring effects would be constant.

A series of five control images were acquired first, using only the point source and the gamma camera. Planar gamma camera images were acquired with a 256x256 image matrix size and a 10 minute acquisition time, which yielded approximately 500,000 counts in the image. Energy windows were set to 20% around 245 keV and 15% around 171 keV, following the manufacturer recommendations for ^{111}In-ProstaScint® imaging; the counts from both windows were combined into a single image. Successive thicknesses of polyethylene were then placed on top of the point source to attenuate the

^{111}In emissions. The polyethylene was in the shape of rectangular slabs approximately 0.5" thick (their exact thicknesses were measured and recorded using a micrometer), so increasing attenuation was achieved by simply placing more slabs on top of the point source. After the addition of each polyethylene slab, another planar gamma camera image was acquired. The final image was acquired with approximately 4.5" of polyethylene between the point source and the gamma camera. The entire imaging process was then repeated using 3 mCi of ^{99m}Tc as the radioactive source and a 7% energy window around 140 keV, so that we could check this experimental method using a single-energy photon source.

The resulting images were 2-dimensional distributions similar to those shown in Figure 5-11. Images were analyzed by extracting the maximum pixel value (corrected for any radioactive decay losses) and its location within the image. We calculated a mean and standard deviation for the values from the unattenuated images, in order to determine the variability in this measurement. The values from the unattenuated measurements and the attenuated measurements (as a function of material thickness) were then plotted, and an exponential curve was fit to these points using a least-squares fitting method (Excel, Microsoft, Redmond, WA). From this fit, we calculated an attenuation coefficient. We also compared these measurements against theoretical calculations of narrow-beam attenuation coefficients for photons in polyethylene, using standard physical reference data[2].

3. Spatial Uniformity measurements

A basic test for an attenuation correction methodology is the reconstruction of image data from a uniform phantom. Photons emitted from the center of the phantom are more

likely to be attenuated than photons emitted from the edges of the phantom, so it also represents a good test for the dual-energy attenuation correction theory. A reconstruction with accurate attenuation correction should produce a uniform image, whereas one with erroneous or non-existent attenuation correction will underestimate the activity concentration in the center of the phantom.

We created a uniform tank phantom by filling a cylindrical tank (Data Spectrum, Hillsborough, NC) with an aqueous solution containing 5 mCi of ^{111}In and agitating the tank so that the concentration of the radioisotope would be constant throughout the tank. The tank has an interior diameter of 217 mm and an internal height of 188mm for a total internal volume of approximately 6800 cm^3. The tank was placed on the patient table of the CT/SPECT system so that the axis of the cylinder and the axis of the CT system were collinear. Masking tape was used to secure the tank to the table, so that it would not move. Fiducial markers were prepared and placed on the tank and the table as described in Chapter 4.

The tank was initially imaged on the CT scanner. CT slices were acquired using 5 mm slice thickness, 140 kVp tube potential, 120 mA tube current, and 3 second scan time. Tomographic slices were reconstructed using the built-in reconstruction software and a 256x256 image matrix size with a 48 cm field of view, resulting in a pixel size of 1.875 mm x 1.875 mm. The table of the CT/SPECT system was then moved so that the tank could be imaged by the gamma camera. The gamma camera energy window for ^{111}In was set to 20% at 245 keV and 15% at 171 keV, which is the standard window setting for ^{111}In-ProstaScint® imaging. SPECT projection data were acquired using a 128x128 image matrix size, 64 views, and 30 seconds per view. The count rate for this

SPECT acquisition was roughly 28 kcts/sec. A second image using a 7% window around 140 keV was simultaneously acquired so that the fiducial markers could be visualized on this SPECT image.

Tomographic CT slices and raw SPECT projection data were downloaded from the CT/SPECT system and transferred to a computer for further analysis. Initially, tomographic SPECT images were created from the ^{99m}Tc window data, by using 30 iterations of an iterative reconstruction that did not include attenuation or collimator corrections. These tomographic slices were registered with the CT tomographic slices using the locations of the fiducial markers, and an attenuation map was generated as described previously in this chapter. SPECT projection data were then reconstructed under 4 different conditions: (1) without any corrections, (2) with attenuation correction, but without collimator corrections, (3) with collimator corrections, but without attenuation correction, and (4) with both attenuation and collimator corrections. Based on previous experience in our research group with these tomographic SPECT reconstructions, we used 30 iterations for each reconstruction. We also reconstructed the SPECT data using filtered backprojection, which does not compensate the radionuclide image for photon attenuation or collimator effects. For each set of reconstructed SPECT data, line profiles were drawn across a tomographic slice in the center of the phantom to assess the uniformity. We also drew circular regions of interest over several slices in the center of the phantom, and computed the standard deviation of the pixel values within these regions to assess the overall uniformity of the images.

D. Experimental Results

1. Dual-energy attenuation results

Although these measurements made with the gamma camera are not strictly in the 'narrow-beam' geometry because the source is uncollimated, energy discrimination will reject photons that have scattered through large angles. Furthermore, by taking the maximum pixel value in the image, which is at the center of the point spread function, we ensure that we only recorded those photons that have traveled along the shortest path between the source and the detector. These characteristics make this experimental setup very similar to the 'narrow beam' geometry.

Figure 5-15 shows the results from the measurements made with the ^{99m}Tc source. Since this radioisotope emits only a single 140 keV gamma ray, these measurements serve as a check on the experimental method. The repeated measurements of the unattenuated source had a mean maximum pixel value of 9969±106, indicating that the effect of statistical noise on this measurement should be very small.

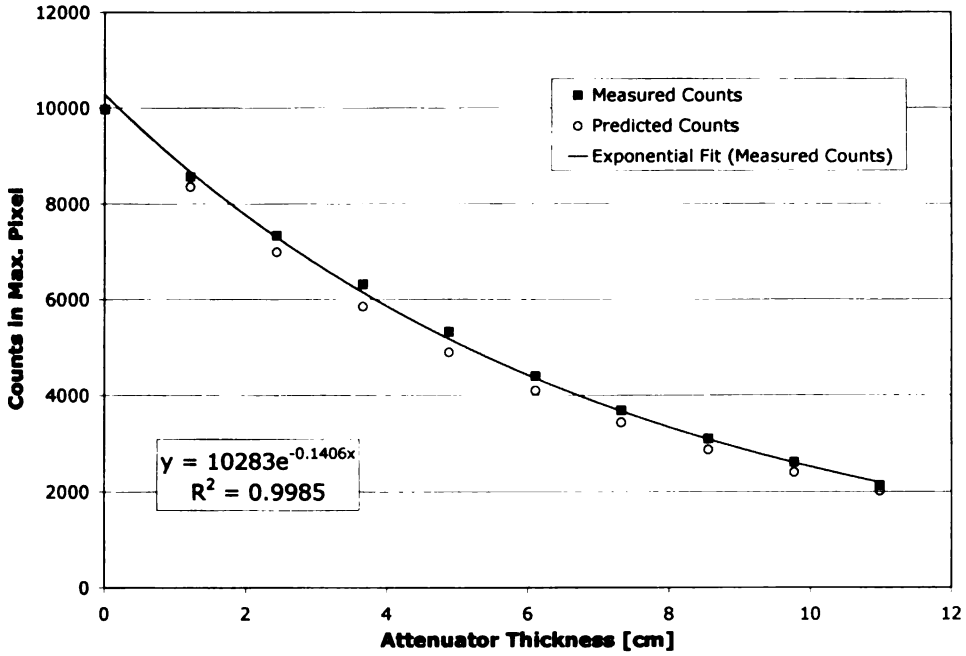


Figure 5-15: Direct measurement of the effective attenuation coefficient for ^{99m}Tc photons in polyethylene. The error bars are approximately the size of the square points on the graph.

The filled squares on the graph represent the measured values from this experiment, and the line is an exponential fit through these points; the equation for the line is displayed in the lower left corner of the chart. The predicted counts, represented by the open circles, are based on tabulated values of linear attenuation coefficients for polyethylene[2] and $\phi=\phi_0\exp(-\mu x)$ (Equation 2.3). The tabulated linear attenuation coefficient for polyethylene at 140 keV is 0.146 cm^{-1}; from the measurements in this experiment, we derive a linear attenuation coefficient of 0.141±0.001 cm^{-1}. These numbers are in good agreement with each other, and so this method of measuring the attenuation coefficient is quite accurate, even if it is not precisely a 'narrow-beam' measurement.

The corresponding measurements of the ^{111}In source are shown in Figure 5-16. The repeated measurements of the unattenuated ^{111}In point source had a mean maximum pixel value of 8962±114, so once again statistical noise is not an issue.

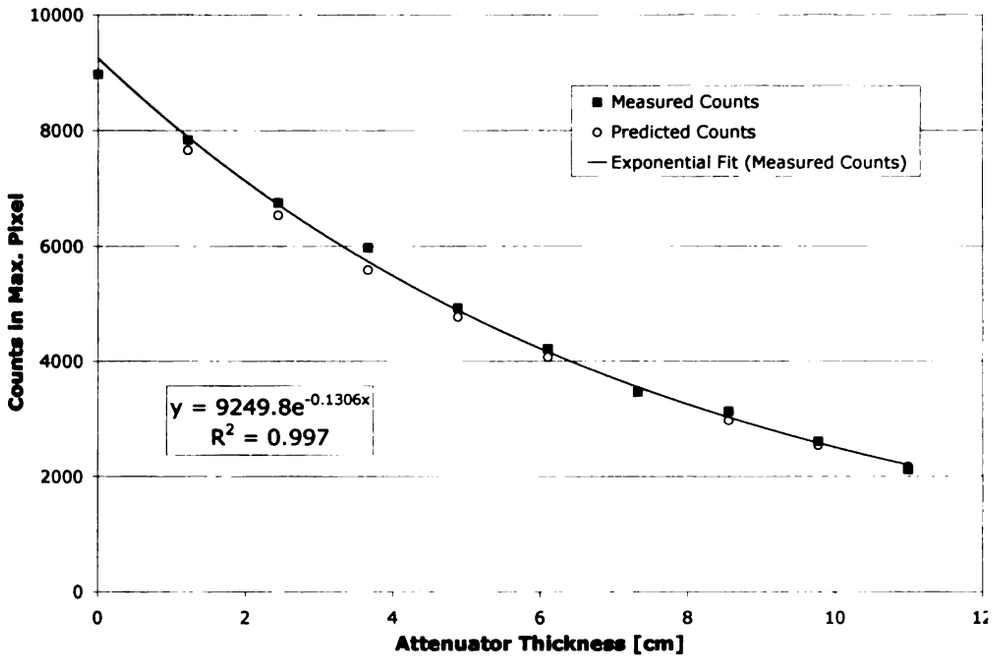


Figure 5-16: Direct measurement of the effective attenuation coefficient for ^{111}In photons in polyethylene. The error bars are approximately the size of the square points on the graph.

In this graph, the predicted counts are based on Equation 5.10 and the tabulated linear attenuation coefficients for polyethylene[2] at 171 and 245 keV. The predicted effective attenuation coefficient μ_{eff} is thus between 0.1293 cm^{-1} and 0.1290 cm^{-1}, depending on the thickness of the attenuating material. We could also have used the reference data to predict the linear attenuation coefficient for 210 keV photons, since 210 keV is our effective photon energy E_{eff} for ^{111}In. Based on E_{eff}, the predicted linear attenuation coefficient is 0.1284 cm^{-1}. From the measurements in this experiment, we derive a linear attenuation coefficient of 0.1306±0.001 cm^{-1}. Once again, these numbers are all in fairly close agreement. These results demonstrate that we can treat the emissions from ^{111}In as a single photon with energy E_{eff}, and use that effective energy as a basis for attenuation correction.

2. Spatial Uniformity measurements

Example line profiles from the uniformity images taken using the combined ^{111}In window and dual-energy attenuation correction are plotted below, along with sample images from each of the different reconstructions of the uniform tank. The dark horizontal line indicates the approximate location of the profiles on the tomographic images. In these images, we expect the profiles to be flat, reflecting the uniform distribution of radioactivity in the uniform tank. However, the profile shape can deviate from being flat due to errors introduced by photon attenuation and the geometric response of the collimator, if they are not corrected adequately by the algorithm used to reconstruct the radionuclide data.

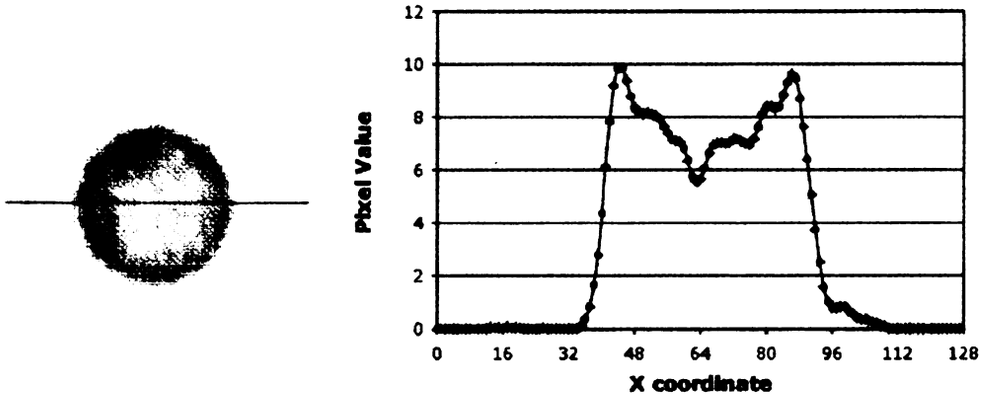


Figure 5-17: Tomographic image and line profile of the uniform tank, reconstructed with filtered backprojection.

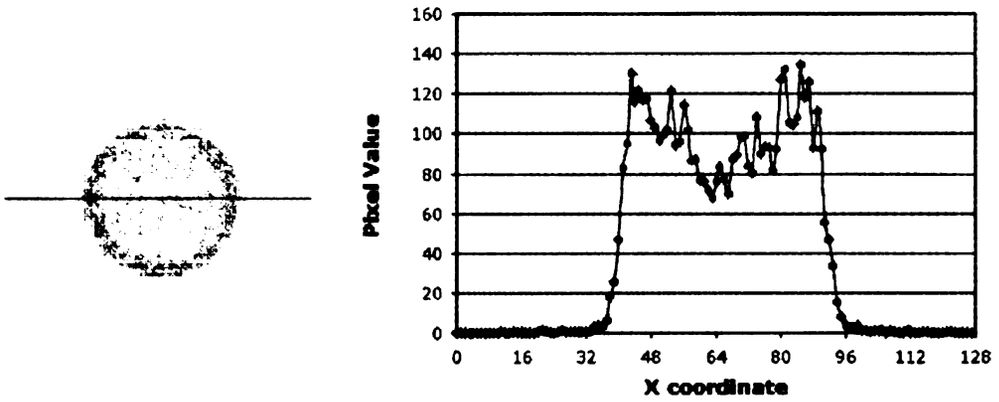


Figure 5-18: Tomographic image and line profile of the uniform tank, reconstructed using an iterative algorithm without attenuation or collimator correction.

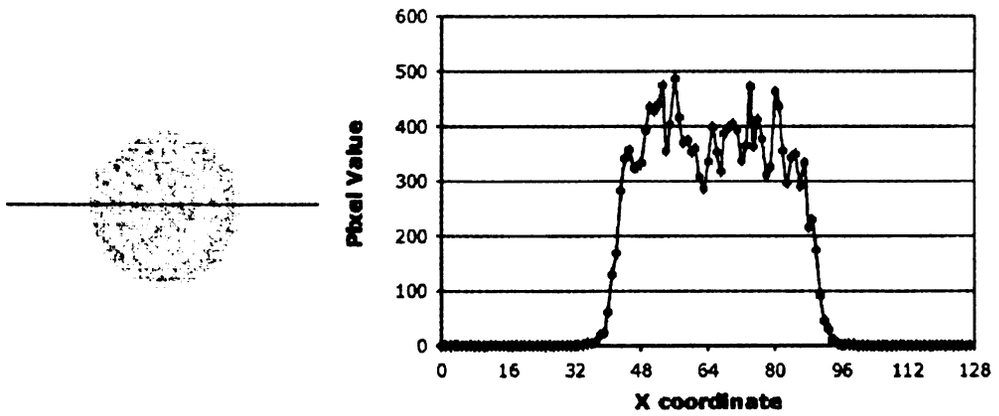


Figure 5-19: Tomographic image and line profile of the uniform tank, reconstructed using an iterative algorithm with attenuation correction, but without collimator correction.

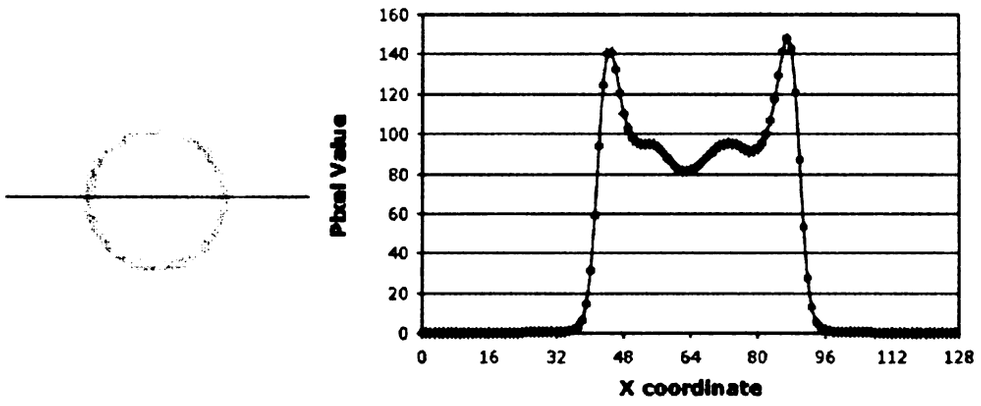


Figure 5-20: Tomographic image and line profile of the uniform tank, reconstructed using an iterative algorithm without attenuation correction, but with collimator corrections.

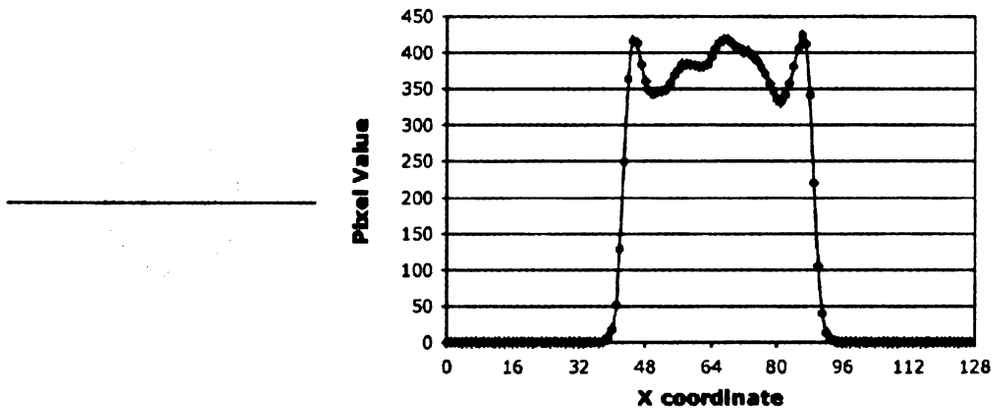


Figure 5-21: Tomographic image and line profile of the uniform tank, reconstructed using an iterative algorithm with attenuation and collimator correction.

The image in Figure 5-17 was reconstructed with a filtered backprojection algorithm, while the images in Figures 5-18 through 5-21 were reconstructed using the iterative ML-EM algorithm described earlier in this Chapter. Figures 5-17, 5-18 and 5-20 were reconstructed without using attenuation correction, and therefore show a noticeable depression of the image counts in the center of the tank. The overall reconstructed counts in the image are also significantly lower (by a factor of roughly 3.5 for the iterative

reconstructions, and two orders of magnitude for the filtered backprojection), because the reconstruction assumed that no photons were lost during the imaging process. By contrast, Figures 5-19 and 5-21 include correction for photon attenuation and therefore are much more even across the center of the phantom, and have a higher number of overall counts in the image.

Figures 5-20 and 5-21 demonstrate the effects of including collimator corrections in the iterative reconstruction. One advantage of this type of reconstruction is that the collimator blurring corrections are essentially filtering operations, so these images have significantly decreased high-frequency noise. However, they also exhibit a 'ringing' artifact, where the edges of the image are artificially enhanced. This effect has been noted by other investigators[1, 14, 15], and is an unavoidable consequence of attempting to recover the high spatial-frequency information lost in the imaging process. Even though we can model the point spread function of the gamma camera, it is not possible to recover all of the lost spatial frequency information from the original image, so the pixel values at the edges of the image become skewed.

To assess the spatial uniformity, we drew circular regions of interest over the central slices of the phantom, as illustrated in Figure 5-22. This region included most of the phantom, but did not include the entire image since the line profiles shown previously demonstrate a ringing artifact at the edges of the phantom. Including the entire image would also count the edge pixels that are partly inside the phantom and partly outside the phantom, which would incorrectly magnify the variance of the pixel values. The statistics for these regions of interest are listed in Table 5.I

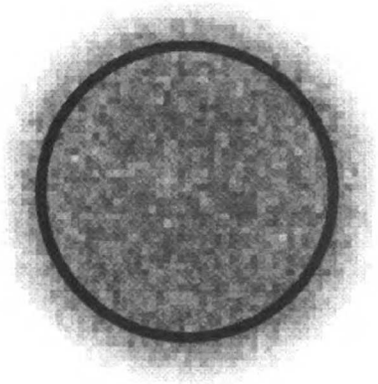


Figure 5-22: Illustration of the central ROI used for calculating image uniformity. This region extends over 5 slices in the center of the uniform tank phantom.

Attenuation Correction?	Collimator Correction?	Mean Pixel Value	Standard Deviation	StdDev /Mean
Filtered Backprojection		7.663	1.017	0.1327
No	No	96.88	15.77	0.1628
Yes	No	358.00	53.20	0.1486
No	Yes	96.79	16.82	0.1738
Yes	Yes	362.00	35.09	0.0969

Table 5-III: Mean and standard deviation of the pixel values in the central region of the uniform tank phantom, for the different reconstruction methods. This region contained 6320 pixels. The first row shows values obtained from an image reconstructed with a filtered backprojection algorithm. The data in rows 2 through 5 were obtained from images reconstructed with iterative ML-EM algorithms.

These results demonstrate that the reconstruction with both attenuation and collimator corrections produces the most uniform image, and that not including attenuation correction tends to decrease the overall uniformity, since the pixels in the central region have a lower value than those on the periphery. We can more closely examine the effects of attenuation correction by choosing a smaller diameter region of interest. If we halve the diameter of the region of interest, we obtain the results listed in Table 5.IV.

Attenuation Correction?	Collimator Correction?	Mean Pixel Value	Standard Deviation	StdDev /Mean
Filtered Backprojection		6.834	0.8662	0.1267
No	No	86.66	13.23	0.1527
Yes	No	376.70	61.22	0.1625
No	Yes	85.17	6.95	0.0816
Yes	Yes	373.00	32.20	0.0863

Table 5-IV: Mean and standard deviation of the pixel values in a smaller central region of the uniform tank phantom, for the different reconstruction methods. This region contained 1465 pixels. The first row shows values obtained from an image reconstructed with a filtered backprojection algorithm. The data in rows 2 through 5 were obtained from images reconstructed with iterative ML-EM algorithms.

In general, choosing this smaller region of interest increases the uniformity within the region, since we are now looking at only the very center of the phantom. The most dramatic shift is in the fourth line of the table, which represents the iterative reconstruction with collimator corrections, but without attenuation corrections. For this type of reconstruction, the data indicate that most of the variance in the image pixel values stems from (1) not using attenuation correction, and (2) ringing artifacts near the phantom edges. Thus, we might expect that patient images reconstructed with this technique might have a smooth and relatively noise-free interior, despite some artificially enhanced edges. We will continue these comparisons in future chapters as we discuss image quantitation and patient imaging, but the overall conclusion from this study is that the iterative reconstruction including collimator and attenuation corrections produces the most accurate tomographic images.

E. Discussion

1. Benefits of the dual-energy attenuation theory

The results of the attenuation measurements indicate that the dual-energy attenuation approach is very accurate, and we can treat the dual-photon emissions from ^{111}In as a single photon having an effective energy E_{eff} of 210 keV. The benefit of this approach to ^{111}In-ProstaScint® patients is that the gamma camera can collect data from two energy windows and merge them. Many gamma cameras (including the one used for the CT/SPECT system) can only record 2 energy windows simultaneously, and since ^{111}In-ProstaScint® must be imaged simultaneously with ^{99m}Tc-labeled red blood cells, these cameras ordinarily would have to ignore one of the photopeaks of ^{111}In. Because nuclear medicine images are always count-starved, we need to make use of all of the available photons to limit the effects of statistical noise, and the dual-energy attenuation correction theory provides a simple means of doing so. Furthermore, the dual-energy attenuation correction approach allows us to include attenuation effects with ^{111}In-ProstaScint® reconstruction using the same methodology that would be used for conventional single-energy isotopes such as ^{99m}Tc. Thus, we get the statistical benefit of being able to record counts from two photopeaks and the attenuation correction ease of a single photopeak.

2. Benefits of attenuation and collimator corrections.

We have used this dual-energy attenuation theory to develop iterative reconstruction algorithms that include corrections for attenuation and collimator blurring. This algorithm closely models the imaging physics, so we would expect it to produce

tomographic images that are more accurate and precise than those produced by filtered backprojection or an iterative algorithm without these corrections. The results from the uniform tank study support this hypothesis.

Without attenuation correction, there is a significant decrease in the overall reconstructed activity in the phantom, and activity in the central region of the phantom is disproportionately lowered. When attenuation correction is included, the line profiles across the phantom are flatter, and the overall reconstructed activity is increased. Thus, attenuation correction provides two kinds of quantitative benefits. The first is that the **relative** pixel values in the center of the reconstructed image are undiminished, and the second is that the **absolute** pixel values are significantly increased (presumably closer to their true values).

The collimator corrections result in a smoother image, albeit at the expense of some ringing artifacts. Of course, it is possible to take a noisy image and simply apply low-pass filtering to make it smooth, but such an approach indiscriminately blurs out everything in the image, which could eliminate spatial details of the image as well as noise. The distance-dependent blurring model used to correct these reconstructions applies filtration in a much more realistic and sensible way, and so we can gain the benefits of a less noisy image without sacrificing image details. In the following chapters, we will see how these benefits translate into accurate quantitative imaging for a more complex phantom model, and how they can improve the image quality of ^{111}In-ProstaScint® images for radiological interpretation.

F. Summary

In this chapter, we have described how the information from the CT/SPECT system can be used to implement a significantly more accurate SPECT reconstruction than filtered backprojection. This reconstruction makes use of the iterative ML-EM algorithm and includes corrections for collimator blurring (based on measurements of the system point spread function) and photon attenuation (based on a co-registered CT scan and calibration measurements). We also introduced a novel approach to attenuation correction for dual-energy emitters such as ^{111}In. This approach allows us to collect photons in multiple energy windows and treat them as a single photon with an effective energy E_{eff} and attenuation coefficient μ_{eff}. Finally, we have experimentally demonstrated the validity of this dual-energy attenuation correction theory and the ability of the reconstruction to accurately reproduce tomographic images from a uniform phantom. In the following chapter, we will assess the reconstruction algorithm in more demanding phantom tests, and measure its ability to quantify radionuclide concentration on an absolute basis. These results will pave the way for the application of this reconstruction to human patient studies with ^{111}In-ProstaScint® and CT/SPECT.

References:

[1] H. R. Tang, "A Combined X-ray CT-Scintillation Camera System for Measuring Radionuclide Uptake in Tumors," Bioengineering Ph.D. Dissertation, University of California Berkeley and University of California San Francisco, 1998, pp. 171.

[2] M. J. Berger, J. H. Hubbell, S. M. Seltzer, J. S. Coursey, and D. S. Zucker, "XCOM: Photon Cross Sections Database," National Institute of Standards and Technology, 1998.

[3] G. L. Zeng and G. T. Gullberg, "Frequency domain implementation of the three-dimensional geometric point response correction in SPECT imaging," *IEEE Transactions on Nuclear Science*, vol. 39, pp. 1444-1453, 1992.

[4] T. Ichihara, K. Ogawa, N. Motomura, A. Kubo, and S. Hashimoto, "Compton scatter compensation using the triple-energy window method for single- and dual-isotope SPECT," *J Nucl Med*, vol. 34, pp. 2216-21., 1993.

[5] I. Buvat, M. Rodriguez-Villafuerte, A. Todd-Pokropek, H. Benali, and R. Di Paola, "Comparative assessment of nine scatter correction methods based on spectral analysis using Monte Carlo simulations," *J Nucl Med*, vol. 36, pp. 1476-88., 1995.

[6] J. Q. Luo, K. F. Koral, M. Ljungberg, C. E. Floyd, Jr., and R. J. Jaszczak, "A Monte Carlo investigation of dual-energy-window scatter correction for volume-of-interest quantification in 99Tcm SPECT," *Phys Med Biol*, vol. 40, pp. 181-99., 1995.

[7] J. A. Heanue, J. K. Brown, H. R. Tang, and B. H. Hasegawa, "The effect of radionuclide scatter in emission-transmission CT," presented at 1996 Nuclear Science Symposium and Medical Imaging Conference (NSS/MIC), Anaheim, CA, USA, 1996.

[8] H. R. Tang, A. J. Da Silva, and B. H. Hasegawa, "The relative impact of scatter on absolute myocardial perfusion quantitation: an EGS4 Monte Carlo study," presented at Nuclear Science Symposium and Medical Imaging Conference, Seattle, WA, USA, 1999.

[9] A. J. Da Silva, H. R. Tang, K. H. Wong, M. C. Wu, M. W. Dae, and B. H. Hasegawa, "Absolute quantification of regional myocardial uptake of 99mTc-sestamibi with SPECT: experimental validation in a porcine model. [Comment In: J Nucl Med. 2001 May;42(5):780-1 UI: 21235439]," *Journal of Nuclear Medicine*, vol. 42, pp. 772-9, 2001.

[10] M. Shotwell, B. M. Singh, C. Fortman, B. D. Bauman, J. Lukes, and M. C. Gerson, "Improved coronary disease detection with quantitative attenuation-corrected Tl-201 images," *J Nucl Cardiol*, vol. 9, pp. 52-62., 2002.

[11] F. Harel, R. Genin, D. Daou, R. Lebtahi, N. Delahaye, B. O. Helal, D. Le Guludec, and M. Faraggi, "Clinical impact of combination of scatter, attenuation correction, and depth-dependent resolution recovery for (201)Tl studies," *J Nucl Med*, vol. 42, pp. 1451-6., 2001.

[12] C. Bai, G. L. Zeng, and G. T. Gullberg, "A slice-by-slice blurring model and kernel evaluation using the Klein-Nishina formula for 3D scatter compensation in parallel and converging beam SPECT," *Phys Med Biol*, vol. 45, pp. 1275-307., 2000.

[13] Y. K. Dewaraja, M. Ljungberg, A. Majumdar, A. Bose, and K. F. Koral, "A parallel Monte Carlo code for planar and SPECT imaging: implementation, verification and applications in (131)I SPECT," *Comput Methods Programs Biomed*, vol. 67, pp. 115-24., 2002.

[14] D. L. Snyder, M. I. Miller, L. J. Thomas Jr., and D. G. Politte, "Noise and edge artifacts in maximum-likelihood reconstructions for emission tomography," *IEEE Transactions on Medical Imaging*, vol. MI-6, pp. 228-238, 1987.

[15] D. R. Gilland, R. J. Jaszczak, W. Huili, T. G. Turkington, K. L. Greer, and R. E. Coleman, "A 3D model of non-uniform attenuation and detector response for efficient iterative reconstruction in SPECT," *Phys Med Biol*, vol. 39, pp. 547-561, 1993.

Chapter 6: ^{111}In SPECT Phantom Studies

A. Introduction

1. Motivation

In the previous chapter, we described the tools necessary for improving SPECT images by developing a mathematical model of the imaging system that can be incorporated into an iterative reconstruction. This approach compensated for the major physical effects (photon attenuation and collimator blurring) that degrade the SPECT image. We validated this reconstruction approach for basic image reconstruction tasks, and will directly apply it to ^{111}In-ProstaScint® patient imaging in Chapter 7. In this chapter, we will extend the tools used for image reconstruction to incorporate the task of quantitative imaging. Quantitative imaging is the ability to noninvasively determine the amount of radiotracer in an organ or body region in terms of μCi/g or μCi/ml. This ability can provide an important adjunct to radiological interpretation of images by assessing the functional status of an organ or tissue objectively. For example, in the case of ^{111}In-ProstaScint® imaging, the uptake of the radiopharmaceutical is dependent on the expression of the prostate-specific membrane antigen (PSMA), which has been correlated with biological aggressiveness[1] and androgen resistance[2] in prostate cancer cells. Absolute quantitative imaging with ^{111}In-ProstaScint® thus could be used to determine the level of PSMA present in the prostate or a suspected metastatic lymph node, which could provide additional staging information about the cells in that region. Because ^{111}In-ProstaScint® images are complex and difficult to interpret visually, an independent,

quantitative measure of the distribution of ^{111}In-ProstaScint® could be used to 'grade' potential tumors according to their PSMA expression, or even to globally evaluate an image for suspicious regions that might contain cancer.

2. Limitations of existing quantitation techniques.

The vast majority of ^{111}In-ProstaScint® users do not use any kind of image quantitation, and depend solely on image interpretation to draw conclusions about a patient's condition. The notable exception is the semi-quantitative analysis applied to ^{111}In-ProstaScint® images by Sodee[3]. In this study, regions of interest were drawn directly on the SPECT images (reconstructed using an iterative algorithm without attenuation or collimator corrections), as illustrated in Figure 6-1. One region was drawn within the area of the prostate, and the other was drawn within the area of the external obturator muscle. Both regions were drawn to be the same size, so a prostate/muscle ratio was calculated based on the mean voxel values in each region. Although this study demonstrated that a high prostate/muscle ratio tended to correspond to the presence of cancer on biopsy, no attempt was made to relate the voxel values to true activity concentrations (nCi/ml or a similar quantity).

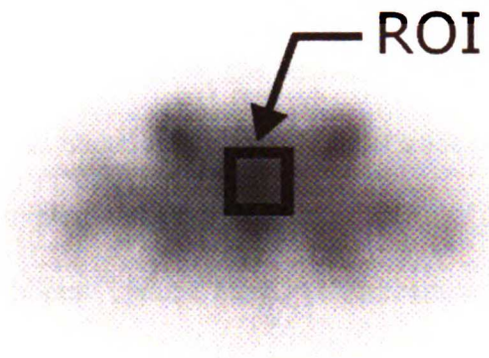


Figure 6-1: Illustration of semi-quantitative imaging approach used for ^{111}In-ProstaScint® by Sodee, *et al*[3].

'Quantitative' analysis is often applied to positron emission tomography (PET) images using a technique known as the Standardized Uptake Value (SUV). In this technique, two similar-sized regions of interest are drawn directly onto the PET image; one of these regions is in a location where cancer is suspected, and the other region is a contralateral or nearby location considered to be background. The SUV is defined as the ratio of voxel values between these regions, and can potentially be used to discriminate benign uptake of ^{18}FDG (caused by inflammation or another normal physiological process) from cancer[4, 5]. As with the results from Sodee's study, the SUV derived from this analysis is a ratio of voxel values, and the absolute concentration of ^{18}FDG in the suspected tumor is never determined.

We ultimately wish to use ^{111}In-ProstaScint® to determine the density of PSMA in a tissue or organ, so we need to be able to measure the true activity concentration of ^{111}In-ProstaScint® (i.e. nCi/ml) and not just a ratio. Unfortunately, there are few standard methods for making this kind of measurement. Planar-conjugate views have been used

for the measurement of internally administered therapeutic radionuclides[6]. In this method, opposing planar gamma camera images of both a patient and a radioactive source with known activity are recorded, and activity in organs is calculated based on the counts in these two images. However, this method does not make use of tomography, so organs that overlap on the planar views cannot be separated. Thus, this method is unsuitable for ^{111}In-ProstaScint®, where there is significant non-specific uptake throughout the abdomen and the organs of interest (i.e. the prostate and lymph nodes) are deep within the body. Furthermore, as we shall see in a following section, conjugate view methods can be very inaccurate for small objects.

Some attempts have been made to measure absolute activity concentrations from reconstructed SPECT images of the brain[7], myocardium[8], and thorax[9-11], with varying degrees of success. These methods generally use a reconstructed image of a uniform tank phantom to measure the sensitivity of the gamma camera, and thereby obtain a conversion factor between voxel values in the reconstructed image and absolute activity. Patient images are then reconstructed using the same algorithm, and the voxel values of the reconstructed patient image can thus be converted to estimates of the activity distribution. Regions of interest can then be drawn over an organ (similar to the illustration in Figure 6-1) to determine its activity concentration. Koral[11] also proposed using a manually registered CT scan for measurement of organ size, in order to correct for partial-volume effects.

Unfortunately, these approaches to absolute quantitative imaging have significant potential limitations. The first problem is that the region of interest must be drawn based on the poor spatial resolution of the SPECT image. The SPECT image also has very few

anatomical details, so it can be very difficult to accurately delineate regions within an organ (or, often, the organ itself). The second problem is that effects such as attenuation and collimator blurring degrade the SPECT image, and if these have not been adequately corrected, the reconstructed pixel values will not correspond to the real activity distribution in the object. Photon attenuation will mask the true strength of sources deep inside the body or artificially enhance the strength of superficial sources. The blurring induced by the collimator causes counts from the background (everything outside the region) to be 'spilled-in' to the region of interest; conversely, counts from the region of interest will be 'spilled-out' into the background, further complicating the measurement.

The CT/SPECT imaging system provides a means of overcoming these barriers to quantitative imaging. The high spatial resolution and anatomic detail of the CT images allows an observer or computer program to precisely define the regions of interest, which can then be transferred to the SPECT image using the known image registration transformation (as described in Chapter 4). The electron density information provided by the CT scan provides a means to correct for attenuation effects, and an accurate model of the collimator blurring can correct for resolution limitations. Using this information, quantitative measurements based on the reconstructed SPECT images will be more accurate and precise. However, the CT/SPECT system also enables an entirely different approach to quantitative imaging, based on CT-defined regions of uniform activity and an accurate mathematical model of the imaging process. Although this method incorporates many of the elements used for improved SPECT reconstruction, it also has key differences. In the next section, we will review these different approaches to quantitative imaging and explain their relative strengths and weaknesses. This theoretical information

will provide the background needed for the experimental quantitative imaging tests discussed later in this chapter. In Chapter 7, we will apply quantitative imaging to patient studies, in order to measure objectively the distribution of ^{111}In-ProstaScint® in prostate cancer patients.

B. CT/SPECT Quantitation Techniques

1. Direct measurements from the reconstructed image

As mentioned above, conventional radionuclide quantitation techniques extract counts by defining a region of interest (ROI) on a lesion or target region in the radionuclide image. The goal of this procedure is to extract the number of counts in that region, which can be transformed to a corresponding value of radioactivity using a suitable calibration factor. As we also noted, this method is prone to inherent errors caused by the physical effects such as photon attenuation and the spatial resolution limitations of the radionuclide imaging system. One method of potentially overcoming these limitations is to use a priori information from CT or another anatomical imaging technique in the radionuclide quantitation process. For example, if correlated SPECT and CT image data are available, we can define a region of interest on the high spatial resolution CT image. This region of interest can be defined as a second, binary image in the CT coordinate system, where all of the pixels inside the region of interest have a value of one, and all of the pixels outside the region of interest have a value of zero. Thus, the coordinates of these voxels can be transferred into the SPECT coordinate system using the methods outlined in Chapter 4. We can then make quantitative measurements by simply evaluating the pixel values of the SPECT image, as illustrated in Figure 6-1. Assuming that the reconstruction has

accurately accounted for all of the physical perturbations of the SPECT imaging process, the pixel values will reflect the true activity distribution in the object. Uniform phantoms filled with known activity can serve as calibration sources, allowing us to keep track of variations within the system and also to correlate the reconstructed units with actual measures of activity.

Although this method is straightforward, it has some notable disadvantages. This method requires a very accurate reconstruction process, which can be computationally expensive and difficult to formulate. The activity in the region of interest is also usually slightly underestimated because of the blurring imposed by the gamma camera's finite resolution[12], which is difficult to recover completely, even with an iterative reconstruction such as the one discussed in Chapter 5[13]. However, the advantage of this technique is that the reconstructed image (which presumably has been generated for radiologic interpretation already) contains all of the quantitative information. Thus, once the reconstruction is complete, an arbitrary number of regions can be chosen and measured with little additional effort. Thus, it can be advantageous in situations where the anatomy is complex and the region of interest may not be completely known in advance.

2. Template-projection-reconstruction methods

a) Limitations of the SPECT image

Although the 'direct method' described above has significant flexibility, it is limited by the quality and accuracy of the reconstructed image. Even assuming that one can correct for the physical perturbations that affect the SPECT image, the projection

data still are affected by statistical noise that imposes a fundamental uncertainty on the measurement. The iterative reconstruction process modifies the activity distribution in the object so that the simulated projection data match the actual projection data as closely as possible, but the SPECT reconstruction problem is extremely ill-conditioned. Thus, there is no unique solution that produces the true activity distribution in the object. Rather, there are multiple solutions, all of which are equally valid estimates of the true activity distribution. The reconstruction selects one of these solutions, but does so based on a 'global' assessment of the mismatch between the simulated and the actual projection data, i.e. it attempts to minimize the error for every detector pixel simultaneously. Furthermore, there is no standard for SPECT reconstruction; so even ML-EM iterative reconstruction is a somewhat undefined process, with no universally accepted criteria for stopping conditions, number of iterations, or a particular software implementation.

b) Overview of template-projection-reconstruction

A different approach to quantitative imaging that circumvents some of these limitations was developed by Tang[13], based on concepts devised by Formiconi[14] and Liu[15]. This approach, called 'template-projection-reconstruction', depends on the delineation of 'templates', which are anatomical regions of interest that are assumed to have uniform activity. For example, one might model a prostate tumor as two templates: one would represent the prostate itself, and the other would represent the surrounding tissues. These regions are transformed into projection data using a 'projector', which models the radionuclide imaging system to generate simulated projection data from an estimated activity distribution. Thus, this 'projector' can incorporate physical perturbations (e.g., photon attenuation, spatial resolution limitations) that affect the

SPECT image, as described in the previous chapter. Once we have obtained simulated projection data based on the templates, we can apply tomographic reconstruction to these data to generate SPECT images of the templates. The type of reconstruction used does not matter, so long as **exactly the same** reconstruction is used both on the template and on the measured projection data. The end result of this process is a pair of SPECT images that have used a common reconstruction algorithm, and that therefore have accounted equally for any errors in the acquisition and reconstruction processes. This process is illustrated conceptually in Figure 6-2.

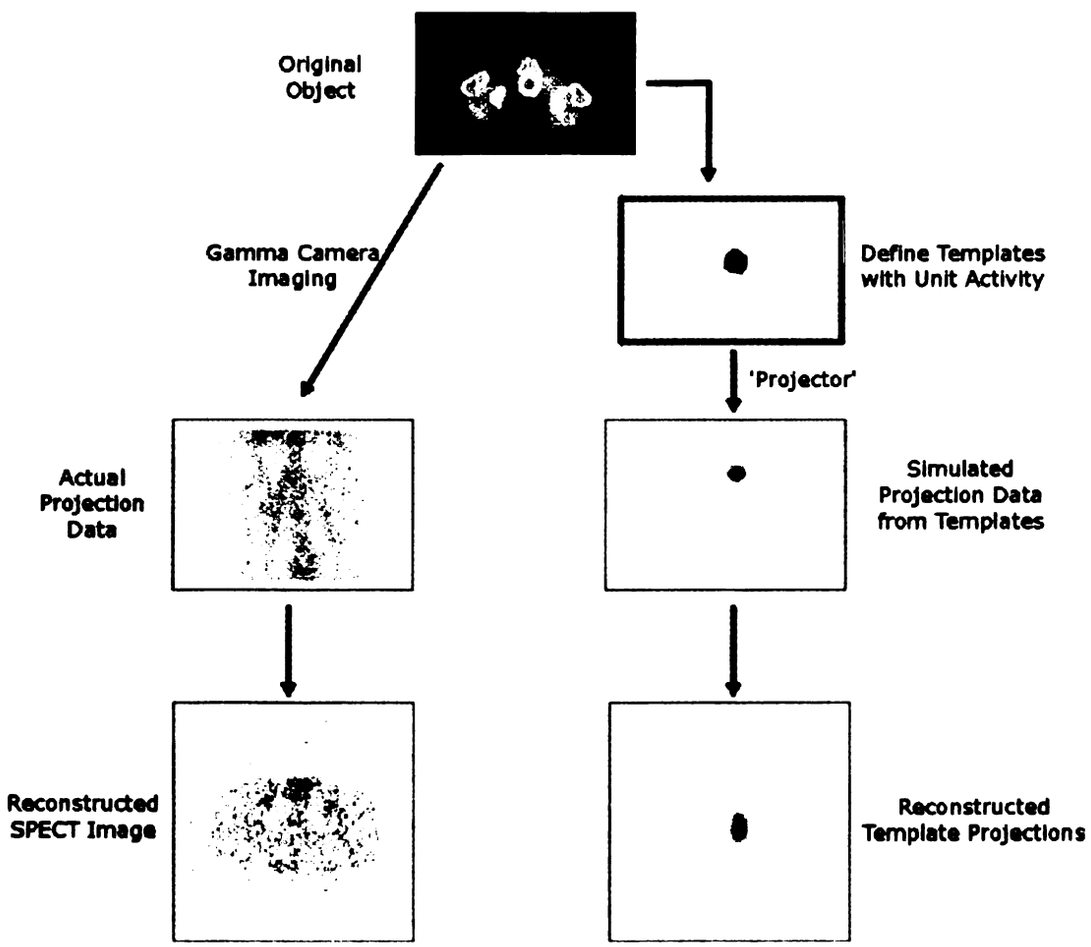


Figure 6-2: Illustration of the template-projection-reconstruction process. The CT-defined template is used to generate simulated SPECT projection data, which can then be reconstructed in the same manner as the actual projection data.

The template projection-reconstruction process can be expressed mathematically as follows. We define a template region corresponding to the target region in which we want to quantify radionuclide uptake. We then assign the template unit activity, generate simulated projection data based on that template and a mathematical model of the imaging process, and reconstruct the simulated projection data as shown in Figure 6-2. Additional templates can be used to delineate background regions or additional target regions in the image. The result of the template projection-reconstruction process is set of a reconstructed template images which we define as $f_m(b)$, where the index m enumerates the m^{th} template and b enumerates the object voxels. Then, we can estimate the activity concentration in the reconstructed SPECT image as a product of the true activity in the template and $f_m(b)$:

$$\rho_m(b) = A_m f_m(b) \tag{6.1}$$

where $\rho_m(b)$ is the estimated activity concentration (from the m^{th} template) in the reconstructed SPECT image for object voxel b, and A_m is the true activity in the m^{th} template. We can repeat this process for all templates of interest, so that the total estimated activity concentration in a particular object voxel is just the sum from all of the templates:

$$P(b) = \sum_{m=1}^{M} A_m f_m(b), \tag{6.2}$$

assuming that the imaging and reconstruction process is linear. The imaging process is linear so long as the count rates on the gamma camera do not exceed the ability of the camera to resolve individual photons, which is certainly true for the very low count rates

normally encountered in an ^{111}In-ProstaScint® examination. The reconstruction process is linear if filtered backprojection is used, and is approximately linear if ML-EM is used[13]. If we use the example of a prostate tumor being modeled as a tumor template and a background template, then the expected activity in a particular object voxel b is given by:

$$\mathrm{P}(b) = A_{tumor} f_{tumor}(b) + A_{background} f_{background}(b). \tag{6.3}$$

Thus, we obtain an instance of Equation 6.3 for every object voxel in the reconstructed SPECT image, which gives us a system of many equations and two unknowns: A_{tumor} and $A_{background}$. This system of equations can be solved in two potential ways. The first is to adjust the values of A_{tumor} and $A_{background}$ to minimize the squared-difference between the reconstructed SPECT image and the reconstructed template image, which can be expressed mathematically as minimizing

$$\delta^2 = \sum_{b=1}^{N_b} \left[\mathrm{P}^*(b) - \sum_{m=1}^{M} A_m f_m(b) \right]^2, \tag{6.4}$$

where N_b is the number of object voxels inside the region that we are attempting to quantify (in this example, it would be the number of voxels inside the tumor region), $\mathrm{P}^*(b)$ is the activity concentration in voxel b of the actual reconstructed SPECT image, and δ^2 is simply a measure of the squared-difference. This minimization can be accomplished through the use of a least-squares fitting routine, such as singular value decomposition or any linear regression algorithm. Conceptually, this approach is a sparse reconstruction problem. In a tomographic reconstruction, we adjust the estimated activity in the object voxels so that the estimated projection data match the actual projection data

as closely as possible. In Equation 6.4, we adjust the estimated activity in a small number of templates so that the reconstructed templates match the actual reconstructed SPECT projections as closely as possible. We will therefore refer to Equation 6.4 as the 'least-squares fitting' approach.

The second approach (if we only have a tumor template and a background template) is to solve Equation 6.3 for A_{tumor}:

$$A_{tumor} = \frac{\mathrm{P}^*(b) - A_{background} f_{background}(b)}{f_{tumor}(b)} \tag{6.5}$$

where we have replaced the estimated activity concentration P(b) with the measured activity concentration in the reconstructed SPECT image $\mathrm{P}^*(b)$. For every object voxel b, Equation 6.5 estimates a value of A_{tumor}, so we can use the mean value of A_{tumor}, calculated for all object voxels in the tumor region, to define the activity concentration in the tumor:

$$A_{tumor} = \frac{1}{N_b} \sum_{b=1}^{N_b} \frac{\mathrm{P}^*(b) - A_{background} f_{background}(b)}{f_{tumor}(b)}. \tag{6.6}$$

This method is even simpler computationally, and has the advantage of smoothing over statistical noise if we estimate the activity in the background by averaging over a large uniform region. Conceptually, this approach takes a voxel value from the reconstructed SPECT image, subtracts a contribution from the background, and then divides the difference by the expected value of the reconstructed image **if the true activity was unity**. Thus, Equation 6.6 uses the ratio between the corrected $\mathrm{P}^*(b)$ and $f_{tumor}(b)$ to scale

the activity in the tumor region to its true value. We refer to this method as the 'voxel scaling' approach.

The choice of the background region is somewhat arbitrary. However, the background closest to the tumor will certainly have the strongest effect on the reconstructed activity within the tumor region. Since the spatial resolution of the gamma camera is at best 7 to 8 mm, a sensible requirement on the background region is that it encompass a region extending out from the tumor by at least this distance. Thus, if the tumor were a 1 cm diameter sphere, the background should at least be a spherical shell around the tumor with a outer diameter of 2.6 cm (1 cm + 8 mm + 8mm). Making the background larger will probably improve our estimate of A_{tumor}, but Equation 6.6 is only valid when $A_{background}$ is uniform within the background region, so we cannot simply make the background area as large as the image. In the phantom studies, we will use this quantitation method with varying size backgrounds, in order to determine a suitable method for choosing background regions on the ^{111}In-ProstaScint® patient images.

c) Benefits/Limitations of template-projection-reconstruction.

Since the template-projection process simplifies the object into a few templates, it is computationally much simpler than a full iterative SPECT reconstruction and has far fewer adjustable parameters (i.e. number of iterations). The simulated projection data can be generated using the mathematical model of the imaging process designed for iterative SPECT reconstruction, but this takes only a small fraction of the time required for the reconstruction, since the calculation is only performed once. Any reconstruction algorithm (filtered backprojection, ML-EM without any corrections, etc.) can then be used on the templates and the actual SPECT projection data, so we may choose one based

solely on speed or ease of use. Once we have obtained the two reconstructed images, the minimization problem only has a few unknown parameters (the activity in the templates) and many equations to define them, unlike a SPECT reconstruction where all of the voxels have an unknown activity. This simplicity means that the determination of the activity in the template can be done very quickly. This simplicity comes with a price, however, because it means that the quantitation is less flexible. For every region of interest in the body, we must define separate templates for that region and surrounding background regions. If we decide in the future that we wish to make a quantitative measurement in a different region, then the process must be repeated. Fortunately, the computational cost of the template-projection process is low, so this requirement does not place a large additional burden on the user.

Another potential limitation of the template projection process is that the template is assumed to have (1) well-defined boundaries on CT, and (2) uniform activity. Although this may be true for some tissues in the body, such as a region of the myocardium fed by a particular coronary vessel, it may not be true for other tissues, such as a large tumor with a necrotic core and a heterogeneous population of cells. Furthermore, in some patients the region of interest may not be known in advance. Of course, we can circumvent this problem somewhat by making more and more templates. However, as the number of templates increases, the quantitation task begins to take on the complexity of a reconstruction, and we may not be able to use simple computational tools to minimize the difference between the actual reconstructed SPECT image and the reconstructed template image. A final limitation of the template-projection-reconstruction process is that it produces reconstructed SPECT images that suffer from

all of the limitations discussed in previous chapters. If we are only interested in quantitation, this is not a significant drawback; however, most nuclear medicine studies depend on visual evaluation by an expert reader to fully assess the patient's condition, so a high-quality reconstructed SPECT image is still an important goal.

3. Previous quantitative studies using these methods

Previous work by Tang [13] tested the quantitative abilities of these different methods in cylindrical and anthropomorphic phantoms, both for repeated measurements and for varying target-to-background concentrations. This work found that the template methods could accurately recover the true activity concentration in spherical tumor models to within 10%. Direct quantitation from the reconstructed SPECT image fared less well, although it was able to approach this accuracy for large objects when attenuation and collimator blurring were included in the reconstruction and registered CT scans were used to define object boundaries. By contrast, the nuclear medicine technique of image quantitation using planar conjugate views produced errors as large as 600% for simulated lesions having a volume of 2.7 ml.

DaSilva [16] used the template-projection-reconstruction method to quantify activity in a porcine myocardium. Pigs with various degrees of coronary artery occlusions were imaged using the CT/SPECT system; following imaging, the myocardium of the pig was excised, subdivided, and measured to determine its true activity concentration. Template-projection methods were then used to estimate the activity concentrations from the SPECT data. Using an uncorrected projection model without collimator or attenuation corrections resulted in a measurement error of roughly 90%. Inclusion of attenuation effects lowered this error to approximately 50%, but

correction for both attenuation and collimator blurring effects resulted in an absolute measurement error of only 10%. This study demonstrated that the template projection method could provide highly accurate myocardial quantitation in a complex and realistic physiological system.

Based on these previous studies, we felt that these methods could be used for quantitative imaging of ^{111}In-ProstaScint® patients, with the proviso that they be evaluated specifically for the task of measuring activity concentrations of ^{111}In-ProstaScint® (using dual-energy attenuation correction). However, both approaches to quantitation have strengths and weaknesses, and thus there may be situations where one or the other is better suited to the quantitation task. We will address these situations more specifically in the context of ^{111}In-ProstaScint® patient studies in Chapter 7, but in this chapter we will study both methods using phantoms, in order to confirm their quantitative accuracy.

C. Experimental Methods

1. Overview

Our experimental goal was to evaluate the ability of the CT/SPECT system to quantitatively measure the concentration of ^{111}In using a phantom model of patient imaging. Although it is impossible to fully model the complexity of a living patient, the phantom model provides a more challenging test than a uniform tank, and also allows us to evaluate the quantitative process for objects of varying size and under conditions similar to actual ^{111}In-ProstaScint® imaging. In addition, unlike patients, the radionuclide content of the phantom is known accurately, and thereby provides a "gold-standard"

against which we can compare measurements obtained using the imaging techniques. The experimental measurement begins by acquiring CT/SPECT scans of a uniform tank in order to provide a calibration for the system. This step allows us to relate voxel values in a reconstructed image to known activity concentrations. We then designed a phantom to mimic the total activity and relative activity distribution of an ^{111}In-ProstaScint® patient, and imaged this phantom under conditions similar to patient imaging. Finally, we applied 'direct measurement' quantitation and template-projection-reconstruction to the phantom data, to determine how well these techniques recovered the known activity values within the phantom. Thus, these experiments will help us to choose the most suitable techniques for quantitative imaging, so that these techniques can be applied to the patient studies.

2. Uniform Calibration Tanks

It is theoretically possible to design a reconstruction algorithm so that it returns tomographic slices whose values exactly correspond to the activity distribution in the object. However, the difficulty with this approach is that it is inflexible to variations in image acquisition parameters, such as the radioisotope being imaged, the energy window settings, the type of collimator, and the image matrix size. Therefore, we would need a different reconstruction code for each possible set of acquisition parameters, which is challenging to maintain and update. A more flexible approach would be to calibrate the system using a source with known activity, so that any variations in the acquisition could be addressed by simply imaging the known source with the same parameters that are to be used in the patient or phantom imaging. In this scheme, we can have a general-purpose tomographic reconstruction for any type of SPECT acquisition, and then measure

specific calibration information for quantitative imaging as needed. This approach has been used for previous quantitative studies in our research group, so our goal in this experiment was to obtain the calibration information for ^{111}In.

To calibrate the CT/SPECT system for ^{111}In-ProstaScint® imaging, we scanned a uniform tank filled with an aqueous solution of ^{111}In. The calibration tank was a cylinder (Data Spectrum, Hillsborough, NC) with an internal diameter of 217 mm and an internal height of 188 mm. The measured internal volume was 6826 ml. The tank was filled with water and 5.77 mCi of ^{111}In, so that it had an initial activity concentration of 0.845 μCi/ml.

We placed the uniform tank on the CT/SPECT imaging table with its axis aligned with the axis of the CT scanner, so that tomographic slices through the tank would be circular. Fiducial markers for registration were placed on the tank and the table as described in Chapter 4. The tank was imaged on the CT scanner using a tube current of 140 kVp, a tube current of 120 mA, a scan time of 3 seconds, and a slice thickness of 5 mm. CT slices were reconstructed using a 256x256 image matrix size and a 48 cm field of view. Following CT imaging, the tank was moved under the gamma camera for SPECT imaging using a medium-energy collimator. Projection data were acquired using a 128x128 image matrix size and a combined energy window with one 15% width photopeak centered at 171 keV and another 20% width photopeak centered at 245 keV. A 7% window at 140 keV was acquired simultaneously so that the ^{99m}Tc-filled fiducial markers could be visualized. Sixty-four angular views were acquired, with an acquisition time of 30 seconds per view. The radius of rotation of the gamma camera was fixed at 24 cm.

After acquisition was complete, the tomographic CT slices and raw SPECT projection data were downloaded from the CT/SPECT system and transferred to a workstation for further analysis. The SPECT projection data from the ^{99m}Tc window were initially reconstructed using an ML-EM algorithm (30 iterations) without attenuation or collimator corrections, and these tomographic slices were used to perform image registration as described previously. An ^{111}In-specific attenuation map was generated using the methods outlined in Chapter 5. The SPECT projection data from the combined ^{111}In window were then reconstructed using (1) an ML-EM algorithm that included attenuation correction, and (2) an ML-EM algorithm that included attenuation and collimator corrections. (We did not use reconstructions without attenuation correction, because we demonstrated in Chapter 5 that not including attenuation correction caused the reconstructed voxel values to significantly underestimate their true radionuclide values). Based on previous experience of our research group with these types of calibration measurements, we used 30 iterations for each algorithm. Cylindrical regions of interest were placed on the reconstructed SPECT images (these regions had a diameter of approximately 90% of the internal diameter of the tank, so that ringing artifacts at the edges were not included), and the mean voxel value in these regions was calculated. These values were used to calibrate reconstructed voxel values against the known activity concentration in the uniform tank (in units of nCi/ml). We repeated the scan of the uniform tank at three additional time points over two weeks, in order to ensure that the calibration value scaled correctly with the total activity in the tank.

3. Phantom Simulation of ^{111}In-ProstaScint® Study

a) Target:background ratio

In order to make the phantom a realistic model of the ^{111}In-ProstaScint® imaging process, we evaluated ^{111}In-ProstaScint® scans acquired on the clinical gamma camera systems in the UCSF Nuclear Medicine department. Although these images are not acquired with a coregistered attenuation map (and thus cannot be considered truly quantitative), they do provide information on the relative uptake between suspected tumor regions and non-tumor background tissue. Ten patient studies were selected randomly from a database of nuclear medicine patients, and tomographic ^{111}In-ProstaScint® SPECT images were downloaded from a central archive to a workstation for further analysis. The images were retrieved and stripped of any identifying patient information, according to institutional guidelines for retrospective imaging studies (this process ensured that these data could not be linked back to individual patients, which is a cardinal requirement for review studies that cannot obtain informed consent from each individual patient). Cubic regions of interest (approximately 2 cm on a side) were then drawn on the tomographic images. One region was placed inside the prostate, which is expected to have relatively high uptake of ^{111}In-ProstaScint®. Another region was placed in an area of low uptake considered to be 'background', which was usually the surrounding muscle bed. Because the prostate lies along the midline of the body, it is not possible to define a background region in a contralateral area, but we attempted to place both of these regions fairly deep in the body, so as to normalize potential attenuation effects on the two regions. The regions were both drawn to be the same size. Pixel

values in the regions of interest were summed, and from these measurements a target:background ratio was calculated for each patient. The range of target:background ratios was 10:1 to 2:1, and the mean value was 6:1. Based on these data, we used a target:background ratio of 6:1 for the experimental phantom. Using a similar analysis, Sodee has reported target:background ratios in the range of 2:1 to 20:1 for ^{111}In-ProstaScint® patients[17].

b) Total activity concentration

The total number of counts recorded by the gamma camera determines the statistical quality of the data, so we chose the total activity in the phantom and the imaging time to match that of a clinical image. During a typical ^{111}In-ProstaScint® study, a patient is injected with approximately 5 mCi of ^{111}In-ProstaScint®. Imaging takes place 4 days after the injection, in order to allow the radiotracer time to bind to its target tissue and be cleared from the bloodstream, so radioactive decay decreases this 5 mCi to:

$$5 \text{ mCi } (0.5)^{4 \text{ days}/2.83 \text{ days}} = 1.9 \text{ mCi} = 1900 \ \mu\text{Ci} \qquad (6.7)$$

based on the 2.83 day half-life of ^{111}In. ^{111}In-ProstaScint® is also cleared from the body by biological systems, and is excreted in bodily wastes. However, determining the biological clearance for individual patients can be complex, so we used the overall count rate from the previously retrieved patient studies to estimate the activity remaining in a typical ^{111}In-ProstaScint® patient. In these patients, we measured the total number of counts recorded by the detector over the entire imaging study. The mean value for total counts was 3.44×10^6 (the range of these values was 5.31×10^6 to 2.25×10^6), which translates to a count rate of approximately 1075 counts/second based on the standard

clinical acquisition parameters of 64 views and 50 seconds/view. The efficiency of the collimator is 367 counts/minute/μCi, according to the manufacturer specifications, so we estimated the total activity in the camera field of view to be:

$$\frac{1075\ \text{counts/sec}}{367\ \text{counts/min/}\mu\text{Ci}}\left(\frac{60\,\text{sec}}{\text{min}}\right)=176\ \mu\text{Ci} \tag{6.8}$$

Based on these data, we filled the phantom with a total activity of 600 μCi, but imaged for a shorter amount of time per view than the clinical studies. This compromise allowed us to complete the imaging studies in less time, but with roughly the same statistical quality.

^{111}In-ProstaScint® patients are also injected with autologous ^{99m}Tc-labeled red blood cells immediately prior to imaging, in order to provide an image of their vasculature. The total counts in these images were roughly the same as those from the ^{111}In-ProstaScint® images (mean value of $3.21\text{x}10^6$), but the energy window for ^{99m}Tc is only half as wide (7%) as the window for ^{111}In (15%). Thus, we estimated the ^{99m}Tc activity in the field of view to be approximately 350 μCi.

c) Phantom construction

The experimental phantom, shown in Figure 6-3, was used to simulate the uptake of ^{111}In-ProstaScint® in human solid tumors. The main compartment of the phantom (Data Spectrum, Hillsborough, NC) is a cylinder measuring 197 mm internal diameter by 188 mm internal height, and has a wall thickness of 3 mm. A plastic bar with several threaded attachment points was placed along the central axis of the cylinder, and hollow spheres simulating tumors were attached to this bar with plastic standoffs. The standoffs

are threaded on both ends, so that one end can be used to seal the opening in the sphere, and the other end can be screwed into the central bar. The standoffs are normal to the axis of the cylinder, and are roughly 5 cm in length. The total internal volume of the cylinder, excluding the space occupied by the bar, is approximately 5700 cc.

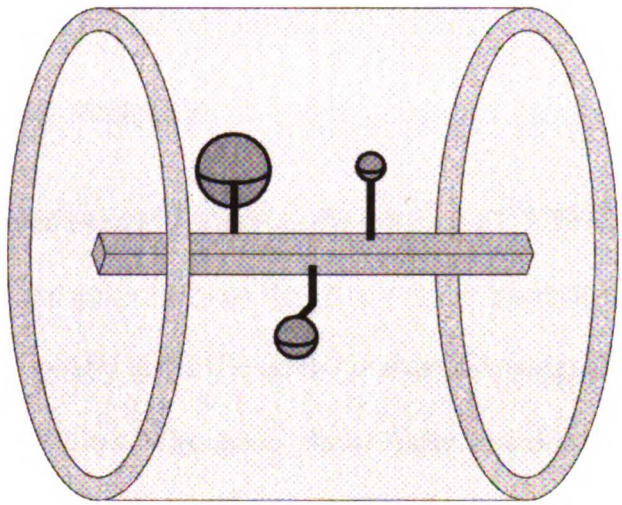


Figure 6-3: Diagram of the cylindrical ^{111}In-ProstaScint® phantom.

Table 6-I below lists the sphere sizes that were used in these experiments.

Phantom Sphere Sizes

Sphere Nominal Size (according to manufacturer)	Sphere External Diameter [mm] (measured)	Sphere Internal Volume [ml] (measured)
32	31.4	11.7
18	18.5	2.0
12	12.3	0.5

Table 6-I: List of the spheres that were used to simulate tumors inside the cylindrical phantom.

The spherical 'tumors' were filled with an aqueous solution of ^{111}In-indium chloride and a CT contrast material (300 mg/ml of K_2HPO_4) so that they could be easily visualized on the CT scan. In addition, the cylinder was filled with an aqueous solution of ^{111}In-indium

chloride to provide background activity. The activity concentrations in the target spheres and the background were chosen to match the parameters discussed in the previous sections: 0.6 μCi/ml for the target spheres and 0.1μCi/ml for the background. ^{99m}Tc was also added to the background at a concentration of 0.2 μCi/ml, to simulate the blood pool labeling.

d) Imaging Protocol

The phantom was imaged 5 times on the combined CT/SPECT system. Fiducial markers were created and placed around the phantom as described previously, and the phantom was centered axially in the CT gantry so that the tomographic slices would be in the middle of the field of view. The axis of the cylinder was aligned with the axis of the CT system, so that the tomographic slices would be circular cuts through the cylinder. CT slices were acquired using a typical pelvic technique of 140kVp, 120 mA and a 3 second scan time. CT data were acquired using a 256x256 image matrix size, and a slice thickness and spacing of 5 mm. Tomographic CT slices were reconstructed using the built-in reconstruction software and a 48 cm axial field of view.

Following CT imaging, we moved the imaging table so that the phantom could be imaged under the gamma camera. Images here were acquired using a 128x128 matrix, with 64 angular views. Energy windows were set at 7% around 140 keV for ^{99m}Tc, and 15% around 171 keV, 20% around 245 keV for ^{111}In. We used an acquisition time per view of 30 seconds and a circular orbit with a fixed radius of 23.5 cm.

e) Reconstruction and Image Analysis

Tomographic CT slices and raw SPECT projection data were transferred from the CT/SPECT system to a computer workstation for further analysis. SPECT projection data were reconstructed using an ML-EM reconstruction algorithm (without attenuation or collimator corrections) to determine the location of the fiducial markers on the SPECT images, and then the SPECT and CT images were registered to one another as described previously. The registered CT images were used to create attenuation maps for the ^{111}In and ^{99m}Tc photons, following the methodology detailed in Chapter 5. SPECT images were then reconstructed using 2 different versions of the iterative reconstruction algorithm: (1) attenuation correction but no collimator correction, and (2) attenuation and collimator and attenuation corrections. This allowed us to test the effects of including these corrections on the quantitative accuracy of the reconstruction. The convergence rate of the iterative reconstruction can vary with object size, especially when collimator corrections are used. In previous studies of this algorithm, the optimal number of reconstructions was found to be 30 for the reconstruction without collimator corrections and 100 for the reconstruction with collimator corrections. The number of iterations used for the reconstruction was therefore varied between 1 and 100, in order to measure the effect of the number of iterations, and to help choose an optimal value for use in the patient studies.

The CT images were thresholded to identify the target spheres, since they contained CT contrast material that gave them a Hounsfield Unit (HU) value approximately 200 HU greater than the water in the tank. This thresholding generated three regions of interest (one per sphere), and the volumes of these regions were

compared against the sphere volume as listed above in Table 6-I, to ensure that the thresholding produced an accurate assessment of the true sphere volume. These regions of interest were then transferred to the SPECT images, and a direct measurement of the activity concentration in the spheres was made by averaging over all the SPECT pixels within the regions of interest. This measurement was repeated for the different types of reconstructions and the different numbers of iterations. The calibration measurements discussed in a previous section of this chapter were used to scale the pixel values in the reconstructed images to true activity concentrations.

For template-projection measurements, the regions of interest corresponding to the spheres were transformed into templates with unit activity. We also drew background regions around each of the spheres, according to the minimum size criteria discussed previously. Thus, these background regions were cylindrical shells with an inner diameter equal to the size of the sphere and an outer diameter equal to the size of the sphere plus 1.6 mm. These were referred to as the 'small' background regions. A fourth background region was created that represented the entire tank except for the spheres and the plastic bar in the middle of the phantom – this was referred to as the 'large' background region. These regions are illustrated conceptually in Figure 6-4.

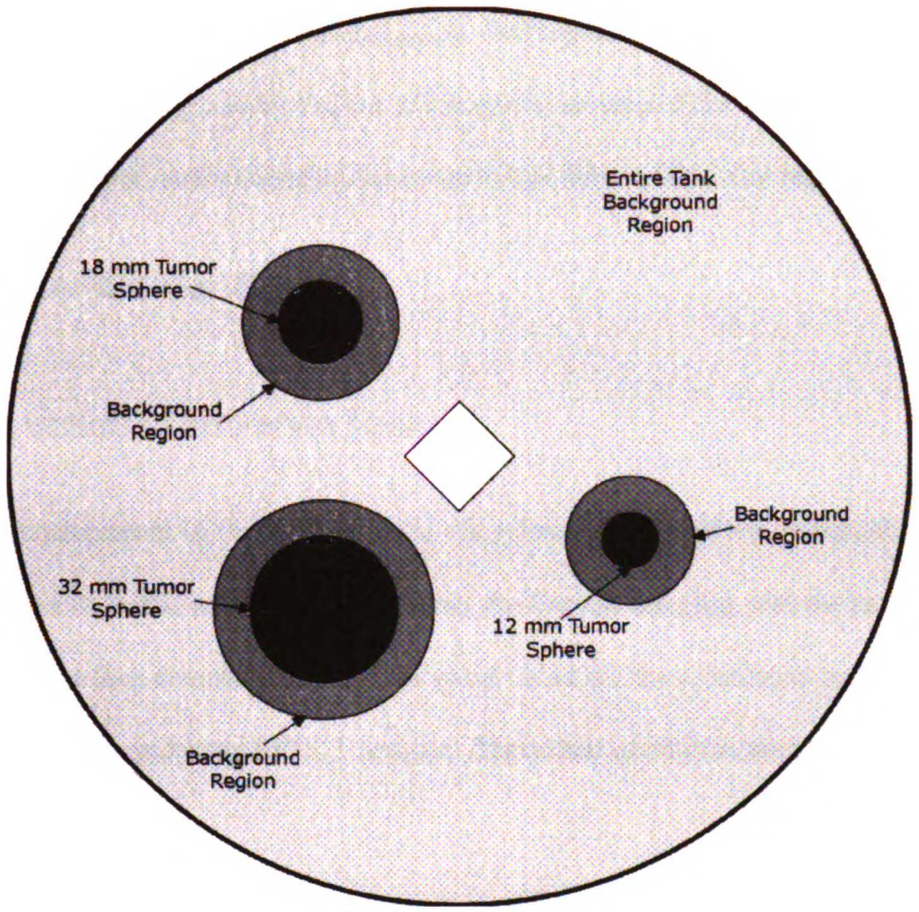


Figure 6-4: Illustration of background regions used for template-projection reconstruction. The background regions overlap, i.e. the background region representing the entire tank includes all the areas that are not tumor spheres or the plastic mounting bar along the axis of the phantom.

These regions were used to generate templates with unit activity. The templates were used to create simulated projection data that included attenuation and collimator blurring effects. The simulated projection data were then reconstructed using both filtered backprojection and an iterative reconstruction that only included attenuation correction. The actual SPECT projection data were reconstructed using the same methods. We then calculated the activity in the tumor spheres using Equation 6.4 and Equation 6.6, using both the small and the large background regions. For the minimization in Equation 6.4, we used a multiple least-squares linear regression (Excel, Microsoft, Redmond, WA) to

simultaneously solve for A_{tumor} and $A_{background}$. For Equation 6.6, we determined a value for $A_{background}$ by placing a cubic region of interest in an area of the tank separated from all of the target spheres, and measuring the mean voxel value within that region.

D. Experimental Results

1. Uniform Calibration Tank

For each measurement of the uniform tank, we calculated the activity concentration in the tank based on its initial activity concentration, the time of imaging, and the radioactive decay law. We then determined the mean voxel value for the cylindrical region of interest on the reconstructed SPECT images. These two quantities are plotted against one another in Figure 6-5.

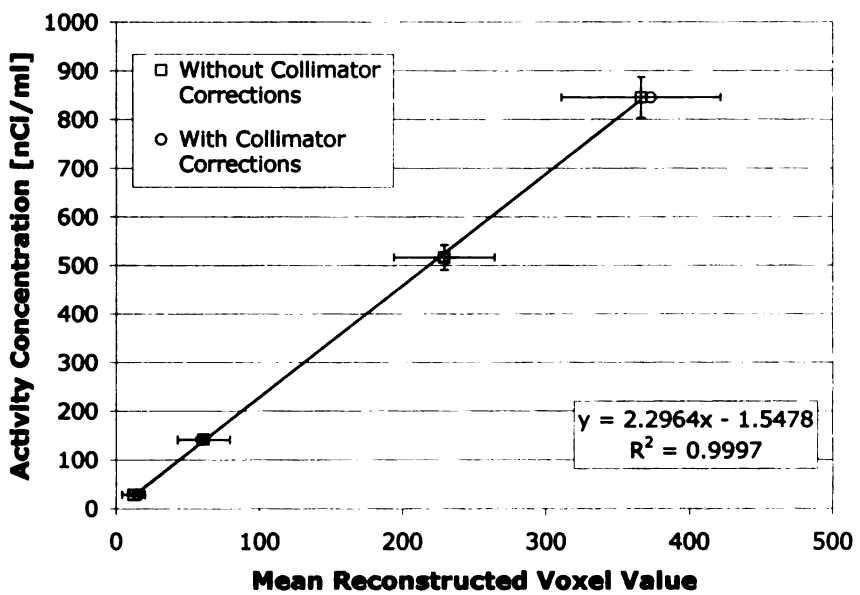


Figure 6-5: Reconstructed voxel values versus activity concentration for the uniform indium tank. Horizontal error bars represent one standard deviation around the mean voxel value, whereas vertical error bars represent the measurement error of the activity concentration in the uniform tank. We can use this graph to convert reconstructed voxel values to activity concentrations.

The inclusion of collimator corrections does not make a significant difference in the mean voxel value. This similarity is not surprising, though, because the uniform tank is essentially featureless and has no structures that would be blurred by the camera's distance dependent resolution except its edges (which are not included in the region of interest). We can also see that this calibration measurement is independent of the total activity in the tank, which means that this measurement should be valid over a wide range of activity concentrations. The linear fit through these points provides an equation that converts reconstructed counts to activity concentration in nCi/ml:

$$\text{Activity Concentration [nCi/ml]} = 2.2964(\text{Reconstructed Voxel Value}) - 1.5478. \quad (6.9)$$

2. ^{111}In-ProstaScint® Phantom

a) Measurement of target sphere volume by CT

The concentration of K_2HPO_4 within the target spheres should produce a CT value of approximately 200 HU. To determine the optimum threshold for identifying the target spheres, we varied the threshold value between 120 and 240 HU, and then measured the sphere volumes by counting the number of CT voxels that exceeded this threshold and multiplying by the voxel size. The spheres were separated by sufficient distance so that there was no overlap in the thresholded regions, so we were able to compute a volume for each individual target sphere. Figures 6-6 and 6-7 show the sphere volume calculated by CT as a function of the CT value threshold.

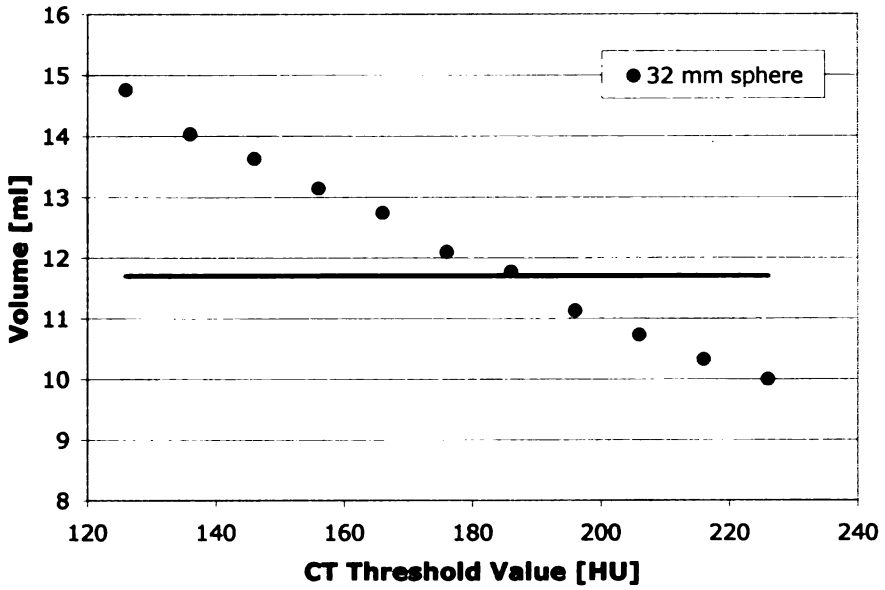


Figure 6-6: CT-measured target sphere volume (for the 32 mm sphere) as a function of the CT value threshold.

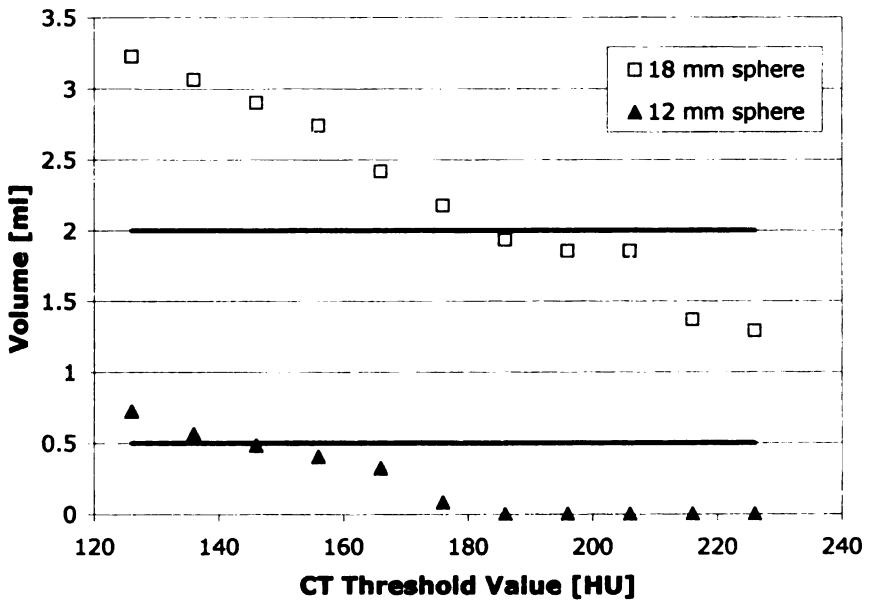


Figure 6-7: CT-measured target sphere volume (for the 18 and 12 mm spheres) as a function of the CT value threshold.

The dark horizontal lines on these plots represent the known sphere volume, which was measured by carefully filling and emptying each sphere, and is listed in Table 6-I. From these plots, we can see that a threshold value of 186 HU correctly identifies the sphere volume for the 32 mm sphere and the 18 mm sphere, whereas this threshold must be reduced to 146 HU in order to correctly identify the sphere volume of the 12 mm sphere. These results are an excellent illustration of the partial volume effect; even though the concentration of K_2HPO_4 is the same in all spheres, the 12 mm sphere has a lower CT value because of averaging with the surrounding materials. The thresholds determined by this analysis were used to define the regions of interest representing each sphere, and background regions were also defined on the CT image according to Figure 6-4, for the template-projection-reconstruction process.

b) Direct measurements from the reconstructed image

Using the calibration from Equation 6.9, we converted the voxel values in each reconstructed SPECT image into activity concentrations. Figures 6-8 and 6-9 show the results of these measurements as a function of the number of iterations for the iterative reconstruction with collimator corrections and without collimator corrections. The plotted values represent the average value obtained from the 5 separate scans of the ^{111}In-ProstaScint® phantom.

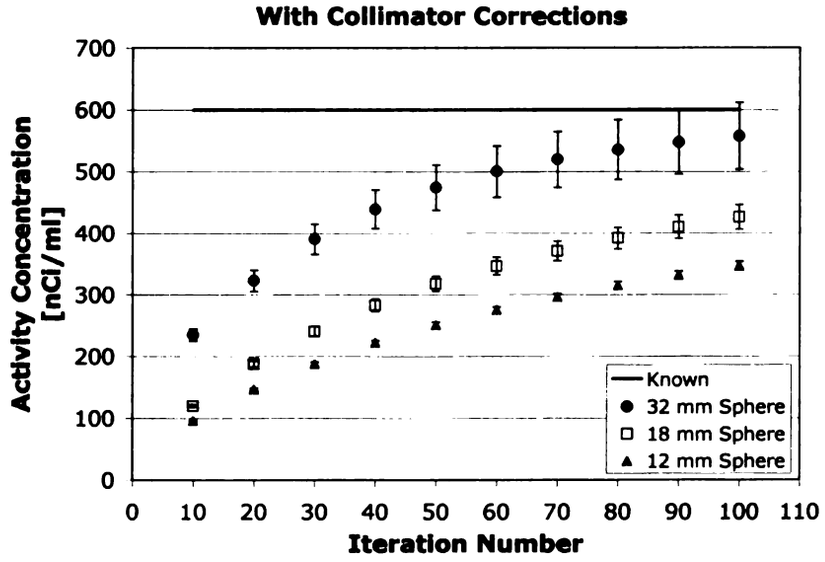


Figure 6-8: Direct measurement of the activity concentration in the tumor spheres, based on iterative reconstruction with attenuation correction and collimator corrections.

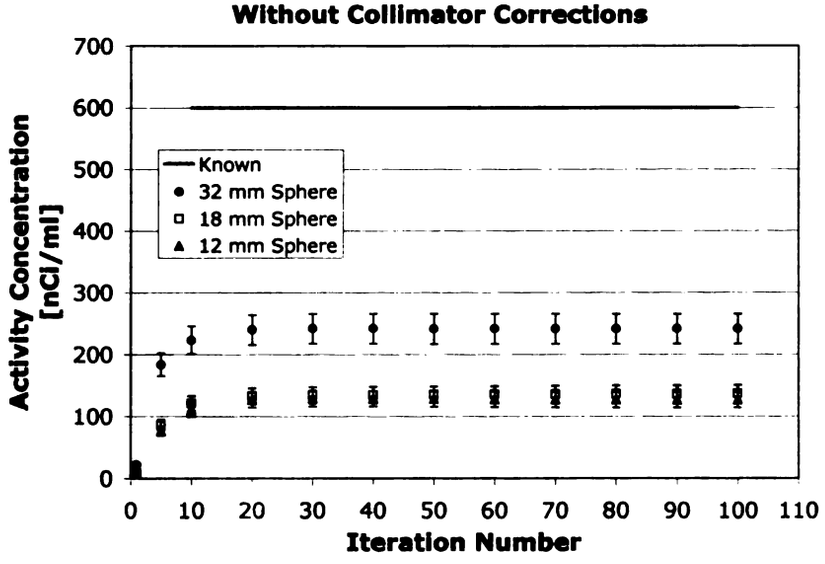


Figure 6-9: Direct measurement of the activity concentration in the tumor spheres, based on iterative reconstruction with attenuation correction, but without collimator corrections.

These graphs clearly show that if we are attempting to make direct measurements of the reconstructed SPECT image, it is crucial that we include attenuation and collimator effects. Without these corrections, the error in estimating the activity concentration is approximately 60% for the largest spheres and 75% for the smaller spheres. By including these effects in the reconstruction, we can lower this estimation error to 10% for the largest tumor sphere, and 30% and 40% for the smaller spheres. When we also consider that excluding attenuation correction underestimates the true activity by more than threefold (from Chapter 5), the argument for a reconstruction that includes collimator and attenuation corrections is even more compelling.

In terms of the optimum number of iterations needed to carry out this measurement, the iterative reconstruction with attenuation correction but without collimator corrections converges fairly quickly and seems stable after 30 iterations, which agrees with previous experiments by our research group. The iterative reconstruction with attenuation and collimator corrections converges more slowly, but the rate of change of this curve has dropped significantly by the time 100 iterations are complete. It is possible that some further improvement could occur with a much larger number of iterations, but this would require additional time for an already lengthy process, and would significantly increase the ringing artifacts that occur at object boundaries[13]. Therefore, we opted to continue to use 100 iterations as the endpoint for the iterative reconstruction with attenuation and collimator corrections.

c) Template-projection-reconstruction measurements

In the following table, we show the quantitation results from the different template-projection-reconstruction methods. The values in the table are activity concentrations in nCi/ml, averaged over the results from the 5 scans of the phantom. For comparison, the known activity concentration in the spheres is 600 nCi/ml.

Template-Projection-Reconstruction Results

	Filtered Backprojection				Iterative Reconstruction			
	Least-Squares Fitting		Voxel Scaling		Least-Squares Fitting		Voxel Scaling	
Sphere Size	Small Bkgrnd	Large Bkgrnd	Small Bkgrnd	Large Bkgrnd	Small Bkgrnd	Large Bkgrnd	Small Bkgrnd	Large Bkgrnd
32 mm	662	751	621	621	659	675	689	682
18 mm	1031	1174	931	931	803	1546	959	948
12 mm	1699	1068	1818	1817	1155	2873	3152	2885

Table 6-II: Template-projection-reconstruction measurements for the ^{111}In-ProstaScint®-simulating phantom.

As we would expect, the most accurate quantitation is obtained for the 32 mm sphere, and the template-projection-reconstruction technique provides excellent quantitative results in this case, even when using filtered backprojection for the reconstruction. The results for the 18 mm and 12 mm spheres are somewhat discouraging – on average, the error in estimating the activity concentration in these spheres is 70% for the 18 mm sphere and 230% for the 12 mm sphere. In these spheres, the choice of the background region also seems to have a larger effect on the resulting activity concentration in the sphere. This is probably due to the fact that the smaller spheres have a greater fraction of their voxels adjacent to the background than the large spheres. Although we would certainly like to have better quantitation, part of the goal of these experiments was to

determine the quantitative abilities of this system, so it is important to understand the limitations as well as the benefits of these approaches.

In terms of evaluating the technique itself, the voxel scaling method seems to produce more precise estimates of the activity concentration than the least-squares fitting method. This effect is probably due to statistical noise in the image. The voxel scaling method takes an average voxel value when computing the activity in the background and also averages over the voxel values in the object to compute an activity within the target sphere. By contrast, the least-squares fitting method attempts to minimize differences in many voxels simultaneously, so random variations in the voxel values will affect this method more strongly. For the reconstruction method, filtered backprojection seems to produce slightly better results than iterative reconstruction, which probably results from the fact that the iterative reconstruction is only approximately linear, whereas filtered backprojection is linear. Since this process assumes that the imaging and reconstruction processes are linear, it is not surprising that filtered backprojection produces somewhat better results.

E. Discussion

The radionuclide quantitation technique discussed in this chapter requires several steps so that radioactivity concentrations in units of nCi/ml can be measured accurately from SPECT images. The first step involves acquiring and reconstructing images of a uniform calibration tank containing a known radionuclide concentration. Reconstructed voxel values from the uniform calibration tank provide a means of calibrating the CT/SPECT system for a particular imaging task, without requiring a change in the software for the reconstruction algorithm. Although this particular project is concerned with imaging

^{111}In-ProstaScint®, the CT/SPECT system has been used for other tasks such as myocardial perfusion imaging with ^{99m}Tc-sestamibi and radiation dosimetry with ^{131}I-mIBG (meta-iodobenzylguanidine), and different future applications are certainly possible. Creating a new reconstruction algorithm for each of these applications is unnecessarily complicated, and from a programming standpoint it makes improvements difficult and increases the potential for errors. The calibration method described in this dissertation allows us to insulate the reconstruction algorithm from the particular details of the imaging system, but still provide quantitative accuracy through a calibration measurement.

A different calibration strategy might be to make sensitivity measurements of a point source, in order to calibrate the counts in the projection data against known quantities of activity, which would potentially simplify the calibration measurement by avoiding the preparation of a uniform tank having a known concentration of the radionuclide. However, the use of the uniform tank has a key advantage over a point-source based approach in terms of accounting for photon scatter. A uniform point source will not generate scatter radiation at the detector, except for a small amount from the primary photons interacting with the lead collimator. However, the uniform tank provides a large volume of material for photon scattering, and so when we make a calibration measurement of the tank, the counts recorded by the detector reflect this effect. This is probably why this study and others from our group were able to successfully quantify activity concentrations (for larger objects) without explicitly correcting for scatter in either the reconstruction or the 'projector' used to generate template projections.

The fact that we can accurately quantify the activity concentration in the largest sphere in this study is encouraging and agrees with the results from previous quantitation experiments by our research group. The normal human prostate has only a slightly smaller volume than this sphere, so we should be able to apply either quantitation technique to measure the uptake of ^{111}In-ProstaScint® within the prostate. The choice of the specific quantification algorithm will be based solely on ease of implementation and whether or not the basic criteria of the template-projection-reconstruction method (uniform activity within well-defined boundaries) are satisfied. Similarly, we should be able to measure ^{111}In-ProstaScint® uptake in the large intestine or liver with high accuracy as well. Quantifying ^{111}In-ProstaScint® uptake in a suspicious lymph node will be more problematic, because these nodes are typically only a few millimeters in size, except in cases of significant lymphadenopathy. For objects of this size, we can probably only compare their relative uptake against some other small structure in the body, or compare similar-sized objects among different patients. However, even in this case we will benefit from the improved reconstruction, because correcting for attenuation and collimator effects always increases the accuracy of the reconstructed image.

One unexpected result from this study was that the template-projection-reconstruction method tended to overestimate the activity concentration. In previous studies using ^{99m}Tc, this technique usually underestimated the activity concentration, even in cases where the quantitation error was small. For ^{99m}Tc, scattered photons will have little chance of being detected again due to the energy discrimination of the camera, so scatter will deplete the number of counts in the projection data. However, 245 keV photons from ^{111}In could potentially scatter down into the energy window centered at 171

keV, so in this case scatter might increase the number of counts in the projection data. Future studies using simulations to explicitly model the scattered radiation could help to shed light on this question.

Although quantitation can potentially be a useful adjunct to the radiological interpretation of ^{111}In-ProstaScint® images, it does have some important potential limitations. Each individual has a different physiology, which will affect the rate at which ^{111}In-ProstaScint® is cleared from the bloodstream and transported into potential target areas. Other areas of variation between patients include the local circulation in an organ or tumor and the proximity of PSMA-expressing cells to the capillaries. Thus, even though we can accurately and precisely measure the concentration of ^{111}In-ProstaScint® in larger objects, the measurement is still affected by factors other than the density of PSMA on the cells. In the following chapter, we will examine this issue more closely by examining ^{111}In-ProstaScint® uptake in clinical patients, and relating that uptake to other methods of prostate cancer staging.

F. Summary

Quantitative SPECT imaging can provide potentially valuable information about a patient's condition, by relating image voxel values to absolute measures of activity concentration (nCi/ml) that cannot be obtained from visual interpretation of the image data alone. In this chapter, we have covered two different methods for quantitative SPECT imaging, both of which depend on combined CT and SPECT imaging to provide high resolution anatomic detail and information about photon attenuation. In the 'direct measurement' method, we use an iterative SPECT reconstruction such as the one outlined in Chapter 5 to produce a SPECT image where the voxel values closely correspond to the

true activity distribution in the object. The CT image is used to define a region of interest, which is then transferred to the SPECT image, and the voxel values are simply read out from the region. In the 'template-projection-reconstruction' method, we use the CT image to define templates, which are regions of uniform activity. These templates are used to create simulated SPECT projection data. The simulated and the actual SPECT projection data then are reconstructed using the same algorithm, and the images are compared by voxel scaling or by least-squares fitting to estimate the true activity concentration within the templates. All of these approaches should be capable of providing accurate measurements of ^{111}In-ProstaScint® uptake in the prostate and other organs, although absolute quantitation in smaller structures such as lymph nodes is not currently feasible. In the following chapter, we will apply these quantitation techniques to patient studies with ^{111}In-ProstaScint®, to determine if this type of information can help to provide staging information for these patients, and thereby help to guide their therapy.

References:

[1] S. D. Sweat, A. Pacelli, G. P. Murphy, and D. G. Bostwick, "Prostate-specific membrane antigen expression is greatest in prostate adenocarcinoma and lymph node metastases," *Urology*, vol. 52, pp. 637-40, 1998.

[2] A. A. Elgamal, E. H. Holmes, S. L. Su, W. T. Tino, S. J. Simmons, M. Peterson, T. G. Greene, A. L. Boynton, and G. P. Murphy, "Prostate-specific membrane antigen (PSMA): current benefits and future value," *Seminars in Surgical Oncology*, vol. 18, pp. 10-6, 2000.

[3] D. B. Sodee, R. J. Ellis, M. A. Samuels, J. P. Spirnak, W. F. Poole, C. Riester, D. M. Martanovic, R. Stonecipher, and E. M. Bellon, "Prostate cancer and prostate bed SPECT imaging with ProstaScint: semiquantitative correlation with prostatic biopsy results," *Prostate*, vol. 37, pp. 140-8, 1998.

[4] W. A. Weber, M. Schwaiger, and N. Avril, "Quantitative assessment of tumor metabolism using FDG-PET imaging," *Nucl Med Biol*, vol. 27, pp. 683-7., 2000.

[5] S. N. Yang, J. A. Liang, F. J. Lin, A. S. Kwan, C. H. Kao, and Y. Y. Shen, "Differentiating benign and malignant pulmonary lesions with FDG-PET," *Anticancer Res*, vol. 21, pp. 4153-7., 2001.

[6] B. L. Shulkin, J. C. Sisson, K. F. Koral, B. Shapiro, X. H. Wang, and J. Johnson, "Conjugate view gamma camera method for estimating tumor uptake of iodine-131 metaiodobenzylguanidine," *J Nucl Med*, vol. 29, pp. 542-8., 1988.

[7] P. Almeida, M. J. Ribeiro, M. Bottlaender, C. Loc'h, O. Langer, D. Strul, P. Hugonnard, P. Grangeat, B. Maziere, and B. Bendriem, "Absolute quantitation of iodine-123 epidepride kinetics using single- photon emission tomography: comparison with carbon-11 epidepride and positron emission tomography," *Eur J Nucl Med*, vol. 26, pp. 1580-8., 1999.

[8] J. Maddahi and J. Czernin, "Absolute quantitation of myocardial blood flow: the technical and clinical prospects for single-photon emission computed tomography," *J Nucl Cardiol*, vol. 3, pp. S60-5., 1996.

[9] P. B. Zanzonico, R. E. Bigler, G. Sgouros, and A. Strauss, "Quantitative SPECT in radiation dosimetry," *Semin Nucl Med*, vol. 19, pp. 47-61., 1989.

[10] G. L. DeNardo, D. J. Macey, S. J. DeNardo, C. G. Zhang, and T. R. Custer, "Quantitative SPECT of uptake of monoclonal antibodies," *Semin Nucl Med*, vol. 19, pp. 22-32., 1989.

[11] K. F. Koral, K. R. Zasadny, M. L. Kessler, J. Q. Luo, S. F. Buchbinder, M. S. Kaminski, I. Francis, and R. L. Wahl, "CT-SPECT fusion plus conjugate views for determining dosimetry in iodine-131-monoclonal antibody therapy of lymphoma patients," *J Nucl Med*, vol. 35, pp. 1714-20., 1994.

[12] R. M. Kessler, J. R. Ellis, and M. Eden, "Analysis of emission tomographic scan data: Limitations imposed by resolution and background," *Journal of Computer Assisted Tomography*, vol. 8, pp. 514-522, 1984.

[13] H. R. Tang, "A Combined X-ray CT-Scintillation Camera System for Measuring Radionuclide Uptake in Tumors," Bioengineering Ph.D. Dissertation, University of California Berkeley and University of California San Francisco, 1998, pp. 171.

[14] A. R. Formiconi, "Least squares algorithm for region-of-interest evaluation in emission tomography," *IEEE Transactions on Medical Imaging*, vol. 12, pp. 90-100, 1993.

[15] A. Liu, L. E. Williams, and A. A. Raubitschek, "A CT assisted method for absolute quantitation of internal radioactivity," *Medical Physics*, vol. 23, pp. 1919-28, 1996.

[16] A. J. Da Silva, H. R. Tang, K. H. Wong, M. C. Wu, M. W. Dae, and B. H. Hasegawa, "Absolute quantification of regional myocardial uptake of 99mTc-sestamibi with SPECT: experimental validation in a porcine model. [Comment In: J Nucl Med. 2001 May;42(5):780-1 UI: 21235439]," *Journal of Nuclear Medicine*, vol. 42, pp. 772-9, 2001.

[17] D. B. Sodee, "ProstaScint Users Group Meeting," presented at Society of Nuclear Medicine Annual Meeting, St. Louis, MO, 2000.

Chapter 7: ^{111}In-ProstaScint® Patient Studies with the CT/SPECT System

A. Introduction and Motivations

1. Prostate cancer staging and ^{111}In-ProstaScint®.

As we discussed in Chapter 1, the proper staging of prostate cancer is essential for determining a patient's course of therapy. Patients with localized prostate cancer potentially can be cured of their disease through a local therapy such as prostatectomy or radiation therapy. However, patients with regional tissue invasion or metastatic disease will need a more comprehensive and systemic therapy, which may include hormone therapy or chemotherapy in addition to surgical or radiation treatments. Thus, a correct assessment of the extent of the prostate cancer is a key prerequisite for optimal treatment.

^{111}In-ProstaScint® has several characteristics that provide unique and valuable information regarding prostate cancer staging. First, since it is a radiological technique, it can noninvasively evaluate the prostate and a large region of the body for disease in a single scan. This gives it an advantage over tissue sampling techniques, which are limited to those regions of the body that can be easily accessed through surgical procedures. Second, it provides patient-specific information, as opposed to the generalized risk assessment of empirical staging methods such as the Partin tables. Third, the high sensitivity of nuclear medicine techniques makes it possible to detect ^{111}In-ProstaScint® in very small amounts, so this scan theoretically can detect the presence of prostate cancer cells in a lymph node long before the cancer creates

morphological changes visible with anatomical imaging such as CT and MRI. Finally, because ^{111}In-ProstaScint® is based on an antibody to the prostate-specific membrane antigen (PSMA), it provides biochemical information about the patient's condition.

However, despite the potential benefits of ^{111}In-ProstaScint®, it suffers from the same limitations as many other antibody-based nuclear medicine studies. The images generated by a typical ^{111}In-ProstaScint® SPECT scan are noisy, count-starved, have poor spatial resolution, and are not quantitatively accurate. To make matters worse, these images have little structural or anatomical detail, and there is significant non-specific uptake of ^{111}In-ProstaScint® in the bowel, vasculature, bone marrow, and liver. Although a ^{99m}Tc-labeled red blood cell scan is usually acquired simultaneously with the ^{111}In-ProstaScint® scan to outline the vasculature, the blood pool image provides only very limited anatomical information. For these reasons, ^{111}In-ProstaScint® images are very challenging to interpret, and often produce ambiguous results.

Combined CT/SPECT provides a means to overcome many of the limitations associated with current ^{111}In-ProstaScint® SPECT imaging. A coregistered CT scan provides high-resolution structural imaging, so that the functional information from the ^{111}In-ProstaScint® can be easily referenced to anatomical features. For example, a 'hotspot' on the ^{111}In-ProstaScint® scan can be compared with regional anatomy to determine whether it corresponds to nonspecific uptake in the bowel or uptake in a lymph node. The information from the CT scan also provides a means of compensating for physical effects that degrade the SPECT image, such as photon attenuation, photon scattering, and collimator blurring. By incorporating these effects into a mathematical model of the imaging process, we can use an iterative reconstruction to dramatically

improve the quality and quantitative accuracy of the tomographic images. The CT information also enables new approaches to quantitation such as the template-projection-reconstruction method discussed in the previous chapter. There still are some fundamental limitations to the ^{111}In-ProstaScint® imaging process, (i.e., one cannot inject the patient with an arbitrarily large dose of radiotracer to reduce the noise). Nevertheless, CT/SPECT has the potential to dramatically improve ^{111}In-ProstaScint® imaging, which will allow this unique staging test to achieve its full potential.

2. Review of Research Goals

In this final stage of the project, the research shifted focus from the technical preparation and evaluation of the CT/SPECT system to a more clinical evaluation. At the core of our inquiry was this fundamental question: would the additional information obtained from CT/SPECT affect the interpretation of ^{111}In-ProstaScint® images, and, if so, would it improve the staging abilities of this particular prostate cancer test? To answer this question, we divided our efforts into two areas.

a) Radiologic Interpretation

The techniques introduced in Chapters 4 and 5 allow us to improve the quality of the SPECT image and precisely register the SPECT image to a CT image, which should make the interpretation of ^{111}In-ProstaScint® scans more straightforward. To test this hypothesis, we presented the CT/SPECT images to expert nuclear medicine physicians, and asked them to assess these images with respect to the typical criteria for ^{111}In-ProstaScint® (e.g. is disease present outside of the prostate?). We compared these results to the standard ^{111}In-ProstaScint® imaging report generated by the UCSF nuclear

medicine clinic, to determine the difference, if any, between the two imaging techniques. We also asked the physicians to qualitatively evaluate the images from the CT/SPECT system (in terms of general properties such as noise and sharpness), in order to ascertain which characteristics of these images were the most useful to them.

b) Quantitative Assessment

CT/SPECT imaging allows us to reconstruct tomographic SPECT images that are more quantitatively accurate than conventional SPECT images. It also enables novel quantitative methods (based on CT-defined regions of interest) for measuring the radionuclide concentration in a specific organ or tissue, so long as these regions are similar in size to the large target sphere described in the previous chapter. We used these quantitation techniques to measure the level of ^{111}In-ProstaScint® uptake in the prostate, surrounding tissues, vasculature, and distant organs. Although some of the regions (bone marrow, vasculature) were too small for truly accurate quantitation, the measurement could still be used as a relative means of comparing the patients to each other. We finally attempted to correlate these quantitative results with other clinical data about these patients to determine whether or not this analysis provided extra information that could alter, and hopefully improve, the staging of these patients.

B. Experimental Methods

1. Overview

A clinical study such as this one is complex and contains many interlocking components that influence its outcome. In reviewing the methods for this study, we will first describe

the patient population used for these experiments, including selection criteria and general demographics. Then, we will describe the imaging protocol used to generate both the conventional ^{111}In-ProstaScint® SPECT images and the CT/SPECT ^{111}In-ProstaScint® images, including image acquisition, reconstruction, and viewing/interpreting parameters. Finally, we will review the application of quantitative imaging methods to the CT/SPECT ^{111}In-ProstaScint® studies, and how we chose methods suitable for each quantitation task.

2. Patient Recruitment and Selection

The UCSF Committee on Human Research initially approved this research protocol, and provided annual review of its progress and compliance with federal and institutional regulations. All research volunteers were recruited from patients who had been referred by their primary care physician to the UCSF Nuclear Medicine Clinic for ^{111}In-ProstaScint® imaging, and thus were at increased risk for pelvic lymph node involvement. For newly diagnosed patients with no treatment history, this criterion meant that they met at least one of the following conditions:

Clinical Indications for ^{111}In-ProstaScint® Imaging

PSA > 10 times upper normal limit and Gleason score > 7
Gleason score > 8
Stage C or T3 disease and Gleason score > 5 or 6
Equivocal evidence of extraprostatic disease on CT or ultrasound and PSA > 8 times upper normal limit
Prostatic acid phosphatase (PAP) level above upper normal limit

Table 7-I: Indicators for ^{111}In-ProstaScint® scanning for newly diagnosed prostate cancer patients[1].

Volunteers were also recruited from patients who had undergone definitive treatment (usually radical prostatectomy, but radiotherapy also qualified) but who had elevated PSA levels (PSA > 4.0 ng/ml) with negative or equivocal results for recurrent disease.

Given that this study was directed at improved diagnosis of prostate cancer, only men were enrolled in this study. Special populations of patients (minors, those unable to consent for themselves, or any patient unable to give free and informed consent) were excluded. Patients over 350 pounds were excluded, because it would not be possible to image them in the CT/SPECT system. Allergies to shellfish or iodine, or previous allergic reactions to radiographic contrast media were also exclusion factors. Subjects were not excluded based on racial, ethnic, social, economic or linguistic status.

For recruitment, patients were approached by a member of the research group before their ^{111}In-ProstaScint® injection. The goals and procedures involved in the research study were explained to them, and they were invited to participate in the research protocol. Following institutional and ethical guidelines, we ensured that they knew that participation in research was voluntary and would have no bearing on their treatment within the UCSF hospital. Patients who declined to participate in the study received the standard ^{111}In-ProstaScint® scan from the Nuclear Medicine Clinic. Patients who opted to participate in the research protocol received both the standard ^{111}In-ProstaScint® scan and the CT/SPECT scan. Approximately 35% of the recruited patients agreed to participate in the research study. There was no additional cost to the patient for the CT/SPECT scan, and transportation expenses to the laboratory site were reimbursed.

The patients enrolled in this pilot study had a fairly wide range of disease states and histories. Given that the total population of patients referred for ^{111}In-ProstaScint® scanning is small (approximately 1-2/month), we did not attempt to select out specific subgroups of patients based on their treatment status or other medical history data. Most

patients lived in the Northern California region. Further demographic information about these patients is given below in Table 7-II.

Research Patient Demographics

Total Patients	13
Newly diagnosed patients	8
Patients with treatment history	5
Patient Ethnic Background	
Caucasian	11
African-American	2
PSA Range	1.4 - 46.2
Gleason Sum Range	4 – 9

Table 7-II: Research patient demographics.

3. Imaging Protocol

a) Protocol for Standard SPECT Imaging

Patients who participated in the research project first received conventional ^{111}In-ProstaScint® SPECT imaging at the UCSF Nuclear Medicine Clinic. This procedure began with the intravenous injection of approximately 5 mCi (the exact activity varied, but was carefully measured and recorded for each patient) of ^{111}In-ProstaScint®. Following the injection, the patient went home and carried on their normal activities. During the days after the injection, patients were asked to adhere to dietary restrictions that limited their intake of fat, carbohydrates, and other foods that might cause constipation. On the third day after the injection, patients were asked to consume only clear soups or other liquid foods such as Jell-O, and to ingest a standard dose of magnesium citrate laxative. These directions were designed to maximize clearance of non-specifically bound ^{111}In-ProstaScint® from the bowel, since ^{111}In-ProstaScint® in the

bowel can potentially complicate interpretation of the images. On the morning of the fourth day after injection, the patients self-administered a Fleet enema and returned to the Nuclear Medicine Clinic for imaging.

At the Nuclear Medicine Clinic, approximately 3 cc of the patient's blood was drawn. Anterior and posterior whole-body planar images or static planar spot images were then acquired to assess the general distribution of the ^{111}In-ProstaScint®. During this time, the red blood cells were labeled with 3-5 mCi of ^{99m}Tc using UltraTag (Mallinckrodt, St. Louis, MO) or an equivalent kit synthesized in-house. Once the planar images were complete, the labeled cells were reinjected into the patient. SPECT projection data were then acquired around the pelvis and abdomen of the patient to provide a three-dimensional map of uptake in these regions. Images were typically acquired using a 128x128 matrix, although some studies were acquired using a 64x64 matrix (this discrepancy was due primarily to differences in the camera or the technologist acquiring the study). The SPECT images had two windows: one for the ^{99m}Tc-labeled red blood cells (RBCs) and one for the ^{111}In-ProstaScint®. The energy window setting for ^{99m}Tc was 7% width at 140 keV, and for ^{111}In a combined window was used, with 15% width at 171 keV and 20% width at 245 keV. The time per view was 60 seconds, and 64 views were acquired in a circular orbit around the patient. The total imaging time was between 2.5 and 3 hours.

b) Protocol for Research CT/SPECT Study

Following their imaging at the Nuclear Medicine Clinic, patients traveled to the UCSF Physics Research Laboratory, approximately 12 miles from the hospital, for combined CT/SPECT imaging. This trip usually took about 30 minutes. Once the patient arrived at

the Laboratory, they were given a chance to rest and ask any questions about the imaging study. They were also given a final opportunity to decline the research scan if they so chose.

Imaging was first done using the CT portion of the system. The patient was placed on the table so that the pelvis was aligned with the axis of the table and centered from right to left and top to bottom within the scanning region. Pillows and closed-cell foam mattresses were used to allow them to remain as comfortable as possible during the imaging session. Fiducial markers were prepared and spaced around the pelvis to provide adequate coverage of this region, as described in Chapter 4. A scout CT image was acquired with the x-ray tube in a fixed anterior-posterior position, so that the anatomy of the region could be visualized. Using this scout image, the CT acquisition was set up so that it would cover a region at least 40 cm long, which extended from 4-5 cm below the pubic symphysis to roughly the middle of the liver. The most critical factor here was to ensure that the CT data fully enveloped the region that would be viewed during the SPECT acquisition. CT slices were then acquired using a standard pelvic technique of 140 kVp, 120 mA, and a 3 second scan time. For the first few patient studies, we used a 10 mm slice thickness and spacing to minimize the imaging time, but the poor registration results (discussed in Chapter 4) necessitated a change to 5 mm slice thickness and spacing. Reconstruction was done using the CT system's standard reconstruction filters, a 256x256 image matrix, and a 48 cm field of view. Patients were asked to breathe gently during the acquisition of the CT data, but no attempt was made to have the patients hold their breath during the scan. Respiratory motion in the pelvis and lower abdomen is minimal, so breath-holding would have been an unnecessary complication to

the protocol. CT scanning typically required 20-30 seconds to acquire and reconstruct each slice, so this portion of the exam required 35-45 minutes. CT contrast media was not used during the study.

Once the CT examination was complete, the patient table was translated forward so that the patient would lie within the orbit of the gamma camera. The camera was positioned so that the penile blood pool (which lies inferior to the prostate) was clearly visible in the lower portion of the image, and so that the inferior surface of the liver could be seen at the top of the image. The image was also checked to make sure that the fiducial markers were visible. Once the camera orbit was simulated to ensure that the camera would not collide with the patient or the table, the SPECT acquisition began. This scan used a 128x128 matrix, 64 views, and 60 seconds per view. The ^{99m}Tc-labeled RBCs and ^{111}In-ProstaScint® were imaged simultaneously using the energy windows available on the gamma camera. For ^{99m}Tc, a 7% window around 140 keV was defined. For ^{111}In, a merged window was used, which combined counts from a 15% window at 171 keV and a 20% window at 245 keV. The positioning of the energy windows was always verified manually to be certain that the camera energy resolution had not drifted out of range. This portion of the exam took roughly 70 minutes once the SPECT acquisition began, for a total imaging time of about 2 hours. Static planar images were not acquired.

Most patients tolerated this imaging procedure well, although a few complained of excessive fatigue and muscle soreness towards the end of the research study. Given the length of the study, this comment was not surprising, and discussions with other ^{111}In-ProstaScint® users indicated that such complaints were not uncommon, even for

conventional ^{111}In-ProstaScint® SPECT examinations. Making the study shorter would certainly help to ameliorate this problem, but the long imaging times are necessary to ensure that an adequate number of photons can be collected by the gamma camera. Furthermore, our SPECT system has only one detector and our CT scanner is limited to single-slice operation, both of which added to the overall length of the study. Future studies with helical, multislice CT scanners and multiple-head gamma cameras would be able to complete this imaging protocol in much less time.

4. Image Reconstruction and Analysis

a) Image Processing for Conventional SPECT

Image data acquired at the UCSF Nuclear Medicine Clinic was processed and displayed on workstations following the standard department protocol for ^{111}In-ProstaScint® imaging. This processing used an iterative reconstruction algorithm, although this algorithm did not include corrections for attenuation or collimator blurring. SPECT images were evaluated by displaying the labeled red blood cell images in conjunction with the ^{111}In-ProstaScint® images, so that the image slices were matched exactly in the coronal, sagittal, and transaxial planes. Whole body and static planar images were also available for review. The physician examined these images for areas of abnormal uptake and generated a report on the basis of their findings.

b) CT/SPECT Image Processing

SPECT projection data initially were reconstructed using an iterative reconstruction algorithm that did not include attenuation or collimator corrections. This provided

tomographic SPECT slices where the fiducial markers could be visualized. Using techniques previously described, the CT slices were registered to the SPECT slices, and attenuation maps of the patient were generated for ^{99m}Tc and ^{111}In photons. The SPECT projection data then were reconstructed using an iterative reconstruction algorithm under 3 different conditions: (1) corrections for collimator blurring and attenuation, (2) correction for collimator blurring only, and (3) correction for attenuation only. We used 30 iterations when collimator correction was not applied, and 100 iterations when collimator correction was applied. For comparison, we also reconstructed SPECT slices using filtered backprojection. Once the reconstructions were completed, the finished SPECT images were mapped onto the 256x256 CT images, and images of the SPECT data overlaid onto the CT data were filmed (examples will be shown in subsequent sections). The CT images from the CT/SPECT system were also reconstructed and filmed using a 512x512 image matrix size to produce plain CT films.

For softcopy display, the 256x256 CT images and registered tomographic SPECT images could be displayed side by side or as overlays, where the SPECT images appeared as a color map on the CT image. In this format, only axial views were available. The images were also downsampled to a 128x128 image matrix size and translated into a format that could be read by the standard nuclear medicine display workstation. On this workstation, images could be displayed in sagittal, coronal, or axial views. This workstation could display coregistered images in a side-by-side format, but could not generate overlay images.

These images then were evaluated by a nuclear medicine physician. The physician had access to the images in both softcopy and hardcopy forms, and was asked

to assess the images in terms of quality, noise, sharpness, and the accuracy of the registration. They were also asked to compare the effects of the different types of reconstructions, in order to determine which corrections were most useful for image interpretation. Finally, they were asked to evaluate the CT/SPECT study (using the SPECT images reconstructed with both attenuation and collimator corrections) according to the standard ^{111}In-ProstaScint® criteria, and a staging report was generated from this information. According to institutional research guidelines for clinical trials, this information was made available to the patient's primary care physician (with appropriate caveats for its status as an experimental procedure), but did not become part of the patient's medical record. This CT/SPECT staging report then was compared with the standard ^{111}In-ProstaScint® report to determine any differences between the two. It should be noted that these studies were not carried out in a 'blind' fashion, because it is obvious which images are from the CT/SPECT system and which images are not. However, image interpretation from the conventional and experimental techniques usually was conducted during separate sessions and on separate workstations, in order to minimize the potential for observer bias.

5. Quantitative Measurements

a) Overview

The quantitative image analysis had two specific aims. The first was to quantitatively evaluate the uptake of ^{111}In-ProstaScint® in potential tumor areas, such as the prostate, prostate bed, and lymph nodes. This information could potentially be used to 'grade' these tumor locations, and assess the patient's condition independently of the image

interpretation. The second was to quantitatively measure uptake in regions that are considered to be background, such as the muscle, vasculature, bone marrow, and bowel. Since there is significant nonspecific uptake of ^{111}In-ProstaScint®, the ability to discriminate tumor uptake from other sites on the basis of a quantitative number would be valuable. Furthermore, if tumor sites have a consistently higher concentration of ^{111}In-ProstaScint® than other sites, it might be possible to develop a 'voxel-searching' technique that could evaluate the ^{111}In-ProstaScint® image and flag suspicious regions for further review.

b) Non-ROI-based measurements

We first measured the total counts in the ^{111}In-ProstaScint® images, and normalized them against the injected amount of each radiotracer and the time between injection and imaging. This provided a qualitative estimate of the underlying patient-to-patient variability, in terms of how rapidly the tracer was cleared from the body and excreted, and how much tracer remained in the body and could potentially be available for binding at the tumor sites. We also evaluated the entire ^{111}In-ProstaScint® SPECT image to find the maximum voxel value in the image, and recorded the anatomical structures closest to these voxels, to see if there was any overall consistency in the location of the highest concentrations of ^{111}In-ProstaScint®.

c) Template-projection-reconstruction measurements

Template-projection-reconstruction (described in the previous chapter) is a radionuclide quantitation technique that depends strongly on the identification of distinct anatomical regions of interest, and so is probably most appropriate for measuring uptake

within the prostate itself or the prostate bed. For these measurements, we defined a 'tumor' template that covered the prostate. Background templates were also drawn in the surrounding anatomy to delineate other structures close to the prostate, which were typically bone or surrounding muscle tissue. An example of these templates is illustrated in Figure 7-1.



Figure 7-1: Example of templates used to measure the concentration of ^{111}In-ProstaScint® within the prostate. The regions outlined are the prostate (red), surrounding muscular tissue (green) and pubic symphysis (yellow).

These templates were converted into regions of interest in the SPECT coordinate system, and simulated projection data were generated using a 'projector' that modeled the effects of collimator blurring and attenuation, as described in Chapter 6. The projected templates and actual SPECT projection data were both reconstructed using filtered backprojection, and the least-squares fitting method of Equation 6.4 was used to measure the concentration of ^{111}In-ProstaScint® in the prostate or prostate bed.

d) Direct measurements from the reconstructed SPECT image

For the 'direct method', we used the SPECT images that had been reconstructed with 100 iterations of the reconstruction algorithm including collimator and attenuation

corrections. Using the CT images, we drew regions of interest around or in several anatomical structures. These regions were then transferred to the SPECT images, and we measured the mean voxel values within each region. Calibration measurements, as described in the previous chapter, were used to scale the reconstructed voxel values to actual activity concentrations in nCi/ml. Although many of the regions were smaller than the 32 mm sphere discussed in Chapter 5, we endeavored to make the regions as similar as possible between patients, to facilitate inter-patient comparison even if the absolute measure of activity was underestimated. The specific regions were identified and chosen as described below.

Region 1: Descending aorta. The descending aorta is a major blood vessel that passes through the region typically imaged in an ^{111}In-ProstaScint® scan. It can be a good measure of the vascular activity, because it has a fairly consistent size and a bifurcation that makes it easy to identify a particular location along the vessel. Regions of interest (ROIs) were drawn over the region of the descending aorta immediately superior to the bifurcation. These regions extended through 5-6 axial slices, so they were essentially right circular cylinders with a height of approximately 3 cm and a diameter of 1.5 cm. An example region of interest is shown in Figure 7-2.

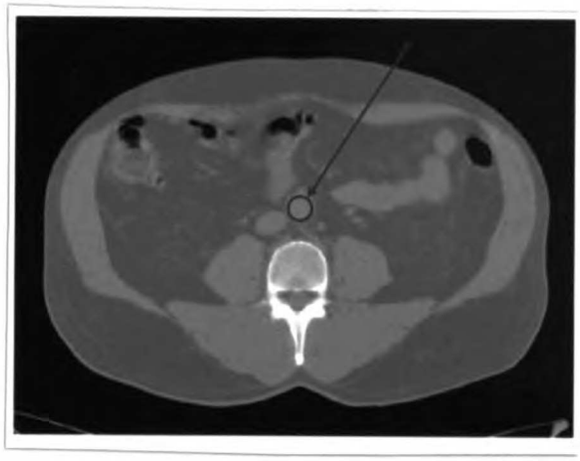


Figure 7-2: Illustration of region of interest in the descending aorta.

Region 2: Bone marrow. The bone marrow in the pelvis is a common location for significant non-specific uptake of ^{111}In-ProstaScint®. ROIs were drawn in the pelvis, in the region of the right posterior superior iliac spine, which is often hyperintense on ^{111}In-ProstaScint® images. The ROIs were drawn using CT, and confirmed visually by comparison with the ^{111}In-ProstaScint® images to make sure that they included the bone marrow regions. These regions were either right cylinders or cubes, with a height and width/diameter of approximately 1.5 cm, as shown in Figure 7-3.

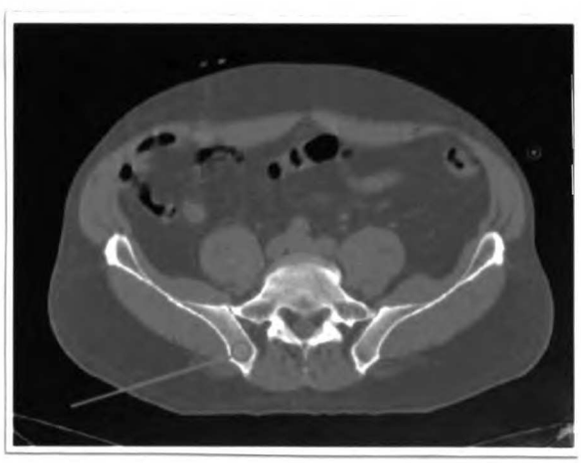


Figure 7-3: Illustration of region of interest in the iliac spine.

Region 3: Obturator muscle. The right external obturator muscle is fairly close to the prostate, and can be located fairly easily on CT since it stretches between the anterior pelvis at the pubis and the trochanteric fossa of the posterior femur. These ROIs were small parallelepipeds measuring approximately 1.5 to 2 cm on a side, and are illustrated in Figure 7-4.

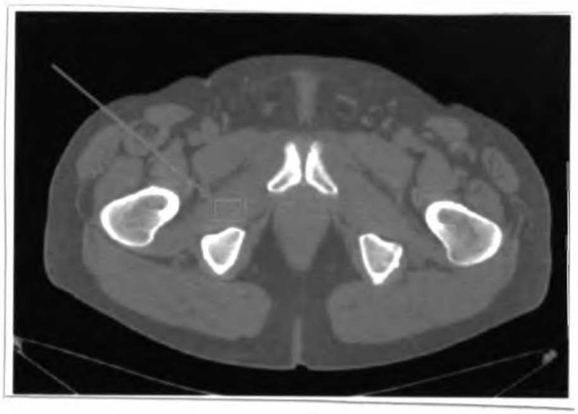


Figure 7-4: Illustration of the region of interest in the obturator muscle.

Region 4: Intestinal uptake: These regions were defined in a slightly different way than the other regions, in that they were defined from a combination of the CT and SPECT images rather than strictly being defined from the anatomical CT information. The intestines are large structures occupying much of the abdomen, and non-specific uptake of ^{111}In-ProstaScint® does not occur uniformly throughout the bowel. Thus, we used the CT images to identify the intestines and the SPECT image to identify regions of increased uptake, and selected a region of interest based on a combination of these images. Typically, these regions were small cylinders or cubes measuring approximately 2 cm on a side (an example region is shown in Figure 7-5). We measured the mean SPECT voxel value within these regions as well.

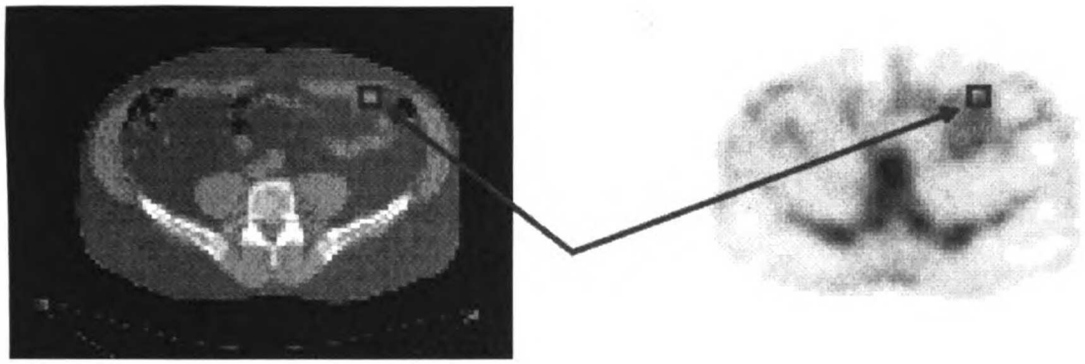


Figure 7-5: Illustration of the region of interest in the intestines. On this image the CT slice has been downsampled and registered into the SPECT coordinates, so that the two images correspond very closely to each other.

e) Statistical comparisons and analysis

We compared these different measures of ^{111}In-ProstaScint® concentration against one another using the Pearson product-moment coefficient, defined by:

$$r = \frac{n(\sum XY) - (\sum X)(\sum Y)}{\sqrt{[n\sum X^2 - (\sum X)^2][n\sum Y^2 - (\sum Y)^2]}} \tag{7.1}$$

where n is the number of points being compared and X and Y represent the two sets of points. This coefficient assesses the level of correlation between different sets of data, i.e. it can determine whether the radionuclide concentration in the descending aorta tends to correlate with the radionuclide concentration in the prostate. Thus, it allows us to determine which of these quantities have similar variations when we compare patients against one another.

For pre-therapy patients, we compared the activity concentration in the prostate against an empirical formula for predicting lymph node involvement in prostate cancer

patients. This formula is based on PSA and Gleason sums, and assigns a numerical percentage risk of lymph node involvement according to the formula:

$$\%rLN+ = 2(iPSA)/3 + 10(GS - 6). \quad (7.2)$$

where %rLN+ is the 'percent risk of lymph node positivity', iPSA is the patient's PSA score in ng/ml at the time of initial diagnosis, and GS is the patient's Gleason Sum from pathological examination[2]. This allowed us to determine whether or not quantitative analysis of ^{111}In-ProstaScint® images produced similar or different results from more conventional, empirical staging methods.

There are no similar metrics for assessing post-therapy patients, because a post-therapy patient who shows biochemical signs of prostate cancer recurrence (typically a rising PSA measurement over several months) is often treated as if they have disseminated disease, since the prostate itself has usually been removed surgically or destroyed with radiation. For these patients, we primarily depended on the image interpretation to detect local disease extensions or lymph node involvement. Previous studies have demonstrated that the presence of disease outside the prostatic fossa is a strong predictor of the success of 'salvage' radiotherapy, which is a radiation oncology treatment protocol that attempts to eradicate a patient's prostate cancer if prostatectomy has been unsuccessful[3], so the visual interpretation of the ^{111}In-ProstaScint® images is likely to provide the most useful information for these patients.

C. Results

1. Comparison of Image Reconstruction Methods

The following figures illustrate the differences between the various reconstruction methods, and provide a powerful example of the improvements that are possible with a more accurate tomographic reconstruction method.

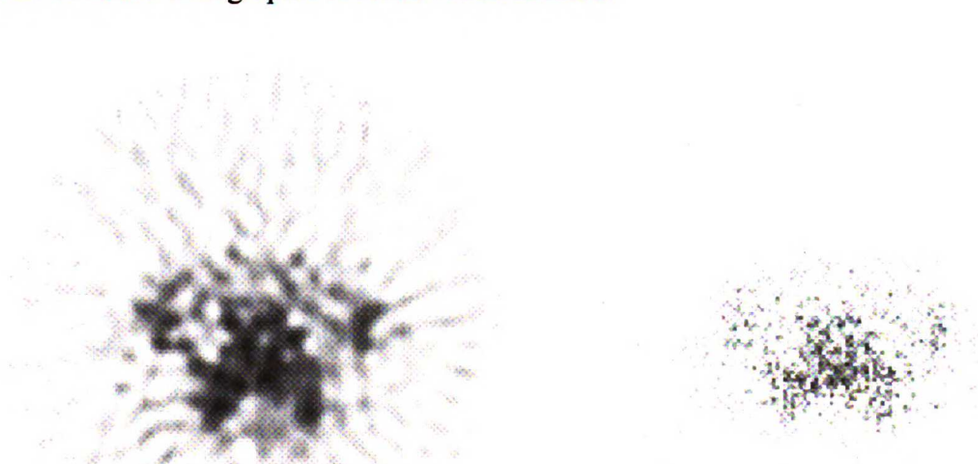


Figure 7-6: SPECT images reconstructed with filtered backprojection (left) and iterative reconstruction with attenuation correction only (right).



Figure 7-7: SPECT images reconstructed with iterative reconstruction with collimator correction only (left) and iterative reconstruction with attenuation and collimator correction (right).

The image on the right side of Figure 7-6 is similar to the image that would be produced by the SPECT cameras in many nuclear medicine clinics (including those at UCSF), although a large number of hospitals are still limited to filtered backprojection for SPECT reconstruction (i.e., left side of Figure 7-6), which is even worse. Although the images in Figure 7-7 presently require a significant amount of computer time -- approximately 21 hours for each image on an AMD 750 MHz computer -- they demonstrate a clear advantage in terms of noise and image detail. With the inclusion of collimator corrections, the bony anatomy in the pelvis is easily resolved, and it is possible to visualize structures in the central region of the body as well. The inclusion of attenuation correction eliminates the stray pixel values exterior to the patient, and also prevents the artificial enhancement of regions near the body surface. For example, the image on the left side of Figure 7-7, which is reconstructed without attenuation correction, shows the posterior iliac spine regions as being much darker than the rest of the pelvis. This artifact

is minimized in the image on the right side of Figure 7-7, which has incorporated both attenuation and collimator corrections.

In many clinical nuclear medicine systems, the SPECT images are post-processed with a low-pass filter before being displayed, in order to reduce the noise in the image. An example of this processing is shown in Figure 7-8.



Figure 7-8: SPECT image reconstructed using iterative reconstruction with attenuation correction only (left) and the same image after application of a low-pass filter (right).

Although filtering does indeed reduce the noise in the image, it also tends to blur the details of the image as well. Clearly, the iterative reconstruction with attenuation and collimator corrections still produces a superior image. In general, the physicians interpreting these images preferred the images reconstructed with attenuation and collimator corrections, although in a few cases the images reconstructed with these corrections were considered to have too much contrast, which detracted slightly from their readability.

2. Advantages of CT/SPECT ^{111}In-ProstaScint® Imaging.

Of the 13 patients studied in this trial, 3 of them had CT/SPECT staging results that differed from those produced by conventional SPECT imaging. In these 3 patients, the combination of coregistered CT slices and improved SPECT images provided additional information that significantly clarified the interpretation of the scan. In this section, we will review the results from these examples, and explain how the CT/SPECT images assisted the physicians in their assessment of the patient.

a) CT/SPECT clarifies suspicious bowel uptake.

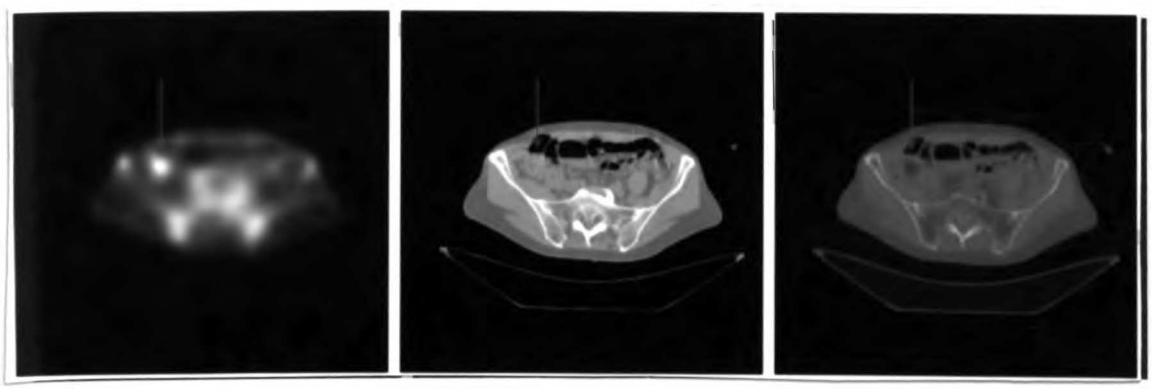


Figure 7-9: CT/SPECT ^{111}In-ProstaScint® images from patient with abnormal uptake in the lower abdomen.

In Figure 7-9, a SPECT image (after reconstruction using attenuation and collimator blurring corrections) shown in the left box reveals an abnormally bright spot in the upper left quadrant of the image (which is the patient's right side), indicated by the arrow. There are other bright regions in the image, but these locations are known to correspond with normal non-specific uptake of ^{111}In-ProstaScint®. The corresponding CT slice is shown in the center box. The bony anatomy of the pelvis can be clearly visualized, along with internal structures such as the bowel, which displays a combination of filled and

empty areas. The dark internal regions correspond to empty space in the intestines. It can be seen that the bright area visualized on the SPECT image corresponds to a loop in the bowel, which is a common location for non-specific uptake of ^{111}In-ProstaScint®. This impression is confirmed by inspecting the overlay image, where the red colors correspond to higher concentrations of ^{111}In-ProstaScint®. In this case, the information provided by the CT/SPECT system was able to rule out the presence of disease, whereas the SPECT information by itself would have produced equivocal results.

b) CT/SPECT highlights potential seminal vesicle invasion

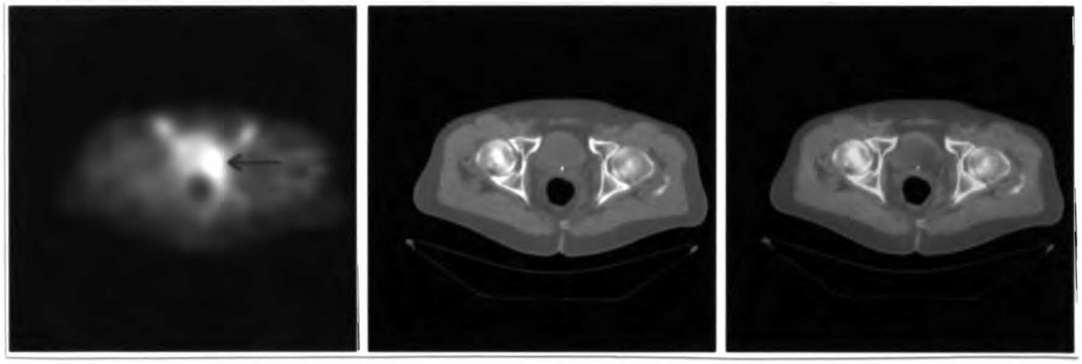


Figure 7-10: CT/SPECT ^{111}In-ProstaScint® images of patient with elevated radiotracer uptake at prostate base.

In Figure 7-10, a focus of increased ^{111}In-ProstaScint® uptake can be seen in the SPECT image shown in the left box. This focus can be identified as being anterior to the rectum (visualized as the darker circle along the midline of the image), but its precise location is difficult to determine due to the poor resolution of the SPECT image and the lack of anatomical landmarks. This ambiguity makes it difficult to determine whether or not it represents actual disease. The coregistered CT slice shown in the center box contains several features of interest. First, one can clearly visualize the outlines of the rectum,

bladder, and bony anatomy. Second, the small bright point near the very center of the image is a metallic marker that was implanted in the patient for an earlier radiation therapy treatment. This marker indicates the base of the prostate, and closer inspection of this region reveals that the seminal vesicles can be seen branching off from the prostate base in this image. Such information is significant because the seminal vesicles are a common location for local cancer extension. Thus, this hotspot on the ^{111}In-ProstaScint® image could potentially indicate seminal vesicle involvement. This result can be seen most clearly on the overlay image in the right box, where the darker orange region shows the 'hot spot'. This particular patient had previously undergone radiation therapy, so the presence of disease in the seminal vesicles could indicate a local recurrence of cancer, but one still treatable by radiation or other local therapies.

Conventional SPECT imaging in this same region did not demonstrate any abnormal uptake. Furthermore, magnetic resonance imaging and spectroscopy in this region were equivocal for the presence of disease. The full evaluation of this image is hampered by the fact that no pathological data exists to confirm or deny the presence of seminal vesicle disease (our experimental protocol did not allow for further interventions in the patient's management beyond imaging). However, nuclear medicine techniques are sensitive to very small amounts of tracer, so it is possible that the CT/SPECT images are revealing a microscopic region of prostate cancer that is not visualized by other imaging modalities. Future data on this patient could possibly reveal more about this question, but there has not yet been sufficient time to generate such follow-up data.

c) CT/SPECT confirms non-specific uptake in the liver

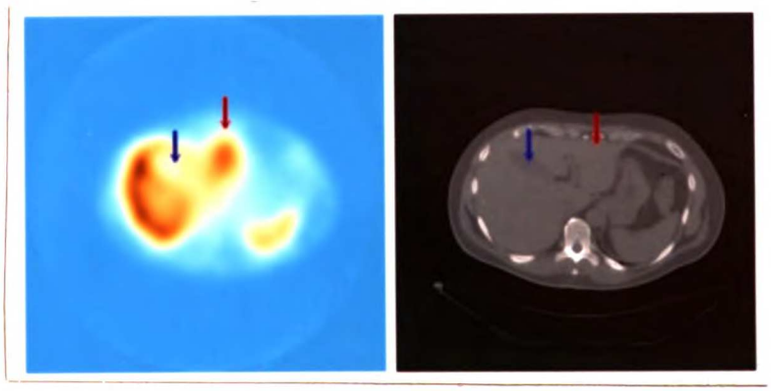


Figure 7-11: CT/SPECT ^{111}In-ProstaScint® image of patient with abnormal but benign liver uptake.

In this case, an exact registration between the two image sets could not be achieved, because the region shown here was too far away from the registration markers for correct matching. This situation was not typical in the CT/SPECT imaging protocol, but occurred in this patient because a secondary CT/SPECT image was requested of this region following evaluation of the patient's images from the UCSF nuclear medicine clinic. The SPECT image has therefore been reconstructed using the collimator corrections, but without attenuation correction (an attenuation artifact is visible along the exterior edge of the liver). Dark orange regions indicate areas of higher uptake; regions with less uptake are colored in blue.

Potential areas of concern are shown on the SPECT image at the left, and are indicated by arrows. The blue arrow marks an area of unexpectedly low uptake, whereas the red area marks an area of suspicious high uptake. The corresponding CT slice is shown on the right. Here we see that the blue arrow points to the gall bladder, which typically does not take up ^{111}In-ProstaScint® with high affinity, and the red arrow points to the left lobe of the liver, which readily takes up ^{111}In-ProstaScint®. Thus, the areas of

concern on the SPECT image can be completely and satisfactorily explained by the patient's anatomy. This example demonstrates that the CT/SPECT system can help to illuminate the nuclear medicine results in patients with unusual anatomical variations. As an aside, this example also shows that for some image interpretation questions, an exact registration is not necessary, although an exact image match would always be preferable.

d) Overall impressions from combined CT/SPECT imaging.

The preceding three examples demonstrated situations where the additional information provided by the CT scan significantly affected the interpretation of the SPECT image. In the remaining ten patients, the reports generated by interpretation of the CT/SPECT images were not appreciably different from those generated by conventional SPECT imaging in the UCSF Nuclear Medicine Clinic. However, there was a clear and strong preference among the interpreting physicians for the combination images, because of the anatomical information that could be obtained from the registered CT data. ^{111}In-ProstaScint® SPECT images have a reputation among the nuclear medicine community as being complex and difficult to interpret; in some situations it may even be difficult to locate the prostate itself because of the lack of body structural detail. Experienced physicians usually are able to draw on their depth of experience to discriminate benign abnormal uptake from disease, but having the CT information makes the interpretation of the SPECT images far more straightforward.

3. Quantitative Results

Although 13 patients were imaged, one patient's set of images could not be registered sufficiently for the proper application of the quantitative analysis techniques. The results for the remaining 12 patients are presented in this section.

a) Total image counts

Figure 7-12 shows the total counts in the raw ^{111}In-ProstaScint® projection data, normalized for the total injected activity and the time between injection and imaging. For these patients, the injected ^{111}In-ProstaScint® dose was 5.2±0.3 mCi and the mean time between injection and imaging was 96±1.6 hours. The error bars on these columns are 10% wide, which is approximately the precision of the camera for repeated SPECT studies.

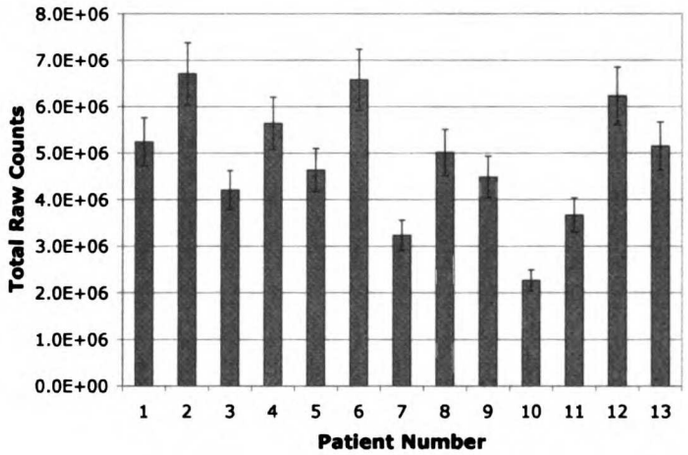


Figure 7-12: Total counts in SPECT projection data from the CT/SPECT system.

The mean and standard deviation of the total ^{111}In-ProstaScint® counts (across all patients) is $(4.8\pm1.3)\times10^{6}$. Thus, the variability in total counts is much larger than the

variability in the injected dose and imaging time, which reflects underlying physiological differences between patients (such as the rate at which ^{111}In-ProstaScint® is washed out of the bloodstream or taken up by the liver). This inter-patient variability should be accounted for when comparing patients to each other.

b) Location of the maximum voxel value.

Figure 7-13 is a histogram of the number of times that the maximum voxel value in the image occurred in a specific anatomical site (i.e., liver, penile blood pool, descending aorta, or spinal vertebrae).

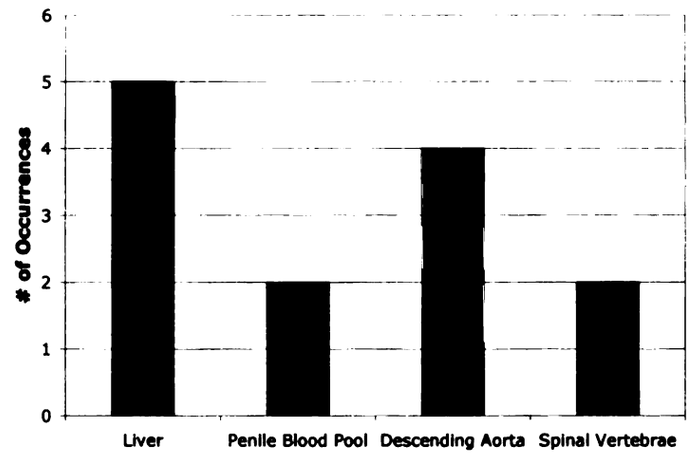


Figure 7-13: Histogram of anatomical locations of the maximum voxel value in the ^{111}In-ProstaScint® SPECT image.

Although the liver is a common location for the maximum concentration of ^{111}In-ProstaScint®, it is not visible in every SPECT study due to differences in the patient anatomy and the limited field of view of the gamma camera. However, in those studies where the liver was visible, it had the most intense uptake of ^{111}In-ProstaScint®. Other areas of maximum uptake were the penile blood pool, descending aorta, and spinal

vertebrae. Based on these results, it seems unlikely that an ^{111}In-ProstaScint® image could be evaluated using an image segmentation routine to locate potential tumor locations, because these areas all represent non-specific uptake of ^{111}In-ProstaScint®, and are areas unlikely to represent true disease. However, these results further reinforce the need for combined CT and SPECT imaging, because they imply that accurate localization will be critical in separating cancer-related uptake from non-specific uptake.

c) Measurements of ^{111}In-ProstaScint® Concentration

Figure 7-14 shows the concentration of ^{111}In-ProstaScint® in the prostate or prostate bed, based on the template-projection-reconstruction method and least-squares fitting.

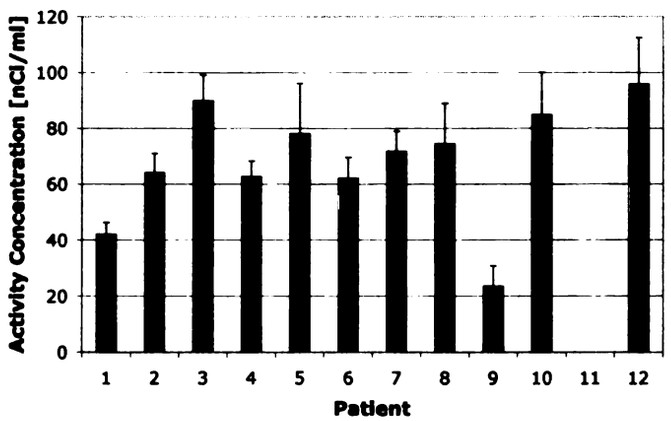


Figure 7-14: ^{111}In-ProstaScint® concentration within the prostate or prostate bed.

We were not able to obtain a measurement of the prostate bed for patient #11 in this analysis, because this patient had been referred for ^{111}In-ProstaScint® scanning specifically to evaluate potential lymph node involvement in the upper abdomen, so the normal scanned region was moved superiorly to accommodate this request. Thus, the

prostate region was incompletely imaged on this patient, and so we could not measure the concentration accurately.

Figure 7-15 shows the average concentration of ^{111}In-ProstaScint® in the region of interest in the descending aorta.

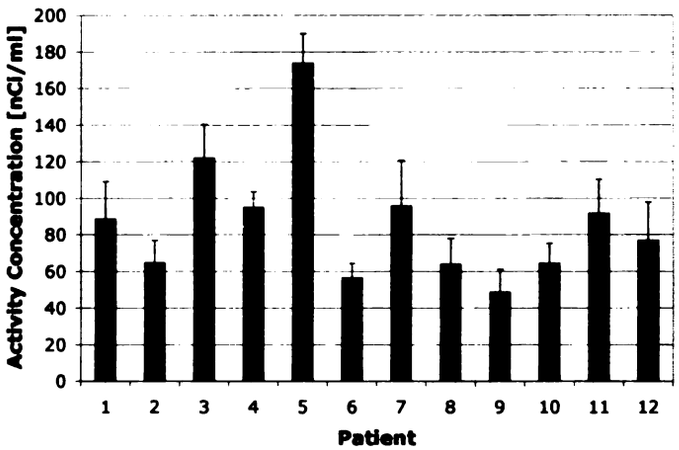


Figure 7-15: ^{111}In-ProstaScint® concentration within the descending aorta.

The regions chosen for this measurement are all located above the bifurcation in order to make them easier to find on anatomical images, but there is nothing distinct about this location physiologically. Thus, this measure is a good indicator of the concentration of ^{111}In-ProstaScint® in the bloodstream.

Figure 7-16 displays the activity concentration of ^{111}In-ProstaScint® in the bone marrow of the iliac spine.

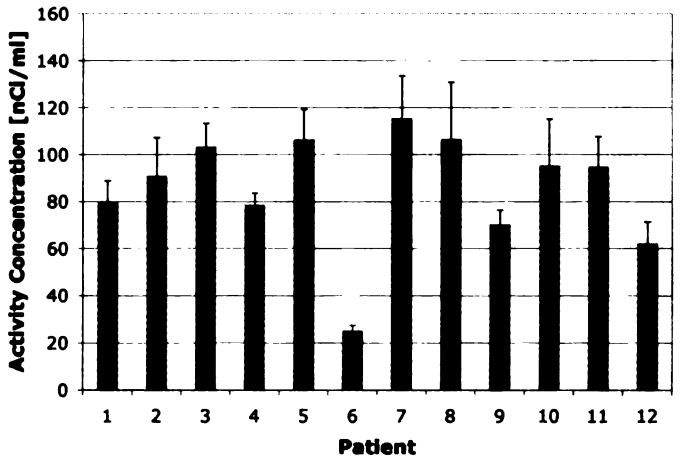


Figure 7-16: ^{111}In-ProstaScint® concentration within the iliac spine.

Although the bone marrow is not a specific target for ^{111}In-ProstaScint®, we can see from this chart that there is still a significant concentration of the radiotracer in these areas.

Figure 7-17 shows the concentration of ^{111}In-ProstaScint® in the obturator muscle in the pelvis.

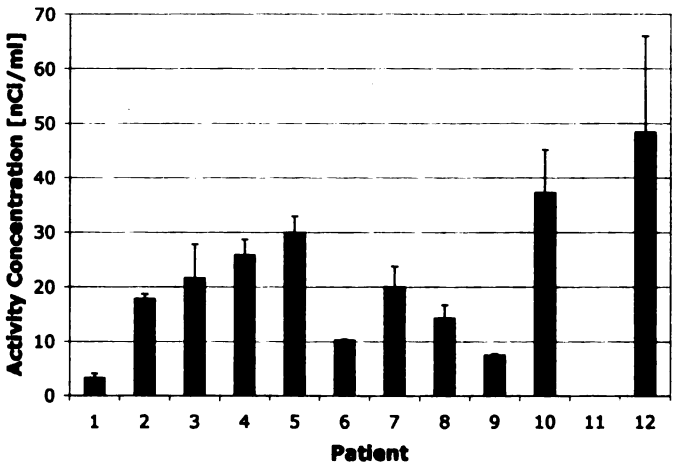


Figure 7-17: ^{111}In-ProstaScint® concentration within the obturator muscle.

The results for patient #11 are again excluded because of incomplete imaging of this area of the pelvis for this patient. In general, these concentrations are lower than in some of the other non-tumor areas, which is most likely due to the fact that there are no specific uptake or trapping mechanisms for ^{111}In-ProstaScint® in muscle.

Figure 7-18 shows the concentration of ^{111}In-ProstaScint® in the intestinal regions of interest.

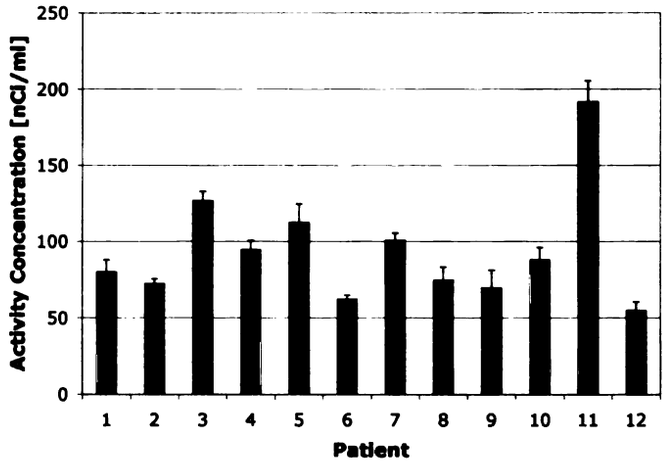


Figure 7-18: ^{111}In-ProstaScint® concentration within the intestinal region.

The intestines are a location of significant non-specific uptake of ^{111}In-ProstaScint®, and although the dietary restrictions and bowel cleansing treatments in the ^{111}In-ProstaScint® protocol can lessen this effect, they do not completely eliminate it.

d) Summary and Statistical Analysis

In Figure 7-19, we plotted the five previous graphs on a single scale, to facilitate comparison between the various quantitative measures of ^{111}In-ProstaScint® concentration.

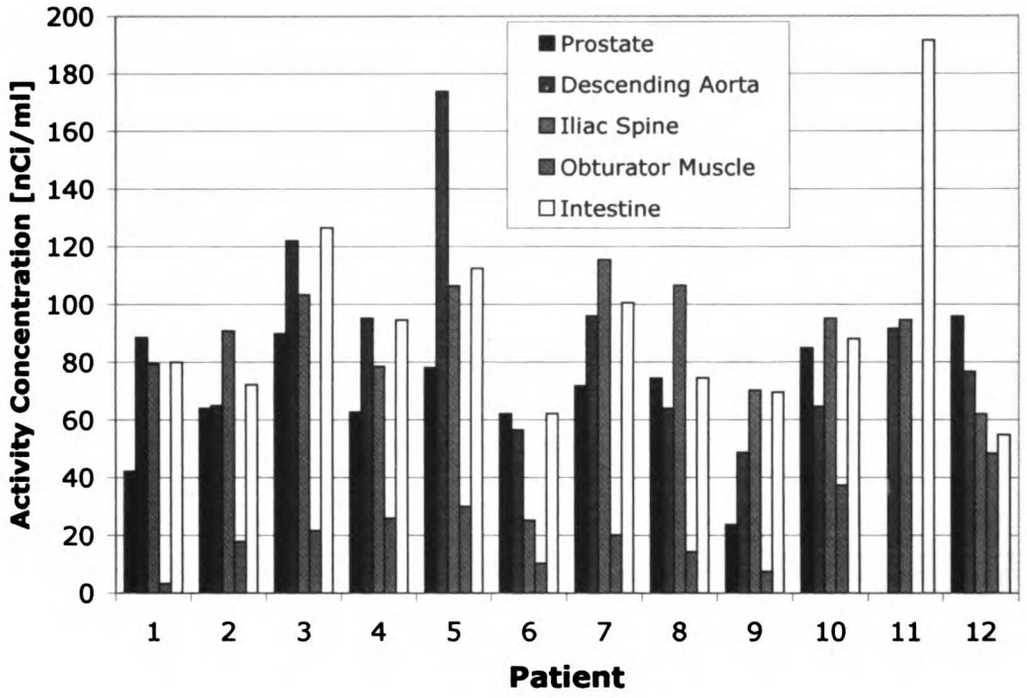


Figure 7-19: Summary chart of quantitative measurements of ^{111}In-ProstaScint® uptake.

In general, the uptake in the prostate (or prostate bed) is higher than in the obturator muscle, and lower than in the descending aorta, intestines, and bone marrow. This graph is another good illustration of the challenges of ^{111}In-ProstaScint® imaging – the prostate region cannot be identified based solely on concentrations of ^{111}In-ProstaScint®, even though it presumably has a higher concentration of PSMA than any of the other tissues chosen for analysis. This graph further reinforces the concept that coregistered anatomical information will be essential for improving ^{111}In-ProstaScint® imaging.

Table 7-III lists the correlations between the different quantitative measures of uptake. Because the Pearson product-moment correlation is symmetric, cells above the diagonal have been left blank. The 'total counts' entry is the total raw counts in the ^{111}In-ProstaScint® projection data, from Figure 7-12.

Correlation Table

	Total Counts	Prostate	Descending Aorta	Iliac Spine	Obturator Muscle	Intestine
Total Counts	1					
Prostate	0.357	1				
Descending Aorta	0.742	0.364	1			
Iliac Spine	0.444	0.286	0.482	1		
Obturator Muscle	0.157	0.785	0.255	0.131	1	
Intestine	0.536	0.290	0.470	0.468	0.060	1

Table 7-III: Pearson product-moment correlations between the different measures of quantitative uptake.

A perfect correlation would produce a correlation value of 1, as shown by the values along the diagonal of Table 7-III. In general, the different quantitative measures are only weakly correlated, with the exception of the total counts/descending aorta and prostate/obturator muscle correlations. Since ^{111}In-ProstaScint® is administered via intravenous injection, it naturally follows that the amount of ^{111}In-ProstaScint® in the bloodstream should correlate to the total counts in the image. The relatively high correlation between concentrations in the prostate and obturator muscle probably reflects the fact that these two structures are fairly close to each other in the body, so they receive similar blood flow. The correlation also suggests that the ratio between the concentrations in the prostate and the obturator muscle might be a useful measure of comparing patients to each other.

We plotted this prostate/obturator ratio against the 'percentage risk of lymph node positivity' (%rLN+) quantity based on PSA and Gleason sums, as shown in Figure 7-20.

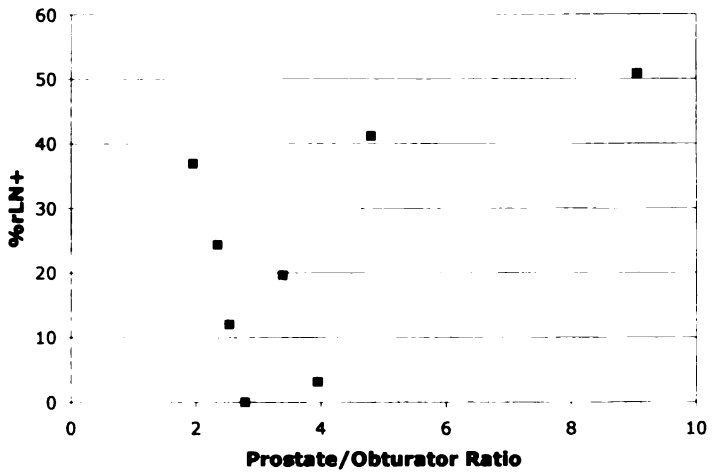


Figure 7-20: Plot of the prostate/obturator ratio versus percentage risk of lymph node positivity.

The correlation between these points is low (0.584) and is dominated by the outlying point in the upper right corner of the graph, so the prostate/obturator ratio is not a good predictor of the %rLN+ score. However, because ^{111}In-ProstaScint® specifically targets the PSMA, it is based on very different biochemical markers than the total PSA level or the Gleason sum. Thus, this result is simply an indication that the ^{111}In-ProstaScint® scan provides different information about the patient than the %rLN+ score. We will assess the value of that difference further in the following section.

D. Discussion

1. Limitations of this study

As this was primarily a pilot study of the CT/SPECT system for ^{111}In-ProstaScint® patient imaging, we faced some key limitations. The first was that none of the patients participating in this study showed evidence of distant disease outside the prostate (one patient, as shown in the case studies, could have had local disease extension). In

particular, none of the research patients were considered to have convincing evidence of prostate cancer in the lymph nodes, either on SPECT alone or on CT/SPECT. Although we did not perform an exhaustive review of all ^{111}In-ProstaScint® patients scanned at UCSF, a review of 30 recent patients revealed only 2 with definitive lymph node disease, so the 'hit-rate' for lymph node positivity is quite low. This fact means that we were not able to make any quantitative measurements of suspected or confirmed lymph node disease. If suspicious lymph nodes had been seen on the CT scan, we could have attempted to measure the concentration of ^{111}In-ProstaScint® in those regions, but no such lymph nodes were observed in the review of the CT images (given the low sensitivity of CT for early-stage lymphadenopathy, this was not surprising). Thus, we are not able to make any concrete statements about the uptake of ^{111}In-ProstaScint® in the lymphatic system or assess how this might appear on CT/SPECT images of ^{111}In-ProstaScint®.

A second limitation was the lack of a satisfactory gold standard for determining the presence of lymph node disease. Even assuming that one could convince research patients to agree to the full dissection of the prostate bed and all potentially involved lymph nodes (a highly unlikely proposition, given the substantial morbidity associated with such a procedure), such a test is still not completely reliable, because of many potential errors in the retrieval of this tissue and its subsequent analysis. Furthermore, this type of dissection is not normally performed at UCSF, which would have made obtaining such data difficult. Most importantly, a typical pelvic lymphadenectomy only samples a small number of the potentially involved lymph nodes, which further limits our ability to assess the sensitivity and specificity of ^{111}In-ProstaScint®. We could simply leave all the patients untreated and determine which of them develop severe lymph node

disease first, but such an approach is clearly unethical. Thus, at this stage of the research, we can only discuss how the results from CT/SPECT and SPECT alone differ from each other, and we cannot assess either of them on the basis of an objective 'truth'.

Future studies will be able to address these limitations more effectively. As additional patients are studied, we are more likely to find patients with convincing evidence of prostate cancer-related lymphadenopathy. As the follow-up time on these patients increases, we will also be able to review survival data on these patients (controlled for the type of treatment that they receive) and retrospectively perform risk stratification on them, to see if the combination of ^{111}In-ProstaScint® and CT/SPECT truly provides a significant benefit for staging prostate cancer.

2. Quantitation results

Despite these limitations, we have obtained several encouraging results. Although we obviously could not remove the tissues from the patient to confirm the quantitative measurements, we did find that both quantitation techniques used in this analysis were easy to apply to these patient data. The template-projection-reconstruction method is more suited to the prostate, where we can define organ boundaries and quickly project and reconstruct several templates. The only disadvantage is that the assumption of uniform activity within the region may not always be correct, but this could be solved with more templates or by switching to the 'direct method' of image quantitation that was used for measurements of activity concentration in other areas. In either case, the presence of the coregistered CT image provides helpful anatomical landmarks, and makes identification of the regions much simpler.

The results of the quantitative measurements indicate that the prostate/prostate bed does not usually have the highest concentration of ^{111}In-ProstaScint®, so it is unlikely that a potential lymph node would either (and the small size may create a lower apparent concentration, as we saw for the small 'tumor' spheres in Chapter 5). Therefore, an image segmentation routine based on SPECT voxel values is unlikely to be able to automatically discriminate between areas of prostate cancer and areas of non-specific uptake, unless anatomical information is somehow also included in the image processing.

The pre-therapy patients all had prostate/obturator concentration ratios of at least 2:1, which agrees with a similar analysis of this quantity by Sodee[4]. Sodee used a semiquantitative analysis of the ratios between the image voxel values in the prostate and the image voxel values in the external obturator muscle on ^{111}In-ProstaScint® SPECT scans, and found that this ratio predicted the presence or absence of prostate cancer on quadrant or sextant biopsy. Ratios in excess of 3:1 generally corresponded to prostate cancer, and ratios less than 3:1 generally corresponded to the absence of disease. Although this analysis was done without the benefit of an attenuation and collimator corrected SPECT image, it further supports the idea of using the prostate/obturator quantity as a means of comparing patients to each other.

The comparison between the %rLN+ score and our measure of the prostate/obturator ratios is intriguing, because the two results are essentially uncorrelated with each other. Thus, they are likely to be providing different types of information about the patient's prostate cancer. Polascik *et al* compared the results of ^{111}In-ProstaScint® scanning (based on image interpretation alone) with empirical staging algorithms such as the %rLN+ score, using pelvic lymphadenectomy of the middle chain

of external iliac vessels as the basis for comparison. They reported that ^{111}In-ProstaScint® scanning had a lower sensitivity and negative predictive value than the empirical algorithms, but higher specificity and positive predictive value. When empirical and ^{111}In-ProstaScint® results were combined, the result was a higher positive predictive value (72.1) than any of the individual tests (40.5-66.7) separately[5]. Thus, in future studies with larger numbers of patients, we may be able to evaluate empirical staging algorithms and quantitative ^{111}In-ProstaScint® scanning together using a proportional hazards analysis, to more precisely determine the benefits of this type of measurement.

3. Improved image reconstruction and combined CT/SPECT

The most valuable impact of this study has been the demonstration that CT/SPECT ^{111}In-ProstaScint® imaging is possible and provides significant benefits in terms of image interpretation. The example images in this chapter clearly show that a significant benefit in image quality can be obtained by using the information from a coregistered CT scan, an accurate mathematical model of the imaging process, and an iterative reconstruction method. Although the computational time to produce these images is currently too long for clinical use, computer speeds are improving relentlessly, so these types of reconstructions will eventually be fast enough to use in a busy nuclear medicine clinic. Even at their current speeds, they can be completed in a day, so they could be selectively applied to certain patients whose images produced equivocal or unclear findings.

Although the UCSF CT/SPECT system is a unique machine, other research teams have investigated combined imaging for ^{111}In-ProstaScint®. These investigators have acquired CT, MRI, and ^{111}In-ProstaScint® SPECT images on separate machines, and then

registered them together on a graphical workstation, either by manually manipulating the images or by using semi-automated methods based on mutual information seen on the two images. Hamilton *et al* used the blood vessels seen in the ^{99m}Tc-labeled red blood cell nuclear images and the contrast-enhanced blood vessels in a conventional CT scan as corresponding structural elements. By aligning these structures together, they were able to produce registered images in the pelvis, which improved the interpretation of the ^{111}In-ProstaScint® scans[6]. The most noticeable improvement was being able to identify suspicious bowel uptake, similar to what we observed in the first CT/SPECT example case. Ellis *et al* used a manual, visual registration technique for fusing SPECT with CT or MRI images of the pelvis, and reported similarly encouraging results, including the possibility of image-guided prostate brachytherapy[7].

Our approach to combined CT/SPECT imaging has two primary advantages over these other techniques. The first is that the patients are imaged in a single session, preserving the relative positions of the body and the state of internal organs between the two scans. Second, our image registration depends on fiducial markers, which are less susceptible to interpretation errors since their shape and size are so simple. Thus, we can acquire images with almost no separation in time, and generate CT and SPECT images that can be quickly correlated over a wide region of the body. For these reasons, we feel that we currently have the highest-performance system for combined CT and SPECT imaging.

This study has clearly demonstrated the benefits of this system for image registration. Having a CT scan in exactly the same coordinates as the SPECT image, and being able to move through the two data sets accurately and simultaneously, was a major

benefit to interpreting physicians. In three of the thirteen patients, combined imaging had a significant impact on the staging report, and was useful both for identifying areas of potential prostate cancer and for excluding areas of non-specific uptake. In every case, the presence of the coregistered CT information was preferred, because the anatomical information helped to identify and locate structures in the body, and enabled the image readers to be more confident in their assessment of the image. Even though we cannot formally assess the sensitivity and specificity of the CT/SPECT imaging technique with these data, there is an overwhelming opinion that the benefits of combined imaging will indeed enable improved interpretation of ^{111}In-ProstaScint® imaging.

E. Summary

In this chapter, we have described the application of the CT/SPECT system to the task of ^{111}In-ProstaScint®-based staging. Patients in this research protocol were imaged using both conventional SPECT and the combined CT/SPECT system, to compare the results from the two studies. We also applied quantitative imaging methods to measure the concentration of ^{111}In-ProstaScint® in different organs and tissues. The benefits of the CT/SPECT technology – image registration, improved reconstruction, and image quantitation – can dramatically affect the resulting ^{111}In-ProstaScint® images and provide new information that may help to manage these patients. Although this particular study was not able to fully answer the question of whether or not CT/SPECT improves the staging of patients with prostate cancer, it has convincingly demonstrated that we can greatly improve the quality and quantity of information available to the nuclear medicine physician. This information will enable physicians to make optimal use of the unique

information enabled by ^{111}In-ProstaScint®, thereby providing the best possible information to the patients in their care.

References:

[1] H. M. Lamb and D. Faulds, "Capromab pendetide. A review of its use as an imaging agent in prostate cancer," *Drugs and Aging*, vol. 12, pp. 293-304, 1998.

[2] S. A. Seaward, V. Weinberg, P. Lewis, B. Leigh, T. L. Phillips, and M. Roach, 3rd, "Improved freedom from PSA failure with whole pelvic irradiation for high-risk prostate cancer," *International Journal of Radiation Oncology, Biology, Physics*, vol. 42, pp. 1055-62, 1998.

[3] D. Kahn, R. D. Williams, M. K. Haseman, N. L. Reed, S. J. Miller, and J. Gerstbrein, "Radioimmunoscintigraphy with In-111-labeled capromab pendetide predicts prostate cancer response to salvage radiotherapy after failed radical prostatectomy," *J Clin Oncol*, vol. 16, pp. 284-9., 1998.

[4] D. B. Sodee, R. J. Ellis, M. A. Samuels, J. P. Spirnak, W. F. Poole, C. Riester, D. M. Martanovic, R. Stonecipher, and E. M. Bellon, "Prostate cancer and prostate bed SPECT imaging with ProstaScint: semiquantitative correlation with prostatic biopsy results," *Prostate*, vol. 37, pp. 140-8, 1998.

[5] T. J. Polascik, M. J. Manyak, M. K. Haseman, R. T. Gurganus, B. Rogers, R. T. Maguire, and A. W. Partin, "Comparison of clinical staging algorithms and ^{111}Indium-capromab pendetide immunoscintigraphy in the prediction of lymph node involvement in high risk prostate carcinoma patients," *Cancer*, vol. 85, pp. 1586-92, 1999.

[6] R. J. Hamilton, M. J. Blend, C. A. Pelizzari, B. D. Milliken, and S. Vijayakumar, "Using vascular structure for CT-SPECT registration in the pelvis," *Journal of Nuclear Medicine*, vol. 40, pp. 347-51, 1999.

[7] R. J. Ellis, E. Y. Kim, R. Conant, D. B. Sodee, J. P. Spirnak, K. H. Dinchman, S. Beddar, B. Wessels, M. I. Resnick, and T. J. Kinsella, "Radioimmunoguided imaging of prostate cancer foci with histopathological correlation," *International Journal of Radiation Oncology, Biology, Physics*, vol. 49, pp. 1281-6, 2001.

Chapter 8: Future Possibilities for ^{111}In-ProstaScint® and CT/SPECT Imaging

In this dissertation, we have presented a system for combining CT and SPECT imaging. Although each imaging technology has significant benefits of its own, the information obtained from each modality also can be improved by combining it with information from the other. SPECT has tremendous sensitivity and the capability to monitor physiological processes that would be invisible to CT. Conversely, CT has the capability for high-resolution anatomical imaging that cannot be matched by SPECT. In addition, the data provided by CT can help to overcome some of the physical effects that negatively impact the SPECT image. We have presented and tested methods for overcoming these negative impacts, and have demonstrated that CT/SPECT can provide important benefits to ^{111}In-ProstaScint® imaging by improving image quality, providing an anatomical framework for image interpretation, and enabling quantitative imaging. In achieving these goals, we have reached a valuable point on the path to better care for prostate cancer patients. However, the combination of ^{111}In-ProstaScint® and CT/SPECT has much future potential, both for the immediate need of accurate staging and the long-term need of improved prostate cancer care. Thus, although this work produced several valuable results, it should be only the beginning of a larger and more comprehensive endeavor. In this chapter, we will build on the foundation established by this research, and describe some of its future opportunities and potential.

A. Future developments for combined CT/SPECT Imaging.

1. A brief historical perspective.

When the CT/SPECT project began in our research group in 1994, the thought of combining CT and SPECT into a single imaging machine was seen by the imaging community as being quite farfetched, and its usefulness was completely untested. Much has changed during the intervening years, and combined imaging (particularly combined CT/SPECT and combined CT/PET) now is seen as a rich new horizon for nuclear medicine in particular and the field of radiology in general. Although improvements in technology have been partly responsible for this shift in attitudes, the major driving force has been the success of combined imaging in its early trials. In addition to the results from this study, research in our group has demonstrated that CT/SPECT brings useful improvements to myocardial perfusion imaging [1] and dosimetry for radionuclide-based therapies[2]. A research group at the University of Pittsburgh has taken a parallel approach to ours, by combining CT and PET scanners into a single machine with a common patient table. This approach has demonstrated notable successes in oncology imaging [3] for several different types of cancer, including esophageal[4] and ovarian[5] cancers. Although the field is still new and there is still much room for additional technological improvements, the case for multimodality imaging is extremely strong and currently is the focus of much clinical and commercial activity.

Because of the unique advantages of multimodality imaging, medical imaging equipment companies are beginning to manufacture commercial imaging systems based on these principles. At the present time, three different combined CT/PET systems are in

production: the

Discovery™ LS

complete PET s

in quality from e

commercially, b

route, which we

2. A ne

General Electric

known as the Mi

CT technologies

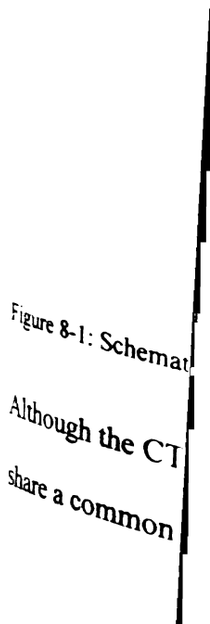


Figure 8-1: Schemat

Although the CT

share a common

production: the Philips Gemini™, the Siemens Biograph™, and the General Electric Discovery™ LS. These systems combine modern, multislice capable CT scanners with complete PET scanners, and can therefore produce both types of images without any loss in quality from either modality. CT/SPECT systems are also being produced commercially, but in this area the technology development has chosen a slightly different route, which we will examine more closely in the next section.

2. A new system for combined CT/SPECT imaging.

General Electric (GE) Medical Systems has recently introduced a commercial product known as the Millenium VG 'Hawkeye'. This scanner is based on combining SPECT and CT technologies into a single gantry, as illustrated in Figure 8-1:

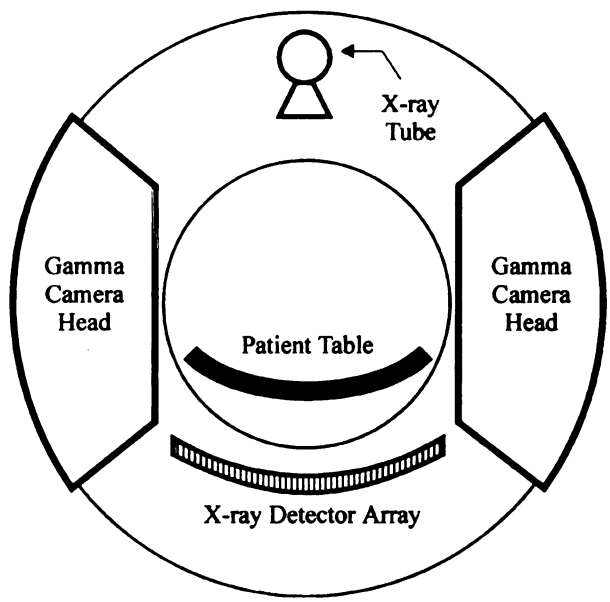


Figure 8-1: Schematic of the GE Medical Systems Hawkeye CT/SPECT system.

Although the CT and SPECT systems are mounted on a common gantry, they do not share a common detector, as with the ETCT system described in Chapter 3. Photons

from the radiopharmaceutical are detected by two conventional gamma cameras, and the x-ray CT fan beam and detector array are mounted between these cameras. The central axis of the x-ray fan beam is perpendicular to the central axes of the gamma camera heads, and the CT and SPECT studies are acquired sequentially rather than simultaneously. The positions of the x-ray tube and detector are fixed, but the gamma camera heads are free to move radially and thus can do automatic body contouring (which reduces the collimator blurring effect). All of the components are attached to a single gantry, which rotates around the patient for tomographic acquisitions. This common gantry allows the registration to be essentially automatic, without the need for fiducial markers or image fusion software. The CT subsystem acquires slices using a 256x256 image matrix size and a 10 mm slice thickness. The x-ray tube can produce a maximum of 140 kVp and 2.5 mA. The angular range of acquisition is 180 degrees plus the fan angle (approximately 215 degrees), and data is acquired in single slice mode. The gantry rotates at 2-3 rpm, so a typical CT acquisition takes about 15 minutes. The SPECT cameras produce a pixel size of 3.45 mm at 128x128 image matrix size.

This scanner takes a somewhat different approach to combined imaging than the UCSF CT/SPECT system. The SPECT component of the Hawkeye is an improvement over the current UCSF system, because it uses two gamma cameras and has the benefit of more modern detector technology. On the other hand, the CT scanner is significantly different from both the GE 9800 used in the UCSF system and a current, modern CT scanner. These differences are highlighted in Table 8-I.

Comparison of CT Systems

	Hawkeye CT	GE 9800	GE Lightspeed Plus
Maximum X-ray Tube Current	2.5 mA	200 mA	250-300 mA
Slice Thickness	10 mm (fixed)	1.5-10 mm (variable)	1-10 mm (variable)
Minimum Scan Time	20 seconds/slice	2 seconds/slice	< 1 second/slice
Image Matrix Size	256x256	256x256 or 512x512	256x256 or 512x512
Number of slices/rotation	1	1	up to 16

Table 8-I: Comparison of CT parameters between the Hawkeye System and Conventional CT

The Hawkeye CT system thus is much more limited than the GE 9800 or a modern CT scanner, but this design choice also carries several advantages. First, the low beam current means that the shielding requirements are much lower than those required for a normal CT scanner, making the requirements for the site concordantly simpler. Second, the system is designed so that it can be easily added to existing nuclear medicine cameras, thus enabling an upgrade of the camera's capability without the cost of replacing an entire imaging machine. Finally, the addition of this type of CT system to a gamma camera increases its cost by only a small percentage, whereas the cost to attach a modern CT scanner would likely be a large fraction of the cost of the gamma camera itself.

For these reasons, the Hawkeye represents a new area for combined imaging, and the possibility for a fairly wide deployment of this technology. However, it also has some notable disadvantages when compared to a system such as the UCSF CT/SPECT system and these disadvantages pose two technical research questions:

(1) We observed in Chapter 4 that a 10 mm CT slice thickness was inadequate for image registration between CT and SPECT, given our current approach to image registration. Thus, if we wish to test the registration accuracy of the Hawkeye's single gantry against our existing system, we will need to devise a new image registration system that is not so dependent on CT slice thickness. One potential approach to this could be to use line sources instead of small points. These lines would be imaged in cross-section on every tomographic slice, so we could derive equations for the lines in CT and SPECT coordinates and determine the registration accuracy based on those lines.

(2) The quantitation methods developed by our research group depend on accurate delineation of the regions of interest on the CT images, so the slice thickness limitation of the Hawkeye may be a factor in accurate quantitation as well. For larger structures, such as the myocardium, this limitation may not be significant, but it will certainly have an effect on our measurement of smaller targets in the body. Thus, we should apply some of the same tests from this work to the Hawkeye system, so that we can measure its ability to perform radioactivity quantitation, and determine whether or not it can be as accurate as the UCSF CT/SPECT system for this task.

Despite these potential technical limitations, one of the prime advantages of the Hawkeye system will be its increasing deployment in nuclear medicine clinics. This will help to move CT/SPECT imaging out of a purely research arena and into a more practical setting. Such a change will allow many more patients to be imaged on a combined system. We have seen in this project that there are some prostate cancer staging questions that are difficult to answer with a small patient population, so the Hawkeye should provide us with a more effective means of addressing those questions.

B. The future for ^{111}In-ProstaScint®

^{111}In-ProstaScint® is unique among prostate cancer staging techniques, because it evaluates for metastases over a wide area in a single study, and specifically targets the prostate-specific membrane antigen. However, its acceptance in the field of prostate cancer care has been slow for several reasons. The first is that the images generated from a conventional ^{111}In-ProstaScint® scan are difficult to interpret, leading to ambiguities and reports with equivocal findings. Second, its specificity also is a potential drawback, because while many types of prostate cancer express the prostate-specific membrane antigen (PSMA), there are certainly those that do not. For these types of cancer, ^{111}In-ProstaScint® cannot provide much information, and could even be misleading. Finally, the treatment of prostate cancer has evolved and developed largely based on the existing staging tools, and thus has a very conservative approach. Even if a patient does not have demonstrated metastases, even a small potential risk (according to an empirical staging method) is enough to cause patients to choose a combination of hormonal and surgical/radiation treatments. Although this 'better safe than sorry' approach could lead to overtreatment in some patients, most patients are willing to accept significant side effects rather than the potential of undertreating the disease. Until we can develop a staging methodology that is 100% accurate (or very close to it), this conservative approach to treatment will remain the most palatable option for many patients.

As we have shown in this work, CT/SPECT has the potential for significantly improving ^{111}In-ProstaScint® imaging, and making it far more accessible to the entire nuclear medicine community, (assuming that the Hawkeye and systems like it continue to be manufactured). However, even under the most optimum conditions, it may take time

for ^{111}In-ProstaScint® to achieve its goal of markedly improved prostate cancer staging. Therefore, we should consider other potential applications for ^{111}In-ProstaScint®, which will also make use of its special capabilities.

1. Image-guided radiation therapy.

Radiation oncology researchers at UCSF have identified a subgroup of prostate cancer patients who benefit from whole pelvic radiation therapy in addition to radiation therapy of the prostate itself. The group obtaining the maximum benefit from this treatment approach are those who have a %rLN+ (as described in the previous chapter) between 15% and 35%[6]. The presumed mechanism behind this benefit is that patients with lower risk scores (%rLN+ < 15%) do not have disease in the lymph nodes, and those with higher risk scores (%rLN+ > 35%) have metastatic disease beyond the pelvis, so neither group will be helped by whole pelvic irradiation. For the group with medium risk, the whole pelvic irradiation is thought to affect occult pelvic lymph nodes, thereby increasing the disease-free survival of these patients.

CT/SPECT and ^{111}In-ProstaScint® could play an important role in the management of these patients. With the increased image quality and quantitative accuracy of CT/SPECT, it might be possible to reliably identify those lymph nodes that contain cancer. If such nodes could be identified, they could be treated selectively, which would presumably provide the same survival benefits while reducing radiation-induced side effects. Alternatively, one could treat the suspicious lymph nodes to a higher dose, and potentially increase the survival of these patients while keeping the rate of side effects constant. In both cases, the CT/SPECT would provide a secondary benefit of assisting in the therapy planning process. Modern conformal radiation therapy, including

intensity-modulated radiation therapy (IMRT), depends on CT information for treatment planning and dose calculations. Thus, the coregistered CT/SPECT images could provide anatomical landmarks to guide the treatment planners, or the treatment plan could even be based on the CT/SPECT information itself. Not all prostate cancer patients would benefit from this type of treatment, but for certain patients this technology could prove very useful.

2. PSMA-based therapies.

Many staging tests for prostate cancer are based on determining the presence or absence of disease in a particular location (i.e. prostate, seminal vesicles, lymph nodes, etc.). Therapies for prostate cancer are similarly location-based, such as removal of the prostate and lymph nodes, or radiation treatments to an anatomical region. However, the increasing body of knowledge about the human genome and its protein products is giving rise to new types of staging questions and tests. These tests focus on biochemistry, and attempt to classify the prostate cancer based on its genotype as well as its extent in the body. Although such information is helpful in understanding the nature of prostate cancer, it is even more important for designing therapies, which can be tailored to the individual and their specific type of prostate cancer.

An example of this approach can be found in breast cancer treatment. Some types of breast cancer overexpress the human epidermal growth factor receptor 2 (HER2), and such overexpression can be determined by testing extracted tissue samples from cancer sites. In patients that overexpress this receptor, a treatment (Herceptin®) is available that specifically blocks the HER2 receptor, thereby targeting these specific types of breast

cancer. Such an approach is more specific than a general hormone blockade or chemotherapy regimen, and has been shown to increase the survival time and overall response rate of these patients[7].

The specificity of ^{111}In-ProstaScint® for PSMA could enable it to play an important role in similar therapies for prostate cancer. There are several cancer therapies based on PSMA currently in development[8-10] that exploit either the PSMA protein or its underlying genetic sequence. These therapies either use a non-radiolabeled molecule to interfere with the functioning of the prostate cancer cell or an antibody similar to the one used for ^{111}In-ProstaScint® to target cells with a cytotoxic agent. Thus, these therapies depend on a high concentration of PSMA to be effective. Obviously, tissue biopsy could be used for measuring the presence of PSMA. However, a key advantage of ^{111}In-ProstaScint® for measuring PSMA concentrations would be that the results of the imaging test could be a strong predictor of therapeutic effectiveness, because both the ^{111}In-ProstaScint® and the planned therapeutic would be delivered by intravenous injection. Thus, the successful delivery and subsequent binding of ^{111}In-ProstaScint® to the tumor sites would mean that the diagnostic agent would reflect the uptake mechanism of the therapeutic agent. In this scenario, ^{111}In-ProstaScint® would be used to simulate the therapy and identify those patients that would receive the most benefit from treatment. Based on such data, the therapy could then be applied in the most efficient way.

C. Conclusions

There is great promise in the future for both combined CT/SPECT imaging and ^{111}In-ProstaScint®. Both are fairly new technologies, but the doors that they open today will lead to many new applications and ideas. The synergy between ^{111}In-ProstaScint® and CT/SPECT will both improve the current practice of prostate cancer staging and allow for the development of new and more powerful therapeutic approaches. Likewise, as combined imaging becomes more widely available, the potential for its uses will extend far beyond its initial tasks, and be limited only by the creativity and hard work of the radiopharmaceutical designers. The fields of nuclear medicine and radiology will benefit tremendously from these advances, and ultimately they will allow us to take better care of our patients, who are the true reason and guiding motivation for this work.

References:

[1] A. J. Da Silva, H. R. Tang, K. H. Wong, M. C. Wu, M. W. Dae, and B. H. Hasegawa, "Absolute quantification of regional myocardial uptake of 99mTc-sestamibi with SPECT: experimental validation in a porcine model. [Comment In: J Nucl Med. 2001 May;42(5):780-1 UI: 21235439]," *Journal of Nuclear Medicine*, vol. 42, pp. 772-9, 2001.

[2] H. R. Tang, "A Combined X-ray CT-Scintillation Camera System for Measuring Radionuclide Uptake in Tumors," Bioengineering Ph.D. Dissertation, University of California Berkeley and University of California San Francisco, 1998, pp. 171.

[3] T. Beyer, D. W. Townsend, T. Brun, P. E. Kinahan, M. Charron, R. Roddy, J. Jerin, J. Young, L. Byars, and R. Nutt, "A combined PET/CT scanner for clinical oncology," *J Nucl Med*, vol. 41, pp. 1369-79., 2000.

[4] C. C. Meltzer, J. D. Luketich, D. Friedman, M. Charron, D. Strollo, M. Meehan, G. K. Urso, M. A. Dachille, and D. W. Townsend, "Whole-body FDG positron emission tomographic imaging for staging esophageal cancer comparison with computed tomography," *Clin Nucl Med*, vol. 25, pp. 882-7., 2000.

[5] S. Makhija, N. Howden, R. Edwards, J. Kelley, D. W. Townsend, and C. C. Meltzer, "Positron emission tomography/computed tomography imaging for the detection of recurrent ovarian and fallopian tube carcinoma: a retrospective review," *Gynecol Oncol*, vol. 85, pp. 53-8., 2002.

[6] S. A. Seaward, V. Weinberg, P. Lewis, B. Leigh, T. L. Phillips, and M. Roach, 3rd, "Identification of a high-risk clinically localized prostate cancer subgroup receiving maximum benefit from whole-pelvic irradiation," *Cancer Journal from Scientific American*, vol. 4, pp. 370-7, 1998.

[7] M. D. Pegram and C. O'Callaghan, "Combining the Anti-HER2 Antibody Trastuzumab with Taxanes in Breast Cancer: Results and Trial Considerations," *Clin Breast Cancer*, vol. 2 Suppl 1, pp. S15-9., 2001.

[8] J. Tasch, M. Gong, M. Sadelain, and W. D. Heston, "A unique folate hydrolase, prostate-specific membrane antigen (PSMA): a target for immunotherapy?," *Crit Rev Immunol*, vol. 21, pp. 249-61, 2001.

[9] A. Uchida, D. S. O'Keefe, D. J. Bacich, P. L. Molloy, and W. D. Heston, "In vivo suicide gene therapy model using a newly discovered prostate- specific membrane antigen promoter/enhancer: a potential alternative approach to androgen deprivation therapy," *Urology*, vol. 58, pp. 132-9., 2001.

[10] F. Watt, A. Martorana, D. E. Brookes, T. Ho, E. Kingsley, D. S. O'Keefe, P. J. Russell, W. D. Heston, and P. L. Molloy, "A tissue-specific enhancer of the prostate-specific membrane antigen gene, FOLH1," *Genomics*, vol. 73, pp. 243-54., 2001.

For reference

Not to be taken from the room.

7062402

3 1378 00706 2402